STRUCTURE, PROCESSING, AND PROPERTIES OF POLYACRYLONITRILE/CARBON NANOTUBES COMPOSITE FILMS

A Thesis
Presented to
The Academic Faculty

by

Huina Guo

In Partial Fulfillment
of the Requirements for the Degree
Doctor of Philosophy in the
School of Polymer, Textile and Fiber Engineering

Georgia Institute of Technology
May 2007

STRUCTURE, PROCESSING, AND PROPERTIES OF POLYACRYLONITRILE/CARBON NANOTUBES COMPOSITE FILMS

Approved by:

Dr. Satish Kumar, Advisor
School of Polymer, Textile and Fiber Engineering
Georgia Institute of Technology

Dr. John Muzzy
School of Chemical Engineering
Georgia Institute of Technology

Dr. Samuel Graham
Woodruff School of Mechanical Engineering
Georgia Institute of Technology

Dr. Art Ragauskas
School of Chemistry and Biochemistry
Georgia Institute of Technology

Dr. Johannes Leisen
School of Polymer, Textile and Fiber Engineering
Georgia Institute of Technology

Date Approved: December 18, 2006

ACKNOWLEDGEMENTS

I would like to express my sincere gratitude to many people for support during the course of this study. Firstly, I wish to thank deeply my advisor Dr. Satish Kumar for his insight in resolving many of the problems encountered throughout my work. Dr. Kumar has advised me right from the beginning of my study at Georgia Tech, encouraged me to solve the problems, and gave me invaluable suggestions and endless support during all stages of my Ph.D. research. He has been a great source of ideas and given me the freedom to work on approaches interesting to me. He has also given me encouragement and suggestions beyond the academic field.

I would like to thank my committee members, Drs. Sam Graham, Johannes Leisen, John Muzzy and Art Ragauskas for their encouragement, support, and advice.

Also, I would like to thank Dr. Johannes Leisen for guiding the NMR study, Dr. Tao Liu for guiding the optical absorption study, Sudhakar Jagannathan for surface area measurement, and Marilyn Minus for TEM study and assistance with the X-ray diffraction. I wish to appreciate the help of Drs. Asif Rasheed, Sreekumar Veedu, and all other members of our group during my research and thesis writing.

Finally, I would like to express my appreciation to my parents and my husband, Jidong Zhang, for their long-standing encouragements, support and sacrifice.

TABLE OF CONTENTS

LIST OF TABLES

LIST OF FIGURES

SUMMARY

Vapor grown carbon nanofibers (VGCNFs) developed in 1980s are being widely used for reinforcing composites. Carbon nanotubes (CNTs) discovered in early 1990s can be classified as single wall carbon nanotubes (SWNTs), double wall carbon nanotube (DWNTs) and multi wall carbon nanotubes (MWNTs) depending on the number of graphene layers forming the carbon nanotube. SWNT, DWNT, MWNT and VGCNF are being incorporated in various polymers to improve mechanical, thermal, and electrical properties of the resulting composites. Polyacrylonitrile (PAN), a commercially important polymer is a predominant precursor for carbon fiber. Carbonized and activated PAN/SWNT films can find application as electrochemical supercapacitor electrodes. This study is focused on the structure, processing and properties of polyacrylonitrile/carbon nanotube composite films. Limited studies on composite fibers are also reported. History, synthesis, properties and characterization of carbon nanotubes and the literature on polymer/CNT composites are briefly reviewed in Chapter 1.

PAN/SWNT composite films in the weight ratio of 60/40 have been processed from dispersions in dimethyl formamide (DMF) with a unique combination of properties including tensile strength, tensile modulus, in plane dc electrical conductivity, dimensional stability, low density, solvent resistance, and thermal stability. PAN molecular motion above the glass transition temperature (T_g) in the composite film is significantly suppressed, resulting in high PAN/SWNT storage modulus above T_g (40 times the PAN storage modulus at 180ºC). In order to understand the PAN-SWNT interaction, the composite film has been treated in DMF at various temperatures and the

resulting film has been characterized using X-ray diffraction. This study is presented and discussed in Chapter 2.

Processing, structure, and properties of PAN/VGCNF composite films, in the weight ratios of 95/5, 90/10, 80/20, 60/40, 40/60, and 10/90, are presented in Chapter 3. The specific modulus of PAN/VGCNF composite films is consistent with the predictions of the Halpin-Tsai equation up to 20% VGCNF loading. The magnitude of modulus and other property enhancement is reduced as the nanofiber loading is increased (up to 40 %). Above 40 wt% VGCNF, modulus and tensile strength values are lower than those of the control PAN. Electrical percolation was observed at 3.1 vol% VGCNF loading. These composites have also been characterized by dynamic mechanical analysis, wide angle X-ray diffraction, as well as scanning and transmission electron microscopic techniques.

Structure, processing, and properties of PAN/carbon nanotubes (CNTs) composite films containing SWNTs, DWNTs, MWNTs and VGCNFs are reported in chapter 4. Five different types of SWNTs have been used. Weight percentage of carbon nanotubes was 5 and 10 wt%, with limited studies being carried out at 20 wt% carbon nanotube loading. Surface area of all carbon nanotubes was characterized using nitrogen gas adsorption analysis. In general tensile modulus and tensile strength of the films increased with the increasing surface area, though from the data it is clear that other factors such as catalytic impurity and amorphous carbon content also play a role in controlling the mechanical properties. PAN/CNT films have been characterized by wide angle X-ray diffraction (WAXD), Raman spectroscopy, and scanning as well as transmission electron microscopy. Films have also been characterized for electrical conductivity, tensile, thermo-mechanical, and dynamic mechanical properties. Mechanical property results

have been analyzed in terms of the nanotube surface area determined by nitrogen gas adsorption. Solution behavior of various composite films has been monitored using DMF, suggesting that PAN exhibit stronger interaction with all five types of SWNTs than PAN interaction with DWNT, MWNT, or VGCNF.

PAN/CNTs composite films and fibers have been characterized using solid state ^{1}H NMR spin lattice relaxation time (T_1) saturation recovery experiments as described in Chapter 5. With the addition of nanotubes, the T_1 values for the PAN matrix generally decreased, and the reduction mechanism is discussed. Usefulness of this technique to assess carbon nanotube dispersion as well as problems posed by catalytic and other impurities are also discussed.

The optical anisotropy of SWNT in PAN/SWNT composite fibers was observed in their polarized infrared spectra and analyzed using the effective medium theory in Chapter 6. This data has been used to calculate SWNT optical constants using the modified Maxwell Garnet (MG) theory. This method can be used to determine the optical constants of other nano materials.

Conclusions and recommendations for future work are presented in Chapter 7.

CHAPTER 1

INTRODUCTION

1.1 HISTORICAL BACKGROUND OF CARBON NANOTUBE

Carbon nanotubes (CNTs) and carbon nano fibers (CNFs) have attracted the attention of many scientists and engineers for their potential applications in nanocomposites. The first carbon fiber was processed in 1889[1] and developed during 1960s. A patent published in 1986 first reported the production of carbon nano fibers grown on a nucleated ceramic surface by passing a methane gas stream over the surface.[2] In the 1980s, CNFs were widely developed and found applications as additive in polymers and as catalyst support material.[3, 4] Vapor grown carbon nano fibers (VGCNFs) are distinguished from other types of CNFs, such as polyacrylonitrile- and mesophase pitch-based fibers, in their physical properties, method of production, and low cost fabrication. The history of carbon nanotubes goes back to 1960[5], when Bacon grew the graphite whiskers on a nucleated ceramic surface. However, these graphite whiskers were not recognized as CNTs until the 1990s. In 1991, Iijima[6] discovered multi wall carbon nanotube (MWNT) in the samples grown on the negative end of the electrode used in the arc-discharge evaporation of carbon in an argon-filled vessel. In 1993, Iijima and Ichihashi[7], and Bethune et al.[8] reported the preparation of single wall carbon naotube (SWNT) independently. In 1996, Dai et al.[9] and Thess et al.[10] independently discovered double wall carbon nanotube (DWNT) when they synthesized SWNT. The time-line for the carbon nanotubes development is listed in Table 1.1.

Table 1.1. Chronology of the developments of carbon fibers and carbon nanotubes

When	Whos	Event
1889	Hughes, T. V. and Chambers, C. R.	Discovery of carbon fibers[1]
1960s	Scientists	Wide development of carbon fibers
1960	Bacon, R.	Production of graphite whiskers with graphite layers [5] (grown in a dc arc under a pressure of 92 atmospheres of argon and at 3900 ^{o}C; 1-5 μm in diameter; and up to 3 cm in length)
1986	Tibbetts, G. G. and Devour, M. G.	Discovery of CNF[2].
1980s	Scientists	Wide development of CNF[3, 4]
1991	Iijima	Discovery of MWNT[6] (arc-discharge evaporation method; 4-30 nm in diameter; and up to 1 μm in length)
1993	Iijima and Ichihashi	Discovery of SWNT[7] (arc-discharge evaporation method with the presence of iron; 0.7-6 nm in diameter; and 700 nm in the longest length)
1993	Bethune et al.	Discovery of SWNT[8] (arc-discharge evaporation method with the presence of cobalt; and 1.2 nm in diameter)
1996	Dai et al.	Discovery of DWNT[9]
1996	Thess et al.	Discovery of DWNT[10]

1.2 SYNTHESIS OF CNT

Synthesis techniques for CNT include arc discharge[6-8], laser ablation[10, 11], chemical vapor deposition (CVD)[12-16], and high pressure carbon monoxide (HiPCO)[17, 18].

Arc-discharge method is based on an arc discharge which is generated by running an a.c or d.c current (50-100 A) at certain voltage (~20 V) between two graphite electrodes under an inert atmosphere of Helium or Argon.[19] The diameter of SWNT prepared by this method by Iijima and Ichihashi[7] is in the range of 0.7 to 1.65 nm. In laser ablation method, graphite target is vaporized by a pulsed or continuous laser in an oven (~1200 ^{o}C) filled with helium or argon gas.[11] The carbon species produced during laser vaporization are then removed by the flowing gas from the high temperature zone and deposited on a conical water-cooled copper collector outside the furnace to form nanotubes. For the production of SWNT, a small amount of metal catalyst such as Ni and Co is added to the graphite target. These SWNTs have uniform diameter and are formed into bundles with 5-20 nm in diameter and tens to hundreds of micron long. In CVD synthesis, a gaseous carbon source which commonly includes methane, carbon monoxide and acetylene is heated by using an energy source such as plasma or a resistively heated coil. Then the resultant carbon diffuses towards the substrate to form carbon nanotubes. For the production of SWNT, the metal catalyst such as Ni, Fe or Co is used. The diameters of SWNTs prepared by CVD method are in the range of 2-4 nm[13] while that of MWNTs are in the range of 70 -100 nm.[16]

Recently, SWNTs are processed using the high pressure carbon monoxide (HiPCO) method. SWNTs used in our work are synthesized based on this method by Carbon Nanotechology Inc. (CNI). CO provides the carbon source (CO+CO =

C(solid)+CO_2) and $Fe(CO)_5$ is the catalyst precursor. SWNTs are produced by flowing CO mixed with a small amount of $Fe(CO)_5$ through a heated reactor.[17] By controlling the pressure of CO, the size and diameter distribution of nanotubes can be roughly controlled. SWNTs as small as 0.7 nm in diameter have been produced by this method and the average diameter of SWNTs is approximately 1.1 nm.[18] This method is promising for bulk production of carbon nanotubes.

1.3 PHYSICAL PROPERTIES OF CNT

1.3.1 Mechanical Properties

SWNT exhibits remarkable mechanical properties. Young's modulus of individual (10,10) nanotube is predicted to be 0.64 TPa[20], close to that of silicon carbide nanofibers (~0.66 TPa). Ruoff et al.[21] predicted tensile strength of SWNT to be ~20 GPa. The bending modulus of the armchair SWNT (n, n) is calculated to be 963 GPa and that of the zigzag tube (n, 0) is 912 GPa.[22] Recently, some experiments have been done to estimate the mechanical properties of SWNT.[22, 23] The stiffness of SWNT was estimated by directly observing their freestanding room temperature vibrations in a transmission electron microscope (TEM) and the average Young's modulus is determined to be 1.3 TPa.[22] Li et al.[23] experimentally estimated the tensile strength of individual SWNT to be 22.2 ± 2.2 GPa based on the measured tensile strength of PVC/SWNT rope minicomposites. SWNTs tends to aggregate together to form rope (or bundle) with several tens of nanometers. Many studies have predicated that the Young's modulus along the SWNT rope to be 1 TPa.[20, 24] The Young's modulus transverse to the SWNT rope has been calculated as 15 GPa[25] or 60.3 GPa[26]. The shear modulus has been predicted to be 19.5 GPa[27] or 22.5 GPa[26]. Using AFM, Yu et al.[28] determined the

Young's modulus of fifteen SWNT ropes to be in the range of 320-1470 GPa with a mean of 1002 GPa. These SWNT ropes have a tensile strength ranging from 13 to 52 GPa (mean 30 GPa) and break at a strain of 5.3 %. Li et al.[23] measured directly the tensile strength of PVC/SWNT composites and then extrapolated the tensile strength of SWNT rope to be 2.3±0.2 to 14.2±1.4 GPa. Walters et al.[29] used AFM to measure the elastic strain of the SWNT rope and determined the tensile strength and breaking strain to be 45 GPa and 5.8 %, respectively. The theoretical and experimental mechanical properties of carbon nanotubes are listed in Table 1.2.

1.3.2 Electrical Properties

The axial electrical conductivity for one SWNT rope reaches to 10^6 S/m at 300 K.[10] The small diameter SWNTs can become superconductive at low temperature: 1.4 nm diameter SWNT shows superconductivity at 0.55 K[30] and 0.5 nm diameter SWNT shows superconductivity at 5 K.[31] The axial electrical conductivity of the aligned MWNT film is 5000 S/m.[32]

Table 1.2. Mechanical properties of carbon nanotubes

Sample	Mechanical Properties	Calculated Data	Experimental Data
Individual SWNT	Young's modulus (GPa)	1000[23] (10,10) tube: 640.3[20]	1250[22]
	Tensile strength (GPa)	20[21]	3.6±0.4 to 22.2±2.2[23]
	Shear modulus (GPa)	500[23] 270-300[33]	
	Bending modulus (GPa)	(n,n) tube: 963[20] (n,0) tube: 912[20]	
SWNT rope	Young's modulus (GPa)	1000[23]	320-1470 (mean:1002)[25] 1000[28]
	Tensile strength (GPa)		2.3±0.2 to 14.2±1.4[23] 45±7[29] 13-52 (mean: 30)[28]
	Shear modulus (GPa)	22.5[26] 19.5[27]	6.0[26] 1.0[27]
	Break strain (%)		5.3[28] 5.8±0.9[29]

1.3.3 Thermal Properties

The thermal expansion behavior of carbon nanotubes can be quantified by the coefficient of thermal expansion (CTE). CTE can be volumetric (β) or linear (α) coefficient of thermal expansion as expressed in the following equations:[34]

$$\beta = (\frac{\partial V}{\partial T})_p \frac{1}{V} \tag{1.1}$$

$$\alpha = (\frac{\partial L}{\partial T})_p \frac{1}{L} \tag{1.2}$$

Where V is the volume, L is the length, T is the temperature and the derivative is at constant pressure P. The radial shrinkage of SWNT bundles was observed in the temperatures ranging from 290 to 1600 K by the X-ray diffraction (XRD) measurements.[35] Figure 1.1 shows the XRD profile of SWNT bundles measured at 290 K and the 2D triangular arrangement of SWNT bundles. In Figure 1.1, parameter V is the van der Waals gap between nanotubes, D is the diameter of an individual SWNT, and L_0 is the triangular lattice constant (L_0=D+V). The linear CTE perpendicular to the tube axis was determined to be $(-1.5\pm0.1)\times10^{-6}$ K^{-1} between 290 and 330 K, and $(-2.5\pm0.1)\times10^{-6}$ K^{-1} between 1300 and 1550 K. By assuming that the expansion along the tube axis in the SWNT bundle is similar to the in-plane expansion of graphite, the volumetric CTE is expected to be negative. Maniwa et al.[36] also determined the CTE in the SWNT bundles by X-ray studies. The linear CTE was determined as $(-1.5\pm2)\times10^{-6}$ K^{-1} for the tube diameter and $(7.5\pm2.5)\times10^{-6}$ K^{-1} for the lattice constant between 300 K and 950 K. The CTE for the inter-tube gap (V) was determined to be $(42\pm14)\times10^{-6}$ K^{-1}, which is larger than that for the c-axis thermal expansion in graphite (26×10^{-6} K^{-1}). The CTE of individual SWNT is only studied theoretically[37-39]. CTE in the direction perpendicular to

the tube axis is simulated to be -12×10^{-6} K^{-1} at 400 K[39]. Based on molecular dynamics (MD) simulation[37] and a effective analytical method[38], the CTE in the radial direction in the armchair SWNT is found to be less than that in the axial direction. However, the radial CTE is larger than the axial one for zigzag SWNTs. The radial CTE is independent on the chirality, however the axial CTE depends on the chirality of SWNT.[37, 38] The CTEs in both radial and axial directions are negative at low temperature and become positive at high temperature. With increasing SWNT diameter, the CTEs decrease and approach that of the graphene sheet.

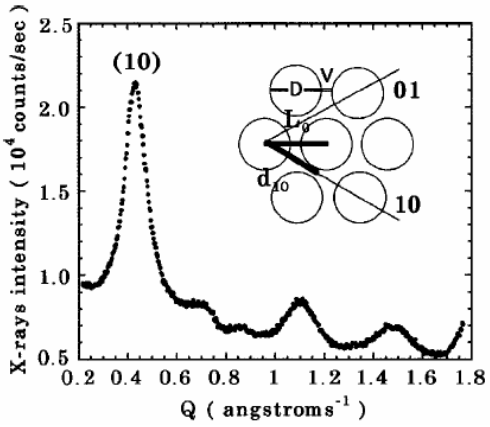

Figure 1.1. XRD profile measured at 290 K and the lattice arrangement of the SWNT bundles.[35]

The CTE along the fiber axis in VGCNF is in a range from 1.2×10^{-6} K^{-1} to 1.8×10^{-6} K^{-1} at about 1500K[40]. Bandow[41] found that the radial thermal expansion in MWNT is almost the same as the c-axis thermal expansion of graphite in the temperature ranging from 10 to 320 K. From their x-ray diffraction experiments, the CTE along the

radial direction of MWNT is determined to be in a range from 1.6×10^{-5} K^{-1} to 2.6×10^{-5} K^{-1}.[42]

1.4 DISPERSION OF SWNT

SWNTs tend to aggregate and form 20-35 nm diameter ropes (or bundles) due to the strong van der Waals interaction between tubes (binding energy is about 900 meV/nm[43]). The SWNT ropes entangle together in the solid state to produce a highly dense, complex network structure. SWNTs are extremely resistant to wetting and do not have any surface functional groups. As SWNTs are dispersed in the polymer matrix, the viscosity of the polymer/SWNT dispersion increases due to the high surface area of nanotube especially when the SWNT loading is higher.[44] All of above factors make the dispersion of SWNT extremely difficult in any media. Therefore, achieving uniform dispersion or exfoliation of SWNT ropes in the solvent or polymer matrix is a critical challenge. The dispersion of SWNT can be improved by using non-covalent approaches such as the use of organic solvent, surfactant, ionic salt, and in-situ polymerization, and covalent approach (or chemical modification). In order to achieve good dispersion of nanotubes, sonication and shear mixing are used in many cases. However, the high-power sonication of nanotubes for a long time may cut tubes into small pieces and reduce the aspect ratio.[45] Therefore the power of sonicator and sonication time should be controlled.

1.4.1 Dispersion in Solvent

Bahr et al.[46] have studied the solubility of SWNT in various solvent (Table 1.3). The solubility of SWNT is only 95 mg/L for the best solvent, 1,2-dichlorobenzene. Ausman et al.[47] investigated the room-temperature solubility of SWNTs in five types of solvents and found that the non-hydrogen-bonding Lewis bases such as N,N-

dimethylformamide (DMF) and N-methylpyrrolidone (NMP) give the good solubility of SWNTs. The reason is that DMF and NMP have high values for β (the hydrogen bond acceptor ability), negligible values for α (the hydrogen bond donor ability), and high values for π* (solvatochromic parameter).

Table 1.3. Room-temperature solubility of SWNT in various solvents

Solvent	mg L^{-1}
1,2-Dichlorobenzene	95
Chloroform	31
1-Methylnaphthalene	25
1-Bromo-2-methylnaphthalene	23
N-Methylpyrrolidinone	10
Dimethylformamide	7.2
Tetrahydrofuran	4.9
1,2-Dimethylbenzene	4.7
Pyridine	4.3
Carbon disulfide	2.6
1,3,5-Trimethylbenzene	2.3
Acetone	—[b]
1,3-Dimethylbenzene	—[b]
1,4-Dimethylbenzene	—[b]
Ethanol	—[b]
Toluene	—[b]

[a] The sonicator bath water temperature rose to *ca.* 35 °C over the course of 1 h. [b] Solubility in these solvents was < 1 mg L^{-1}

1.4.2 Surfactant Assisted Dispersion

Moor et al.[48] suspended individual SWNTs in aqueous media using various anionic, cationic, nonionic surfactants and polymers, and compared their ability to suspend individual SWNT. For the ionic surfactants, sodium dodecylbenzene sulfonate (SDBS) is the best for the dispersion of individual SWNT while for the nonionic systems, surfactants with higher molecular weight suspend more SWNTs. The mechanism of SWNT dispersion in water using sodium dodecyl sulfate (SDS), sodium

dodecylbenzenesulfonate (NaDDBS) and TX100 has been studied in detail.[49] The surface of SWNTs can show negative or positive charges depending on the pH values of the media. SWNT is covered by the surfactant molecules that lie on the tube surface parallel to the tube axis. Surfactant introduces a repulsive force between nanotubes by overcoming the van de Waals attractive force between tubes. Because of their benzene rings, NaDDBs and TX100 disperse tubes better than SDS. Because of its head group and slight longer alkyl chain, NaDDBS disperses better than TX100. Smalley's group obtained the individual SWNT surrounded by SDS when dispersed nanotubes in SDS.[50]

1.4.3 Polyelectrolyte

Upon reduction with alkali metals such as Li or Na, SWNT forms polyelectrolyte which dissolves spontaneously in polar organic solvents in concentration up to 2.0 mg/mL in DMSO and 4.2 mg/mL in sulfolane. This method does not need sonication, surfactants or fuctinalization of SWNT.[51] With the treatment of the hydroxylamine hydrochloric acid salt (NH_2OH)(HCl), SWNTs were exfoliated or dispersed well in organic and aqueous solution.[52]

1.4.4 Polymer Assisted Dispersion

The semi conjugated organic polymer, poly (m-phenylene-co-2,5-dioctyloxy-p-phenylenevinylene (PmPV-co-DOctOPV) enhance the dispersion of SWNT in toluene.[53] During the formation of hybrid solution with 3 wt% SWNT loading, SWNT ropes are exfoliated due to the intercalation of polymer. The solubility of SWNT in $CHCl_3$ is up to about 2.2 mg/mL in the conjugated polymer, poly(aryleneethynylene) solution.[54] Star et al.[55] reported that the PmPV wrapped SWNTs disperse well in organic solvents. The

individual SWNT surrounded by SDS were mixed with polyvinyl pyrrolidone (PVP) obtaining the solubility of the PVP wrapped SWNTs to be as high as 1.4 g/L in water.[50]

1.4.5 In-situ Polymerization

During electrochemical polymerization of the aniline containing SWNTs, the donor-acceptor complexes formed, from which polyaniline/SWNT composite films with good uniformity and dispersion were prepared.[56] The in-situ polymerized SWNT/PMMA composites exhibit an increase in the low-temperature elastic modulus (10% higher than that of pure PMMA) with the addition of less than 0.1 wt % SWNT.[57] By in-situ polymerization, the polyimide/SWNT (0.1 vol% SWNT) composite films with enhanced electrical conductivity and thermal stability were obtained.[58]

1.4.6 Chemical Modification

Functionalization of carbon nanotubes improves their solubility or dispersibility in solvent or polymer matrices. However, during the chemical modification process, CNTs may be cut into short pieces (100-300 nm length)[59] and the nanotubes with smaller diameter are easily destroyed[60], which causes the reduction of aspect ratio. The ends of nanotubes contain highly curved hemispheres, therefore are highly reactive as compared with sidewalls. SWNTs can be chemically modified by strong acids such as HNO_3[59, 61-63], HCl[64], H_2SO_4/HNO_3[65] or H_2SO_4/H_2O_2[66], and by other strong oxidizing agents such as $KMnO_4/H_2SO_4$[67] or oxygen gas[68] to generate oxygenated functional groups at the ends and defect sites and to open the ends[69]. The 30 vol% HNO_3-treated SWNTs dispersed well in butanol/toluene or xylene/ethanol mixtures, which are poor solvents for the pristine ones.[70] The dispersibility of the acid-treated tubes increases with the hydrogen-bonding ability of solvents reaching 27 mg/L in ethanol and 35 mg/L in water. The

oxidized SWNT is reacted with thionyl chloride producing the acylchloride group on SWNT that can be linked to alkyl-aryl amine[71] or esters[72] to form the long alkyl tail modified SWNTs. These chemical modifications improve the solubility of nanotubes in solvents such as THF, CH_2Cl_2 and CS_2. The HCl and thionyl chloride treated SWNTs is attached to lipophilic and hydrophilic dendrons via amidation and esterification, resulting in the improvement of SWNT solubility in hexane and chloroform.[64] The acid treated SWNTs is reacted with derivatized pyrenes via esterification helping nanotubes dissolve in THF, chloroform and toluene.[73] The nitric acid and octadecylamine (ODA) treatment of SWNTs improve their solubility in tetrahydrofuran and 1,2-dichlorobenzene.[74] The H_2SO_4/HNO_3 (70 wt% HNO_3) treated SWNTs disperse well in the epoxy/SWNT (99/1) composites.[75]The sidewalls of nanotubes contain the defects such as pentagon-heptagon pairs, sp^3-hybridized defects and vacancies in the nanotube lattice. Strong acid can oxidize the sidewalls to generate the carboxylic acid, ketone, alcohol and ester groups.[76] The acid- treated SWNTs were then treated with thionyl chloride to form acyl chloride that then was reacted with ODA. These modifications of SWNTs improve the solubility of nanotubes.[76] The sidewalls of SWNTs have also been chemically modified using direct fluorination and subsequent nucleophilic substitution.[77]

1.5 CHARACTERIZATION OF CNT

1.5.1 Raman Spectroscopy

A powerful and nondestructive tool to characterize SWNT and SWNT/polymer composites is Raman spectroscopy. Figure 1.2 shows the Raman spectrum of SWNTs. There are four main features: radial breathing mode (RBM), G band, D band, and G' band (overtone of D* band).[78]

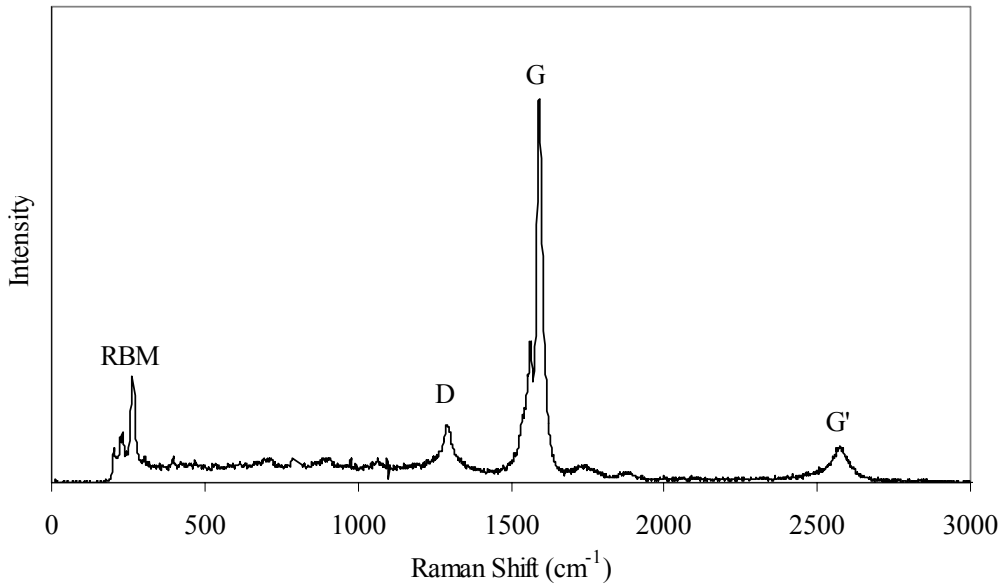

Figure 1.2. Representative Raman spectrum of SWNT.

RBM (in the 200-500 cm^{-1} range) corresponds to the in-phase radial displacement of the carbon atoms. SWNT shows sharp van Hove singularities in their density of state (DOS) at the Fermi surface.[79] Based on tight-binding model, the energy transition between the pairs of van Hove singularity for SWNT can be determined by Equation (1.3).

$$E_{ii}(d_t) = \frac{ka_{c-c}\gamma_o}{d_t} \tag{1.3}$$

where a_{C-C} is the nearest-neighbor C–C separation (1.42 Å[80]), γ_0 is the hopping matrix element (2.9 eV for best fitting Raman data or 2.7 eV for best fitting STS data[81]), d_t is the diameter of nanotubes, i is the order of van Hove transitions of SWNTs, and k is constant. When k is 2, 4, 8, the energy transitions are the first, second, third order van

Hove transitions for the semi-conducting nanotubes, respectively. When k is 6, 12, the van Hove transitions correspond to the first, second order transitions for the metallic tubes, respectively. The energy separation $E_{ii}(d_t)$ between van Hove singularities in the valence and conduction band DOS depends only on the tube diameter, as shown in Figure 1.3. The two low energy transition are the first order energy transition E_{11}^S and the second order energy transition E_{22}^S for semi-conducting nanotubes. The next higher energy transition is the first order energy transition E_{11}^M for metallic nanotubes followed by the third order energy transition E_{33}^S. For the small diameter nanotubes, E_{11}^M and E_{11}^S depend on the tube chirality due to the trigonal warping effect.

The RBM frequency ω_{RBM} is inversely proportional to the nanotube diameter d ($\omega_{RBM}=\alpha/d$) and α is experimentally found to be 248 cm^{-1} for the isolated SWNTs.[82] Considering the van der Waals forces between nanotubes in the SWNT bundles, the RBM frequency is related with diameter by Equation (1.4):

$$\omega_{RBM} = \frac{232}{d} + 6.5 \tag{1.4}$$

The intensity of RBM bands depends on the laser excitation energy (E_{laser}). It reaches its maximum intensity when E_{laser} matches the energy separation E_{ii} between the van Hove singularities in the electronic DOS of SWNT.[83] As the energy difference $\left|E_{laser} - E_{ii}\right|$ increases, the RBM linewidth increases and reaches the narrowest when $E_{laser}=E_{ii}$.[84] At the fixed laser energy, the linewidth of RBM increase with increasing SWNT diameter.[84] Recently, RBM band has been used to probe the aggregation state of SWNTs in solution or as solids.[85]

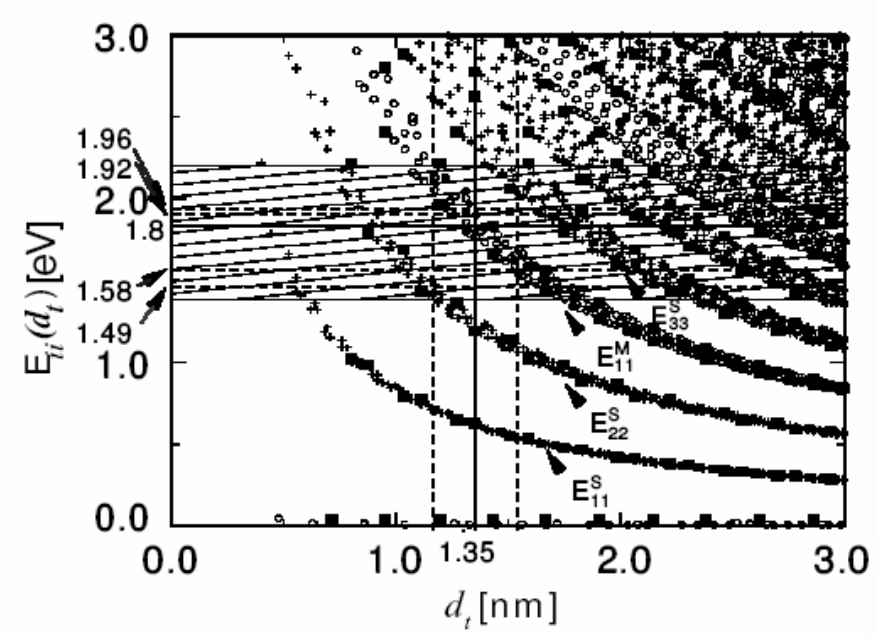

Figure 1.3. Calculation of the energy separations $E_{ii}(d_t)$ versus SWNT diameter in the range $0.7 < d_t < 3.0$ nm using $\gamma_0 = 2.9$ eV and a nearest neighbor carbon–carbon distance $a_{C-C} = 1.42$ Å. Semiconducting (S) and metallic (M) nanotubes are indicated by crosses and open circles, respectively. The filled squares denote zigzag tubes. The vertical lines denote $d_t = 1.35 \pm 0.20$ nm for a SWNT.[79]

The G band ranging from 1500 to 1605 cm^{-1} characterizes the vibrations mode along the nanotube axis. G band can be used to distinguish metallic from semi-conducting nanotubes. Semi-conducting nanotubes show two dominate Lorentzian features at the upper and lower frequency but metallic nanotubes show one Lorentzian at the upper frequency and the other Breit–Wigner–Fano (BWF) line at the lower frequency.[86] The lower frequency component attributes to vibrations along the circumferential direction (ω_G^-) while the higher frequency component associates with vibrations along the tube axis (ω_G^+). ω_G^+ is independent on the tube diameter while ω_G^- show the strong d^{-2} dependence which is different for the semi-conducting and metallic tubes.[78] G band can be used to determine the orientation factor of SWNT in the

polymer/SWNT composites by measuring Raman VV and VH intensities at a series of angles to the orientation direction.[87] D band (in the 1250-1450 cm^{-1} range) induced by the defect on the nanotube can be used to characterize the structure perfection of nanotubes. G' band (or second-order overtone of D band) which appears in the range of 2500-2900 cm^{-1}, is used to monitor the load transfer between SWNT and the matrix.[88]

At the given laser energy, the Raman bands of SWNTs are influenced by the environment such as temperature, pressure, and doping. Raman modes shift to the lower energy frequency with increasing temperature. The shift in the frequency of the G band in SWNT was reported to be -0.038 $cm^{-1}K^{-1}$, which is larger than that in MWNT and graphite.[89] The temperature coefficient in the frequency of the RBM in SWNT was determined to be -0.013 $cm^{-1}K^{-1}$.[89] G and G' bands of SWNT shift to higher frequency upon the application of pressure or compression. From the Raman spectra of SWNTs measured at room temperature under different pressure, the pressure dependence of the Raman mode frequency $\omega(P)$ was fit by Equation (1.5) and the value of a_p and b_p are listed in Table 1.4. The shift constant of G (8.7 cm^{-1}/GPa[90]) and that of G' bands (23 cm^{-1}/GPa[91]) have been reported.

$$\omega(P) = \omega(0) + a_p P + b_p P^2 \quad (1.5)$$

Table 1.4. Values of the fitting parameters a_p and b_p in Equation (1.5) obtained by fitting the measured pressure dependent Raman frequencies[92].

$\omega(0)$ (cm^{-1})	a_P (cm^{-1} GPa^{-1})	b_P (cm^{-1} GPa^{-2})
186 ± 1	7 ± 1	–
1550 ± 1	8 ± 1	–
1564 ± 1	10 ± 1	-0.9 ± 0.3
1593.0 ± 0.7	7.1 ± 0.8	-0.4 ± 0.2

The intensity of Raman bands of SWNT decreases and linewidth increases with increasing pressure, and the Raman spectra are largely but not completely recovered when the pressure is released.[92] By studying the strain-induced RBM intensity variations of SWNT in epoxy/SWNT composites, Lucas and Young[93] found that the magnitude of the intensity variations under pressure depends on the nanotube diameter and chirality, which can be explained by the resonant Raman effect. The value of E_{ii} shifts with strain, becoming closer or further away from E_{laser}, affecting the resonance condition and thus causing the intensity variations. The RBM intensity increases when the difference $\left|E_{ii} - E_{laser}\right|$ decreases and decreases in the other case. If the equation (n-m=3q+p) is defined, E_{22}^{S} decreases under compression when q=-1 and increases under compression if q=1. Doping can also cause the shift of Raman modes. Under p-doping (electrons transfer from carbon nanotubes), G band of SWNT shifts to higher frequency while that shifts to lower frequency under n-doping (electrons transfer to carbon nanotubs).

1.5.2 Other Techniques

The quality of nanotube dispersion in polymer matrices or solvents and structure of CNT can be examined by many methods including Raman spectroscopy, optical

microscopy, scanning electron microscopy (SEM), transmission electron microscopy (TEM), scanning tunneling microscopy (STM) etc. UV-vis spectroscopy is a useful tool for the qualitative determination of the dispersion state in SWNT solution and polymer/SWNT composites since only individual SWNT, or small SWNT bundles show the sharp peaks, which are van Hove singularities.[94] Large SWNT bundles show the monotonically decreasing absorbance with increasing wavelength without van Hove singularities.[95] Small-angle X-ray, neutron or light scattering with wave vectors Q in the range from 10^{-3} to 10^{0} nm^{-1} have been used to study the nanotube structures in suspension.[96-98] In neutron scattering , the scattered intensity for the dilute suspension of SWNT (0.01-0.1%) in water decrease as Q^{-1} in the range $0.003 < Q < 0.02$ $Å^{-1}$, which is characteristic of isolated rigid rods, suggesting the presence of isolated SWNT or very small SWNT bundles in suspension.[97] The scattered intensity followed power law dependence with exponents of Q in the range from -2 to -3, indicating the formation of a loose network with a mesh size of similar to 160 nm. The exponent of Q is used to evaluate semi-quantitatively the degree of nanotube dispersion in suspension: exponents is closer to -1 suggesting better dispersion of nanotube.[98] Recently, confocal microscopy is used to evaluate the nanotube dispersion in PS/MWNT nanocomposites.[99]

1.6 NON-BONDED INTERACTIONS

The non-covalent approaches for the dispersion of SWNT conserve the tube electronic structure by preventing disruption of the intrinsic sp^2 structure and conjugation. The resultant interaction between SWNT and polymer (or solvent or other molecules) is not covalently bound, but can nevertheless be quite strong. The improved interaction at the nanotube/matrix interface is a critical issue in the processing of nanocomposites.

1.6.1 Interfacial Interaction Model

The molecular mechanics of interfacial binding of polymer/CNT composites was first studied by Lordi and Yao.[44] Using force-field-based molecular mechanics, they found that the nature of interfacial binding energy between the nanotubes and epoxy resin comes from the electrostatic and van der Waals forces. When SWNTs were dispersed in PmPV-co-DOctOPV/toluene solution, polymer wrapped SWNT structure were formed.[53] O'Connell et al.[50] proposed possible wrapping arrangement of polymer on a nanotube by studying the dispersion of SWNT in polyvinyl pyrrolidone (PVP)/water solution. During solution formation, polymers disrupt the hydrophobic interface with water and reduce the inter-tube interactions in SWNT bundles. The structure of poly (metaphenylenevinylene) (PmPV) wrapped SWNTs was proposed.[55, 100] Interaction between PmPV and SWNT changes the conformation of PmPV. The side groups of PmPV are bound onto the cylindrical SWNT while PmPV backbone has curvature imposed upon SWNT[100]. The short, rigid backbone of poly(aryleneethynylene) cannot wrap around the SWNTs.[101] The π-π interaction between nanotube and the conjugated polymer backbones results in the formation of irreversible polymer-SWNT complexes.[101]

Mismatch in the coefficients of thermal expansions (CTEs) between CNT and epoxy resins result in thermal residual radial stress and deformation along the tube: compressive radial stress results in closer CNT-polymer contact enhancing the electrostatic and van der Waals interaction, while deformation promotes mechanical interlocking.[102] Local non-uniformity of CNT in this epoxy/nanotube composite also result in mechanical interlocking. From molecular mechanics simulations and elasticity

calculations, Liao and Li[103] proposed the presence of mechanical interlocking in CTE between CNT and PS matrix, as well as electrostatic and van der Waals interaction.

Electron donor–acceptor (EDA) complex can be formed between SWNT and polymer (or solvent or other molecules). EDA complexes are typically formed between a molecule with high electron affinity and one with low ionization potential. SWNTs behave amphoterically and thus interact strongly with both electron donors and electron acceptors. Researchers have studied the molecules for doping with SWNT, which include alkali metals (donors)[104-107], halogens (acceptors)[106], gas [108, 109] ((NH_3, H_2) as donors, (O_2, NO_2) as acceptors), aromatic acceptors (anthracene derivatives[110]), organic amine donors[47, 111] and polymers[112]. The interaction between SWNTs and polyethylene imine (PEI) leads to the evolution of SWNTs from p-type to n-type.[112] SWNT was well dispersed in the polymer, (-CN)APB/ODPA, forming the EDA interaction between nanotubes and the (-CN)APB subunit of the polymer[113].

A series of nanocomposite films consist of SWNT and copolymers of styrene and vinyl phenol (PSVPh) with varying vinyl phenol content were processed. The intermolecular interactions (hydrogen bonding) between the hydroxyl group of the vinyl phenol and the functional groups of nanotube were connected with the mechanical properties of composite films.[114, 115]

1.6.2 Interfacial Strength

Simulation results suggest that in determining the interfacial strength of polymer/CNT composites, the interfacial binding energy and frictional force play a minor role and helical conformation of polymer around the nanotube is essential.[44] Therefore the interfacial strength may result from the molecular-level entanglement of the nanotube

and polymer matrix. Molecular dynamics simulations predict the interfacial strength (van der Waals interactions) of a SWNT/polyethylene system to be 2 MPa.[116] CNT pullout experiments have been used to estimate the interfacial strength of polymer/CNT composites by using atomic force microscopy (AFM). Using this method, the average interfacial stress required to remove a single MWNT from the polyethylenebutene matrix was estimated to be 47 MPa[117], which is about 10 times larger than the adhesion between the same polymer and carbon fibers. From the pullout experiment, the interfacial shear strength of a SWNT/epoxy system were determined to be 366±74 MPa[118] and that of a CNT/PS system was estimated to be about 160 MPa[103]. Polymers comprised of aryl groups containing electron-withdrawing subgroups exhibit stronger interfacial interactions with the sidewalls of nanotubes as compared to polymers comprised of extended alkyl moieties. The strength of adhesive interactions between SWNTs and thiolated AFM cantilever tips can be examined by chemical force microscopy (CFM).[119] The interfacial interactions between substituted alkane- and arylthiol molecules and the sidewalls of SWNT were measured using CFM.[120] Based on fragmentation experiments, the interfacial strength required to remove a CNT from polyurethane matrix was estimated to be 500 MPa.[121]

1.7 POLYMER/CNT COMPOSITES

The unique combination of mechanical (tensile strength 45 GPa[29], Young's modulus ~640 GPa[18]), electrical conductivity (10^6 S/m)[122], thermal conductivity (6600 W/mK)[123], low density[20] as well as high aspect ratio, make CNTs excellent candidates for multifunctional polymer/CNT composites. The methods for the CNTs dispersion in polymer matrices include solution blending, melt blending[124, 125] and in-situ

polymerization[126]. Solution blending is the most common method for processing polymer/CNT composites. The nanotubes are dispersed in a suitable solvent, and then mixed with the polymer to form a dispersion of polymer/SWNT/solvent. The composite is then formed from the resultant dispersion by precipitating or casting a film.[127, 128] The polymers acting as the matrices for polymer nanocomposites includes thermoplastic[129-132], thermosetting[133-136], semi-crystalline[137, 138], amorphous[125, 139-142], water soluble[88, 143, 144], conjugated[145-147] and liquid crystalline ones[126, 132]. The mechanical, electrical and thermal properties of polymer/CNT composites will be introduced in the following section.

1.7.1 Mechanical Properties

The mechanical properties of polymer/carbon nanotube composites are influenced by polymer matrix, dispersion quality, orientation of nanotubes, and nanotube loading. Enhancement of 145 % and 300 % in tensile modulus and tensile strength, respectively have been achieved in the 1 wt% fluorinated SWNT/poly (ethylene oxide) composites.[148] By fabricating PVA/MWNT composite film, PVA formed a crystalline coating around the nanotubes, improving the interfacial stress transfer and leading to increase in Young's modulus, tensile strength, and toughness by 3.7, 4.3, and 1.7 times, respectively at less than 1 wt% nanotube loading.[149] The multilayer polymer/SWNT composite thin film with SWNT loading as high as 50 wt% was prepared by layer-by-layer assembly using functionlized SWNT, PEI, and poly (acrylic acid) (PAA) obtaining the tensile strength to be 220 ± 40 MPa with some values as high as 325 MPa.[150]

The orientation of CNTs in polymer matrices is expected to improve the mechanical properties of polymer/CNT composites. Highly aligned MWNT/PS

composite films with 5 wt% nanotube loading processed by melt extruding method, have the improved tensile modulus, yield strength and ultimate strengths.[151] The improvement in elastic modulus of the aligned MWNT/PS composite film is five times greater than that for the randomly oriented composite film. SWNTs were firstly dispersed in PP by solvent process. After the solvent was removed, the solid polymer was melt-spun obtaining the oriented SWNT/PP fibers.[152] The resultant PP/SWNT composite fiber with 1 wt % nanotube loading exhibited 40 % enhancement in tensile strength and 55 % increment in modulus. The poly (p-phenylene benzobisoxazole) (PBO) fiber in the presence of 10 wt% SWNT loading exhibits 50 % increment in tensile strength as compared with the control PBO fiber.[126] By the melt spinning technique, poly (ethylene terephthalate) (PET)/CNF composite fibers were processed and improvement in compressive strength and torsion modulus was achieved.[153] PMMA/CNF composite fibers processed by melt blending shows the improved compressive strength, enhanced thermal stability, as well as significantly reduced shrinkage.[154] The interconnected network of PVA and SWNT formed in the PVA/SWNT composite fibers leading to a 4-fold increase in Young's modulus.[155] Dalton et al.[156] spun the PVA/SWNT super-tough composite fiber with 60 wt% SWNT loading by using optimized coagulation spinning. The tensile strength of the super tough PVA/SWNT composite fiber is as high as 1.8 GPa comparable to that of spider silk. The fiber modulus reaches 80 GPa, elongation at break of about 100 % and the energy to break is as high as 570 J/g which is significantly larger than that of silk fiber (165 J/g). Polyacrylonitrile (PAN) containing 10 wt% SWNT composite fiber exhibits enhancement of 105 % (from 0.79 to 1.6 GPa) and 43 % (from 0.23 to 0.33 GPa) in tensile modulus and tensile strength, respectively and decrease of 16 % in elongation

to break.[157] Thermal oxidation of this PAN/SWNT (10 wt% SWNT) composite fiber at 250 ^{o}C under continuous air flow results in enhanced mechanical properties. The tensile modulus, tensile strength, and elongation at break of the oxidized composite fiber are 160 %, 100 %, and 115 %, respectively, higher than the control oxidized PAN fiber.[158] PAN was spun with various CNTs to obtain composite fibers with 5 wt% CNT loading achieving improvement in modulus (75 %), tensile strength (70 %), strain to failure (110 %) and work of rupture (230 %) as compared to control PAN fiber.[159] PAN/SWNT composite fibers with an orientation factor of SWNT as high as 0.915 were obtained by gel spinning.[160] The draw ratio of PAN/SWNT fiber reached to 51 and the SWNT exfoliation were observed by using UV–vis spectroscopy and high resolution transmission electron microscopy (HRTEM). With the addition of 1 wt% SWNT, tensile modulus of PAN increased by 6.6 GPa (from 22.1 to 28.7 GPa).[160] PAN/MWNT composite fibers containing up to 5 wt% MWNT were prepared by dry-jet wet spinning and exhibited 36 % increase in tensile modulus and 31 % increase in tensile strength as compared to control PAN fiber.[161] The highly oriented PAN/MWNT composite nanofiber sheets were prepared by electrospinning.[162] With the addition of 20 wt% MWNT, the tensile modulus of composite nanofiber sheets was enhanced by 10 GPa (from 4.5 to 14.5 GPa). The tensile strength of composite nanofiber sheets with 10 wt% MWNT loading was improved by 0.11 GPa (from 0.26 to 0.37 GPa).

The introduction of chemical bonding between polymer and nanotubes containing functional groups leads to the improvement in mechanical properties of polymer/CNT composites. In-situ polymerization of caprolactam in the presence of carboxylated SWNT yielded nylon-6/SWNT composites with nylon-6 chains grafted to the SWNT via

covalent linkage.[163] A 153 % enhancement in Young's modulus and 103 % increment in tensile strength were obtained in the nylon-6/SWNT composite fiber with 1 wt % nanotube loading. In the chlorinated PP/MWNT composite film at less than 1 wt% nanotube loading, the covalent bond formed been chlorinated PP chains and nanotubes led to the enhancement in Young's modulus, tensile strength and toughness by 3.1, 3.9 and 4.4 times, respectively.[149]

1.7.2 Electrical Properties

Carbon nanotubes are good candidates to impart electrical conductivity to insulating resins due to its high electrical conductivity and large aspect ratio. When the filler loading exceeds a critical value, composites containing conducting filler in an insulating polymer matrix become electrically conductive. The minimal volume fraction of nanotubes at which a continuous conducting network of the filler appears in the matrix is defined as percolation threshold. The composite conductivity, σ_c, is related with the volume fraction of the conductive filler, V, as expressed by Equation (1.6).[136]

$$\sigma_c \propto (V - V_c)^t \tag{1.6}$$

Where V_c is the percolation threshold and t is the critical exponent. The percolation threshold in polymer/CNT composites is influenced by the volume fraction, dispersion, aspect ratio, and orientation of nanatubes. The homogeneous solution was formed by dispersing PPE-functionalized SWNT in polycarbonate (PC) & PS. The PC/SWNT composite film prepared from the uniform solution exhibit the lower percolation threshold of 0.045 wt.% and higher electrical conductivity of 4.81×10^2 S/m with 7 wt% SWNT loading, which is 15 orders of magnitude higher than that of PC.[164] The percolation threshold in the PS/SWNT composite film is 0.11 wt% and the electrical

conductivity is 6.89 S/m with 7 wt% SWNT loading, which is 14 orders of magnitude higher than that of PS.[164] The PC/SWNT composite films can find applications in electrostatic painting and electromagnetic interference (EMI) shielding. The percolation threshold was observed to be 0.05 vol% for the polyimide/SWNT composites.[165] Epoxy/SWNT composites exhibit a percolation threshold at the volume fractions as low as 0.0052 vol% and achieve several orders of magnitude enhancement in electrical conductivity.[166] In polymer/ MWNT composites, the percolation threshold of 0.0025 vol% was observed and t was equal to 1.2.[167]

Bryning et al.[166] studied the effect of aspect ratio on the electrical conductivity of epoxy/SWNT composites using two types of SWNTs synthesized by HiPCO and laser ablation method. The composites prepared using SWNTs with higher aspect ratio (laser SWNTs ~380) give the lower percolation threshold than that with lower aspect ratio (HiPCO SWNTs ~150). As the length of MWNT increase from 1 to 5 μm, the epoxy/MWNT composites shows more than 8-fold decrease in the percolation threshold.[168]

Alignment of nanotubes in the polymer matrix has an effect on the electrical properties. Choi et al.[169] observed the significant improvement in electrical properties of epoxy/SWNT composite with the oriented SWNT that was aligned by magnetic filed. At 2 wt% SWNT loading, the electrical conductivity parallel to the alignment direction for the SWNT/PMMA composites decrease with the increasing SWNT orientation.[127] The electrical conductivity is about 10^{-10} S/cm and 10^{-4} S/cm for the SWNT/PMMA composites with and without SWNT orientation, respectively. The percolation threshold in these composites increases with increasing alignment of nanotubes. The reason may be

that the high orientation of SWNT in the composites results in the smaller contact area between tubes and thus cause the decrease in electrical conductivity and higher percolation threshold.[127] The percolation threshold for the PAN/SWNT composite film was observed to be lower than 1 wt% and its electrical conductivity decreases with increasing SWNT orientation.[170] The electrical conductivity of PAN/MWNT composite nanofiber sheets with 20 wt % MWNT loading is up to 1 S/cm.[162]

The chemical modification of CNT also influences the electrical conductivity of polymer/functionalized CNT composites. With the treatment of the concentrated HNO_3 or H_2O_2/NH_4OH, MWNTs are negatively charged and functionalized with carboxylic groups , disrupts the extended π- π conjugation of nanotubes, resulting in the decrease in electrical conductivity at a low content of MWNT and hence an increase in percolation threshold.[171]

1.7.3 Thermal Properties

Due to the low coefficient of thermal extension (CTE) values of CNT, the incorporation of CNT in polymer results in a decrease in the composite CTE[172]. Improved thermal shrinkage properties with the incorporation of SWNT, DWNT, MWNT or VGCNF in PAN matrix has been reported.[157, 159] The shrinkage of PAN/SNWT (90/10) composite fiber is almost half that of control PAN fiber at 200 ^oC.[157] Ge et al.[162] prepared the highly oriented PAN/oxidized MWNT composite nanofibers which exhibited enhancement in thermal deformation temperature and thermal stability. The CTEs of the composite nanofibers containing 20 wt % MWNTs were reduced by more than an order of magnitude to 13×10^{-6} /^oC along the fiber axis.

1.8 THESIS OBJECTIVES

This thesis has the following objectives:

- To compare the reinforcement efficiency of various types of carbon nanotubes in PAN.
- To study PAN-CNT interaction.
- To develop characterization tools for assessing CNT dispersion in polymer matrices.
- To characterize PAN/CNT interface.
- To characterize the anisotropic optical properties of carbon nanotubes.

1.9 REFERENCES

[1] T. V. Hughes and C. R. Chambers, U.S. Patent 405, 480 (1889).

[2] G. G. Tibbetts and M. G. Devour, U.S. Patent 4,565,684 (1986).

[3] M. L. Lake and J. M. Ting, "Carbon Materials for Advanced Technologies," edited by T.D. Burchell, Oxford, U. K. , pp. 139 (1999).

[4] K. P. De Jong and J. W. Geus, Catalysis Reviews-Science and Engineering **42**, 481 (2000).

[5] R. Bacon, Journal of Applied Physics **31**, 283 (1960).

[6] S. Iijima, Nature **354**, 56 (1991).

[7] S. Iijima and T. Ichihashi, Nature **363**, 603 (1993).

[8] D. S. Bethune, C. H. Kiang, M. S. Devries, G. Gorman, R. Savoy, J. Vazquez, and R. Beyers, Nature **363**, 605 (1993).

[9] H. J. Dai, A. G. Rinzler, P. Nikolaev, A. Thess, D. T. Colbert, and R. E. Smalley, Chemical Physics Letters **260**, 471 (1996).

[10] A. Thess, R. Lee, P. Nikolaev, H. J. Dai, P. Petit, J. Robert, C. H. Xu, Y. H. Lee, S. G. Kim, A. G. Rinzler, D. T. Colbert, G. E. Scuseria, D. Tomanek, J. E. Fischer, and R. E. Smalley, Science **273**, 483 (1996).

[11] T. Guo, P. Nikolaev, A. Thess, D. T. Colbert, and R. E. Smalley, Chemical Physics Letters **243**, 49 (1995).

[12] M. Joseyacaman, M. Mikiyoshida, L. Rendon, and J. G. Santiesteban, Applied Physics Letters **62**, 202 (1993).

[13] M. H. Ge and K. Sattler, Applied Physics Letters **64**, 710 (1994).

[14] J. Kong, A. M. Cassell, and H. J. Dai, Chemical Physics Letters **292**, 567 (1998).

[15] J. H. Hafner, M. J. Bronikowski, B. R. Azamian, P. Nikolaev, A. G. Rinzler, D. T. Colbert, K. A. Smith, and R. E. Smalley, Chemical Physics Letters **296**, 195 (1998).

[16] C. J. Lee, S. C. Lyu, H. W. Kim, C. Y. Park, and C. W. Yang, Chemical Physics Letters **359**, 109 (2002).

[17] P. Nikolaev, M. J. Bronikowski, R. K. Bradley, F. Rohmund, D. T. Colbert, K. A. Smith, and R. E. Smalley, Chemical Physics Letters **313**, 91 (1999).

[18] R. E. Smalley and B. I. Yakobson, Solid State Communications **107**, 597 (1998).

[19] C. Journet, W. K. Maser, P. Bernier, A. Loiseau, M. L. delaChapelle, S. Lefrant, P. Deniard, R. Lee, and J. E. Fischer, Nature **388**, 756 (1997).

[20] G. H. Gao, T. Cagin, and W. A. Goddard, Nanotechnology **9**, 184 (1998).

[21] R. S. Ruoff and D. C. Lorents, Carbon **33**, 925 (1995).

[22] A. Krishnan, E. Dujardin, T. W. Ebbesen, P. N. Yianilos, and M. M. J. Treacy, Physical Review B **58**, 14013 (1998).

[23] F. Li, H. M. Cheng, S. Bai, G. Su, and M. S. Dresselhaus, Applied Physics Letters **77**, 3161 (2000).

[24] J. P. Lu, Physical Review Letters **79**, 1297 (1997).

[25] V. N. Popov, V. E. Van Doren, and M. Balkanski, Solid State Communications **114**, 395 (2000).

[26] E. Saether, S. J. V. Frankland, and R. B. Pipes, Composites Science and Technology **63**, 1543 (2003).

[27] J. P. Salvetat, G. A. D. Briggs, J. M. Bonard, R. R. Bacsa, A. J. Kulik, T. Stockli, N. A. Burnham, and L. Forro, Physical Review Letters **82**, 944 (1999).

[28] M. F. Yu, B. S. Files, S. Arepalli, and R. S. Ruoff, Physical Review Letters **84**, 5552 (2000).

[29] D. A. Walters, L. M. Ericson, M. J. Casavant, J. Liu, D. T. Colbert, K. A. Smith, and R. E. Smalley, Applied Physics Letters **74**, 3803 (1999).

[30] M. Kociak, A. Y. Kasumov, S. Gueron, B. Reulet, I. I. Khodos, Y. B. Gorbatov, V. T. Volkov, L. Vaccarini, and H. Bouchiat, Physical Review Letters **86**, 2416 (2001).

[31] Z. K. Tang, L. Y. Zhang, N. Wang, X. X. Zhang, G. H. Wen, G. D. Li, J. N. Wang, C. T. Chan, and P. Sheng, Science **292**, 2462 (2001).

[32] W. A. Deheer, W. S. Bacsa, A. Chatelain, T. Gerfin, R. Humphreybaker, L. Forro, and D. Ugarte, Science **268**, 845 (1995).

[33] T. Natsuki, K. Tantrakarn, and M. Endo, Carbon **42**, 39 (2004).

[34] T. H. K. Barron and R. E. Taylor, Thermal Expansion of Solids **1-4** (1997).

[35] Y. Yosida, Journal of Applied Physics **87**, 3338 (2000).

[36] Y. Maniwa, R. Fujiwara, H. Kira, H. Tou, H. Kataura, S. Suzuki, Y. Achiba, E. Nishibori, M. Takata, M. Sakata, A. Fujiwara, and H. Suematsu, Physical Review B **64**, 2414021 (2001).

[37] N. R. Raravikar, P. Keblinski, A. M. Rao, M. S. Dresselhaus, L. S. Schadler, and P. M. Ajayan, Physical Review B **66** (2002).

[38] H. Jiang, B. Liu, Y. Huang, and K. C. Hwang, Journal of Engineering Materials and Technology-Transactions of the Asme **126**, 265 (2004).

[39] Y. K. Kwon, S. Berber, and D. Tomanek, Physical Review Letters **92** (2004).

[40] T. W. Ebbesen, Carbon nanotubes, Preparation and Properties, (Chemical Rubber, Boca Raton, FL) pp. 96 (1997).

[41] S. Bandow, Japanese Journal of Applied Physics Part 2-Letters **36**, L1403 (1997).

[42] Y. Maniwa, R. Fujiwara, H. Kira, H. Tou, E. Nishibori, M. Takata, M. Sakata, A. Fujiwara, X. L. Zhao, S. Iijima, and Y. Ando, Physical Review B **64**, 0731051 (2001).

[43] L. A. Girifalco, M. Hodak, and R. S. Lee, Physical Review B **62**, 13104 (2000).

[44] V. Lordi and N. Yao, Journal of Materials Research **15**, 2770 (2000).

[45] S. Badaire, P. Poulin, M. Maugey, and C. Zakri, Langmuir **20**, 10367 (2004).

[46] J. L. Bahr, E. T. Mickelson, M. J. Bronikowski, R. E. Smalley, and J. M. Tour, Chemical Communications, 193 (2001).

[47] K. D. Ausman, R. Piner, O. Lourie, R. S. Ruoff, and M. Korobov, Journal of Physical Chemistry B **104**, 8911 (2000).

[48] V. C. Moore, M. S. Strano, E. H. Haroz, R. H. Hauge, R. E. Smalley, J. Schmidt, and Y. Talmon, Nano Letters **3**, 1379 (2003).

[49] M. F. Islam, E. Rojas, D. M. Bergey, A. T. Johnson, and A. G. Yodh, Nano Letters **3**, 269 (2003).

[50] M. J. O'Connell, P. Boul, L. M. Ericson, C. Huffman, Y. H. Wang, E. Haroz, C. Kuper, J. Tour, K. D. Ausman, and R. E. Smalley, Chemical Physics Letters **342**, 265 (2001).

[51] A. Penicaud, P. Poulin, A. Derre, E. Anglaret, and P. Petit, Journal of the American Chemical Society **127**, 8 (2005).

[52] Y. Sabba and E. L. Thomas, Macromolecules **37**, 4815 (2004).

[53] A. B. Dalton, C. Stephan, J. N. Coleman, B. McCarthy, P. M. Ajayan, S. Lefrant, P. Bernier, W. J. Blau, and H. J. Byrne, Journal of Physical Chemistry B **104**, 10012 (2000).

[54] J. Chen, H. Y. Liu, W. A. Weimer, M. D. Halls, D. H. Waldeck, and G. C. Walker, Journal of the American Chemical Society **124**, 9034 (2002).

[55] A. Star, J. F. Stoddart, D. Steuerman, M. Diehl, A. Boukai, E. W. Wong, X. Yang, S. W. Chung, H. Choi, and J. R. Heath, Angewandte Chemie-International Edition **40**, 1721 (2001).

[56] J. E. Huang, X. H. Li, J. C. Xu, and H. L. Li, Carbon **41**, 2731 (2003).

[57] K. W. Putz, C. A. Mitchell, R. Krishnamoorti, and P. F. Green, Journal of Polymer Science Part B-Polymer Physics **42**, 2286 (2004).

[58] C. Park, Z. Ounaies, K. A. Watson, R. E. Crooks, J. Smith, S. E. Lowther, J. W. Connell, E. J. Siochi, J. S. Harrison, and T. L. S. Clair, Chemical Physics Letters **364**, 303 (2002).

[59] J. Liu, A. G. Rinzler, H. J. Dai, J. H. Hafner, R. K. Bradley, P. J. Boul, A. Lu, T. Iverson, K. Shelimov, C. B. Huffman, F. Rodriguez-Macias, Y. S. Shon, T. R. Lee, D. T. Colbert, and R. E. Smalley, Science **280**, 1253 (1998).

[60] M. Zhang, M. Yudasaka, and S. Iijima, Journal of Physical Chemistry B **108**, 149 (2004).

[61] C. Bower, A. Kleinhammes, Y. Wu, and O. Zhou, Chemical Physics Letters **288**, 481 (1998).

[62] Z. J. Jia, Z. Y. Wang, J. Liang, B. Q. Wei, and D. H. Wu, Carbon **37**, 903 (1999).

[63] J. M. Moon, K. H. An, Y. H. Lee, Y. S. Park, D. J. Bae, and G. S. Park, Journal of Physical Chemistry B **105**, 5677 (2001).

[64] Y. P. Sun, W. J. Huang, Y. Lin, K. F. Fu, A. Kitaygorodskiy, L. A. Riddle, Y. J. Yu, and D. L. Carroll, Chemistry of Materials **13**, 2864 (2001).

[65] M. S. P. Shaffer, X. Fan, and A. H. Windle, Carbon **36**, 1603 (1998).

[66] W. Zhao, C. H. Song, and P. E. Pehrsson, Journal of the American Chemical Society **124**, 12418 (2002).

[67] H. Hiura, T. W. Ebbesen, and K. Tanigaki, Advanced Materials **7**, 275 (1995).

[68] P. M. Ajayan, T. W. Ebbesen, T. Ichihashi, S. Iijima, K. Tanigaki, and H. Hiura, Nature **362**, 522 (1993).

[69] A. Kuznetsova, D. B. Mawhinney, V. Naumenko, J. T. Yates, J. Liu, and R. E. Smalley, Chemical Physics Letters **321**, 292 (2000).

[70] G. W. Lee and S. Kumar, Journal of Physical Chemistry B **109**, 17128 (2005).

[71] M. A. Hamon, J. Chen, H. Hu, Y. S. Chen, M. E. Itkis, A. M. Rao, P. C. Eklund, and R. C. Haddon, Advanced Materials **11**, 834 (1999).

[72] M. A. Hamon, H. Hui, P. Bhowmik, H. M. E. Itkis, and R. C. Haddon, Applied Physics a-Materials Science & Processing **74**, 333 (2002).

[73] L. W. Qu, R. B. Martin, W. J. Huang, K. F. Fu, D. Zweifel, Y. Lin, Y. P. Sun, C. E. Bunker, B. A. Harruff, J. R. Gord, and L. F. Allard, Journal of Chemical Physics **117**, 8089 (2002).

[74] J. Chen, A. M. Rao, S. Lyuksyutov, M. E. Itkis, M. A. Hamon, H. Hu, R. W. Cohn, P. C. Eklund, D. T. Colbert, R. E. Smalley, and R. C. Haddon, Journal of Physical Chemistry B **105**, 2525 (2001).

[75] J. Zhu, J. D. Kim, H. Q. Peng, J. L. Margrave, V. N. Khabashesku, and E. V. Barrera, Nano Letters **3**, 1107 (2003).

[76] J. Chen, M. A. Hamon, H. Hu, Y. S. Chen, A. M. Rao, P. C. Eklund, and R. C. Haddon, Science **282**, 95 (1998).

[77] P. J. Boul, J. Liu, E. T. Mickelson, C. B. Huffman, L. M. Ericson, I. W. Chiang, K. A. Smith, D. T. Colbert, R. H. Hauge, J. L. Margrave, and R. E. Smalley, Chemical Physics Letters **310**, 367 (1999).

[78] M. S. Dresselhaus, G. Dresselhaus, A. Jorio, A. G. Souza, and R. Saito, Carbon **40**, 2043 (2002).

[79] M. S. Dresselhaus and P. C. Eklund, Advances in Physics **49**, 705 (2000).

[80] R. Saito, G. Dresselhaus, and M. S. Dresselhaus, Physical Review B **61**, 2981 (2000).

[81] S. D. M. Brown, P. Corio, A. Marucci, M. S. Dresselhaus, M. A. Pimenta, and K. Kneipp, Physical Review B **61**, R5137 (2000).

[82] M. S. Dresselhaus, G. Dresselhaus, and R. Saito, Carbon **33**, 883 (1995).

[83] H. Kataura, Y. Kumazawa, Y. Maniwa, I. Umezu, S. Suzuki, Y. Ohtsuka, and Y. Achiba, Synthetic Metals **103**, 2555 (1999).

[84] A. Jorio, A. G. Souza, G. Dresselhaus, M. S. Dresselhaus, R. Saito, J. H. Hafner, C. M. Lieber, F. M. Matinaga, M. S. S. Dantas, and M. A. Pimenta, Physical Review B **6324** (2001).

[85] D. A. Heller, P. W. Barone, J. P. Swanson, R. M. Mayrhofer, and M. S. Strano, Journal of Physical Chemistry B **108**, 6905 (2004).

[86] J. L. Sauvajol, E. Anglaret, S. Rols, and L. Alvarez, Carbon **40**, 1697 (2002).

[87] T. Liu and S. Kumar, Chemical Physics Letters **378**, 257 (2003).

[88] X. F. Zhang, T. Liu, T. V. Sreekumar, S. Kumar, V. C. Moore, R. H. Hauge, and R. E. Smalley, Nano Letters **3**, 1285 (2003).

[89] H. D. Li, K. T. Yue, Z. L. Lian, Y. Zhan, L. X. Zhou, S. L. Zhang, Z. J. Shi, Z. N. Gu, B. B. Liu, R. S. Yang, H. B. Yang, G. T. Zou, Y. Zhang, and S. Iijima, Applied Physics Letters **76**, 2053 (2000).

[90] U. D. Venkateswaran, M. E. Gosselin, B. Postek, D. L. Masica, G. Chen, R. Gupta, and P. C. Eklund, Physica Status Solidi B-Basic Research **235**, 364 (2003).

[91] C. A. Cooper, R. J. Young, and M. Halsall, Composites Part a-Applied Science and Manufacturing **32**, 401 (2001).

[92] U. D. Venkateswaran, A. M. Rao, E. Richter, M. Menon, A. Rinzler, R. E. Smalley, and P. C. Eklund, Physical Review B **59**, 10928 (1999).

[93] M. Lucas and R. J. Young, Physical Review B **69**, 085405 (2004).

[94] M. J. O'Connell, S. M. Bachilo, C. B. Huffman, V. C. Moore, M. S. Strano, E. H. Haroz, K. L. Rialon, P. J. Boul, W. H. Noon, C. Kittrell, J. P. Ma, R. H. Hauge, R. B. Weisman, and R. E. Smalley, Science **297**, 593 (2002).

[95] T. Chatterjee, K. Yurekli, V. G. Hadjiev, and R. Krishnamoorti, Advanced Functional Materials **15**, 1832 (2005).

[96] D. W. Schaefer, J. Zhao, J. M. Brown, D. P. Anderson, and D. W. Tomlin, Chemical Physics Letters **375**, 369 (2003).

[97] W. Zhou, M. F. Islam, H. Wang, D. L. Ho, A. G. Yodh, K. I. Winey, and J. E. Fischer, Chemical Physics Letters **384**, 185 (2004).

[98] H. Wang, W. Zhou, D. L. Ho, K. I. Winey, J. E. Fischer, C. J. Glinka, and E. K. Hobbie, Nano Letters **4**, 1789 (2004).

[99] S. Bellayer, J. W. Gilman, N. Eidelman, S. Bourbigot, X. Flambard, D. M. Fox, H. C. De Long, and P. C. Trulove, Advanced Functional Materials **15**, 910 (2005).

[100] B. McCarthy, J. N. Coleman, R. Czerw, A. B. Dalton, M. I. H. Panhuis, A. Maiti, A. Drury, P. Bernier, J. B. Nagy, B. Lahr, H. J. Byrne, D. L. Carroll, and W. J. Blau, Journal of Physical Chemistry B **106**, 2210 (2002).

[101] R. J. Chen, Y. G. Zhan, D. W. Wang, and H. J. Dai, Journal of the American Chemical Society **123**, 3838 (2001).

[102] M. Wong, M. Paramsothy, X. J. Xu, Y. Ren, S. Li, and K. Liao, Polymer **44**, 7757 (2003).

[103] K. Liao and S. Li, Applied Physics Letters **79**, 4225 (2001).

[104] A. Claye, S. Rahman, J. E. Fischer, A. Sirenko, G. U. Sumanasekera, and P. C. Eklund, Chemical Physics Letters **333**, 16 (2001).

[105] A. M. Rao, P. C. Eklund, S. Bandow, A. Thess, and R. E. Smalley, Nature **388**, 257 (1997).

[106] S. Kazaoui, N. Minami, R. Jacquemin, H. Kataura, and Y. Achiba, Physical Review B **60**, 13339 (1999).

[107] S. Suzuki, C. Bower, Y. Watanabe, and O. Zhou, Applied Physics Letters **76**, 4007 (2000).

[108] J. Kong, N. R. Franklin, C. W. Zhou, M. G. Chapline, S. Peng, K. J. Cho, and H. J. Dai, Science **287**, 622 (2000).

[109] C. K. W. Adu, G. U. Sumanasekera, B. K. Pradhan, H. E. Romero, and P. C. Eklund, Chemical Physics Letters **337**, 31 (2001).

[110] Y. Zhang, A. Kolmakov, S. Chretien, H. Metiu, and M. Moskovits, Nano Letters **4**, 403 (2004).

[111] J. Kong and H. J. Dai, Journal of Physical Chemistry B **105**, 2890 (2001).

[112] M. Shim, A. Javey, N. W. S. Kam, and H. J. Dai, Journal of the American Chemical Society **123**, 11512 (2001).

[113] K. E. Wise, C. Park, E. J. Siochi, and J. S. Harrison, Chemical Physics Letters **391**, 207 (2004).

[114] A. Rasheed, M. D. Dadmun, I. Ivanov, P. F. Britt, and D. B. Geohegan, Chemistry of Materials **18**, 3513 (2006).

[115] A. Rasheed, H. G. Chae, S. Kumar, and M. D. Dadmun, Polymer **47**, 4734 (2006).

[116] S. J. V. Frankland, A. Caglar, D. W. Brenner, and M. Griebel, Journal of Physical Chemistry B **106**, 3046 (2002).

[117] A. H. Barber, S. R. Cohen, and H. D. Wagner, Applied Physics Letters **82**, 4140 (2003).

[118] C. A. Cooper, S. R. Cohen, A. H. Barber, and H. D. Wagner, Applied Physics Letters **81**, 3873 (2002).

[119] M. A. Poggi, L. A. Bottomley, and P. T. Lillehei, Nano Letters **4**, 61 (2004).

[120] M. A. Poggi, P. T. Lillehei, and L. A. Bottomley, Chemistry of Materials **17**, 4289 (2005).

[121] H. D. Wagner, O. Lourie, Y. Feldman, and R. Tenne, Applied Physics Letters **72**, 188 (1998).

[122] J. W. Mintmire, B. I. Dunlap, and C. T. White, Physical Review Letters **68**, 631 (1992).

[123] S. Berber, Y. K. Kwon, and D. Tomanek, Physical Review Letters **84**, 4613 (2000).

[124] P. Potschke, A. R. Bhattacharyya, and A. Janke, European Polymer Journal **40**, 137 (2004).

[125] R. Haggenmueller, H. H. Gommans, A. G. Rinzler, J. E. Fischer, and K. I. Winey, Chemical Physics Letters **330**, 219 (2000).

[126] S. Kumar, T. D. Dang, F. E. Arnold, A. R. Bhattacharyya, B. G. Min, X. F. Zhang, R. A. Vaia, C. Park, W. W. Adams, R. H. Hauge, R. E. Smalley, S. Ramesh, and P. A. Willis, Macromolecules **35**, 9039 (2002).

[127] F. M. Du, J. E. Fischer, and K. I. Winey, Journal of Polymer Science Part B-Polymer Physics **41**, 3333 (2003).

[128] J. M. Benoit, B. Corraze, S. Lefrant, W. J. Blau, P. Bernier, and O. Chauvet, Synthetic Metals **121**, 1215 (2001).

[129] J. Q. Pham, C. A. Mitchell, J. L. Bahr, J. M. Tour, R. Krishanamoorti, and P. F. Green, Journal of Polymer Science Part B-Polymer Physics **41**, 3339 (2003).

[130] M. Sennett, E. Welsh, J. B. Wright, W. Z. Li, J. G. Wen, and Z. F. Ren, Applied Physics a-Materials Science & Processing **76**, 111 (2003).

[131] B. P. Grady, F. Pompeo, R. L. Shambaugh, and D. E. Resasco, Journal of Physical Chemistry B **106**, 5852 (2002).

[132] R. A. Mrozek, B. S. Kim, V. C. Holmberg, and T. A. Taton, Nano Letters **3**, 1665 (2003).

[133] C. A. Martin, J. K. W. Sandler, A. H. Windle, M. K. Schwarz, W. Bauhofer, K. Schulte, and M. S. P. Shaffer, Polymer **46**, 877 (2005).

[134] G. Pecastaings, P. Delhaes, A. Derre, H. Saadaoui, F. Carmona, and S. Cui, Journal of Nanoscience and Nanotechnology **4**, 838 (2004).

[135] M. J. Biercuk, M. C. Llaguno, M. Radosavljevic, J. K. Hyun, A. T. Johnson, and J. E. Fischer, Applied Physics Letters **80**, 2767 (2002).

[136] B. Kim, J. Lee, and I. S. Yu, Journal of Applied Physics **94**, 6724 (2003).

[137] M. Wu and L. L. Shaw, Journal of Power Sources **136**, 37 (2004).

[138] K. Mylvaganam and L. C. Zhang, Journal of Physical Chemistry B **108**, 5217 (2004).

[139] C. Stephan, T. P. Nguyen, M. L. de la Chapelle, S. Lefrant, C. Journet, and P. Bernier, Synthetic Metals **108**, 139 (2000).

[140] C. A. Cooper, D. Ravich, D. Lips, J. Mayer, and H. D. Wagner, Composites Science and Technology **62**, 1105 (2002).

[141] J. M. Benoit, B. Corraze, and O. Chauvet, Physical Review B **65**, 242405 (2002).

[142] L. M. Clayton, A. K. Sikder, A. Kumar, M. Cinke, M. Meyyappan, T. G. Gerasimov, and J. P. Harmon, Advanced Functional Materials **15**, 101 (2005).

[143] M. S. P. Shaffer and A. H. Windle, Advanced Materials **11**, 937 (1999).

[144] B. Zhao, H. Hu, and R. C. Haddon, Advanced Functional Materials **14**, 71 (2004).

[145] A. Satake, Y. Miyajima, and Y. Kobuke, Chemistry of Materials **17**, 716 (2005).

[146] B. McCarthy, J. N. Coleman, R. Czerw, A. B. Dalton, H. J. Byrne, D. Tekleab, P. Iyer, P. M. Ajayan, W. J. Blau, and D. L. Carroll, Nanotechnology **12**, 187 (2001).

[147] N. Ferrer-Anglada, M. Kaempgen, V. Skakalova, U. Dettlaf-Weglikowska, and S. Roth, Diamond and Related Materials **13**, 256 (2004).

[148] H. Z. Geng, R. Rosen, B. Zheng, H. Shimoda, L. Fleming, J. Liu, and O. Zhou, Advanced Materials **14**, 1387 (2002).

[149] J. N. Coleman, M. Cadek, R. Blake, V. Nicolosi, K. P. Ryan, C. Belton, A. Fonseca, J. B. Nagy, Y. K. Gun'ko, and W. J. Blau, Advanced Functional Materials **14**, 791 (2004).

[150] A. A. Mamedov, N. A. Kotov, M. Prato, D. M. Guldi, J. P. Wicksted, and A. Hirsch, Nature Materials **1**, 190 (2002).

[151] E. T. Thostenson and T. W. Chou, Journal of Physics D-Applied Physics **35**, L77 (2002).

[152] J. C. Kearns and R. L. Shambaugh, Journal of Applied Polymer Science **86**, 2079 (2002).

[153] H. M. Ma, J. J. Zeng, M. L. Realff, S. Kumar, and D. A. Schiraldi, Composites Science and Technology **63**, 1617 (2003).

[154] J. J. Zeng, B. Saltysiak, W. S. Johnson, D. A. Schiraldi, and S. Kumar, Composites Part B-Engineering **35**, 245 (2004).

[155] B. Vigolo, P. Poulin, M. Lucas, P. Launois, and P. Bernier, Applied Physics Letters **81**, 1210 (2002).

[156] A. B. Dalton, S. Collins, E. Munoz, J. M. Razal, V. H. Ebron, J. P. Ferraris, J. N. Coleman, B. G. Kim, and R. H. Baughman, Nature **423**, 703 (2003).

[157] T. V. Sreekumar, T. Liu, B. G. Min, H. Guo, S. Kumar, R. H. Hauge, and R. E. Smalley, Advanced Materials **16**, 58 (2004).

[158] B. G. Min, T. V. Sreekumar, T. Uchida, and S. Kumar, Carbon **43**, 599 (2005).

[159] H. G. Chae, T. V. Sreekumar, T. Uchida, and S. Kumar, Polymer **46**, 10925 (2005).

[160] H. G. Chae, M. L. Minus, and S. Kumar, Polymer **47**, 3494 (2006).

[161] M. C. Weisenberger, E. A. Grulke, D. Jacques, T. Rantell, and R. Andrews, Journal of Nanoscience and Nanotechnology **3**, 535 (2003).

[162] J. J. Ge, H. Q. Hou, Q. Li, M. J. Graham, A. Greiner, D. H. Reneker, F. W. Harris, and S. Z. D. Cheng, Journal of the American Chemical Society **126**, 15754 (2004).

[163] J. B. Gao, M. E. Itkis, A. P. Yu, E. Bekyarova, B. Zhao, and R. C. Haddon, Journal of the American Chemical Society **127**, 3847 (2005).

[164] R. Ramasubramaniam, J. Chen, and H. Y. Liu, Applied Physics Letters **83**, 2928 (2003).

[165] Z. Ounaies, C. Park, K. E. Wise, E. J. Siochi, and J. S. Harrison, Composites Science and Technology **63**, 1637 (2003).

[166] M. B. Bryning, M. F. Islam, J. M. Kikkawa, and A. G. Yodh, Advanced Materials **17**, 1186 (2005).

[167] J. K. W. Sandler, J. E. Kirk, I. A. Kinloch, M. S. P. Shaffer, and A. H. Windle, Polymer **44**, 5893 (2003).

[168] J. B. Bai and A. Allaoui, Composites Part a-Applied Science and Manufacturing **34**, 689 (2003).

[169] E. S. Choi, J. S. Brooks, D. L. Eaton, M. S. Al-Haik, M. Y. Hussaini, H. Garmestani, D. Li, and K. Dahmen, Journal of Applied Physics **94**, 6034 (2003).

[170] S. H. Kim, B. G. Min, S. C. Lee, S. B. Park, T. D. Lee, M. Park, and S. Kumar, Fibers and Polymers **5**, 198 (2004).

[171] Y. J. Kim, T. S. Shin, H. D. Choi, J. H. Kwon, Y. C. Chung, and H. G. Yoon, Carbon **43**, 23 (2005).

[172] Y. M. Chen and J. M. Ting, Carbon **40**, 359 (2002).

CHAPTER 2

STRUCTURE AND PROPERTIES OF POLYACRYLONITRILE/SINGLE WALL CARBON NANOTUBE COMPOSITE FILMS

2.1 INTRODUCTION

Single wall carbon nanotube (SWNT) possesses high strength, stiffness, and electrical conductivity[1, 2], and is being incorporated in polymers to obtain composites with unique properties. Various matrix systems that have been studied for this purpose such as: poly (vinyl alcohol) (PVA)[3-5], poly (methyl methacrylate)[6-9], poly (m-phenylenevinylene-co-2, 5-dioctoxyp-phenylenevinylene)[10], polyaniline[11], polypyrrole[12], polypropylene[13], epoxy[14, 15], poly (3-octylthiophene)[16, 17], polyimide[18, 19], polycarbonate[20], polystyrene (PS)[21, 22], alkoxysilane terminated amide acid (ASTAA)[23], PAN[24, 25], and poly (p-phenylene benzobisoxazole)[26]. Most of these studies have been carried out at nanotube loadings generally below 10 wt %. However, several studies at high nanotube loadings have been reported. For example, exceptionally tough PVA fibers with 60 wt% SWNTs have been processed[27]. Polyelectrolyte film with 50 wt% SWNT resulted in a tensile strength of 220 MPa[28]. Improvements in modulus, strength, and toughness of SWNT films have been reported with PVA or PS infiltration.[29] PAN, a commercially important polymer and carbon precursor[30], is generally processed from solution[31]. Carbonized PAN/SWNT films are good candidates for electrochemical capacitor electrodes[32]. This chapter discusses the polymer/SWNT composite film prepared at

higher SWNT loading with unique combination of tensile, electrical, and thermo-mechanical properties, low density, and solvent resistance, and explains its properties with a control polymer film and SWNT bucky paper. Results pertaining to the interaction between PAN and SWNT in the composite films are also presented.

2.2 EXPERIMENTAL

2.2.1 Preparation of Films

Unpurified HiPCO SWNTs (catalytic impurity based on the thermogravemetric analysis was about 30 wt %) obtained from Carbon Nanotechnologies, Inc were used as received. Dimethylformamide (DMF) and Polyacrylonitrile (PAN) containing 10% methyl acrylate (random copolymer, molecular weight 100,000 g/mole) were purchased from Sigma- Aldrich and were also used as received. Vacuum dried 0.137 g SWNTs were dispersed in 50 ml DMF by a combination of sonication (Cole-Parmer 8891 bath sonicator, 80 W, 43 kHz) and homogenization using a bio-homogenizer (Biospec products Inc. M133/1281-0). To this SWNT/DMF dispersion, 0.2055 g PAN was added and dissolved by stirring. The PAN/SWNT/DMF solution was cast onto a hot glass substrate (at 60 ^{o}C) to form 15 to 30 μm thick films. The resulting film was dried under vacuum at 60 ^{o}C. Control PAN and SWNT (bucky paper) films were also made using the same process.

2.2.2 DMF Treatment

The PAN/SWNT composite films were kept in DMF at temperature of 50, 70, 90, 110 and 130 ^{o}C for one hour. The films were then dried under vacuum for one week at 80 ^{o}C.

2.2.3 Tensile and Dynamic Mechanical Analysis

RSA III (Rheometrics Scientific) was used to measure the tensile and dynamic mechanical properties. The gauge length, film width, and strain rate for the tensile test was 25.4 mm, 5 mm and 10 %/min, respectively. Dynamic mechanical tests were carried out at 1 Hz at 1 ^{o}C/min heating rate.

2.2.4 Thermo-Mechanical Analysis

Coefficient of thermal expansion was determined using a thermo-mechanical analyzer (TA Instruments TMA 2940) at 0.05 MPa pre-stress on 10 mm long and 2 mm wide films during the second heating cycle when heated at 5 ^{o}C /min.

2.2.5 Electrical Conductivity and Morphological Characterization

In plane dc electrical conductivity was measured by four-probe method. SEM imaging was done on gold coated films using Leo 1530 Scanning Electron Microscope.

2.2.6 X-ray Diffraction

X-ray diffraction studies were conducted on Rigaku R-AXIS IV^{++} equipped with an image plate. The nickel filtered CuKα radiation (wavelength = 0.15418 nm) was used and data analysis was done using jade software.

2.2.7 Raman Spectroscopy

Raman spectra were collected by an Invia Raman Microscope made by Renishaw Company using 488 nm excitation lasers.

2.3 RESULTS AND DISCUSSION

2.3.1 Properties of PAN/SWNT Composite Film

The initial modulus of the PAN/SWNT composite film is 4 times the modulus of PAN and an order of magnitude higher than that of the SWNT bucky paper, while the tensile strength of the composite is twice the PAN strength, and 13 times the strength of the bucky paper (Table 2.1). In this work, SWNT bucky paper was made from unpurified tubes. By comparison, in the earlier work, it was reported that the bucky paper made from purified tubes exhibited substantially higher strain to failure (~5%)[33]. Bucky paper strain to failure observed in this work is in better agreement with the value reported by Malik et al[34].

Table 2.1. Properties of PAN, PAN/SWNT and SWNT films

Sample	SWNT loading (wt%)	Tensile modulus (GPa)	Tensile strength (MPa)	Elongation at break (%)	Density (g/cm^3)
PAN	0	2.7 ± 0.4	57 ± 4	22.3 ± 6.5	1.01
PAN/ SWNT	40	10.9 ± 0.3	103 ± 18	1.6 ± 0.6	1.08
SWNT bucky paper	100	1.1 ± 0.1	7.6 ±1.5	0.6 ± 0.1	0.80

The storage modulus of PAN/SWNT composite in the plateau region above the glass transition temperature is 40 times the PAN modulus at that temperature (Figure 2.1). Based on the Tan δ peak position, glass transition temperature of the composite film is 103 ^{o}C, while that of the control PAN film it is 91 ^{o}C. The

decrease in the Tan δ magnitude for the PAN/SWNT composite film suggests suppression of the PAN molecular motion above the glass transition temperature.

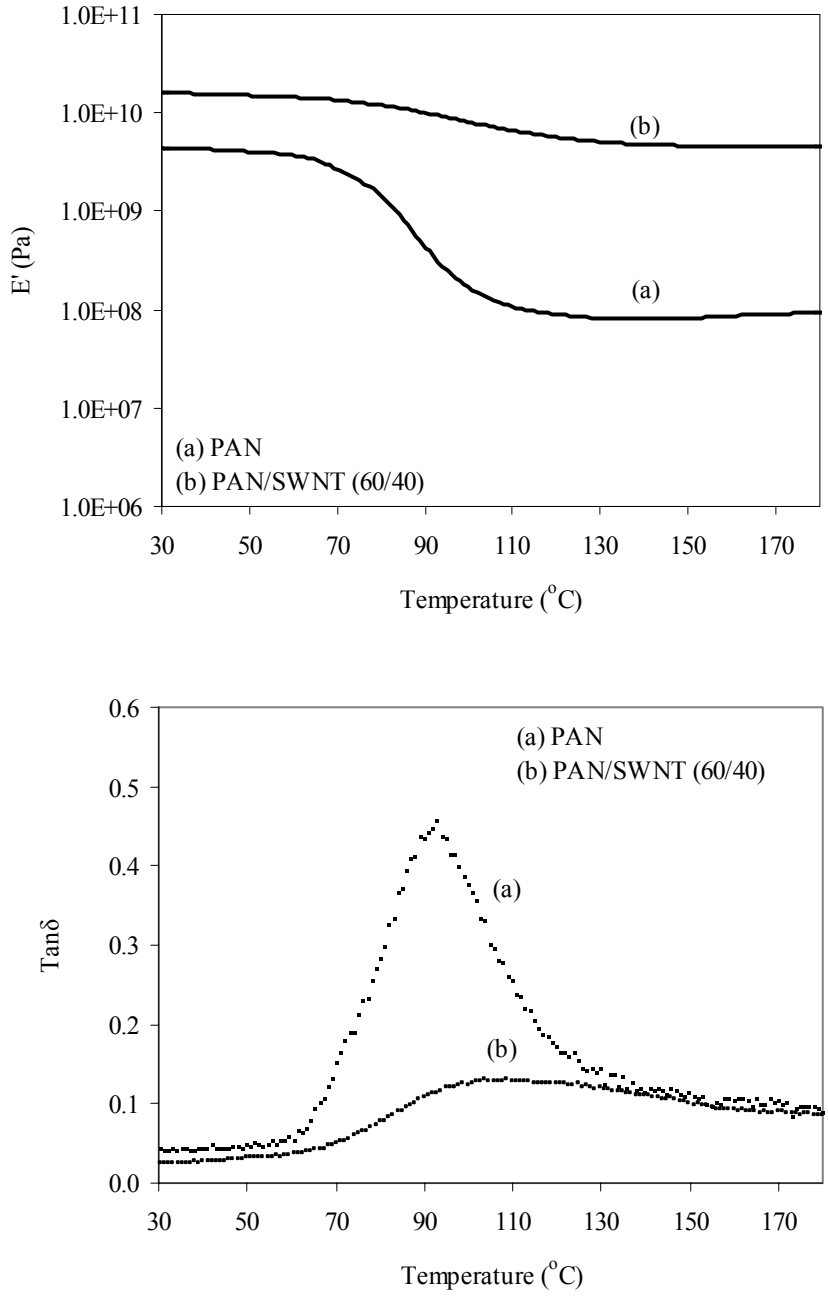

Figure 2.1. Storage modulus (E') and tan δ behavior of PAN and PAN/SWNT (60/40) films as a function of temperature.

The thermal expansion of PAN shows the typical polymer behavior, with CTE value being much higher above T_g than its value below T_g (Figure 2.2, Table 2.2), while the composite film exhibits only one CTE in the entire temperature range. These properties clearly demonstrate the reinforcing effect of PAN in SWNT and vice-versa.

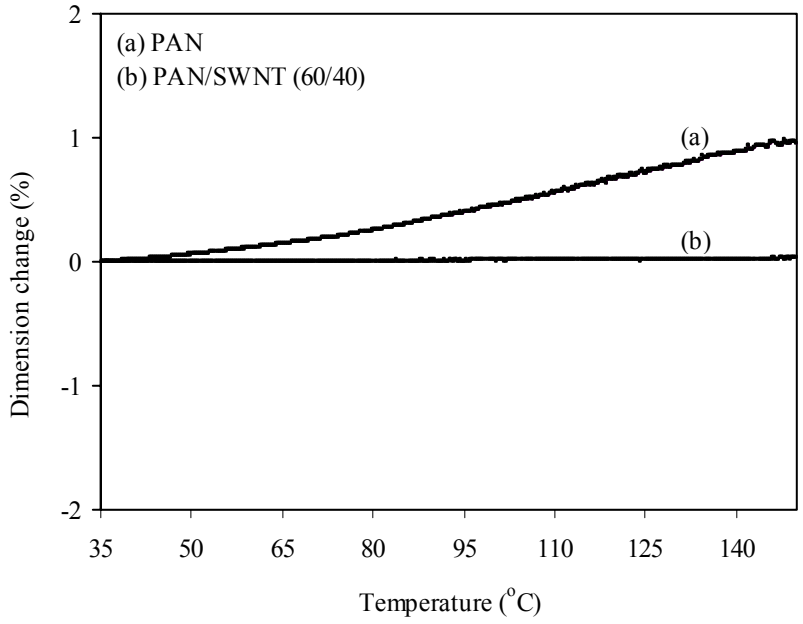

Figure 2.2. Thermal expansion of PAN and PAN/SWNT (60/40) films as a function of temperature.

Table 2.2. CTEs of PAN and PAN/SWNT films

Sample	**CTE (10^{-6}/ °C)**	
	35 -91 °C (T_g)	**91 (T_g) -150 °C**
PAN	57	108
PAN/ SWNT (60/ 40)	1.7 ± 0.6	
SWNT[35]	–1.5	

The CTE of the two-dimensionally isotropic composite is calculated by the following equations[36]:

$$\alpha_c = \frac{\alpha_{11} + \alpha_{22}}{2} + \frac{(E_{11} - E_{22})(\alpha_{11} - \alpha_{22})}{2[E_{11} + (1 + 2\nu_{12})E_{22}]} \tag{2.1}$$

$$\alpha_{11} = \frac{\alpha_{NT} E_{NT} V_{NT} + \alpha_m E_m (1 - V_{NT})}{E_{11}} \tag{2.2}$$

$$\alpha_{22} = (1 + \nu_{NT})\alpha_{NT} V_{NT} + (1 + \nu_m)\alpha_m (1 - V_{NT}) - \nu_{12}\alpha_{11} \tag{2.3}$$

$$\nu_{12} = \nu_{NT} V_{NT} + \nu_m V_m \tag{2.4}$$

ν_m and ν_{NT} are the Poisson's ratio for the PAN and SWNT and are taken to be 0.07[37] and 0.17[38], respectively. V_{NT} is the volume fraction of SWNT in the PAN/SWNT (60/40) film and is equal to 0.38. The axial modulus of the SWNT (E_{NT}) is 640 GPa[1]. α_m and α_{NT} are CTEs of PAN and SWNT, respectively and are taken as the values listed in Table 2.2. E_m is the modulus of the PAN matrix. In a film with a random nanotube orientation in a plane, E_{11} and E_{22} are related to the composite modulus (E_c) by the equations[36].

$$E_C = \frac{3}{8} E_{11} + \frac{5}{8} E_{22} \tag{2.5}$$

$$E_{11} = \frac{1 + 2(l_{NT} / d_{NT})\eta_L V_{NT}}{1 - \eta_L V_{NT}} E_m \tag{2.6}$$

$$E_{22} = \frac{1 + 2\eta_T V_{NT}}{1 - \eta_T V_{NT}} E_m \tag{2.7}$$

$$\eta_L = \frac{E_{NT} / E_m - 1}{E_{NT} / E_m + 2(l_{NT} / d_{NT})} \tag{2.8}$$

$$\eta_T = \frac{E_{NT} / E_m - 1}{E_{NT} / E_m + 2} \tag{2.9}$$

l_{NT} and d_{NT} are the length and diameter of nanotube ropes, respectively. Using E_c and E_m values in Table 2.1, l_{NT}/d_{NT}, E_{11}, E_{22}, were calculated to be 4, 16.6 GPa, 7.5 GPa, respectively. Using these values in Equation (2.1)-(2.4), in plane CTE of the composite film was determined to be 1.8×10^{-6} $^{o}C^{-1}$, which is in excellent agreement with the experimental value of 1.7×10^{-6} $^{o}C^{-1}$.

The electrical conductivity of PAN/SWNT (60/40) composite is 1.5×10^4 S/m. By comparison, electrically conductivity of PVA/MWNT composite film (40/60) was reported[3] to be 10^2 S/m. The conductivity of PAN/SWNT film of the order of 10^4 S/m is comparable to those of the electrically conducting polymers such as polypyrrole (10^4 S/m)[39] , polythiophene (10^4 S/m) [40], and polyaniline (10^3 S/m)[41].

Scanning electron micrographs of the tensile fractures of the control PAN and PAN/SWNT composite films (Figure 2.3) indicate that nanotubes disperse well in the PAN matrix. PAN/SWNT composite film retained its shape after being immersed in DMF for three days at room temperature, and only 27 % of the PAN in PAN/ SWNT (60/40) composite film dissolved in DMF. From the SEM images (Figure 2.4), the rope diameters in the SWNT powder and in the PAN/ SWNT (60/ 40) films were estimated to be 26 ± 3 nm and 40 ± 2 nm, respectively.

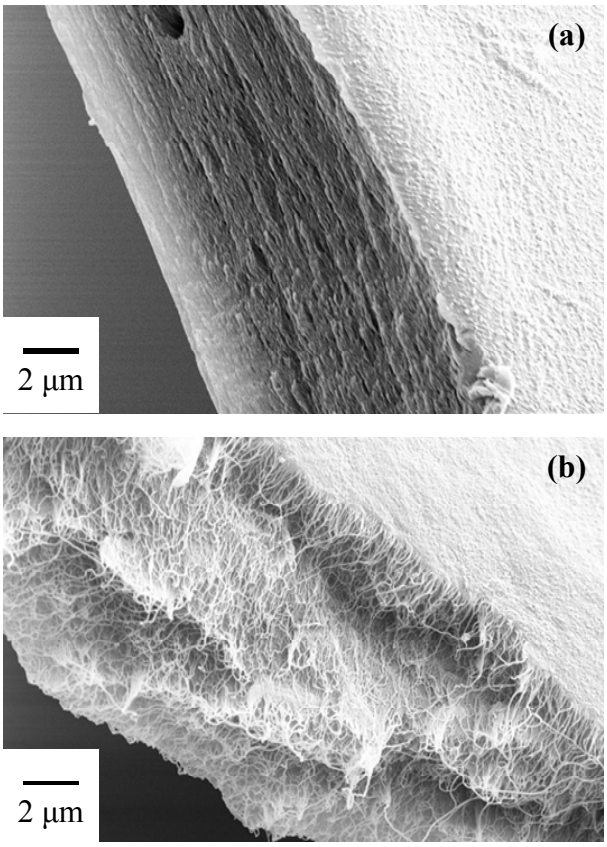

Figure 2.3. Scanning electron micrographs of the tensile fractures of (a) PAN, and (b) PAN/SWNT (60/40) composite film.

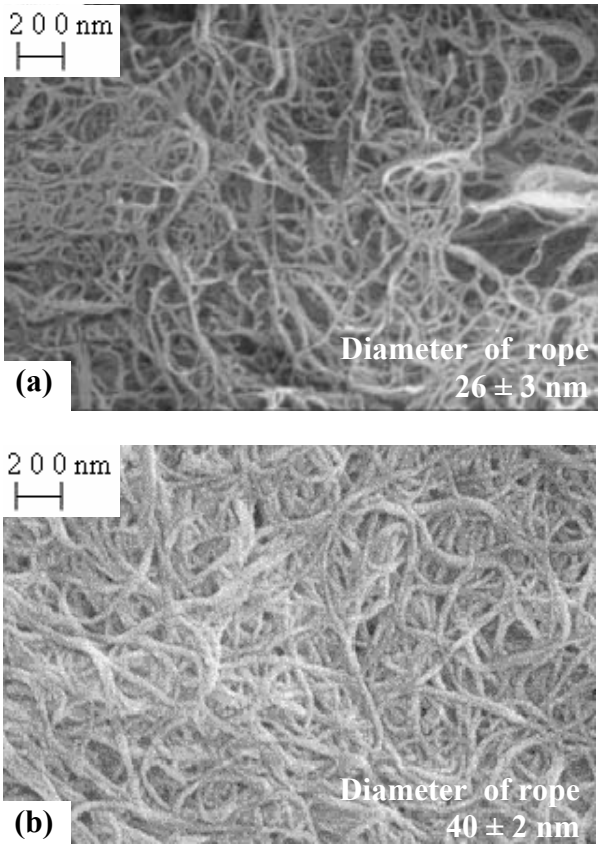

Figure 2.4. Scanning electron micrographs of (a) SWNT powder, and (b) PAN/SWNT (60/40) composite film.

In other work, SWNT rope diameters of 30[42] and 35 nm[32] have been estimated. We attribute these variations in SWNT rope diameter to differences in different batches of nanotubes. Assuming that all PAN is adsorbed on the SWNT rope, the diameter of the PAN wrapped SWNT bundle can be calculated using the following equation:

$$\frac{(d^2 + 2dR_{SWNT})\rho_{PAN}}{R_{SWNT}^2 \rho_{SWNT}} = \frac{m_{PAN}}{m_{SWNT}} \tag{2.10}$$

where R_{SWNT} is the radius of the SWNT bundle, d is the thickness of PAN coating on SWNT bundle, m_{PAN} and m_{SWNT} are the weight fractions, and ρ_{PAN} and ρ_{SWNT} are the densities of PAN and SWNTs, respectively. The measured density of PAN film (1.01 g/cm^3) is lower than the typical PAN polymer density of 1.18 g/cm^3. During PAN film formation, pore structure forms due to solvent evaporation, resulting in reduced PAN density. Using the measured PAN and SWNT densities (Table 2.1), and the 26 nm diameter of SWNT bundle, the diameter of the PAN wrapped SWNT bundle is calculated to be 39 nm for the PAN/ SWNT (60/40) composite. Using PAN and SWNT theoretical densities of 1.18 and 1.30 g/cm^3, respectively, rope diameter for the composite film was calculated to be 42 nm. Composite rope diameter calculated values of 39 and 42 nm are in excellent agreement with the measured value of ~ 40 nm (Figure 2.4b). This suggests that almost all the PAN is adsorbed on the SWNT bundle. The fact that 73% of the total PAN is not accessible to the solvent and can not be re-dissolved in DMF, further confirms the strong PAN association to SWNT.

PAN and PAN/SWNT films exhibit the characteristic PAN x-ray diffraction peaks at 16.7-16.9^o, 24.7-26.4^o and 28.3-29.6^o (Figure 2.5)[43]. PAN crystallite size[44] (without instrumental broadening correction) calculated using Scherrer equation from the 110 peak at 16.8° 2θ and PAN x-ray crystallinity values are given in Table 2.3. The crystal size perpendicular to (110) plane in the composite film is nearly half of the crystal size in the control PAN film. The x-ray diffraction intensity of the composite film is substantially less than that for the PAN for the same exposure time. The suppressed motion of the PAN molecule and reduced thermal expansion, particularly above the glass

transition temperature, reduced x-ray diffraction intensity, decreased PAN solubility in DMF in the composite film point to good interaction between PAN and SWNT.

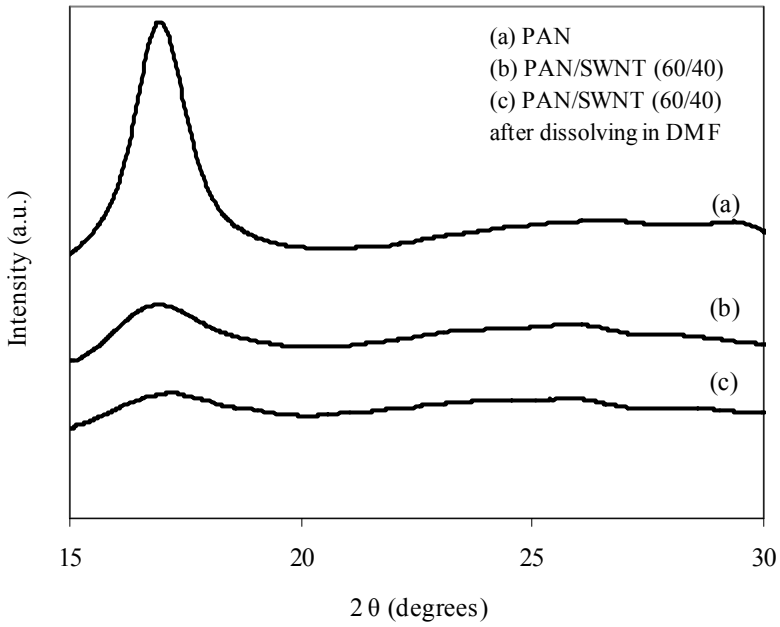

Figure 2.5. Wide angle X-ray diffraction radial scans for PAN and PAN/SWNT (60/40) films.

Table 2.3. Wide angle X-ray diffraction results of PAN and PAN/SWNT films

Sample	Crystal size (nm)	Crystallinity (%)
PAN	5.3	53
PAN/SWNT (60/40)	2.9	45
PAN/SWNT (60/40) after dissolving in DMF	2.6	53

2.3.2 DMF Treated PAN/SWNT Composite Film

The PAN/SWNT composite films with 40 wt% nanotube loading were kept in DMF at temperature of 50, 70, 90, 110 and 130 ^{o}C for one hour, then taken out from DMF and dried completely. A PAN/SWNT composite film with no treatment in DMF is referred to as original composite film.

The weight of PAN/SWNT composite films before and after DMF treatment was measured and listed in Table 2.4. When the composite film is kept in DMF, part of PAN molecules is resistant to solvent DMF. The ratio of PAN not dissolved in DMF to the total PAN in the composite film was calculated (Table 2.4). The fact that 61 % PAN of the total PAN can not be re-dissolved in DMF even at the temperature as high as 130 ^{o}C indicates the strong interaction between PAN and SWNT.

Table 2.4. Weight change for PAN/SWNT (60/40) composite films before and after DMF treatment at different temperatures

DMF treatment temperature (^{o}C)	**Film weight before DMF treatment (mg)**	**Film weight after DMF treatment (mg)**	**(PAN not re-dissolved in DMF)/ (total PAN in the composite film) (%)**
50	1.02	0.85	72
70	1.25	1.00	68
90	1.26	0.96	60
110	1.11	0.85	61
130	2.06	1.59	61

X-ray patterns of SWNT powder, PAN/SWNT composite films and SWNT bucky paper are shown in Figure 2.6. The 2θ values and corresponding d-spacing for samples are listed in Table 2.5. The peaks at 2θ ~ 6.5-7.5 ^{o} and 2θ ~ 10-13 ^{o} correspond to (10) and (11) planes of the 2D hexagonal lattice in the ordered SWNT bundle.[2, 45] The peak at 2θ ~16.8 ° for the PAN/SWNT composite film corresponds to (110) plane of PAN. PAN crystallinity for the composite films is listed in Table 2.5. DMF treated composite films have smaller PAN crystallinity as compared to the original PAN/SWNT composite film possibly due to the destruction of part of the crystalline phase.

The average diameter d_t of nantotubes is related with the d-spacing $d_{(10)}$ of the (10) plane and inter-tube spacing D by Equation (2.11):

$$d_t = \frac{2d_{(10)}}{\sqrt{3}} - D \tag{2.11}$$

Inter-tube spacing of SWNT powder in the powder is 0.34 nm which is the inter-plane spacing of graphite[46]. From this inter-tube spacing value, the average nanotube diameter in the SWNT powder is estimated to be 1.033 nm. Based on measured d-spacing values and the average tube diameter of 1.033 nm, the inter-tube spacing of nanotubes in the buckypaper, original PAN/SWNT composite film, and DMF treated PAN/SWNT films are calculated and listed in Table 2.5. Figure 2.7 shows the inter-spacing of SWNT in samples as a function of DMF temperature. The inter-tube spacing of SWNT in the original composite film is larger than that in the SWNT powder and that in the SWNT bucky paper indicating the possibility of the intercalation of PAN molecules within nanotube bundles. The inter-tube spacing of SWNT in the composite films subjected to DMF has no significant change with increasing DMF temperature.

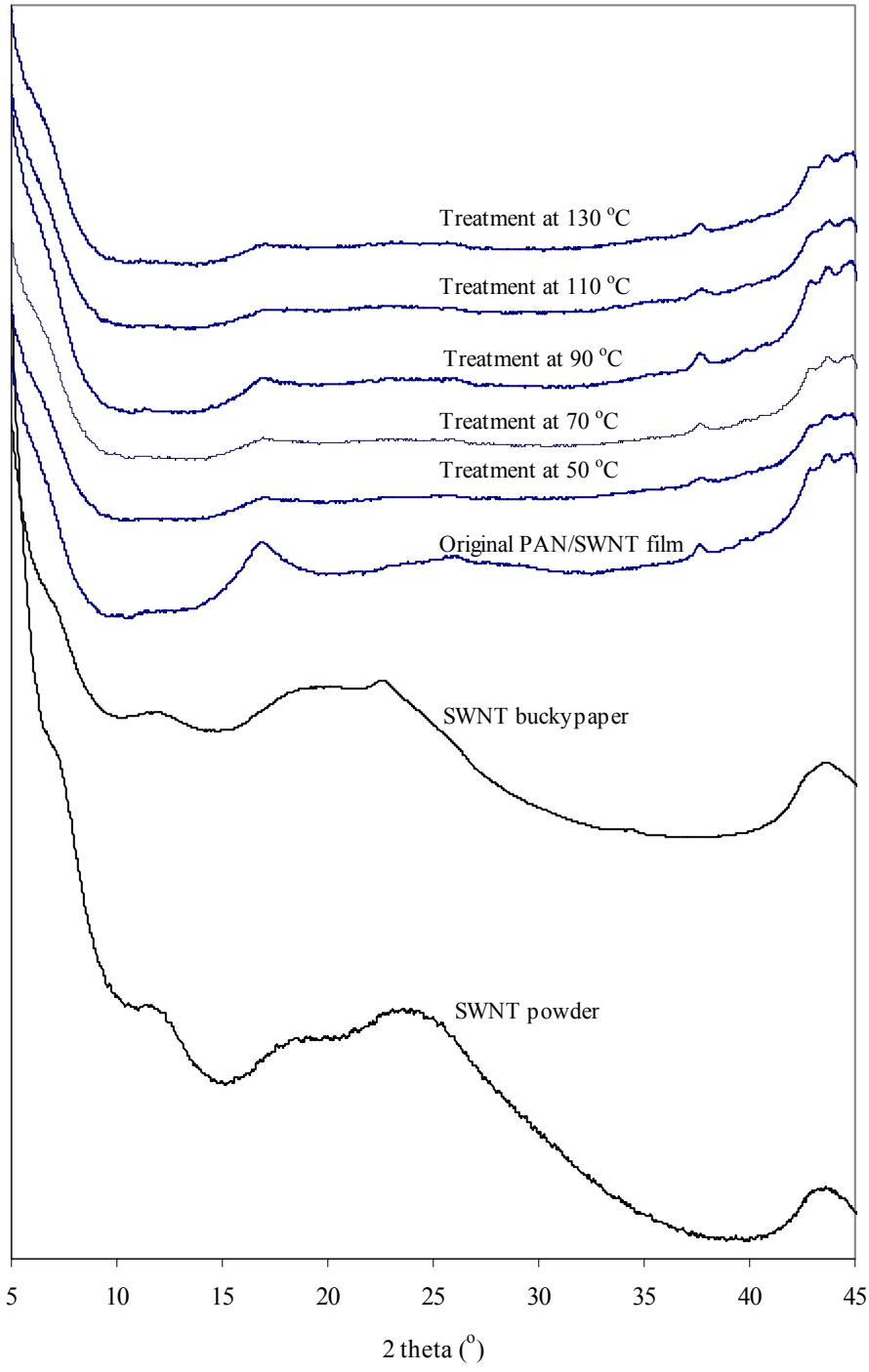

Figure 2.6. X-ray patterns for SWNT powder, SWNT buckypaper and PAN/SWNT composite films.

Table 2.5. X-ray results for SWNT powder, SWNT bucky paper and PAN/SWNT composite films

Samples	d(1,0) (nm)	2θ (^{o})	Inter-tube spacing (nm)	Crystallinity (%)	Crystal size (nm)
SWNT Powder	1.19	7.43	0.340	-	-
SWNT buckypaper	1.25	7.09	0.406	-	-
Original PAN/SWNT film	1.31	6.72	0.485	45	2
Treatment at 50 ^{o}C	1.32	6.71	0.487	25	3
Treatment at 70 ^{o}C	1.31	6.72	0.485	22	3
Treatment at 90 ^{o}C	1.31	6.72	0.485	27	2
Treatment at 110 ^{o}C	1.31	6.76	0.476	18	3
Treatment at 130 ^{o}C	1.31	6.73	0.483	21	3

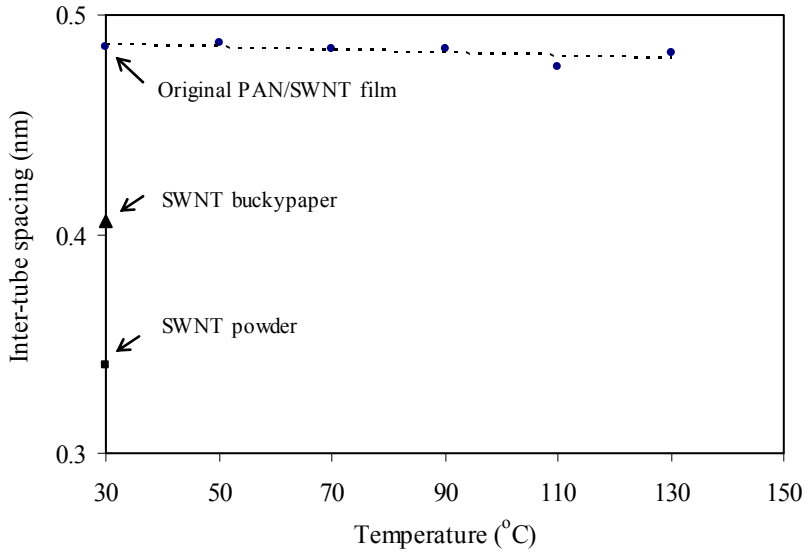

Figure 2.7. Inter-tube spacing as a function of DMF temperatures for SWNT powder, SWNT buckypaper and PAN/SWNT composite films.

In the Raman spectra of SWNT powder and composite films, G' band for the composite films appears at ~ 2580 cm^{-1}. G' peak position for the SWNT powder and composite films is plotted as a function of DMF treatment temperature in Figure 2.8. G' band for the original PAN/SWNT composite film shifts to higher wavenumber relative to the SWNT powder due to the compressive stress exerted by polymer on the SWNT bundles. G' band position shows no significant variation when the composites films are treated in DMF.

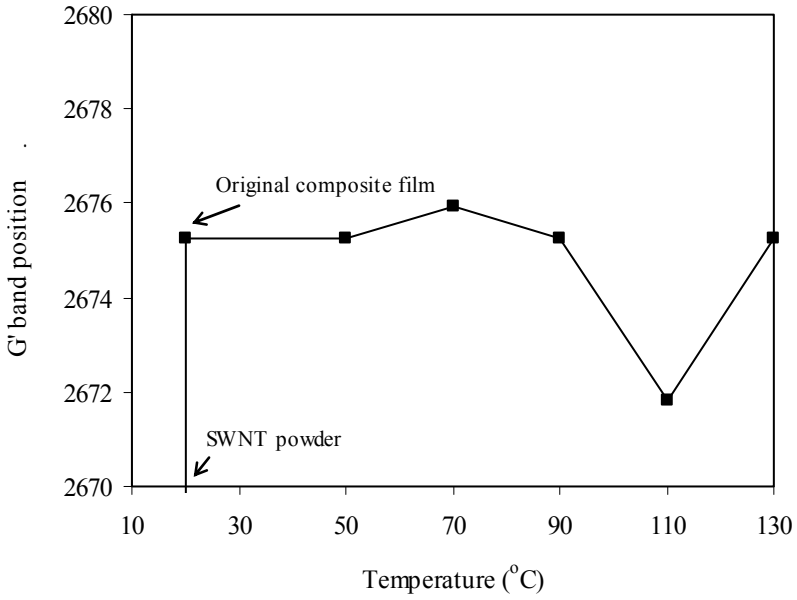

Figure 2.8. G' band position as a function of DMF treatment temperature for SWNT powder and PAN/SWNT composite films.

G band shows two dominant Lorentzian features (Figure 2.9). The low frequency component (ω_G^-) located at ~1564 cm^{-1} is related to the vibrations along the circumferential direction and the higher frequency one (ω_G^+) at ~1592 cm^{-1} is associated

to the vibrations along the direction of the nanotube axis.[47] G bands show no significant shift for the PAN/SWNT composite films as compared to the SWNT powder. The full-width at half maxima (FWHM) of G band for SWNT powder and PAN/SWNT composite films is plotted as a function of frequencies in Figure 2.10. The width of G band decreases for the original composite film relative to the SWNT powder and reduces further with DMF treatment. Stephan et al.[3] have reported the decreased width of G band by the addition of nanotubes to PMMA matrix and attribute them to the intercalation of PMMA between tubes. In our PAN/SWNT case, the decreased width of G band by incorporating SWNT into PAN may be explained by the intercalation of PAN between nanotube bundles. The width of Raman bands of SWNT increases with increasing pressure.[48] When PAN/SWNT is treated in DMF, part of PAN molecules are removed resulting in the reduced compressive stress, which may cause reduction of the width of G band for the DMF treated films as compared to the original film.

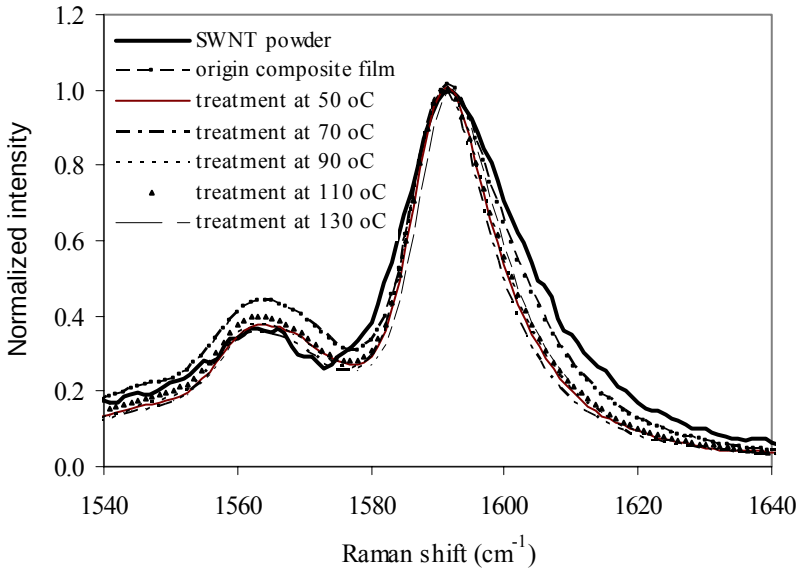

Figure 2.9. G band of the Raman spectra for SWNT powder and PAN/SWNT composite films.

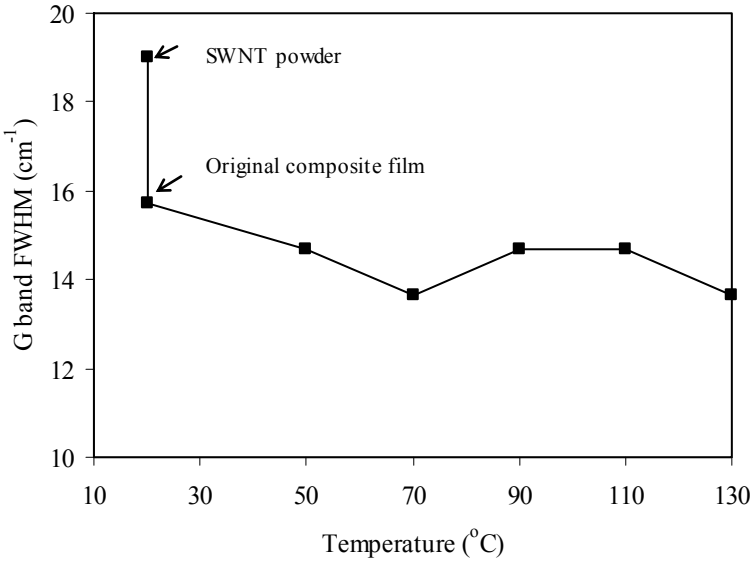

Figure 2.10. G band width as a function of DMF treatment temperature for SWNT powder and PAN/SWNT composite films.

2.4 CONCLUSIONS

SWNTs have been incorporated into PAN to form PAN/ SWNT composite films with unique properties. Tensile strength and modulus of the composite films are higher than that of the control PAN or that of the control SWNT bucky paper. The electrical conductivity of the PAN/SWNT composite film with 40 % SWNT loading is in the order of 10^4 S/m. The modulus of PAN/SWNT film above glass transition temperature is 40 times the PAN modulus. Composite film also shows significantly reduced thermal extension at high temperature as compared to PAN film. SEM image of PAN/SWNT film indicates good dispersion of SWNT in the PAN matrix. Due to PAN adsorption on SWNT, the diameter of SWNT bundle increased from 26 nm to 40 nm with 60 % PAN. The crystal size in the composite film is significantly smaller than that in the control PAN film. The increased inter-tube spacing of the SWNT bundle in the composite film as compared to that in SWNT powder indicates the intercalation of PAN between nanotube bundles, which is also supported by the Raman spectra.

2.5 REFERENCES

[1] R. H. Baughman, A. A. Zakhidov, and W. A. de Heer, Science **297**, 787 (2002).

[2] A. Thess, R. Lee, P. Nikolaev, H. J. Dai, P. Petit, J. Robert, C. H. Xu, Y. H. Lee, S. G. Kim, A. G. Rinzler, D. T. Colbert, G. E. Scuseria, D. Tomanek, J. E. Fischer, and R. E. Smalley, Science **273**, 483 (1996).

[3] M. S. P. Shaffer and A. H. Windle, Advanced Materials **11**, 937 (1999).

[4] X. F. Zhang, T. Liu, T. V. Sreekumar, S. Kumar, V. C. Moore, R. H. Hauge, and R. E. Smalley, Nano Letters **3**, 1285 (2003).

[5] X. F. Zhang, T. Liu, T. V. Sreekumar, S. Kumar, X. Hu, and K. Smith, Polymer **45**, 8801 (2004).

[6] C. Stephan, T. P. Nguyen, M. L. de la Chapelle, S. Lefrant, C. Journet, and P. Bernier, Synthetic Metals **108**, 139 (2000).

[7] R. Haggenmueller, H. H. Gommans, A. G. Rinzler, J. E. Fischer, and K. I. Winey, Chemical Physics Letters **330**, 219 (2000).

[8] C. A. Cooper, D. Ravich, D. Lips, J. Mayer, and H. D. Wagner, Composites Science and Technology **62**, 1105 (2002).

[9] J. M. Benoit, B. Corraze, and O. Chauvet, Physical Review B **65**, 242405 (2002).

[10] B. McCarthy, J. N. Coleman, R. Czerw, A. B. Dalton, H. J. Byrne, D. Tekleab, P. Iyer, P. M. Ajayan, W. J. Blau, and D. L. Carroll, Nanotechnology **12**, 187 (2001).

[11] M. Tahhan, V. T. Truong, G. M. Spinks, and G. G. Wallace, Smart Materials & Structures **12**, 626 (2003).

[12] N. Ferrer-Anglada, M. Kaempgen, V. Skakalova, U. Dettlaf-Weglikowska, and S. Roth, Diamond and Related Materials **13**, 256 (2004).

[13] A. R. Bhattacharyya, T. V. Sreekumar, T. Liu, S. Kumar, L. M. Ericson, R. H. Hauge, and R. E. Smalley, Polymer **44**, 2373 (2003).

[14] M. J. Biercuk, M. C. Llaguno, M. Radosavljevic, J. K. Hyun, A. T. Johnson, and J. E. Fischer, Applied Physics Letters **80**, 2767 (2002).

[15] B. Kim, J. Lee, and I. S. Yu, Journal of Applied Physics **94**, 6724 (2003).

[16] I. Alexandrou, E. Kymakis, and G. A. J. Amaratunga, Applied Physics Letters **80**, 1435 (2002).

[17] E. Kymakis, I. Alexandou, and G. A. J. Amaratunga, Synthetic Metals **127**, 59 (2002).

[18] Y. C. Chen, N. R. Raravikar, L. S. Schadler, P. M. Ajayan, Y. P. Zhao, T. M. Lu, G. C. Wang, and X. C. Zhang, Applied Physics Letters **81**, 975 (2002).

[19] P. T. Lillehei, C. Park, J. H. Rouse, and E. J. Siochi, Nano Letters **2**, 827 (2002).

[20] M. Sennett, E. Welsh, J. B. Wright, W. Z. Li, J. G. Wen, and Z. F. Ren, Applied Physics a-Materials Science & Processing **76**, 111 (2003).

[21] R. Ramasubramaniam, J. Chen, and H. Y. Liu, Applied Physics Letters **83**, 2928 (2003).

[22] J. Q. Pham, C. A. Mitchell, J. L. Bahr, J. M. Tour, R. Krishanamoorti, and P. F. Green, Journal of Polymer Science Part B-Polymer Physics **41**, 3339 (2003).

[23] J. G. Smith, J. W. Connell, D. M. Delozier, P. T. Lillehei, K. A. Watson, Y. Lin, B. Zhou, and Y. P. Sun, Polymer **45**, 825 (2004).

[24] T. V. Sreekumar, T. Liu, B. G. Min, H. Guo, S. Kumar, R. H. Hauge, and R. E. Smalley, Advanced Materials **16**, 58 (2004).

[25] S. H. Kim, B. G. Min, S. C. Lee, S. B. Park, T. D. Lee, M. Park, and S. Kumar, Fibers and Polymers **5**, 198 (2004).

[26] S. Kumar, T. D. Dang, F. E. Arnold, A. R. Bhattacharyya, B. G. Min, X. F. Zhang, R. A. Vaia, C. Park, W. W. Adams, R. H. Hauge, R. E. Smalley, S. Ramesh, and P. A. Willis, Macromolecules **35**, 9039 (2002).

[27] A. B. Dalton, S. Collins, J. Razal, E. Munoz, V. H. Ebron, B. G. Kim, J. N. Coleman, J. P. Ferraris, and R. H. Baughman, Journal of Materials Chemistry **14**, 1 (2004).

[28] A. A. Mamedov, N. A. Kotov, M. Prato, D. M. Guldi, J. P. Wicksted, and A. Hirsch, Nature Materials **1**, 190 (2002).

[29] J. N. Coleman, W. J. Blau, A. B. Dalton, E. Munoz, S. Collins, B. G. Kim, J. Razal, M. Selvidge, G. Vieiro, and R. H. Baughman, Applied Physics Letters **82**, 1682 (2003).

[30] J. B. Donnet, T. K. Wang, J. C. M. Peng, and S. M. D. Ribouillatand, "Carbon Fibers," Marcel Dekker, New York, 3rd Edition (1998).

[31] J. C. Masson, "Acrylic Fiber technology and Application," Marcel Dekker, New York (1995).

[32] T. Liu, T. V. Sreekumar, S. Kumar, R. H. Hauge, and R. E. Smalley, Carbon **41**, 2440 (2003).

[33] X. F. Zhang, T. V. Sreekumar, T. Liu, and S. Kumar, Journal of Physical Chemistry B **108**, 16435 (2004).

[34] S. Malik, H. Rosner, F. Hennrich, A. Bottcher, M. M. Kappes, T. Beck, and M. Auhorn, Physical Chemistry Chemical Physics **6**, 3540 (2004).

[35] Y. Maniwa, R. Fujiwara, H. Kira, H. Tou, H. Kataura, S. Suzuki, Y. Achiba, E. Nishibori, M. Takata, M. Sakata, A. Fujiwara, and H. Suematsu, Physical Review B **64**, 241402 (2001).

[36] P. K. Mallick, "Composite Engineering Handbook," Marcel Dekker, New York, pp. 900 (1997).

[37] M. H. Ozkul, J. E. Mark, and J. H. Aubert, Journal of Applied Polymer Science **48**, 767 (1993).

[38] R. B. Pipes and P. Hubert, Composites Science and Technology **63**, 1571 (2003).

[39] M. K. Song, Y. T. Kim, B. S. Kim, J. Kim, K. Char, and H. W. Rhee, Synthetic Metals **141**, 315 (2004).

[40] A. O. Patil, A. J. Heeger, and F. Wudl, Chemical Reviews **88**, 183 (1988).

[41] J. Stejskal, D. Hlavata, P. Holler, M. Trchova, J. Prokes, and I. Sapurina, Polymer International **53**, 294 (2004).

[42] T. Uchida and S. Kumar, Journal of Applied Polymer Science **98**, 985 (2005).

[43] A. K. Gupta and R. P. Singhal, Journal of Polymer Science Part B-Polymer Physics **21**, 2243 (1983).

[44] B. D. Cullity, "Elements of x-ray Diffraction," Addison-wesley, MA, 2nd edition, pp. 102 (1978).

[45] C. Journet, W. K. Maser, P. Bernier, A. Loiseau, M. L. delaChapelle, S. Lefrant, P. Deniard, R. Lee, and J. E. Fischer, Nature **388**, 756 (1997).

[46] K. Awasthi, A. Srivastava, and O. N. Srivastava, Journal of Nanoscience and Nanotechnology **5**, 1616 (2005).

[47] R. A. Jishi, L. Venkataraman, M. S. Dresselhaus, and G. Dresselhaus, Chemical Physics Letters **209**, 77 (1993).

[48] U. D. Venkateswaran, A. M. Rao, E. Richter, M. Menon, A. Rinzler, R. E. Smalley, and P. C. Eklund, Physical Review B **59**, 10928 (1999).

CHAPTER 3

POLYACYLONITRILE/VAPOR GROWN CARBON NANO FIBER COMPOSITE FILMS

3. 1 INTRODUCTION

Carbon fibers, developed during 1960s are now being widely used for reinforcing composites. Vapor grown carbon nano fibers (VGCNFs) were developed in 1980s.[1-4] VGCNFs are synthesized by exposing a metallic catalyst to hydrocarbon gases.[4] Uchida et al[5] studied the microstructure of nano fibers using transmission electron microscopy. A truncated cone microstructure of VGCNFs was observed with outer and inner diameters of 60 and 25 nm, respectively. The graphite sheets in nano fibers were found to be oriented at an average angle of about 15 degrees with respect to the fiber axis. The tensile modulus along the nano fiber axis was calculated to be as low as 50 GPa using the graphitic plane mis-orientation. VGCNFs have been incorporated into a variety of polymers such as epoxy[6-8], polyethylene[9], polypropylene[10-15], polycarbonate[13, 14, 16-20], polystyrene[21] acrylonitrile-butadiene-styrene (ABS)[22], nylon[23, 24], poly(phenylene sulfide)[7], phenylethynyl terminated polyimide [25], poly(methyl methacrylate)[6,26], poly(ethylene terephthalate) (PET)[27], and poly(p-phenylene benzobisthiazole) (PBZT)[28]. Property improvements in polymer with incorporation of VGCNF include electrical properties[8, 11, 14, 20], mechanical properties[10, 12, 14], thermal stability[10, 20], as well as crystallization rate[10]. Rheological properties of VGCNF-reinforced nanocomposites have also been studied.[9, 11, 13, 17] PP/VGCNF composites were reported to exhibit an electrical conductivity percolation threshold of 9-18 wt%.[11] The percolation threshold of

PC/VGCNF composites was reported at 6.3 wt%.[20] PP/VGCNF composites with 15 wt% fiber loading shows 90% enhancement in Young's modulus over the control polymer.[14] In another study, a 60% increase in Young's modulus and a 35% reduction in the thermal expansion coefficient were observed for PP/VGCNF bulk composites with 5 vol% fiber loading.[10] The storage modulus at room temperature increased by 350% for PP/VGCNF composites containing 60 wt% VGCNF as compared to the control PP.[12] PAN/VGCNF composite fibers with significant property improvements have been reported[29]. In this chapter, processing, structure, and properties of PAN/VGCNF composite films with varying nano fiber loading are presented and discussed.

3.2 EXPERIMENTAL

3.2.1 Materials

PAN (molecular weight =100,000 g/mol) obtained from Exlan, Co. (Japan) and dimenthylformamide (DMF) supplied by Sigma-Aldrich were used as received. VGCNFs (Grade PR-24-HT) were obtained from Applied Sciences, Inc. (Cedarville, OH).

3.2.2 Preparation of PAN/VGCNF Composite Films

Dried VGCNFs were dispersed in DMF by sonication in a sonic bath (Cole-Parmer 8891R-DTH, 80 W, 43 kHz) for 48 hours. Homogenous dispersion of VGCNF in DMF was confirmed by optical microscopy. Dried PAN was dissolved separately in DMF, and the PAN/DMF solution was subsequently added to the VGCNF dispersion. The resultant PAN/VGCNF/DMF dispersion was stirred and excess solvent was evaporated to obtain the desired volume. The PAN/VGCNF/DMF dispersion was cast on the glass substrate to form the film in the vacuum oven at 80 ^{o}C. The composite film was

peeled off the glass substrate and further dried in vacuum oven at 80 ^{o}C for 3 days. The composite films with various loading of VGCNFs (5, 10, 20, 40, 60, 80, 90 wt% CNFs) were prepared using the same procedure. The volume of DMF and the amount of PAN and VGCNF used for the preparation of various composite films are listed in Table 3.1. A control PAN film was also prepared.

Table 3.1. Volume of DMF and amount of PAN and VGCNF for preparation of the composite films

VGCNF loading (wt%)	Volume of DMF (mL)	Weight of VGCNF (mg)	Weight of PAN (mg)	Conc. of PAN in PAN/VGCNF/DMF solution (mg/mL)
0	25	-	250	10
5	50	12.6	240	4.8
10	50	26.7	240	4.8
20	50	60	240	4.8
40	200	100	150	0.75
60	200	150	100	0.5
80	200	200	50	0.25
90	200	200	22.2	0.11

3.2.3 Characterization of Composite Films

RSA III manufactured by Rheometrics Scientific was used to measure the tensile and dynamic mechanical properties. The gauge length, film width, and strain rate for the tensile tests were 20 mm, 2 mm, and 10 %/min, respectively. Dynamic mechanical

measurement was carried out at the testing frequencies of 0.1, 1, 5 and 10 Hz, and temperature increment of 1 ^{o}C/min. Transmission electron microscopy (TEM) studies were conducted using Hitachi HF-2000 (operated at 200 kV). For TEM specimen preparation, the PAN/VGCNF/DMF dispersion was diluted using DMF and dropped on lacey carbon TEM grids. Other experimental procedures are described in Chapter 2.

3.3 RESULTS AND DISCUSSION

The high resolution TEM (HRTEM) images of VGCNF dispersion are given in Figure 3.1. Single-layer structure in carbon nano fibers is shown in Figure 3.1a. Double-layer nano fibers contain well oriented graphite sheets at the outer truncated cone structure and misoriented inner layer (Figure 3.1b). Due to the existence of the higher orientation graphitic sheet at outer layer, the density and mechanical properties of double-layer CNF is higher than that of the single layer CNF. The triple-layer CNF and bamboo type structures were also observed and are shown in Figure 3.1c and 3.1d, respectively.

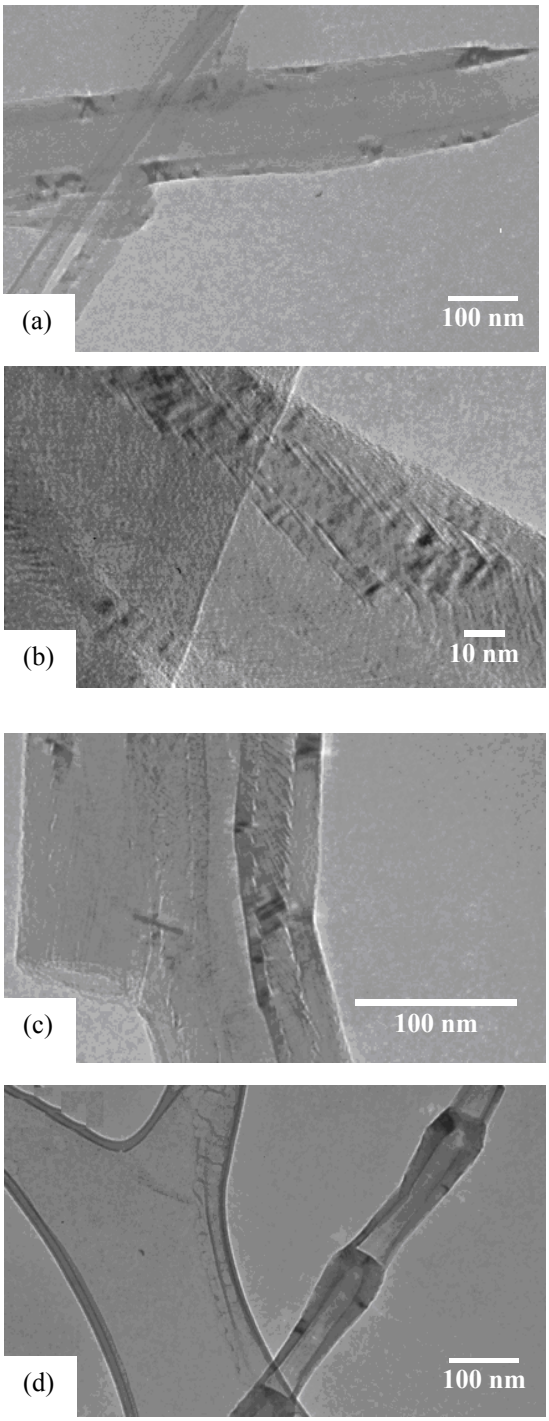

Figure 3.1. HRTEM images of VGCNF showing various types of carbon nano fiber structures: (a) single layer, (b) double layer, (c) triple layer, and (d) bamboo type.

The densities (ρ) of the composite films were determined from their measured weight and volume and are listed in Table 3.2. The measured density of the composite films is lower than the calculated density for all composites except for the film with 5% VGCNF loading. The difference between the theoretical and observed density is attributed to the presence of defects and voids.

Table 3.2. Electrical conductivity and density of control PAN and PAN/VGCNF composite films

VGCNF loading (wt%)	**VGCNF Loading (vol%)**	**Conductivity (S/m)**	**Density (g/cm^3)**	**Theoretical density [a] (g/cm^3)**
0	0	-	1.15 ± 0.06	1.18
5	3.1	0.7 ± 0.6	1.22 ± 0.07	1.20
10	6.3	35.2 ± 11.7	0.91 ± 0.09	1.23
20	13.1	88.8 ± 18.6	0.66 ± 0.05	1.28
40	28.7	$(8.8 \pm 0.2) \times 10^2$	0.81 ± 0.01	1.40
60	47.6	$(1.06 \pm 0.04) \times 10^3$	0.73 ± 0.06	1.55
80	70.8	$(1.57 \pm 0.06) \times 10^3$	0.51 ± 0.06	1.72
90	84.5	$(1.67 \pm 0.08) \times 10^3$	0.50 ± 0.09	1.83

[a] Theoretical density of the composite films is calculated using the following equation:

$$\rho_c = V_f(\rho_f - \rho_m) + \rho_m$$

where ρ_c is the density of the composite film, V_f is the volume fraction of VGCNF, ρ_f is the density of VGCNF (1.95 g/cm^3), and ρ_m is the density of PAN (1.18 g/cm^3).

The tensile test results for various composite films are given in Table 3.3. The initial modulus of the composite film with 5% VGCNF loading is about 1.2 times the modulus of control PAN film, while the tensile strength of this composite film is 1.5 times that of control PAN film. Further enhancement in tensile properties was not observed upon increased VGCNF loading. VGCNF loading higher than 40% in the composite film yielded tensile properties inferior than that for the control PAN film.

Table 3.3. Mechanical properties of control PAN and PAN/VGCNF composite films

VGCNF Loading (wt%)	Thickness (μm)	Tensile Modulus (GPa)	Tensile Strength (MPa)	Elongation (%)
0	24 ± 2	3.7 ± 0.4	53 ± 9	3.2 ± 1.5
5	23 ± 4	4.4 ± 0.3	80 ± 6	5.5 ± 1.6
10	20 ± 2	4.1 ± 0.3	73 ± 6	3.7 ± 0.5
20	30 ± 1	4.0± 0.2	59 ± 3	2.5 ± 0.3
40	21 ± 1	5.4 ± 0.5	57 ± 9	1.4 ± 0.3
60	22 ± 2	3.2 ± 1.2	19 ± 6	0.8 ± 0.2
80	26 ± 0	1.6 ± 0.7	12 ± 4	1.5 ± 0.6
90	29 ± 1	1.1 ± 0.1	5.7 ± 0.7	1.2 ± 0.4

The theoretical modulus of the composite films can be predicted using Halpin-Tsai equation, as discussed in Section 2.3.[30] The parameters used in the Halpin-Tsai equation are listed in Table 3.4. The theoretical specific moduli calculated using VGCNF modulus of 50 GPa for various nano fiber lengths and the experimental specific moduli are plotted as a function of VGCNF loading of up to 40 % (Figure 3.2a). The theoretical

modulus of the composite films increased significantly with increasing nano fiber length from 200 nm up to 10 μm. However, further increase in nano fiber length to 100 μm did not result in significant increase in the calculated modulus. At 5 wt% VGCNF loading, the theoretical modulus of film corresponding to the nano fiber length of 10 μm agrees well with the experimental value. The experimental specific moduli are higher than the theoretical one for the composite films containing 10 and 20% nano fiber. The theoretical modulus for the composite films is calculated based on the VGCNF morphology where all graphite layers are oriented at 15° to the nano fiber axis[31]. However, two types of morphologies in VGCNF were observed: single-layer nano fiber and double-layer nano fiber. The graphite layers in the double-layer nano fiber are highly oriented in a second outer layer resulting in higher modulus.[31] For the double layer VGCNF, the modulus was calculated to be 72 GPa. Using this modulus, the theoretical specific modulus of the composite films for various nano fiber lengths are calculated using Halpin-Tsai equation and plotted as a function of VGCNF loading (up to 40 %) in the composite films (Figure 3.2b). The experimental specific moduli agree well with the theoretical one for the composite films with VGCNF loading as high as 20 %. At VGCNF loading of 40% or more, the experimental modulus of the composite films is significantly lower than the predicted value. Choi et al[6] also reported a similar observation for the epoxy/cup-stacked carbon nanotube nanocomposites.

Table 3.4. Parameters used in Halpin-Tsai equation

Modulus of VGCNF, E_{nf} (GPa)	**Modulus of PAN, E_p (GPa)**	**Length of VGCNF, l_{nf} (μm)**	**Diameter of VGCNF, D_{nf} (nm)**	**Density of VGCNF, ρ_{nf} (g/cm^3)**
50 and 72[5]	3.7	0.2-100	60	1.95[32]

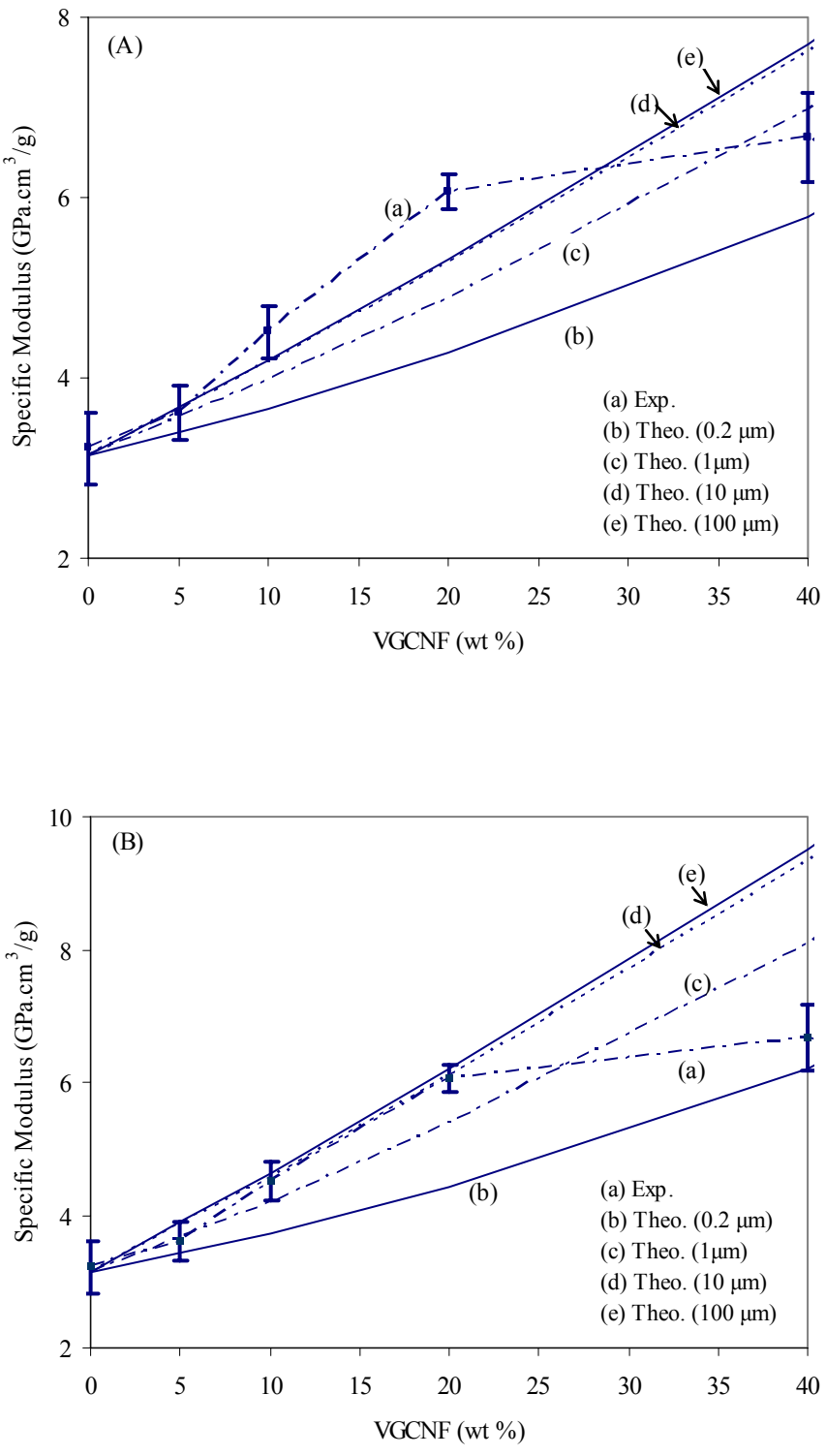

Figure 3.2. Theoretical and experimental modulus of PAN and PAN/VGCNF composite films assuming the modulus of VGCNF to be (A) 50 GPa and (B) 72 GPa.

The electrical conductivity data for PAN and various composite films are shown in Figure 3.3. The inset of Figure 3.3 is the plot of conductivity as a function of nano fiber volume fraction (V), from which a percolation volume (Vc) of 3.1 vol% is obtained. Plotting electrical conductivity as a function of (V-Vc) (both axes in logarithmic scales) results in a slope of 1.29, suggesting two-dimensional electrical percolation behavior.

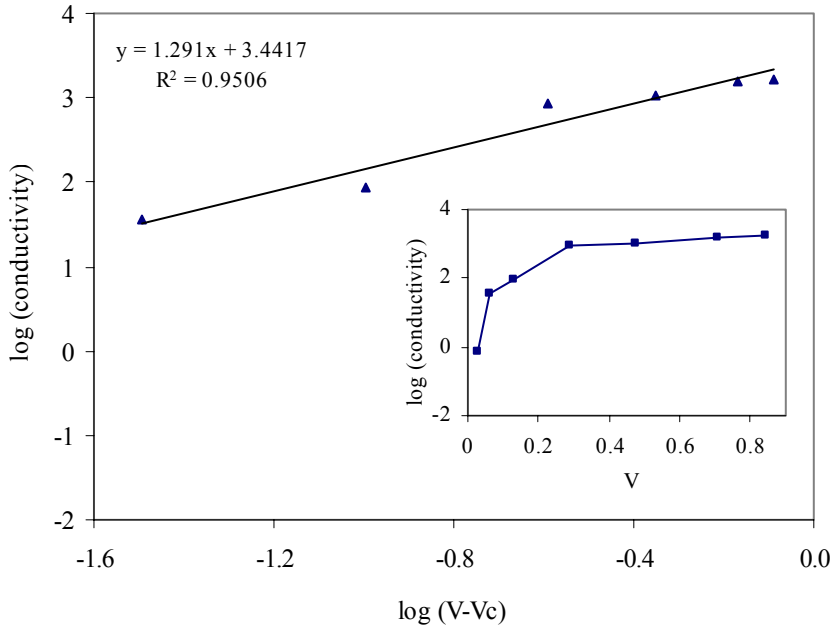

Figure 3.3. Electrical conductivity of PAN/VGCNF composite films.

The storage modulus (E') and Tan δ as a function of temperature for PAN and various composite films are given in Figure 3.4. Consistent with the tensile modulus data (Figure 3.4, top), storage modulus of PAN initially increased with the VGCNF loading. Enhancement in storage modulus is particularly evident above the glass transition temperature. The magnitude of the Tan δ peak decreased (Figure 3.4, bottom) with the

addition of VGCNF indicating the reduction of the damping in the composite with addition of nano fiber. The tan δ peak shifts to higher temperature and broaden towards higher temperatures with the addition of VGCNF. Eitan et al[33] studied the dynamic mechanical properties of multiwall carbon nanotube/polycarbonate composites. The results suggested the presence of a large annular interphase region of immobilized polymer surrounding the nanotubes. The molecular mobility of this non-bulk polymer is reduced, hence contributing to broadening of Tan δ peak towards higher temperature. The composite film with 20 % VGCNF loading did not exhibit a shift in tan δ peak position or the peak broadening to higher temperatures. In general, peak broadening increased with increasing amount of nanofiber in the composite. This observation can be explained in terms of restricted-mobility interphase present in the composite. With increasing amount of nanofiber, the fraction of polymer present at the polymer-nanofiber interphase is also increased. As stated previously, significant amount of this polymer at the interphase becomes immobilized hence results in tan δ peak broadening. This effect is very pronounced at >40 % nanofiber loading (Figure 3.4)

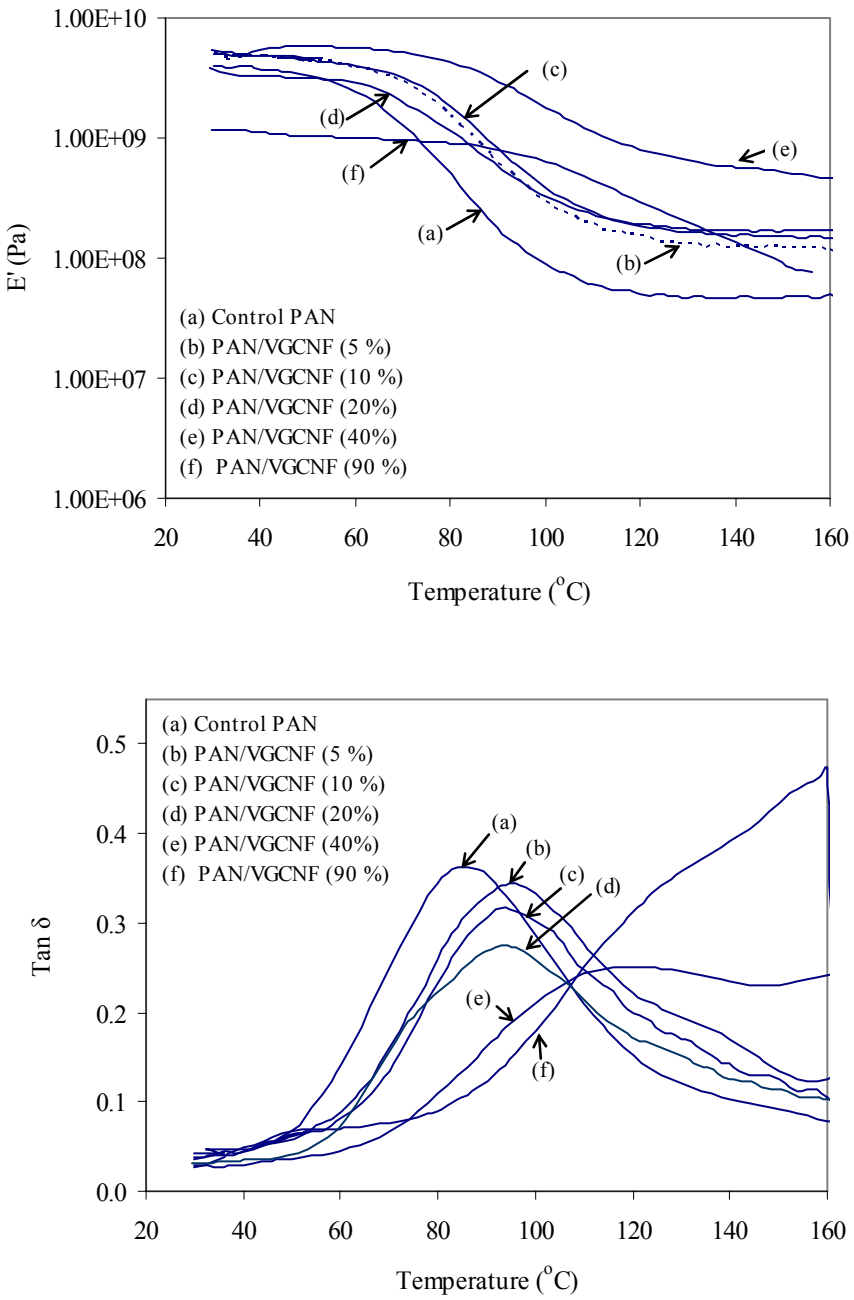

Figure 3.4. Storage modulus (top) and Tan δ (below) as a function of temperature for PAN and PAN/VGCNF composite films.

Figure 3.5 gives the Tan δ peak as a function of temperature for PAN and PAN/VGCNF composite films at various frequencies. The tan δ peak temperatures at various frequencies are listed in Table 3.5. Activation energy for the PAN molecular motion can be calculated using Arrhenius equation:

$$\text{Ln } f = \text{Ln } C - E_a/RT \quad (3.1)$$

where f is frequency, C is the material constant, Ea is the activation energy, R is the gas constant (8.314 KJ/mole) and T is absolute temperature. A plot of Ln f as a function of 1/T for the control and composite films are shown in Figure 3.6. The activation energy is obtained from the slopes of the fitted lines in Figure 3.6. The activation energy for PAN molecular motion in the control PAN film was 425 KJ/mole. For the composite films with 5 and 10 wt% VGCNF loading, the activation energy values were 754 and 535 KJ/mole, respectively. The higher activation energy needed for PAN molecular motion in the composite films indicates interaction between polymer and carbon nano fiber, resulting in hindered motion for polymer molecules. The tensile modulus, tensile strength, and glass transition temperature of PAN/VGNCF (90/10) composite film is lower than those for PAN/VGCNF (95/5) composite film indicating lower reinforcement efficiency in composite film with 10 wt% nano fiber loading. Therefore, lower activation energy is needed for PAN molecular motion in the PAN/VGCNF (90/10) composite film as compared to film with 5 wt% VGCNF loading.

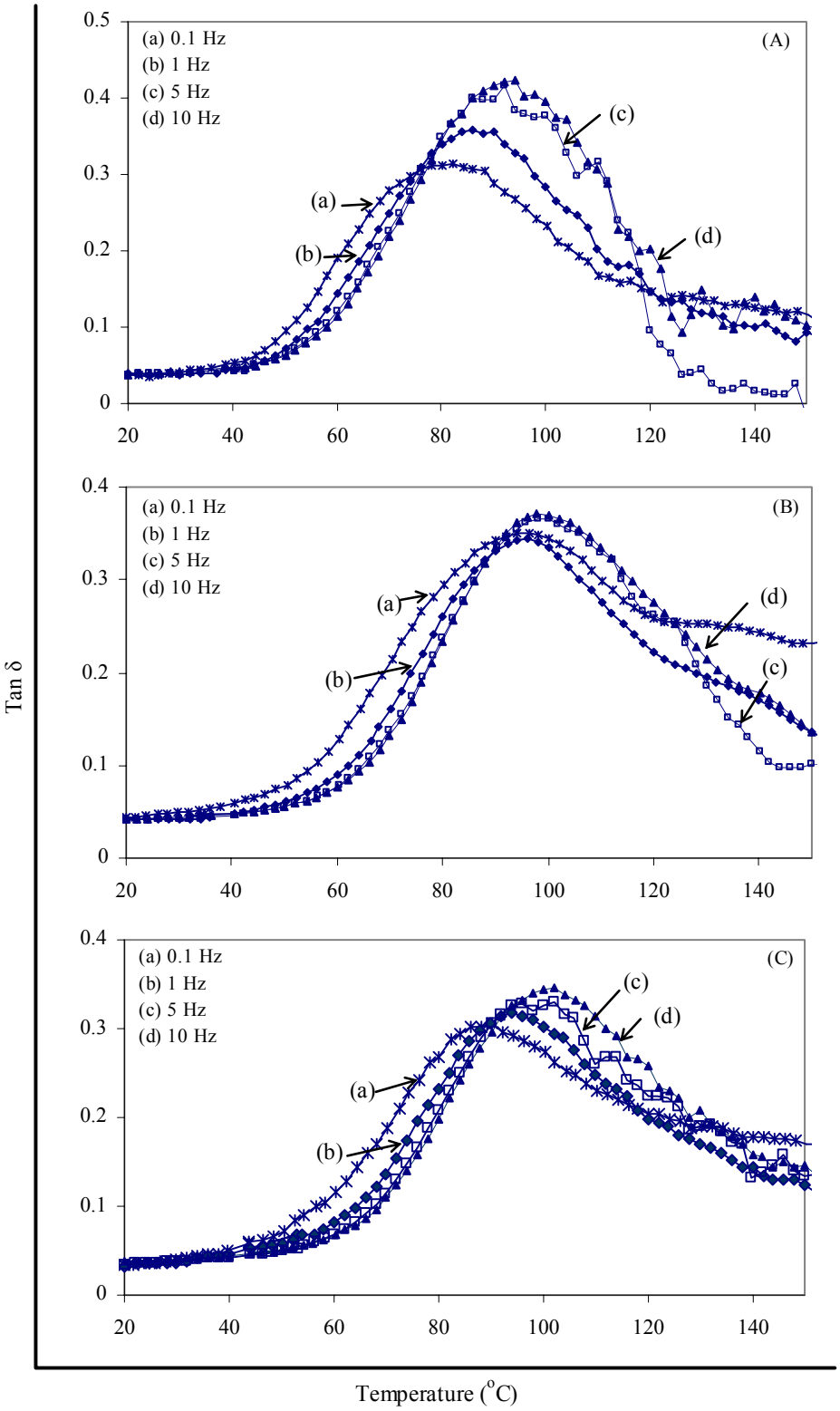

Figure 3.5. Tan δ behavior of (A) Control PAN, (B) PAN/VGCNF (95/5), and (C) PAN/VGCNF (90/10) films as a function of temperature at various frequencies.

Table 3.5. Temperature of Tan δ peak at various frequencies

Frequency (Hz) / Sample	Temperature (^{o}C)			
	0.1	1	5	10
PAN	82.2	88.0	92.1	94.0
PAN/VGCNF (95/5)	94.1	96.1	100.0	100.2
PAN/VGCNF (90/10)	90.3	93.9	97.6	100.1

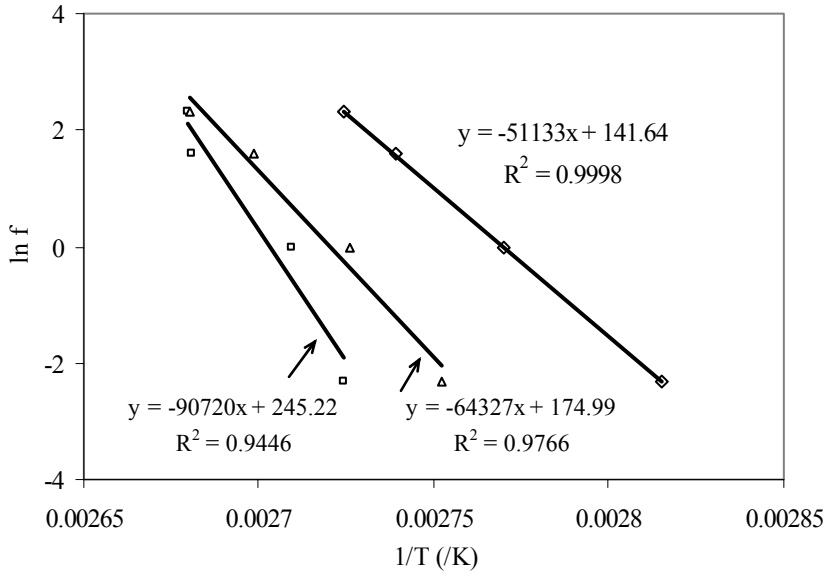

Figure 3.6. Ln f as a function of 1/T for control PAN (◊), PAN/VGCNF with 5 wt% loading (□) and PAN/VGCNF with 10 wt% loading (Δ) films.

The structure of the composite films is characterized using wide angle X-ray diffraction, as shown in Figure 3.7. The peak at 43.5 ^{o} is attributed to the (100) peak in graphite[34]. The crystal size of the graphite (002) plane in composite film is listed in Table 3.6. The crystal size of graphite in the composite film with VGCNF loading higher than 20% is almost same as that in VGCNF powder. However, the average crystal size of graphite in the composite films with lower VGCNF loading (5 wt% and 10 wt%) is smaller than that in VGCNF powder. PAN and PAN/VGCNF films exhibit a characteristic PAN x-ray diffraction peak at 16.9 ^{o} attributed to the PAN (110) peak.[35] PAN crystallite size calculated using Scherrer equation[36] from the (110) peak and PAN crystallinity values are also given in Table 3.6. At lower VGCNF loading (<20 wt%), PAN crystal size in the composite films is larger than that for the control PAN film. When the fiber loading is larger than 40 wt%, PAN crystal size decreases with further addition of nano fibers.

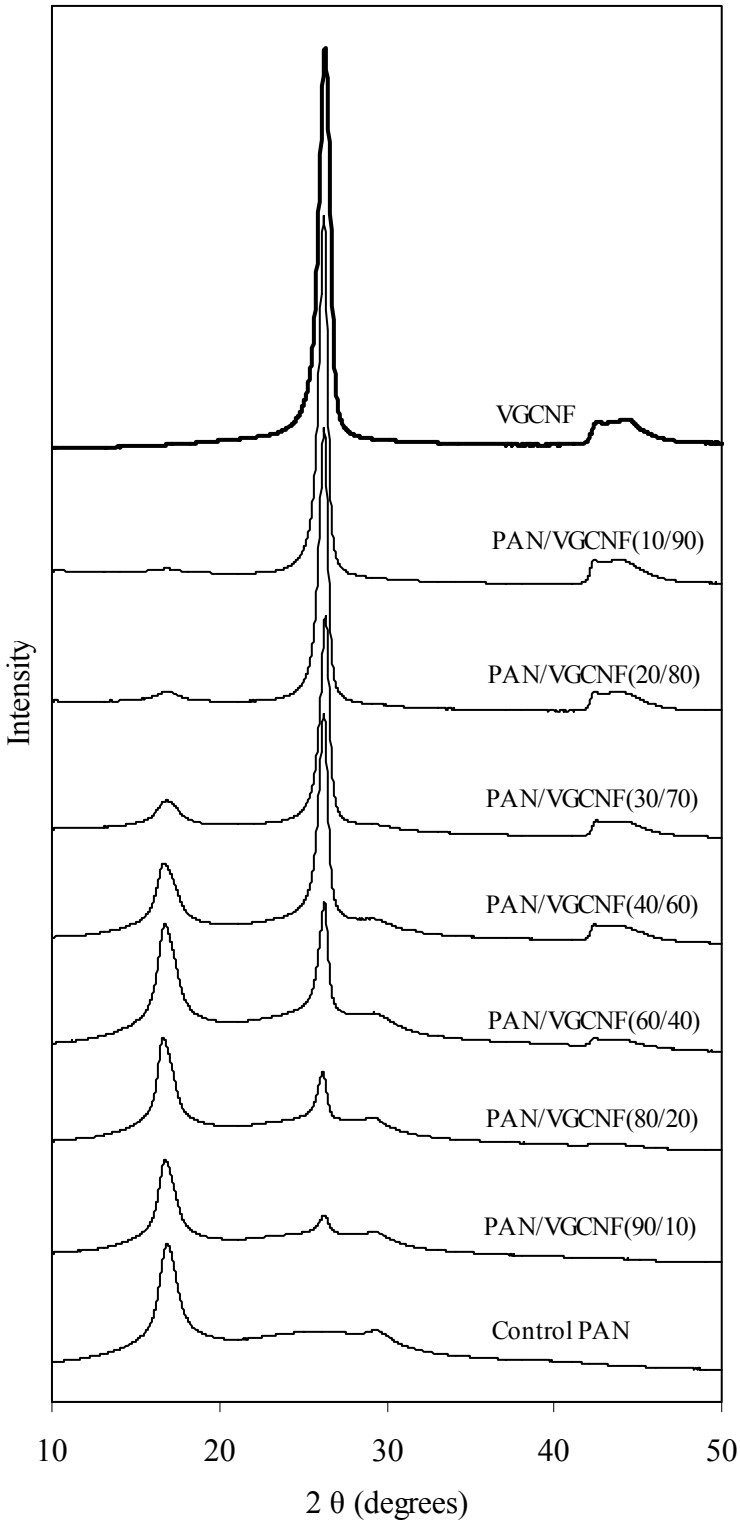

Figure 3.7. Wide angle X-ray diffraction of VGCNF powder, control PAN, and PAN/VGCNF composite films.

Table 3.6. Wide angle X-ray diffraction results of VGCNF powder, control PAN and PAN/VGNF composite films

VGCNF Loading (wt %)	Graphite crystal Size (nm)	PAN crystallite size (nm)	PAN crystallinity (%)
0	-	5.7	43
5	12	6.4	46
10	13	6.7	41
20	14	5.9	43
40	14	5.4	40
60	14	4.7	48
80	15	4.3	47
90	16	4.6	43
100	15	-	-

Figure 3.8 shows the HRTEM for the PAN/VGCNF/DMF dispersion with 90 % VGCNF loading. The wrapping behavior of PAN around nano fiber was observed. Scanning electron micrographs for VGCNF and 20 wt% VGCNF films are shown in Figure 3.9a and b, respectively. The images reveal coating of nano fiber by PAN (arrows in 3.9b) to form a PAN shell and VGCNF core structure. Figure 3.9c shows the morphology of tensile fracture for PAN/VGCNF film with 5 wt% VGCNF loading. When the composite film was stretched and then broken, a hole was left in the polymer matrix due to the weaker interaction between polymer and VGCNF. PAN was observed in the center of the hole suggesting that some PAN molecules do enter into hollow nano fibers.

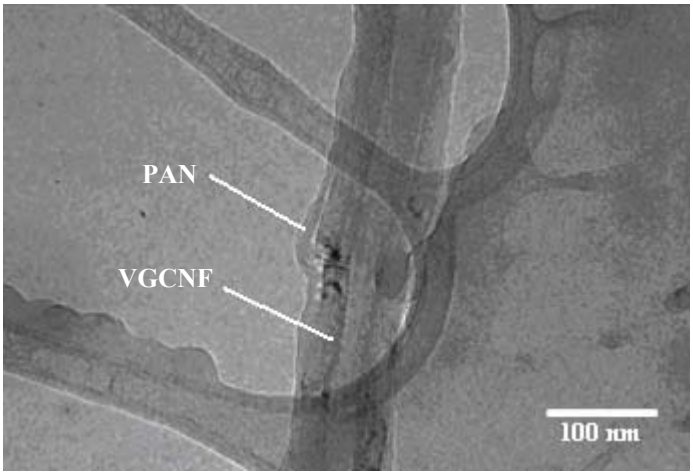

Figure 3.8. HRTEM image for PAN/VGCNF/DMF dispersion with 90 % VGCNF loading.

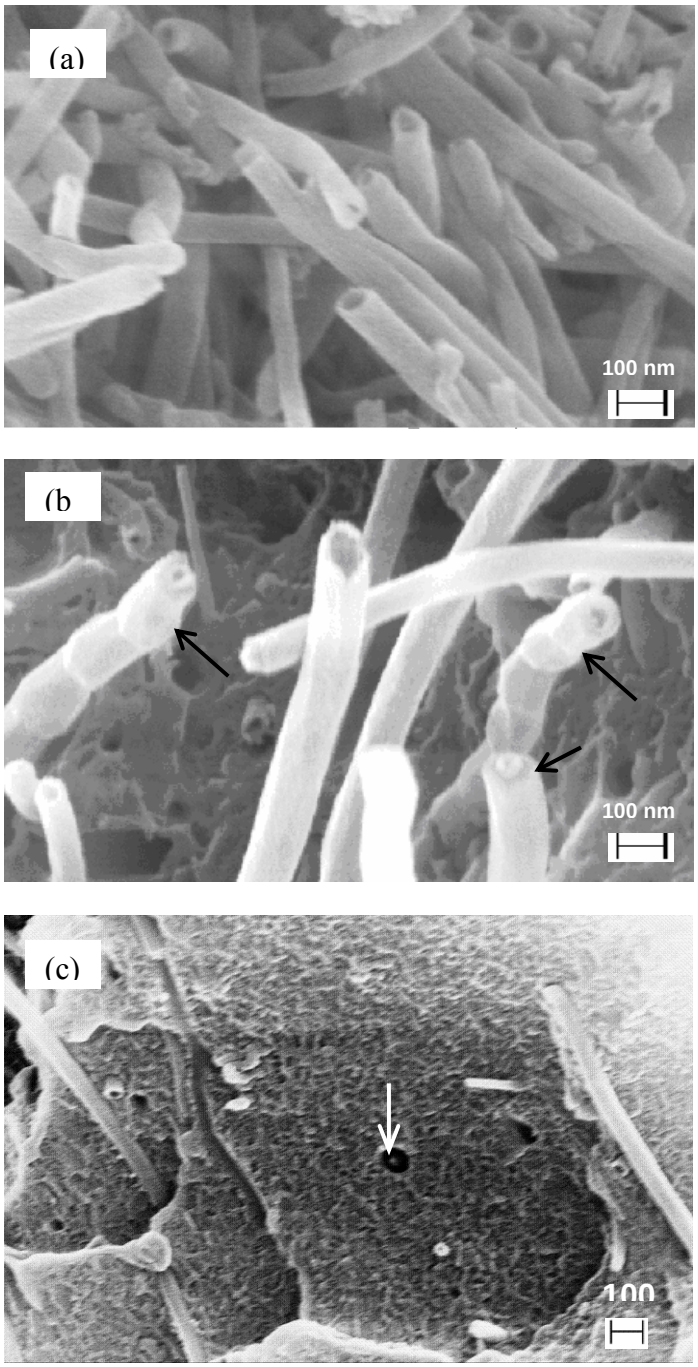

Figure 3.9. Scanning electron micrographs for (a) VGCNF powder, (b) PAN/VGCNF (80/20), and (c) PAN/VGCNF (95/5) composite films.

3. 4 CONCLUSIONS

Single-layer, double-layer, triple-layer and bamboo structured vapor grown carbon nano fibers were observed by transmission electron microscopy. PAN/VGCNF composite films with different VGCNF loading have been processed. The tensile results exhibit enhancement in modulus and tensile strength. The magnitude of enhancement decreases with increasing nano fiber loading up to 40 %. Beyond 40 % CNF loading, the tensile properties are lower than that of the control PAN. Electrical conductivity of composites increased with the nano fiber loading and exhibited percolation at 3.1 vol%. The storage modulus of PAN is enhanced by incorporation of nano fibers, particularly above the glass transition temperature. The tan δ peak broadens and shifts to higher temperatures with the addition of VGCNF. Activation energy needed for PAN molecular motion in the composite films is higher than that in the control PAN film. PAN crystallite size, PAN crystallinity and graphite crystallite size in various films were calculated and compared. The wrapping of PAN around nano fiber was observed by SEM and TEM. Specific modulus of the composites containing up to 20% VGCNF was consistent with the Halpin-Tsai theory.

3.5 REFERENCES

[1] M. L. Lake and J. M. Ting, "Carbon Materials for Advanced Technologies," edited by T.D. Burchell, Oxford, U. K., pp.139 (1999).

[2] K. P. De Jong and J. W. Geus, Catalysis Reviews-Science and Engineering **42**, 481 (2000).

[3] G. G. Tibbetts and M. G. Devour, U.S. Patent 4,565,684 (1986).

[4] G. G. Tibbetts, Carbon **27**, 745 (1989).

[5] T. Uchida, D. P. Anderson, M. L. Minus, and S. Kumar, Journal of Materials Science **41**, 5851 (2006).

[6] Y. K. Choi, Y. Gotoh, K. I. Sugimoto, S. M. Song, T. Yanagisawa, and M. Endo, Polymer **46**, 11489 (2005).

[7] R. D. Patton, C. U. Pittman, L. Wang, and J. R. Hill, Composites Part a-Applied Science and Manufacturing **30**, 1081 (1999).

[8] T. Prasse, J. Y. Cavaille, and W. Bauhofer, Composites Science and Technology **63**, 1835 (2003).

[9] K. Lozano, S. Y. Yang, and Q. Zeng, Journal of Applied Polymer Science **93**, 155 (2004).

[10] P. Hine, V. Broome, and I. Ward, Polymer **46**, 10936 (2005).

[11] K. Lozano, J. Bonilla-Rios, and E. V. Barrera, Journal of Applied Polymer Science **80**, 1162 (2001).

[12] K. Lozano, J. Bonilla-Rios, and E. V. Barrera, Journal of Applied Polymer Science **80**, 125 (2001).

[13] O. S. Carneiro and J. M. Maia, Polymer Composites **21**, 960 (2000).

[14] E. Hammel, X. Tang, M. Trampert, T. Schmitt, K. Mauthner, A. Eder, and P. Potschke, Carbon **42**, 1153 (2004).

[15] S. Kumar, H. Doshi, M. Srinivasarao, J. O. Park, and D. A. Schiraldi, Polymer **43**, 1701 (2002).

[16] G. Caldeira, J. M. Maia, O. S. Carneiro, J. A. Covas, and C. A. Bernardo, Polymer Composites **19**, 147 (1998).

[17] O. S. Carneiro and J. M. Maia, Polymer Composites **21**, 970 (2000).

[18] O. S. Carneiro, J. A. Covas, C. A. Bernardo, G. Caldeira, F. W. J. Van Hattum, J. M. Ting, R. L. Alig, and M. L. Lake, Composites Science and Technology **58**, 401 (1998).

[19] Y. K. Choi, K. I. Sugimoto, S. M. Song, and M. Endo, Materials Letters **59**, 3514 (2005).

[20] B. A. Higgins and W. J. Brittain, European Polymer Journal **41**, 889 (2005).

[21] K. Enomoto, T. Yasuhara, S. Kitakata, H. Murakami, and N. Ohtake, New Diamond and Frontier Carbon Technology **14**, 11 (2004).

[22] M. L. Shofner, K. Lozano, F. J. Rodriguez-Macias, and E. V. Barrera, Journal of Applied Polymer Science **89**, 3081 (2003).

[23] G. G. Tibbetts and J. J. McHugh, Journal of Materials Research **14**, 2871 (1999).

[24] R. T. Pogue, J. Ye, D. A. Klosterman, A. S. Glass, and R. P. Chartoff, Composites Part a-Applied Science and Manufacturing **29**, 1273 (1998).

[25] T. Ogasawara, Y. Ishida, and T. Ishikawa, Advanced Composite Materials **13**, 215 (2004).

[26] J. J. Zeng, B. Saltysiak, W. S. Johnson, D. A. Schiraldi, and S. Kumar, Composites Part B-Engineering **35**, 173 (2004).

[27] H. M. Ma, J. J. Zeng, M. L. Realff, S. Kumar, and D. A. Schiraldi, Composites Science and Technology **63**, 1617 (2003).

[28] T. Uchida, T. Dang, B. G. Min, X. F. Zhang, and S. Kumar, Composites Part B-Engineering **36**, 183 (2005).

[29] H. G. Chae, T. V. Sreekumar, T. Uchida, and S. Kumar, Polymer **46**, 10925 (2005).

[30] P. K. Mallick, "Fiber-Reinforced Composites," Marcel Dekker, New York, pp. 91 (1993).

[31] T. Uchida, D. P. Anderson, M. Minus, and S. Kumar, Journal of Materials Science (in press).

[32] Provided by the manufacturer.

[33] A. Eitan, F. T. Fisher, R. Andrews, L. C. Brinson, and L. S. Schadler, Composites Science and Technology **66**, 1162 (2006).

[34] S. Kumar, D. P. Anderson, and A. S. Crasto, Journal of Materials Science **28**, 423 (1993).

[35] A. K. Gupta and R. P. Singhal, Journal of Polymer Science Part B-Polymer Physics **21**, 2243 (1983).

[36] B. D. Cullity, "Elements of x-ray Diffraction," Addison-wesley, MA, 2nd edition, pp. 102 (1978).

CHARPTER 4

POLYACRYLONITRILE/CARBON NANOTUBES COMPOSITE FILMS

4.1 INTRODUCTION

PAN/SWNT and PAN/VGCNF composite films with significant enhancement in mechanical, thermo-mechanical, and electrical properties have been processed, as discussed in Chapter 2 and Chapter 3. The reinforcement efficiency of SWNT, DWNT, MWNT and VGCNF have been compared in PAN/CNT composite fibers at 5 wt% CNT loading.[1] In this chapter, reinforcement efficiency of five different types of SWNTs, DWNT, MWNT and VGCNF have been compared in PAN films at 5, 10, and 20 wt% nanotube loading. The films have been characterized for mechanical, dynamic mechanical and thermo-mechanical properties as well as electrical conductivity. Films have also been characterized using scanning and transmission electron microscopy, X-ray diffraction, Raman spectroscopy. Surface area of all carbon nanotubes has been characterized using nitrogen gas adsorption and the composite film surface area has been correlated with the nanotube surface area. Solvent behavior of various composite films has also been compared.

4.2 EXPERIMENTAL

4.2.1 Materials

SWNTs were obtained from Carbon Nanotechnologies, Inc. (Houston, TX), DWNTs from Nanocyl, Co. (Belgium), MWNTs from Iljin Nanotech, Co. (Korea), and

VGCNFs from Applied Sciences, Inc. (Cedarville, OH). The catalytic impurity of the each type of nanotube was determined from the thermogravimetric analysis (TGA) based on the residual weight and listed in Table 4.1. PAN (molecular weight =100,000 g/mol) was obtained from Exlan, Co. (Japan). Dimethyl formamide (DMF) was purchased from Sigma- Aldrich and used as received.

Table 4.1. Various carbon nanotubes used in this study

Nanotubes	Source	Impurity (%)	Batch or Lot #
SWNT1	CNI	3	X5054C
SWNT2	CNI	1	XO0PPP
SWNT3	CNI	1	XO1PPP
SWNT4	CNI	6	P0252
SWNT5	CNI	35	R0231
MWNT	Iljin Nanotech, Co. (Korea)	3	-
VGCNF	Applied Sciences, Inc.	0.3	PR24-HHT-LD 2850
DWNT	Nanocyl, Co. (Belgium)	5	270c700056

4.2.2 Preparation of Films

Dried carbon nanotubes (CNTs) were added to 50 ml DMF and sonicated for 48 hours (DWNT was sonicated for 6 days) until a homogenous dispersion was formed. The homogeneity of dispersion was confirmed by optical microscopy. 240 mg PAN was added to the CNT/DMF dispersion and homogenized while stirring. Excess solvent was

evaporated to obtain the final solution volume of 25 mL. The PAN/CNT/DMF solution was cast on a glass substrate and kept in vacuum oven (~ 80 ^{o}C) for solvent removal to form the film. The films were further dried in vacuum oven at 80 ^{o}C for 3 days. The PAN/CNT composite films with various loading of CNTs (5, 10, 20 wt% CNTs) were prepared by the same procedure.

4.2.3 Themogravimetric Analysis

Themogravimetric analysis (TGA) of CNT powders was conducted on TGA 2950 (TA Instruments, Inc.) in air at a heating rate of 10 ^{o}C /min.

4.2.4 Raman Spectroscopy

Raman spectra were collected by a Holoprobe Research 785 Raman Microscope made by Kaiser Optical System using 785 nm excitation lasers.

4.2.5 Surface Area

The isothermal N_2 gas adsorption and desorption at 77 K were carried out on ASAP 2020 (Micromeritics Inc.), on samples degassed at 90 °C for 16 h. The specific surface area and pore size distribution were determined using Brunauer, Emmet, Teller (BET) and density functional theory (DFT) methods. Other experimental procedures are described in Chapters 2and 5.

4.2.6 FTIR Spectroscopy

Carbon nanotube powders are characterized by FTIR spectroscopy. For each measurement, about 1 mg CNT and 250 mg dried KBr were mixed by mortar and pestol till the mixture appears homogenous. The KBr used was dried at ~100 °C overnight. The CNT and KBr mixture was pressed in a mold to form pellet. FTIR spectra were collected

by spectrum one FTIR spectrometer by Perkin-Elmer using 1064 scans at a resolution of 4 cm^{-1} against KBr background. Baseline correction was not performed.

4.3 RESULTS AND DISCUSSION

4.3.1 Thermogravimetric Analysis

TGA curves for various SWNTs, DWNT, MWNT and VGCNF are shown in Figure A.1. The amount of metal catalyst in SWNT samples can be determined by TGA.[2] The residue of the samples is oxidized metal (Fe_2O_3 and Fe_3O_4), from which the metal impurity is estimated and listed in Table 4.1. The degradation temperature for various nanotubes determined from TGA plots is tabulated in Table 4.2. MWNT and VGCNF begin to degrade at higher temperature than various SWNTs and DWNT due to the existence of the layered graphitic structure.[3] SWNT4 and SWNT5 begin to degrade at lower temperature as compared to SWNT1, SWNT2 and SWNT3 due to the presence of higher metal content and the smaller diameter nanotube. The obvious weight increase at ~ 170 ^oC observed for SWNT5 is attributed to the oxidation of large amount of iron[4] present in the nanotube. The temperature at the fastest degradation rate is the highest for SWNT3 among various SWNTs though the initial degradation temperature of SWNT1 is the highest.

Table 4.2 Degradation temperatures of various carbon nanotubes in air

Nanotubes	Initial degradation temperature (^oC)	Temperature at the fastest degradation rate (^oC)	BET surface area (m^2/g)
SWNT1	516	550	583
SWNT2	489	555	830
SWNT3	483	570	795
SWNT4	424	510	823
SWNT5	368	421	434
DWNT	440	456	563
MWNT	584	640	161
VGCNF	695	755	41

4.3.2 Structure

X-ray diffraction plots of various CNTs are given in Figure A.2. The 2θ values and d-spacings obtained for various SWNTs are listed in Table 4.3. All CNT powders show peak at ~ 44 ^{o}, which is attributed to (100) plane in graphite[5] or/and to (110) reflection of the α-Fe body centered cubic lattice. SWNT1, SWNT 2 and SWNT 3 show the peak at 25.9 ^{o} attributed to (002) plane of a defective graphite phase (often referred to as turbostratic carbon) resulting from the oxidative degradation of SWNTs during purification.[6] DWNT, MWNT, and VGCNF also exhibit the peak at 25.4 ~26.3 ^{o} due to the turbostratic graphitic layer. The peaks at ~ 8 ^{o} and ~ 13 ^{o} correspond to (10) and (11) planes of the 2D hexagonal lattice in the ordered SWNT bundles.[7, 8] SWNT4 and SWNT5 show the peaks corresponding to (10) and (11) planes. From the d-spacing for the (10)

plane and the inter-tube distance in the SWNT bundle (0.34 nm), the average diameter of SWNT4 and SWNT5 are estimated to be 0.92 and 0.94 nm, respectively. The absence of (10) and (11) planes in the x-ray pattern of SWNT1, SWNT2 and SWNT3 indicates disruption of these crystalline packing. The peak at 2θ ~21 ^{o} for SWNT4 is attributed to the γ - band of carbon, which arises due to the packing of saturated structures such as aliphatic carbons.[9-12]

Table 4.3. Wide angle X-ray diffraction results for CNT powders

	SWNT1	**SWNT2**	**SWNT3**	**SWNT4**	**SWNT5**	**DWNT**	**MWNT**	**VGCNF**
2θ (^{o}) d (Å)	-	-	-	8.14 10.85	8.02 11.01	-	-	-
2θ (^{o}) d (Å)	-	-	-	13.18 6.71	13.22 6.69	-	-	-
2θ (^{o}) d (Å)	-	-	-	20.74 4.28		-	-	-
2θ (^{o}) d (Å) Crystal Size (Å)	25.92 3.44 30	25.97 3.43 40	25.86 3.44 30	-	-	25.44 3.50 83	25.88 3.44 93	26.30 3.39 150
2θ (^{o}) d (Å)	43.56 2.08	43.01 2.10	43.05 2.10	43.93 2.06	44.28 2.04	43.30 2.09	42.90 2.11	42.60 2.12

4.3.3 Raman Spectra

Raman spectra for various CNT powders are shown in Figure A.3. The intensity in all cases is normalized to the intensity of the G band (1550-1605 cm^{-1}). The peaks located in the region of 200 cm^{-1} ~ 500 cm^{-1} correspond to the radial breathing mode (RBM)[13] (Figure A.4). RBM position is inversely proportional to the diameter of nanotube, and is used to estimate the nanotubes diameter in bundle according to the Equation (4.1) [14]:

$$d_t\ (\text{nm}) = \frac{223.5}{\omega_{\text{RBM}} - 12.5} \tag{4.1}$$

where ω_{RBM} is the wavenumber in cm^{-1}.

The disorder induced D band appears at ~1300 cm^{-1} (Figure A.3). D band originates due to the presence of disordered carbon, and SWNTs with incomplete or modified wall structure.[15, 16] Normalized intensity of D band for SWNT1, SWNT2, SWNT3, SWNT4 and SWNT5 is 0.2, 0.25, 0.1, 0.12 and 0.08, respectively, assuming that the inetsnity of G band in all cases is 1.. High intensity of D band for SWNT1 and SWNT2 indicate that these nanotubes contain more amorphous and disordered carbon among various SWNT powders. This observation is consistent with high-resolution TEM (HRTEM) images where presence of amorphous carbon is evident (Figure 4.1 and Figure A.8). The intensity of D band of MWNTs and of VGCNF is very high, indicating highly defective graphitic structure in these two samples.

G band in Raman spectrum originates from the graphite-like in-plane vibration mode. G band shows two dominant Lorenzian features located at ~1560 cm^{-1} and at ~1590 cm^{-1} (Figure A.5).[17] The low frequency component (ω_G^-) is related to the

vibrations along the circumferential direction and the higher frequency one (ω_G^+) is associated with the vibrations along the direction of the tube axis. The peak position and the full width at half maxima (FWHM) of the G band for the higher frequency component for various CNTs are listed in Table 4.4. G bands for SWNT4 and 5 show a clear separation between the axial and circumferential components as compared to SWNT1, 2 and 3. Jorio et al. reported that frequency ω_G^+ is independent on diameter (d) whereas that of ω_G^- strongly depend on d^{-2} (Equation 4.2).[18]

$$\omega_G^- = \omega_G^+ - A/d^2 \quad (4.2)$$

where A is constant. The presence of the smaller-diameter tubes in SWNT4 and SWNT5 causes ω_G^- to shift to lower frequency resulting in the larger difference between ω_G^- and ω_G^+.

Table 4.4. G band position and FWHM for CNT powders

Sample	**G band position (cm^{-1})**	**FWHM of G band (cm^{-1})**
SWNT1	1586	24
SWNT2	1590	26
SWNT3	1589	25
SWNT4	1595	21
SWNT5	1592	17
DWNT	1587	28
MWNT	1612	54
VGCNF	1582	18

4.3.4 Surface Area and FTIR Spectra

The specific surface area of CNT by BET method can be calculated by Equation (4.3):

$$S = \frac{V_m \sigma N_A}{m V_o} \tag{4.3}$$

where V_m is the quantity of gas absorbed when the entire surface is covered with a monomolecular layer, σ is the area of the surface occupied by individual gas molecules and N_A is the Avogadro's number, m is the mass of absorbing sample, and V_o is the molar volume of the gas (22414 cm^3/mole for gas at atmospheric pressure). The total surface area by DFT method is given by Equation (4.4) and (4.5):

$$S = 16.2 \times 10^{-20} (N_A) (V_{STP}) \tag{4.4}$$

$$V_{STP} = \left(\frac{273.2}{T}\right)\left(\frac{P}{760}\right) V_I \tag{4.5}$$

where N_A is the Avogadro's number, V_{STP} is the volume of absorbate at standard temperature (T) and pressure (P), and V_I is the total amount of absorbed N_2. The amount of absorbed N_2 as a function of pressure for various CNT is shown in Figure A.6. The pore volume and surface area of various CNTs using BET and DFT methods are calculated and listed in Table A.1 and A.2. The surface area of SWNTs and DWNT is higher compared to MWNT and VGCNF. The surface area of SWNT2, SWNT3 and SWNT4 is higher than that of SWNT1 and SWNT5. The BET surface areas for SWNT2, SWNT3 and SWNT4 are 830, 795 and 834 m^2/g, respectively and are significantly higher than those for SWNT1 (583 m^2/g) and SWNT5 (434 m^2/g). BET surface areas for

MWNT and VGCNF are 161 and 41 m^2/g, respectively. The FTIR spectra of various nanotubes do not reveal any significant difference (Figure A.7). A possible reason could be the low sensitivity of the instrument.

4.3.5 High Resolution Transmission Electron Microscopy

Figure 4.1 shows the bright field high resolution TEM (HRTEM) images of various nanotubes (Low-magnification TEM images are shown in Figure A.8). It is evident from the TEM images that SWNTs bundles are highly entangled. Diameter of SWNT bundles is in the range of 8-29 nm. Presence of amorphous carbon was observed in SWNT1 and SWNT2 (Figure A.8). The metal particles were clearly observed in SWNT4 and SWNT5 due to their higher impurity. The size of the metal particles in the SWNT 4 and SWNT5 is in the 3 to 5 nm range. SWNT3 appears to have most uniform bundle diameter distribution (from SEM), least metal content (from TEM and TGA), and least amorphous carbon in all five types of SWNTs.

Most of DWNTs do not form bundles and exist as individual nanotubes and are entangled. The diameter of DWNT is about 5 nm. MWNT mostly exist as individual entangled nanotubes. Figure 4.1 shows the HRTEM images of double-layer VGCNFs (other structures are shown in Chapter 5). VGCNF exists as individual nano fiber. The inner wall of VGCNF is oriented at an angle with the fiber axis while the outer wall is almost oriented along fiber axis. The inner diameter is about 25 nm and the outer diameter is about 60 nm.

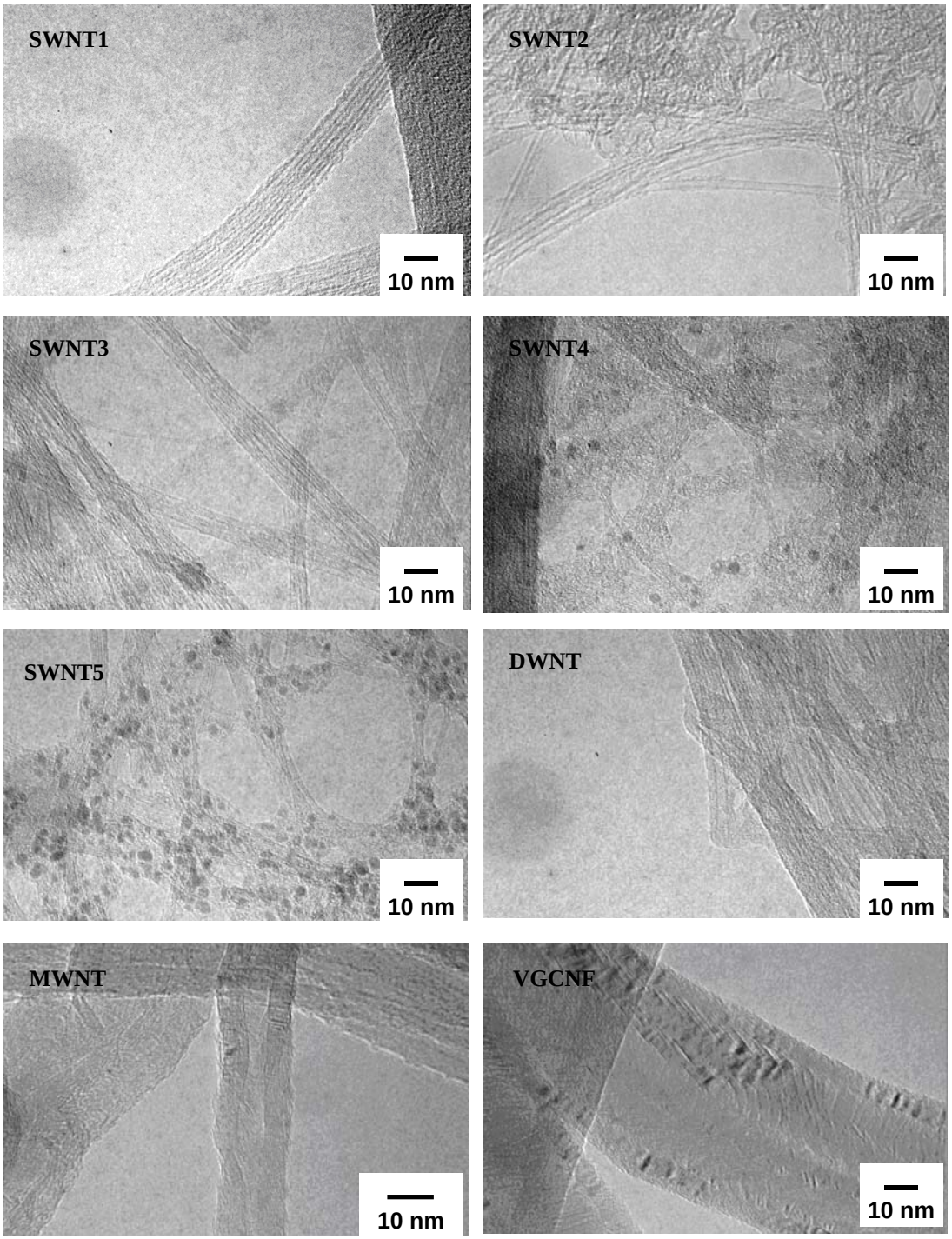

Figure 4.1. Bright field high-resolution TEM (HRTEM) images of CNTs.

4.3.6 Mechanical and Electrical Properties of PAN/CNT Composite Films

Tensile modulus, tensile strength, elongation at break, and electrical conductivity for the control PAN and the composite films are listed in Table 4.5. Comparisons of modulus and tensile strength for various films are shown in Figure A.9. For the 5 wt% CNT composite films, PAN/SWNT2, PAN/SWNT3, PAN/SWNT4, PAN/VGCNF composite films exhibit improved mechanical properties relative to the control PAN film. Among the SWNT containing composites, the composite film prepared using SWNT3 shows the highest improvement in tensile modulus (3.7 GPa for control PAN to 5.6 GPa for PAN/SWNT3) and tensile strength (53 MPa for control PAN to 77 MPa for PAN/SWNT3). Composite films containing SWNT2 and SWNT4 exhibits similar enhancement in tensile modulus (4.9 GPa and 5.0 GPa for PAN/SWNTT2 and PAN/SWNT4, respectively). Relatively lower enhancement in tensile properties for SWNT2 composite film can be attributed to the presence of amorphous carbon evident in the TEM image. Composite films prepared from SWNT1 and SWNT5 show little enhancement in tensile modulus and their tensile strength is lower than that of control PAN. The mechanical properties for SWNT1 and SWNT5 composites can be attributed to their lower surface area as compared to SWNT2, SWNT3 and SWNT4. The role of CNT surface area on the composite properties is discussed later in this section. Among DWNT, MWNT and VGCNF composites, at 5 wt% loading only PAN/VGCNF composite film exhibits improvement in tensile properties (4.4 GPa modulus and 80 MPa strength). For both DWNT and MWNT containing composite films, the tensile modulus and tensile strength were lower than that for the control PAN film. Somewhat similar

trends in tensile modulus and tensile strength are also observed for the PAN/CNT films with 10 wt% CNT loading (Figure A.9).

As CNT loading increases from 5 wt% to 10 wt%, tensile modulus increases significantly for SWNT3, SWNT4 and SWNT5 composites, while the improvement in tensile strength is most prominent in PAN/SWNT3 composites. Overall, among various SWNT composites, the improved tensile strength of films containing SWNT2, SWNT3, and SWNT4 are attributed to their higher surface area as compared to SWNT1 and SWNT5. Among DWNT, MWNT and VGCNF composites, poor tensile properties of DWNT composite can be attributed to its poor dispersion in the polymer matrix as observed by SEM (Figure A.32 & A.33 for the 5 wt% loading composites and Figure A.34 & A.35 for the 10 wt% composites). Improved tensile properties of VGCNF composite despite its low surface area can be attributed to its long length (30 – 100 μm). Though the length of SWNT, DWNT, and MWNT are not exactly known to us, they are typically on the order of a few microns. Four types of CNTs (SWNT1, SWNT3, SWNT5 and VGCNF) were used to prepare the composite films with CNT loading of 20 wt%. PAN/SWNT3 composite film shows the highest increase in modulus (2.5 times that of PAN), tensile strength (twice that of PAN's) and strain to break.

The electrical conductivities of all composite films are improved relative to the control PAN film (Table 4.5). With increasing CNT loading, the electrical conductivity of PAN/CNT composite films increases. Electrical conductivities of various films are also compared in Figure A.10. The PAN/SWNT3 exhibits the highest electrical conductivity among all composite films prepared with same loading of CNTs.

Improvement in tensile modulus, tensile strength as well as electrical conductivity of polymer matrix in the presence of CNT depends on a number of factors. Interaction between CNT and polymer is one of the critical factor that dictates the composite properties. Interaction between CNT and polymer, besides other factors, depends on the interfacial area between the polymer and the CNT. As the surface area of CNT increases, the interfacial area between polymer and nanotube increases resulting in improved polymer-CNT interaction and hence improved composite properties. Figure 4.2 shows the plot of tensile modulus of various PAN/CNT films as a function of CNT surface area. In general, the tensile moduli of the composite films increases with the CNT surface area. The tensile strength of various films is plotted as a function of CNT surface area in Figure 4.3. At the same CNT loading, the tensile strength of various composite films increase with increasing nanotube surface area, except for the composites containing VGCNF, which shows higher strength, despite its low surface area. Effect of nanotube surface area on the reinforcement efficiency has also been studied by Cadek et al.[19] The results suggest that reinforcement scales linearly with the total nanotube surface area in the films. Hence our results are in agreement with the reported results in literature.

Table 4.5. Mechanical and electrical properties of control PAN and PAN/CNT composite films

Sample	CNT loading		Modulus (GPa)	Strength (MPa)	Elongation (%)	Electrical conductivity (S/m)
	(wt%)	(vol%)				
control PAN	0	0	3.7 ± 0.4	53 ± 9	3.2 ± 1.5	-
PAN/SWNT1	5	4.6	3.8 ± 0.3	47 ±9	1.6 ± 0.6	1.2
PAN/SWNT2	5	4.6	4.9 ± 0.1	79 ± 8	5.1 ± 1.3	6.1
PAN/SWNT3	5	4.6	5.6 ± 0.3	77 ± 3	3.9 ± 0.9	88.1
PAN/SWNT4	5	4.6	5.0 ± 0.5	70 ± 12	4.4 ± 1.4	4.1
PAN/SWNT5	5	4.6	3.9 ± 0.3	48 ± 8	2.0 ± 0.5	7.3
PAN/DWNT	5	4.0	3.5 ± 0.2	48 ± 15	1.9 ± 0.8	0.006
PAN/MWNT	5	3.3	3.4 ± 0.1	35 ± 4	1.2 ± 0.2	0.005
PAN/VGCNF	5	3.1	4.4 ± 0.3	80 ± 6	5.5 ± 1.6	0.7
PAN/SWNT1	10	9.2	3.1 ± 1.3	41 ± 17	1.7 ± 0.7	35.2
PAN/SWNT2	10	9.2	4.8 ± 0.4	72 ± 13	5.2 ± 1.6	78.0
PAN/SWNT3	10	9.2	6.8 ± 0.7	93 ± 9	4.3 ± 1	243.0
PAN/SWNT4	10	9.2	6.4 ± 1.3	74 ± 28	1.6 ± 0.9	37.6
PAN/SWNT5	10	9.2	5.6 ± 0.4	56 ± 11	1.3 ± 0.5	30.0
PAN/DWNT	10	8.0	4.4 ± 0.6	64 ± 10	1.9 ± 0.6	5.9
PAN/MWNT	10	6.8	3.6 ± 0.3	56 ± 9	2.1 ± 0.6	1.5
PAN/VGCNF	10	6.3	4.1 ± 0.3	73 ± 6	3.7 ± 0.5	35.2
PAN/SWNT1	20	18.5	4.9 ± 0.3	72 ± 9	1.9 ± 0.3	2.7×10^2
PAN/SWNT3	20	18.5	9.3 ± 0.7	102 ± 8	3.6± 0.6	5.5×10^3
PAN/SWNT5	20	18.5	7.0 ± 1.1	66 ± 22	1.8 ± 0.7	1.3×10^2
PAN/VGCNF	20	13.1	4.0 ± 0.2	59 ± 3	2.5 ± 0.3	88.8

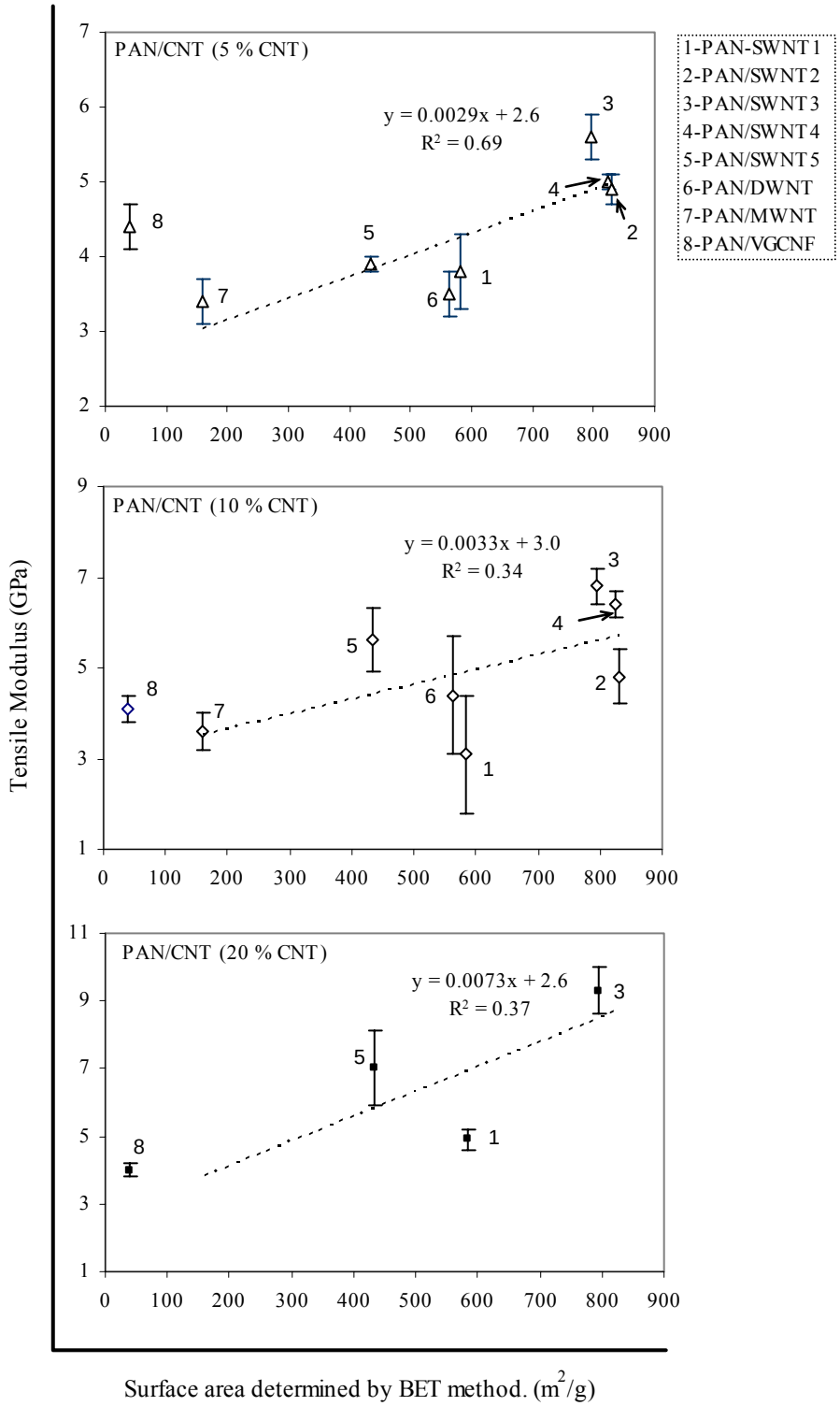

Figure 4.2. Tensile modulus of control PAN and PAN/CNT composite films as a function of CNT surface area. Correlation was based on all the samples except sample number 8 (PAN/VGCNF).

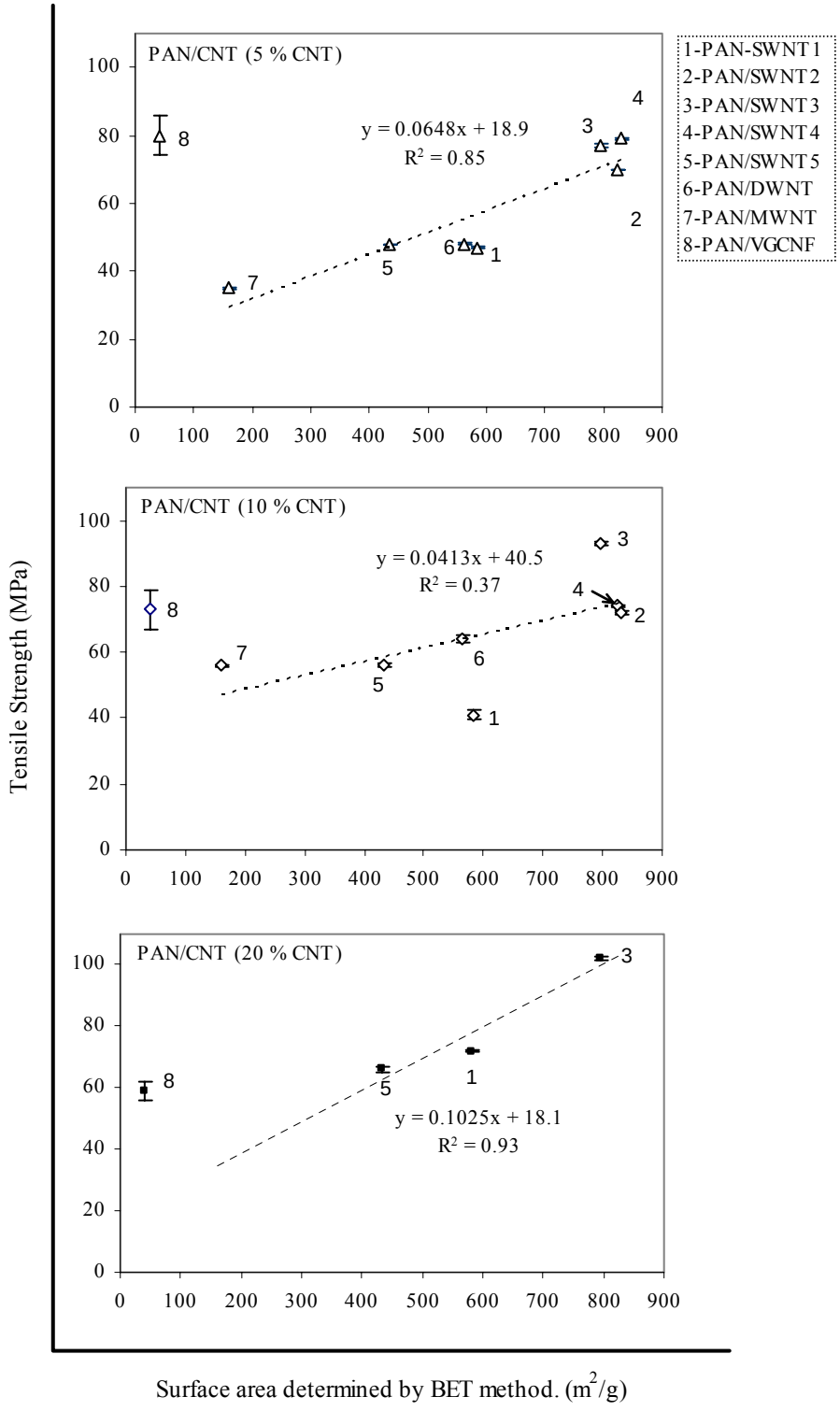

Figure 4.3. Tensile strength of control PAN and PAN/CNT composite films as a function of CNT surface area. Correlation was based on all the samples except sample number 8 (PAN/VGCNF).

4.3.7 Dynamic Mechanical Properties of PAN/CNT Composite Films

The storage modulus and Tan δ of PAN and composite films for 5, 10 and 20 wt% loading are shown in Figures 4.4 to 4.6. Tan δ peak temperatures for PAN/CNT composite films is generally higher than that for the PAN films and the values are listed in Table A.3. Moderate enhancement in storage modulus are obtained for PAN/SWNT2, PAN/SWNT3 PAN/SWNT4, PAN/MWNT and PAN/VGCNF composites at 5 wt% CNT loading, below the glass transition temperature (T_g). At 25 ^oC, PAN/SWNT3 exhibits the highest enhancement in storage modulus (1.7 times that of the control PAN). No improvement in storage modulus is observed for PAN/SWNT1, PAN/SWNT5 and PAN/DWNT composites. With increasing CNT loading to 10 wt%, the magnitude of enhancement in storage modulus also increases.

Enhancement in storage modulus for composite films is significantly higher above the glass transition temperature. The highest increase in storage modulus above T_g is observed for PAN/SWNT3 composite films, followed by PAN/SWNT4, and PAN/SWNT5 or PAN/SWNT2 composites. The storage modulus at 125 ^oC is about 14, 27 and 31 times that of the control PAN for 5, 10, and 20 wt% SWNT3 containing composites, respectively. For PAN/SWNT4, the improvement in storage modulus at 125 ^oC is 7 and 13 times that of control PAN for 5 wt% and 10 wt% composites, respectively, while it is 5 and 9 times for PAN/SWNT2 at 5 wt% and 10 wt% loadings, respectively.

For SWNT1 composite films at low loading, enhancement in storage modulus above T_g is considerably low as compared to SWNT2, SWNT3, SWNT4 and SWNT5, however, at higher CNT loading (20 wt%), significant enhancement in storage modulus (10 times that of control PAN at 125 ^oC) is observed. Storage modulus at 125 ^oC for

PAN/DWNT, PAN/MWNT and PAN/VGCNF is comparable for both 5 wt% and 10 wt% CNT loading. However, enhancement is significantly less as compared to PAN/SWNT3 composite.

Tan δ peak typically shifts to higher temperature and its magnitude decreases for PAN/SWNT composites. The highest reduction in magnitude of Tan δ peak is observed for PAN/SWNT3 composite film at 5 wt% CNT loading, the Tan δ magnitude decreased from ~ 0.37 for control PAN to ~ 0.2 for PAN/SWNT3 composite. For the PAN/SWNT2 and PAN/SWNT4 composites, the magnitude of Tan δ peak is ~ 0.25. For SWNT1 and SWNT5, the value of Tan δ peak height is ~ 0.3. PAN/VGCNF composites show no appreciable reduction in Tan δ magnitude. For PAN/DWNT and PAN/MWNT, the magnitude of Tan δ peak shows slight reduction to ~ 0.3. Similar trend in magnitude of Tan δ peak is observed for the composite films with 10 wt% loading. Reduction in Tan δ peak magnitude for the PAN/CNT composites suggests suppression of polymer molecular motion, hence imparting more elastic behavior. This suppression of molecular motion can be considered a result of interaction between the polymer and CNT. Therefore, PAN/SWNT3 composites exhibit the highest interaction as indicated by the highest reduction in magnitude of Tan δ peak. The trend in tensile modulus, tensile strength, storage modulus and magnitude of Tan δ peak for the PAN/CNT composites are in good qualitative agreement with each other.

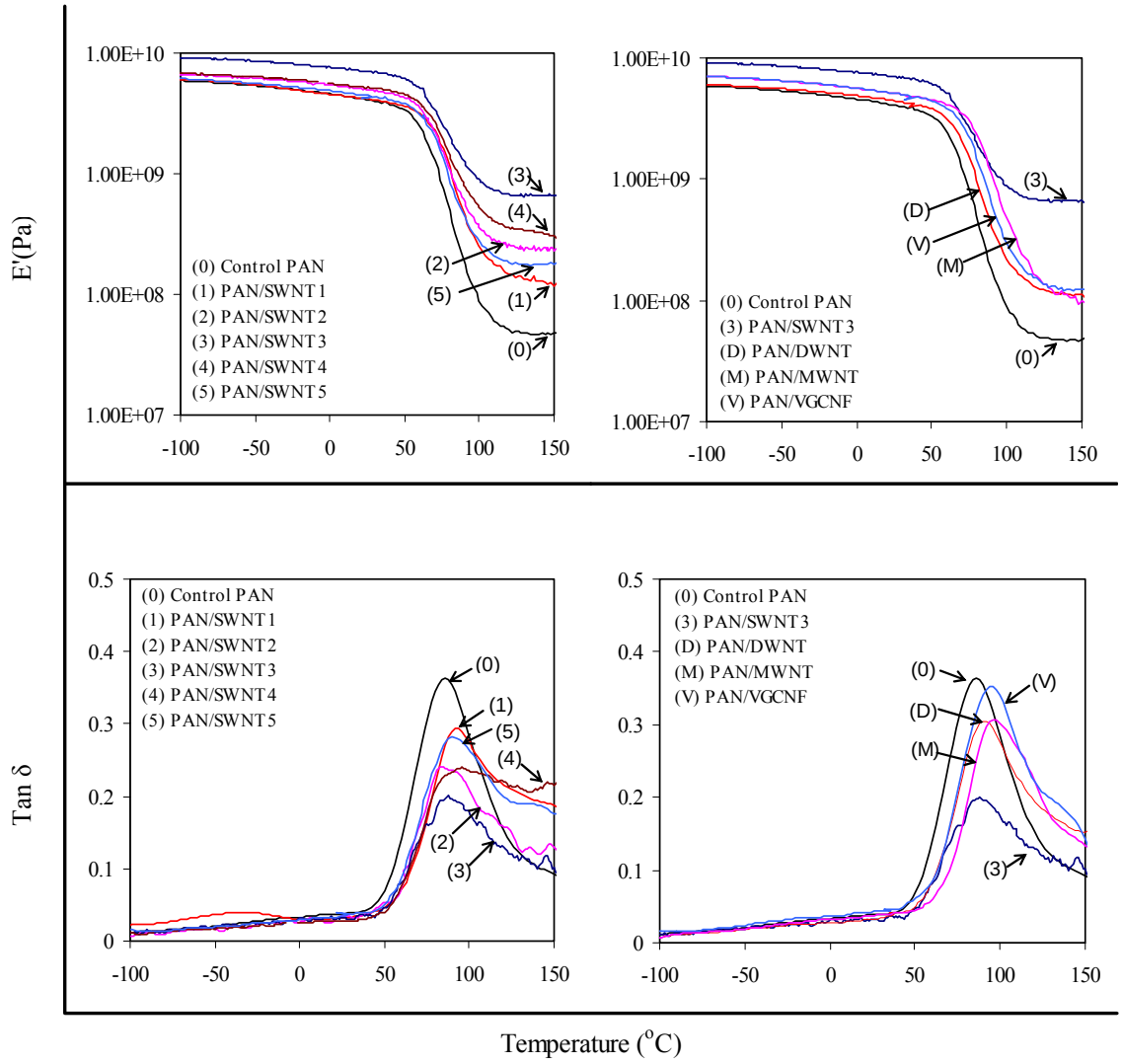

Figure 4.4. Storage modulus and Tan δ versus temperature plots of various PAN/CNT composite films with 5 wt% CNT loading.

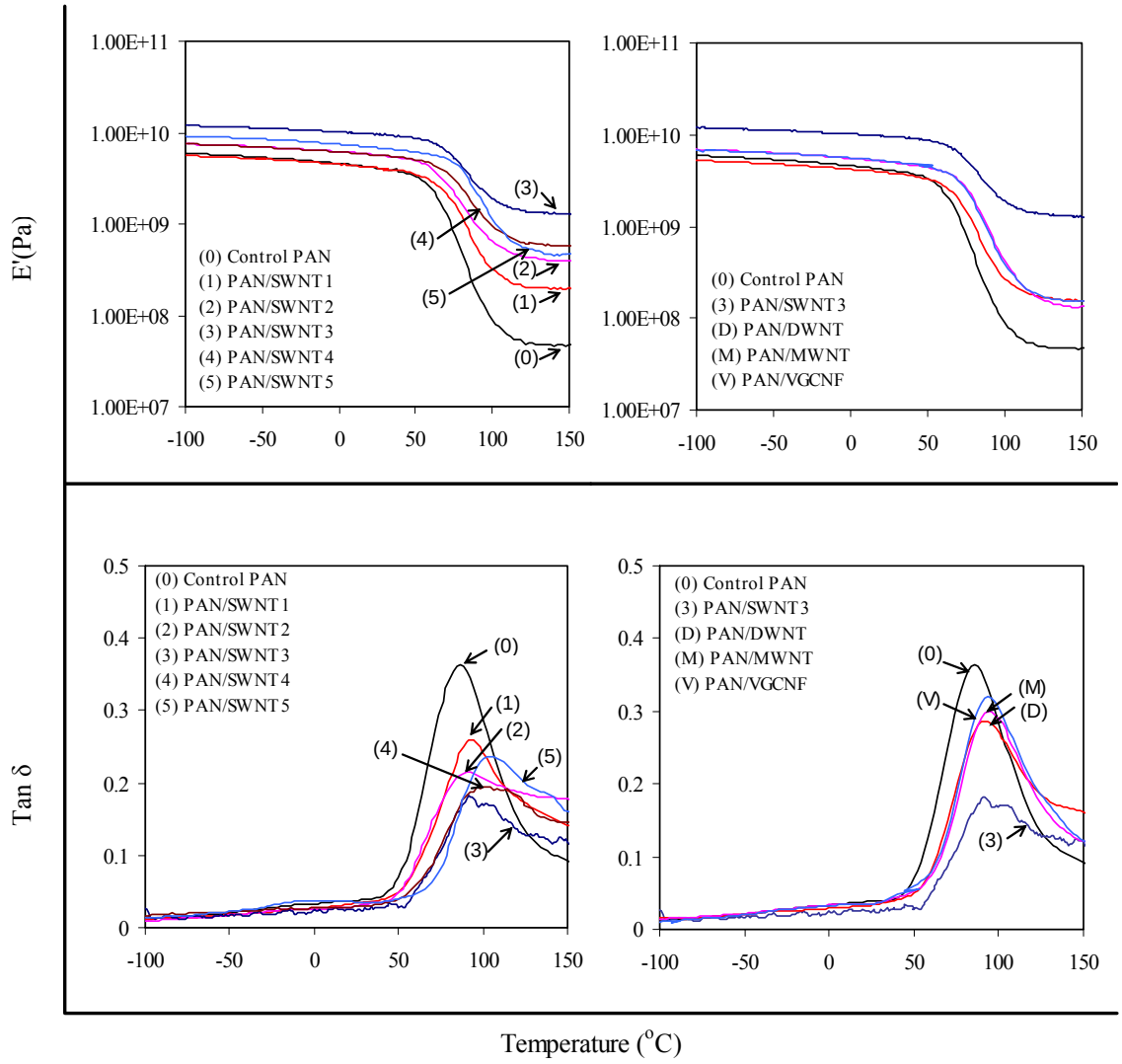

Figure 4.5. Storage modulus and Tan δ versus temperature plots of various PAN/CNT composite films with 10 wt% CNT loading.

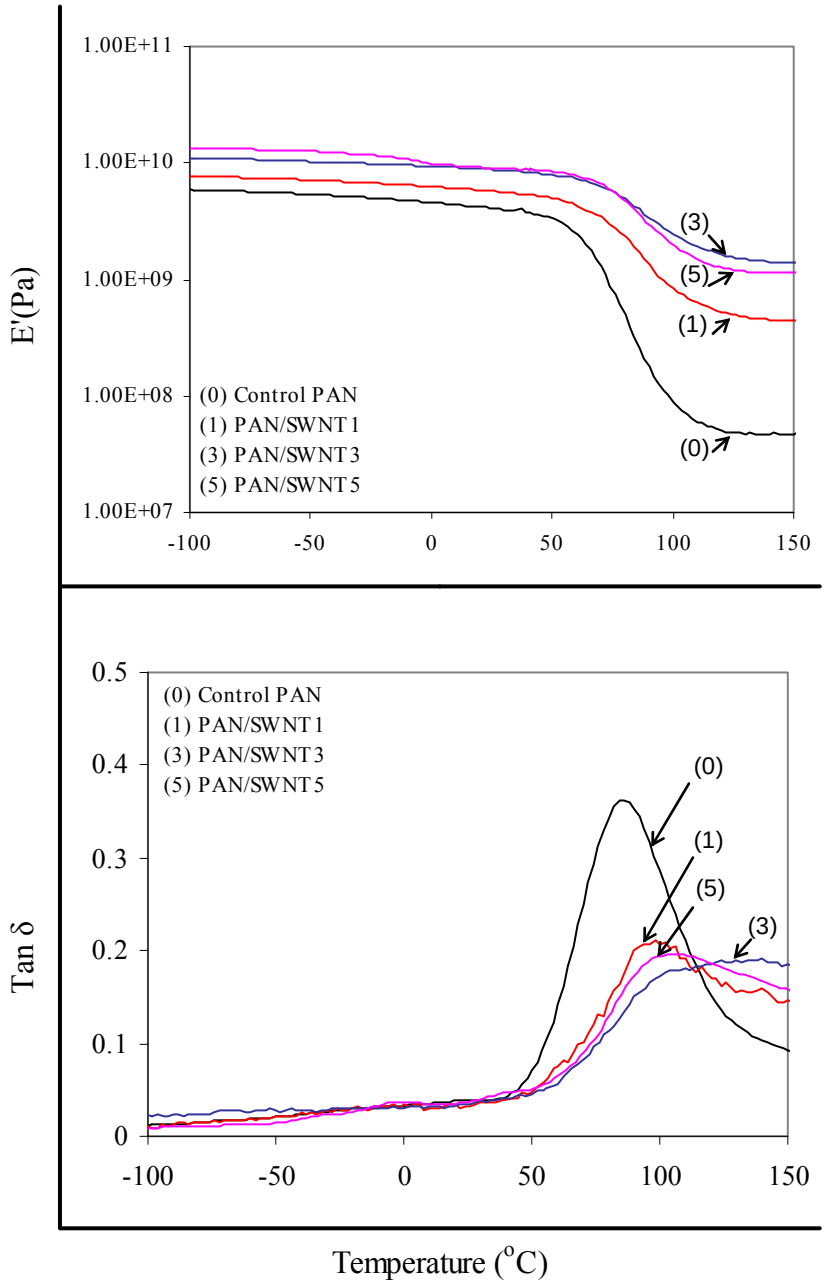

Figure 4.6. Storage modulus and Tan δ versus temperature plots of various PAN/CNT composite films with 20 wt% CNT loading.

The storage modulus of control PAN and various PAN/CNT films at different temperature is summarized in Table A.3. The difference in storage modulus between the composite films and the control PAN film (E'_{comp}-E'_{PAN}) is plotted as a function of temperature and shown in Figure A.11. For all composite films except for PAN/SWNT3 (5 & 10 wt% nanotube loading) and PAN/SWNT2 (10 wt% nanotube loading), the nanotube contribution to the storage modulus does not vary significantly below the glass transition temperature. At the glass transition temperature, the CNT contribution to modulus increases, and then decreases with further increase in temperature. These temperature dependences of modulus contribution from CNTs is similar as those reported for epoxy/CNT composites[20] (Figure A.13). For PAN/SWNT3 (5 & 10 wt% CNT) composite films, the nanotube contribution to the storage modulus decreases with increasing temperature especially above glass transition temperature. The ratio of storage modulus of composites to storage modulus of PAN ($E'_{PAN/CNT}$/ E'_{PAN}) is also plotted as a function of temperature (Figure A.12). This modulus ratio increases at about the glass transition temperature, and decreases above it. The modulus ratio has also been compared to the behavior of epoxy/CNT composites[20] (Figure A.13).

The plot of Tan δ peak as a function of temperature for the PAN/CNT composite films with 10 wt% CNT loading at frequencies (f) of 0.1 Hz, 1 Hz, 5 Hz and 10 Hz are given in Figure A.14. The tan δ peak temperatures (T) at various frequencies are listed in Table A.4. Plots of Ln f as a function of 1/T for the various composite films are shown in Figure A.15. Activation energy for the PAN molecular motion in the composite films with 10 wt% nanotube loading is determined from the slopes of the fitted lines in Figure A.15 using Arrhenius equation and is listed in Table 4.6 and Table A.3. Using the same

method, activation energy for the PAN molecular motion in the composite films with 5 wt% and 20 wt% nanotube loading is obtained and listed in Table 4.6. Activation energy for the PAN molecular motion in various films is compared in Figure 4.7. Increase in activation energy of the polymer chain motion in the presence of CNT is an indication of interaction between polymer and nanotube. At 5 wt% CNT loading, the activation energy of PAN/SWNT3 is 2.3 times that for the PAN film. While, at the same loading, the increase in activation energy for PAN/SWNT1 and PAN/SWNT2 are 1.6 and 2.0 times that of control PAN, respectively. For composites with 10 wt% nanotube loading, activation energy enhancement is the largest for PAN/SWNT2, followed by PAN/SWNT3, PAN/SWNT1, PAN/SWNT4 and PAN/SWNT5. For composites containing 20 wt% CNT, increase in activation energy for PAN/SWNT5 is larger than that for PAN/SWNT1 and PAN/SWNT3 composites. Activation energy for PAN/MWNT composite films shows no significant change as compared to the control PAN.

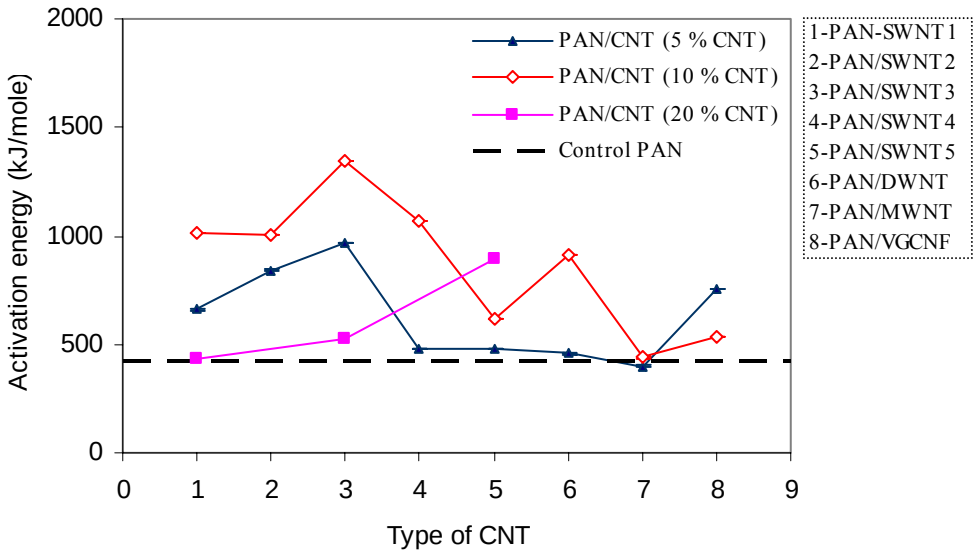

Figure 4.7. Activation energy for the PAN glass transition in control PAN and various PAN/CNT composite films.

Table 4.6. Dynamic and thermo-mechanical analysis results for control PAN film and various PAN/SWNT composite films

Sample	CNT loading (wt%)	Activation Energy (kJ/mol)	Tg [a] (°C)	Transition Temperatures [b] (°C)		CTE (10^{-6}/°C)		
				T_{first}	T_{seco}	Region I	Region II	Region III
Control PAN	0	425	88	75	99	55	91	60
PAN/SWNT1	5	659	94	67	101	35	59	43
PAN/SWNT2	5	843	89	70	109	24	51	28
PAN/SWNT3	5	969	89	64	103	18	30	9
PAN/SWNT4	5	476	96	65	105	19	41	12
PAN/SWNT5	5	479	90	69	105	30	46	17
PAN/DWNT	5	457	92	74	103	41	66	45
PAN/MWNT	5	400	98	67	101	37	63	32
PAN/VGCNF	5	754	96	72	99	39	72	58
PAN/SWNT1	10	1011	92	71	100	32	59	53
PAN/SWNT2	10	1006	90	68	100	23	35	17
PAN/SWNT3	10	1343	92	65	93	11	20	6
PAN/SWNT4	10	1069	102	66	95	18	26	16
PAN/SWNT5	10	619	104	66	98	17	29	16
PAN/DWNT	10	913	92	68	106	28	47	48
PAN/MWNT	10	438	94	71	102	29	55	40
PAN/VGCNF	10	538	94	72	99	36	61	54
PAN/SWNT1	20	434	98	74	97	22	33	44
PAN/SWNT3	20	526	108	65	98	7	9	4
PAN/SWNT5	20	892	103	78	96	14	20	18

Note: [a]. T_g is determined by DMA at a frequency of 1 Hz.

[b]. Transition temperatures are determined by TMA.

T_{first}: the first transition temperature T_{seco}: the second transition temperature.

4.3.8 Thermal Properties of PAN/CNT Composite Films

Dimensional change in PAN/CNT composites as a function of temperature are shown in Figure A.16. According to the different slopes of the curve for certain film in Figure A.16, the curve are divided into three regions, as shown in Figure 4.8 (Taking the control PAN and PAN/SWNT1 composite films with 10 wt% loading as examples).

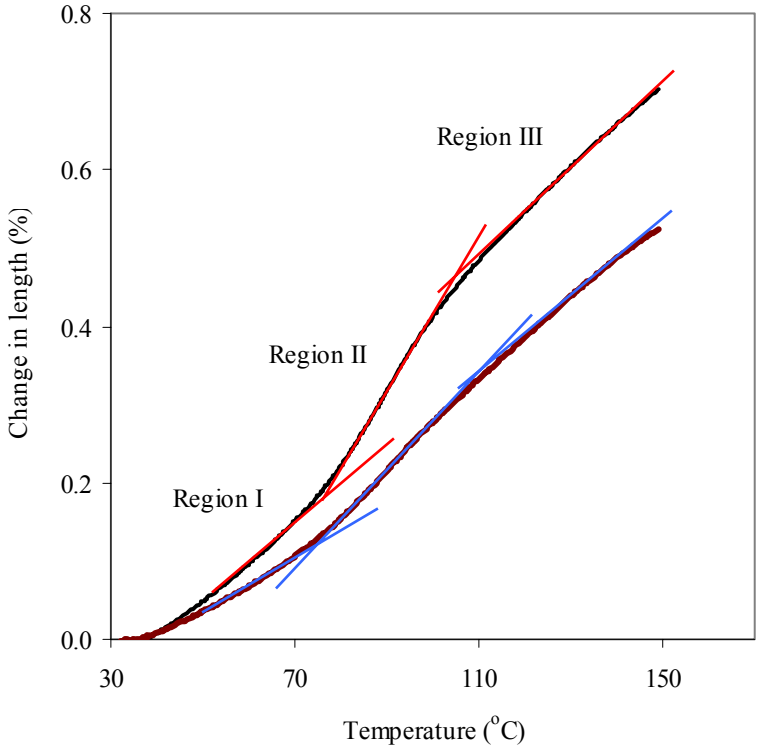

Figure 4.8 Thermal expansion as a function of temperature for control PAN and PAN/SWNT1 (90/10) composite films.

The temperatures at which slope of the curves change are the transition temperatures, named as the first transition temperature (T_{first}) and second transition temperature (T_{second}), respectively and are listed in Table 4.6. The coefficients of thermal

expansion (CTEs) in three regions for various films were determined from Figure A.16 and are also listed in Table 4.6. All PAN/CNT composite films exhibit reduced thermal expansion as compared to the control PAN film. The CTEs of the control PAN film are 55×10^{-6} K^{-1}, 91×10^{-6} K^{-1}, and 60×10^{-6} K^{-1} in Region I, II and III, respectively. Figure 4.9 shows the CTEs of various PAN/CNT composites in three regions. At 5 wt% CNT loading, PAN/SWNT3 shows the highest reduction in CTE relative to the control PAN (CTE reduced from $55\times10^{-6}\,K^{-1}$ for control PAN to $18\times10^{-6}\,K^{-1}$ (Region I), a reduction in CTE of about 67%). PAN/SWNT4 show next higher reduction in CTE followed by PAN/SWNT5, PAN/SWNT2, PAN/SWNT1, PAN/MWNT, PAN/DWNT and PAN/VGCNF. Similar trends in CTE reduction are shown for composites with 10 wt% (except for PAN/MWNT) and 20 wt% CNT loadings.

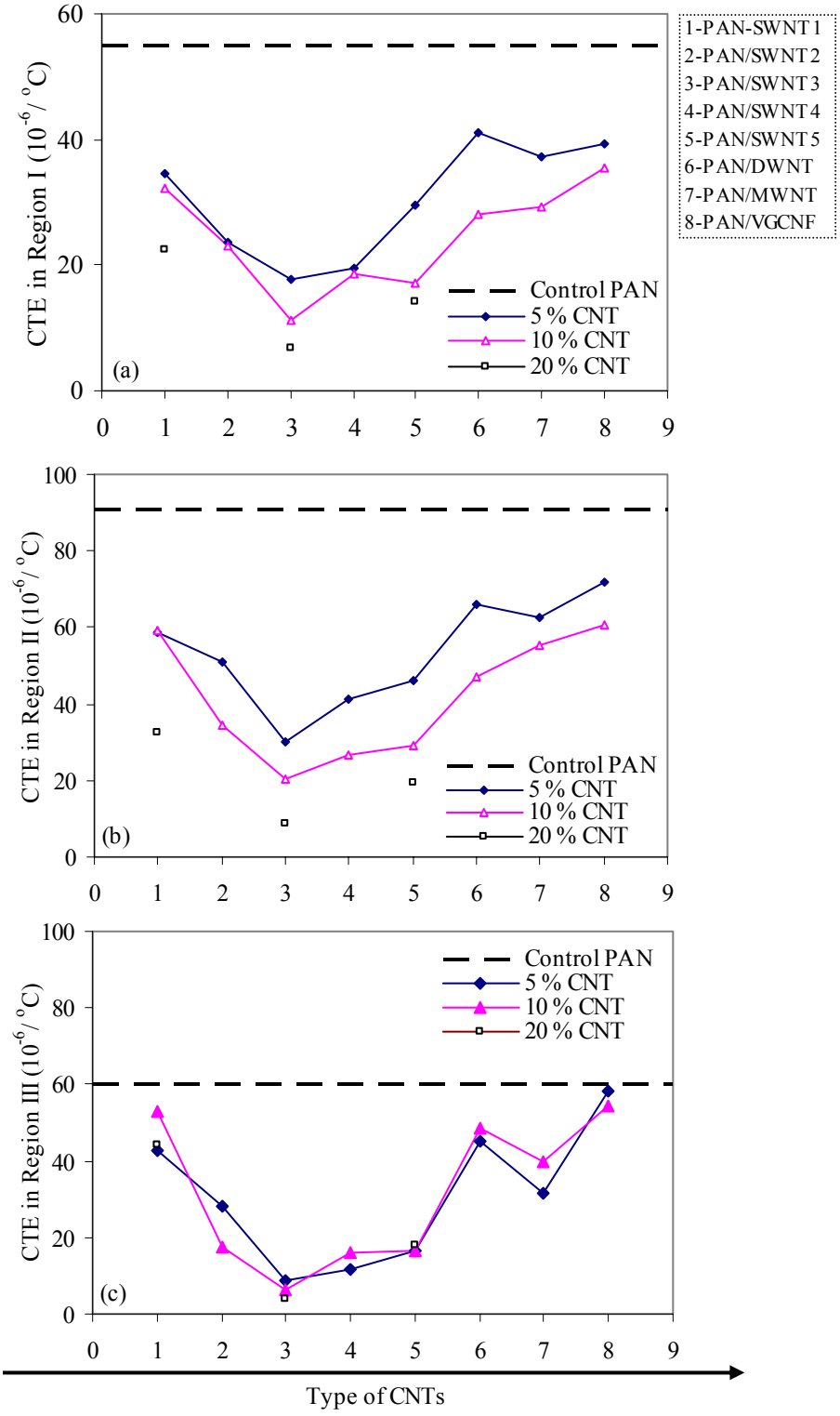

Figure 4.9. CTE in (a) Region I, (b) Region II, and (c) Region III for control PAN and various PAN/CNT composite films.

Xu et al[21] reported a decrease in CTE of SWNT-PVDF composite by 35 % at a 49 % SWNT loading. In our case, CTE of the PAN/SWNT3 composite film with 20 wt% loading is reduced by 90% as compared to the control PAN, indicating good polymer-nanotube interaction. It is noteworthy that for various PAN/SWNT composites, the trend for reduction in CTE follows a similar order as that for enhancement in tensile and dynamic mechanical properties. PAN/VGCNF composite films show the lowest reduction in CTE as compared to other composite films indicating relatively poor interaction between PAN and carbon nano fibers, which is also evident by the SEM images of their tensile fractured surfaces (Figure A.32-A.36). CTEs for various PAN/CNT composites in Region I, Region II and Region II plotted as a function of CNT surface area in Figure A.17, Figure A.18 and Figure A.19, respectively. It is evident that in general CTE decreases with increasing CNT surface area. As mentioned in a previous section, nanotube surface area is an important parameter governing the extent of polymer-nanotube interaction. The CTE clearly shows that the interfacial area is playing a critical role in governing the composite properties. The trend in CTE with CNT surface area is also complemented by the trend in tensile properties (Figure 4.2 and Figure 4.3), where good correlation was observed between tensile properties and CNT surface area.

4.3.9 Raman Spectra of PAN/CNT Composite Films

RBM bands in Raman spectra for CNT powders and various composite films are plotted in Figure A.20-A.25. The RBM bands were fitted with Lorentzian components. Each component corresponds to certain nanotube diameter which can be calculated from the frequencies of the RBM bands (Equation 4.1[14]). The high intensity RBM band positions for various films and CNT powders are listed in Table 4.7.

Table 4.7. Raman spectra data of CNT powders and PAN/CNT composite films

Sample	CNT loading (wt%)	RBM	G band		G'
		Position (cm^{-1})	Position (cm^{-1})	FWHM (cm^{-1})	Position (cm^{-1})
SWNT1	0	264	1586	24	2577
PAN/SWNT1	5	267	1588	26	2584
PAN/SWNT1	10	266	1590	27	2586
PAN/SWNT1	20	266	1591	27	2590
SWNT2	0	267	1589	26	2577
PAN/SWNT2	5	266	1588	20	2585
PAN/SWNT2	10	265	1590	21	2590
SWNT3	0	267	1589	25	2584
PAN/SWNT3	5	267	1589	21	2589
PAN/SWNT3	10	267	1589	20	2589
PAN/SWNT3	20	266	1589	20	2589
SWNT4	0	266	1594	21	2579
PAN/SWNT4	5	268	1592	14	2586
PAN/SWNT4	10	268	1593	16	2588
SWNT5	0	265	1592	17	2576
PAN/SWNT5	5	267	1592	14	2583
PAN/SWNT5	10	267	1593	16	2586
PAN/SWNT5	20	267	1593	14	2586
DWNT	0	265	1587	28	2576
PAN/DWNT	5	267	1585	24	2581
PAN/DWNT	10	267	1587	27	2581
MWNT	0	-	1596	54	2610
PAN/MWNT	5	-	1596	54	2609
PAN/MWNT	10	-	1596	54	2610
VGCNF	0	-	1581	18	2617
PAN/VGCNF	5	-	1581	27	2618
PAN/VGCNF	10	-	1582	56	2618
PAN/VGCNF	20	-	1582	20	2618

For SWNT1, SWNT2, SWNT3 and DWNT powders and their composite films, RBM peaks were fitted with two Lorentzian components located at 263 and 267 cm^{-1}. For SWNT4 powder and PAN/SWNT4 composite films, RBM band was fitted with three Lorentzian components located at 235, 263 and 267 cm^{-1} while RBM band for SWNT5 powder and PAN/SWNT5 films was fitted with three Lorentzian components located at 233, 263 and 267 cm^{-1}. The peaks located at 233, 235, 263 and 267 cm^{-1} correspond to the nanotube diameters of 1.01, 1.00, 0.89 and 0.88, respectively. Not all diameters, chiral, and metallic tubes can be observed with the 785 nm excitation used in the current work.

RBM peak intensity varies for the composite films as compared to the CNT powders. RBM intensity depends on the laser excitation energy (E_{laser}). Under strain, the energy separation between the van Hove singularities E_{ii} shifts closer to or farther away from laser excitation energy (E_{laser}). When the difference $|E_{ii} - E_{laser}|$ decreases, RBM intensity increases and vice versa. RBM intensity reaches maximum when E_{ii} is equal to E_{laser}. The second-order energy separation E_{22}^{s} for semiconducting nanotube for the 263 cm^{-1} peak is in the range of 1.81 eV-1.88 eV.[22] Under compressive stress, E_{22}^{s} of 263 cm^{-1} peak increase (mode 1[23]) and shifts far away from the laser energy value of 1.58 eV resulting in decreased intensity. PAN/SWNT and PAN/DWNT composites do show the decreased intensity of peak at 263 cm^{-1} as compared to CNT powders.

E_{22}^{s} of 267cm^{-1} peak is between 1.81 and 1.90 eV.[22] Under compressive stress, E_{22}^{s} of 267cm^{-1} peak decreases (mode 2[23]) and shifts closer to E_{laser} and resulting in increased intensity.[22-24] PAN/SWNT1 and PAN/SWNT5 composite films exhibit increased intensity of 267 cm^{-1} peak. The intensity for 267 cm^{-1} peak decreased for

PAN/SWNT3, PAN/SWNT4 and PAN/DWNT composite films. PAN/SWNT2 composites show no significant change compared to their corresponding CNT powders. The reason for this decreased intensity is not clear. As mentioned previously, all intensities have been normalized linearly taking the intensity of the G-band as 1.

The intensity of the peak at 235 cm^{-1} decreased for PAN/SWNT4 composite films as compared to that for the SWNT4 powder. With increase in SWNT4 loading, 235 cm^{-1} peak intensity for composite films further decreases. This intensity variation comes from the effect of strain exerted by PAN molecules on resonance. Under compressive strain, E_{22}^{s} of 235 cm^{-1} peak located in the range of 1.59-1.67 eV will decrease (mode 2) and shifts to closer to the laser energy.[22-24] Normalized 235 cm^{-1} peak intensities for the PAN/SWNT5 composite film are suppressed as compared to that for the SWNT5 powder and decrease with increasing SWNT5 loading.

For SWNT1, SWNT4, SWNT5 and DWNT containing composite films, the RBM peak positions show a slight up-shift to higher frequency as compared to their respective CNT powders. The RBM peak positions for the other composite films show no significant difference relative to their CNT powders. Calculation of the pressure dependence of RBM position showed that RBM position increase approximately linearly with increasing pressure.[25] The upshift of RBM for various PAN/CNT films may also be due to the compressive force exerted by the PAN molecules on the nanotube bundles.

G band for CNT powders and various PAN/CNT composite films are shown in Figure A.26. G band positions, FWHM of G band and G' band position (at ~ 2585 cm^{-1}) for CNT powders and various PAN/CNT composite films are listed in Table 4.7. No significant shift of G band position is observed for PAN/CNT composite films (except for

the PAN/SWNT1 composites), as compared to the G band of their CNT powder. The upshift of G' band is observed for the PAN/CNT composite films except for PAN/MWNT and PAN/VGCNF films (Figure A.27). The upshift of G band and G' band in polymer/CNT composites is attributed to the compressive force on the nanotubes exerted by the polymer.[26] G' band is more sensitive to the pressure as compared to G band, resulting in larger band position shift.[27, 28]

4.3.10 Solvent Resistance of PAN/CNT Composite Films

PAN/CNT composite films with 10 wt% CNT loading were immersed in DMF for one hour at room temperature. Figure 4.10 shows the composite films in DMF after 1 hour. Various PAN/SWNT composite films mostly retained their shapes indicating good interaction between PAN and SWNTs. The color of DMF is clear for the PAN/SWNT1, PAN/SWNT4 and PAN/SWNT5 composite films. Some dispersion occurred in PAN/SWNT2 and PAN/SWNT3 composite films as indicated by the gray color of the solvent in these cases. Mechanical and electrical properties and thermal expansion results for various PAN/SWNT composite films indicate that the interaction between PAN and SWNT3 is better. Based on these results, we had expected that PAN/SWNT3 films would show better resistance to DMF. Therefore this result is a bit surprising. As expected PAN/DWNT, PAN/MWNT, and PAN/VGCNF exhibit better dispersion in DMF than various SWNTs. The solvent study does confirm that all SWNTs exhibit better interaction with PAN, than DWNT, MWNT, and VGCNF.

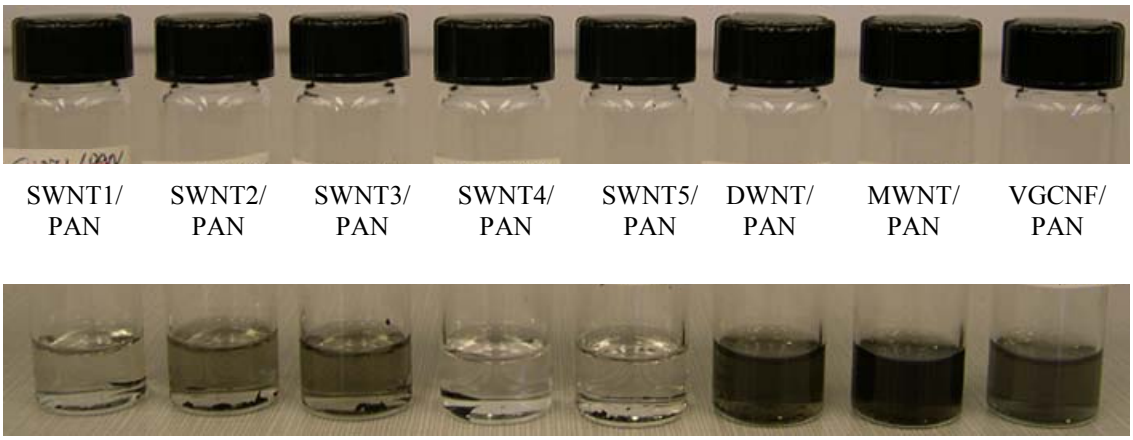

Figure 4.10. PAN/CNT composite films with 10 wt% CNT loading immersed in DMF for one hour.

4.3.11 Structure of PAN/CNT Composite Films

WAXD patterns for various films are shown in Figure A.28-A.30. PAN crystallite size calculated using Scherrer equation from the 110 peak at $2\theta \sim 16.8°$ and PAN X-ray crystallinity values are given in Table 4.8. PAN crystallinity increases by the addition of CNTs. PAN crystal size determined from 110 peaks in the composite films is smaller than that in the control PAN film. PAN crystallinity and crystal size are the largest in the composite film containing MWNT.

Table 4.8. Structural properties and density of control PAN and PAN/CNT composite films

Sample	CNT loading		Crystallinity (%)	Crystal size (nm)	Experimental density (g/cm^3)	Theoretical density [a] (g/cm^3)
	(wt%)	(vol%)				
control PAN	0	0	43	5.7	1.15 ± 0.06	1.18
PAN/SWNT1	5	4.6	48	4.9	0.89±0.05	1.19
PAN/SWNT2	5	4.6	47	5.2	0.97±0.04	1.19
PAN/SWNT3	5	4.6	46	5.1	1.00± 0.01	1.19
PAN/SWNT4	5	4.6	46	4.8	0.98± 0.01	1.19
PAN/SWNT5	5	4.6	48	5.1	0.97±0.02	1.19
PAN/DWNT	5	4.0	48	5.4	0.88±0.01	1.19
PAN/MWNT	5	3.3	50	5.4	0.95±0.01	1.20
PAN/VGCNF	5	3.1	49	5.4	1.22 ± 0.07	1.20
PAN/SWNT1	10	9.2	47	5.2	0.68±0.01	1.19
PAN/SWNT2	10	9.2	46	5.2	0.92±0.03	1.19
PAN/SWNT3	10	9.2	45	4.9	1.08±0.01	1.19
PAN/SWNT4	10	9.2	46	4.7	0.96±0.09	1.19
PAN/SWNT5	10	9.2	49	5.0	0.98± 0.06	1.19
PAN/DWNT	10	8.0	46	4.9	0.87±0.01	1.21
PAN/MWNT	10	6.8	50	5.4	0.88±0.02	1.22
PAN/VGCNF	10	6.3	46	5.1	0.91 ± 0.09	1.23
PAN/SWNT1	20	18.5	41	4.8	0.93±0.02	1.20
PAN/SWNT3	20	18.5	38	4.5	1.03±0.01	1.20
PAN/SWNT5	20	18.5	41	4.8	1.08±0.03	1.20
PAN/VGCNF	20	13.1	43	5.9	0.66 ± 0.05	1.28

[a] Theoretical density of the composite films is calculated using the following equation:

$$\rho_c = V_f(\rho_f - \rho_m) + \rho_m$$

Where ρ_c is the density of the composite film;
V_f is the volume fraction of VGCNF;
ρ_m is the density of PAN (1.18 g/cm^3);
ρ_f is the density of filler: SWNT (1.3 g/cm^3)[29], DWNT (1.5 g/cm^3)[30], MWNT (1.8 g/cm^3)[31], and VGCNF (1.95 g/cm^3)[31].

4.3.12 Morphology of PAN/CNT Composite Films

Scanning Electron Microscopy (SEM) images of various CNT powder are shown in Figure A.31. MWNT and VGCNF exist as individual nanotubes while SWNT form bundles. MWNT, SWNT and DWNT are entangled. Morphologies of the fractured cross-section of the various PAN/CNT composite films are shown in Figure A.32-A.36. CNTs are well dispersed in the PAN matrix except for DWNT. TEM images for CNTs shows that DWNTs are highly entangled. During preparation of composite films, DWNT was the most difficult to disperse in the solvent. Though more sonication time is used to disperse DWNTS, its dispersion quality in the polymer is not very good. The SEM images do not show any significant difference in the dispersion quality of various SWNTs in the PAN matrix.

4.4 CONCLUSIONS

Polyacrylonitrile composite films of about 25 μm thickness have been processed using 8 different type of carbon nanotubes at a nanotube loading of 5, 10, and 20 wt%. Generally, tensile modulus and tensile strength of PAN/CNT composites increase and coefficient of thermal expansion decrease with increasing nanotube surface area. Dynamic mechanical properties of the composite films have been measured and compared to those of the control PAN. In plane dc electrical conductivity and film solvent resistance in dimethyl formamide has been characterized. Based on these studies, it is concluded that in general DWNT, MWNT, and VGCNF exhibit relatively poor interaction with PAN than any SWNT used in this study. However, different SWNTs were observed to have different interaction with PAN. RBM, D, G, and G' Raman bands have been analyzed and discussed for various CNTs and composite films. Structure and

morphology of the films have been examined by scanning electron microscopy and X-ray diffraction. Among all composites, PAN/SWNT3 exhibits the highest improvement in tensile modulus, storage modulus, electrical conductivity and most reduction in thermal shrinkage.

4.5 REFERENCES

[1] H. G. Chae, T. V. Sreekumar, T. Uchida, and S. Kumar, Polymer **46**, 10925 (2005).

[2] I. W. Chiang, B. E. Brinson, R. E. Smalley, J. L. Margrave, and R. H. Hauge, Journal of Physical Chemistry B **105**, 1157 (2001).

[3] H. J. Li, L. Feng, L. H. Guan, Z. J. Shi, and Z. N. Gu, Solid State Communications **132**, 219 (2004).

[4] C. M. Yang, H. Kanoh, K. Kaneko, M. Yudasaka, and S. Iijima, Journal of Physical Chemistry B **106**, 8994 (2002).

[5] S. Kumar, D. P. Anderson, and A. S. Crasto, Journal of Materials Science **28**, 423 (1993).

[6] Z. S. Wronski and G. J. C. Carpenter, Carbon **44**, 1779 (2006).

[7] C. Journet, W. K. Maser, P. Bernier, A. Loiseau, M. L. delaChapelle, S. Lefrant, P. Deniard, R. Lee, and J. E. Fischer, Nature **388**, 756 (1997).

[8] A. Thess, R. Lee, P. Nikolaev, H. J. Dai, P. Petit, J. Robert, C. H. Xu, Y. H. Lee, S. G. Kim, A. G. Rinzler, D. T. Colbert, G. E. Scuseria, D. Tomanek, J. E. Fischer, and R. E. Smalley, Science **273**, 483 (1996).

[9] S. Ergun, Chemistry and Physics of Carbon, Vol. 3, Ed. Walker, Philip L., Marcel Dekker Inc, New York (1968).

[10] W. Ruland, Chemistry and Physics of Carbon, Vol. 4, Ed. Walker, Philip L., Marcel Dekker Inc, New York (1968).

[11] T. F. Yen, J. G. Erdman, and S. S. Pollack, Analytical Chemistry **33**, 1587 (1961).

[12] L. Lu, V. Sahajwalla, C. Kong, and D. Harris, Carbon **39**, 1821 (2001).

[13] M. S. Dresselhaus, G. Dresselhaus, A. Jorio, A. G. Souza, and R. Saito, Carbon **40**, 2043 (2002).

[14] S. M. Bachilo, M. S. Strano, C. Kittrell, R. H. Hauge, R. E. Smalley, and R. B. Weisman, Science **298**, 2361 (2002).

[15] G. S. Duesberg, I. Loa, M. Burghard, K. Syassen, and S. Roth, Physical Review Letters **85**, 5436 (2000).

[16] M. F. Zhang, M. Yudasaka, A. Koshio, and S. Iijima, Chemical Physics Letters **364**, 420 (2002).

[17] R. A. Jishi, L. Venkataraman, M. S. Dresselhaus, and G. Dresselhaus, Chemical Physics Letters **209**, 77 (1993).

[18] A. Jorio, A. G. Souza, G. Dresselhaus, M. S. Dresselhaus, A. K. Swan, M. S. Unlu, B. B. Goldberg, M. A. Pimenta, J. H. Hafner, C. M. Lieber, and R. Saito, Physical Review B **65**, 155412 (2002).

[19] M. Cadek, J. N. Coleman, K. P. Ryan, V. Nicolosi, G. Bister, A. Fonseca, J. B. Nagy, K. Szostak, F. Beguin, and W. J. Blau, Nano Letters **4**, 353 (2004).

[20] Y. K. Choi, K. Sugimoto, S. M. Song, Y. Gotoh, Y. Ohkoshi, and M. Endo, Carbon **43**, 2199 (2005).

[21] Y. S. Xu, G. Ray, and B. Abdel-Magid, Composites Part a-Applied Science and Manufacturing **37**, 114 (2006).

[22] M. S. Dresselhaus and P. C. Eklund, Advances in Physics **49**, 705 (2000).

[23] M. Lucas and R. J. Young, Physical Review B **69**, 085405 (2004).

[24] H. Kataura, Y. Kumazawa, Y. Maniwa, I. Umezu, S. Suzuki, Y. Ohtsuka, and Y. Achiba, Synthetic Metals **103**, 2555 (1999).

[25] D. Kahn and J. P. Lu, Physical Review B **60**, 6535 (1999).

[26] A. Rasheed, M. D. Dadmun, I. Ivanov, P. F. Britt, and D. B. Geohegan, Chemistry of Materials **18**, 3513 (2006).

[27] U. D. Venkateswaran, M. E. Gosselin, B. Postek, D. L. Masica, G. Chen, R. Gupta, and P. C. Eklund, Physica Status Solidi B-Basic Research **235**, 364 (2003).

[28] C. A. Cooper, R. J. Young, and M. Halsall, Composites Part a-Applied Science and Manufacturing **32**, 401 (2001).

[29] J. P. Lu, Physical Review Letters **79**, 1297 (1997).

[30] T. Sugai, H. Yoshida, T. Shimada, T. Okazaki, and H. Shinohara, Nano Letters **3**, 769 (2003).

[31] Provided by the manufacturer.

CHAPTER 5

POLYACRYLONITRILE/CARBON NANOTUBE DISPERSION: A NMR STUDY

5.1 INTRODUCTION

Good dispersion of nanotubes in polymer matrices is the key issue to improve the composites physical properties. Solid state NMR has been used to analyze the nanoclay dispersion in polymer matrices.[1-5] VanderHart et al.[1-3] suggested that the spin-lattice relaxation time T_1 determined from solid-state NMR measurements can characterize the dispersion quality of nanoclay in nylon/nanoclay composites.

Under a magnetic field B_o, the net magnetization M_Z at the equilibrium is along the direction of B_o and is called the equilibrium magnetization M_o (Figure 5.1).[6] The Z component of magnetization M_Z equals M_o and is referred to as the longitudinal magnetization. Spin-lattice relaxation time (T_1) describes how longitudinal magnetization returns to its equilibrium state. Equation 5.1 describes the relationship between M_Z and time t when M_Z is along the +Z axis.

$$M_z = M_0(1 - e^{-t/T_1}) \tag{5.1}$$

If M_z is placed along the -Z axis, the process describing how M_z returns to its equilibrium along the +Z axis is expressed by Equation (5.2).[7]

$$M_z = M_0(1 - 2e^{-t/T_1}) \tag{5.2}$$

Two important techniques for T_1 measurements including inversion recovery and saturation recovery[8] are typically implemented in the software of the modern NMR

spectrometers. When an alternating current is passed through a coil of wire that is along the X axis, a pulsed magnetic field B_1 is produced along the X axis and will cause M_Z to rotate around the direction of B_1. A 90° pulse rotates the magnetization vector clockwise by 90 degrees about the X axis: that is, rotates M_Z down to along the Y axis. A 180° pulse is one that will rotate the magnetization vector by 180 degrees: that is, rotates M_Z down to along the -Z axis. By the inversion recovery method, an 180° pulse is first applied to the sample, the magnetization is then allowed to recover for some time and finally a 90° sampling is used to measure the residual magnetization (Figure 5.1b).[9] In this case, Equation 5.2 is used to determine T_1. By the saturation recovery method, a 90° pulse is applied to sample repeating at intervals, a 90° pulse is then input and the longitudinal component of magnetization is finally measured (Figure 5.1c). In this case, Equation 5.1 is applied to determine T_1.

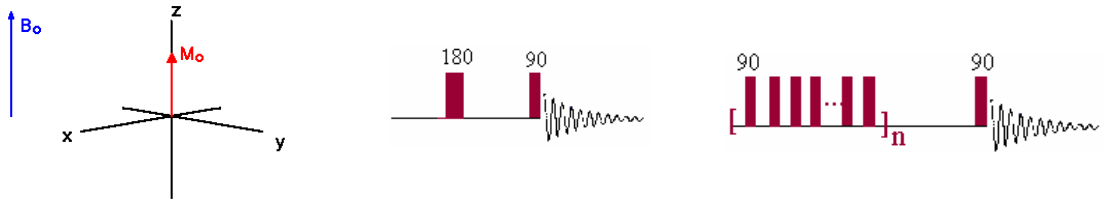

(a) (b) (c)

Figure 5.1. (a) Conventional NMR coordinate system for M_Z, M_o and B_o, (b) Inversion recovery method, and (c) Saturation recovery method.[6, 9]

In a polymer/carbon nanotube system, T_1 relaxation time may be used to assess nanotube dispersions quality due to the presence of magnetic nanotubes. Tang et al.[10] first reported the T_1 relaxation of SWNT determined by ^{13}C NMR. Two relaxation times for

SWNTs were identified: one is at ~ 5 s and the other is at ~90 s due to the metallic and semiconducting carbon nanotubes, respectively.[10] In polymer/nanotube composites, two relaxation mechanisms contribute to the experimental T_1 relaxation time.

(i) Ring currents are produced when clusters of nanotubes interact with radio-frequencies applied in the NMR experiments.[7, 11] These currents induce magnetic fields, which add to the external NMR field, and as a result areas surrounded by the CNT-clusters will become "invisible" to the NMR. Hence only areas free of ring currents can be detected. Spin diffusion between excited spins and spins in the "invisible" area lead to a loss of detected magnetization providing an apparent relaxation mechanism. Very little is known as to the size of domains, where this effect becomes relevant.

(ii) In polymer/CNT composites, carbon nanotubes with magnetic properties will lead to a shortening in relaxation time T_1^{para} of polymer within 0.4-1 nm of the nanotube surface. Polymers in the other region have a relaxation time T_1^{polym} which may be the same as T_1 of the control polymer. By spin diffusion, polymer within 25- 40 nm of the nanotube surface will experience a shortened relaxation time T_1^{exp} which can be measured by solid state NMR experiments. The schematic mechanism resulting in a reduction of T_1 of polymer in the polymer/CNT composites is shown in Figure 5.2[12]. The relationship of T_1^{exp} with T_1^{para} and T_1^{polym} is expressed by Equation 5.3[8]:

$$\frac{1}{T_1^{\exp}} = f\frac{1}{T_1^{para}} + (1-f)\frac{1}{T_1^{polym}} \qquad (5.3)$$

where f is the volume fraction of the polymer within 0.4-1 nm of the tube surface. T_1^{exp} can be calculated from Equation 5.3 using a set of ratios of T_1^{polym} to T_1^{para} (T_1^{polym}/T_1^{para}). Assuming the value of T_1^{para} is equal to one, the calculated T_1^{exp} for various values of f

are calculated and plotted as a function of (T_1^{polym}/T_1^{para}), as shown in Figure 5.3. When $T_1^{polym} > T_1^{para}$, increased f value results in a reduction in T_1^{exp}. Good nanotube dispersion in the polymer matrix leads to increased interface between polymer and nanotubes tubes[3, 5] resulting in the significant increase in the polymer volume fraction (f) within 0.4-1 nm of the nanotube surface. When the nanotube dispersion is poor, the interface volume between polymer and nanotubes is small and thus f value is small, resulting in only a slight reduction in T_1. While a good dispersion will increase f and further reduce T_1. When, $T_1^{polym} < T_1^{para}$, calculated T_1^{exp} for the composite is larger than T_1^{polym} and increases moderately with increasing value of f (Figure 5.3b). The question is, is it physically possible to have $T_1^{polym} < T_1^{para}$. If the polymer at the nanotube interface has higher mobility than the bulk polymer, then T_1^{polym} is expected to be less than T_1^{para}. If such a case ($T_1^{polym} < T_1^{para}$) physically exists, remains to be seen.

The mechanism (ii) is understood and well described for polymer-nanoclay composites while mechanism (i) is still not well understood. In nanotubes, presence of paramagnetic or ferromagnetic impurities such as oxygen, Fe^{3+} or Fe^{2+} also influences the NMR response due to the inhomogeneous local field induced by these impurities[7, 11]. These issues lead to some ambiguity in understanding and explaining the measured T_1 results.

In the current work, carbon nanotube dispersion has been characterized in PAN/CNT composite fibers and films by monitoring their T_1 relaxation times using solid state ^1H NMR. Carbon nanotubes utilized in this work include SWNTs, DWNTs, MWNTs and VGCNFs, as well as nitric acid treated SWNTs.

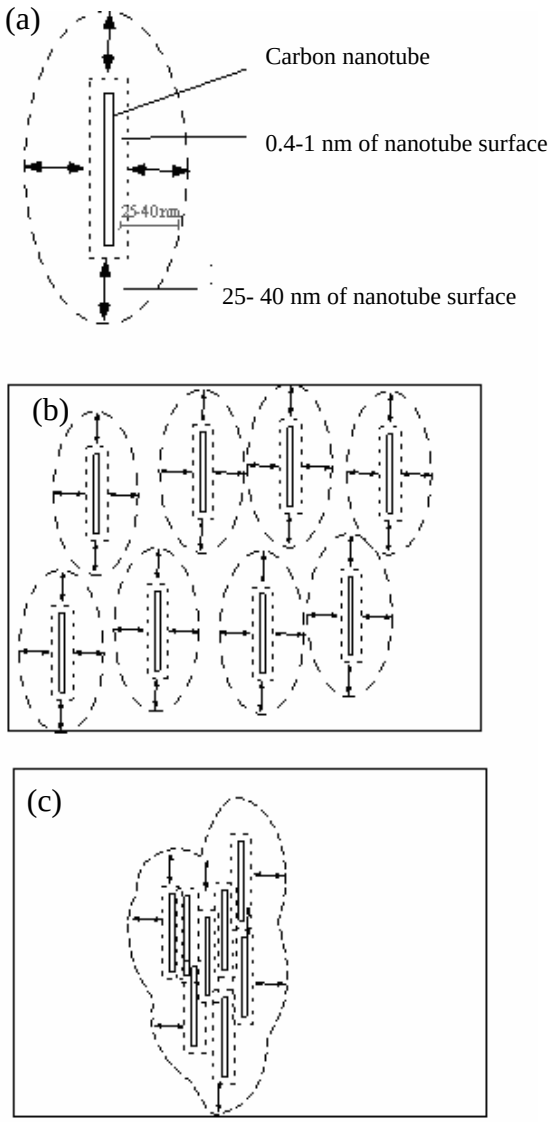

Figure 5.2. Schematic presentation of the mechanism (ii) leading to the reduction of T_1 of polymer in the polymer/CNT composites.[12] (a) Polymers within 0.4-1 nm of the nanotube surface experience a shortened relaxation time T_1^{para}. Polymers in other areas experience a relaxation time, T_1^{polym}. Polymers within 25-40 nm of the nanotube surface experience a spin diffusion resulting in an T_1^{exp}. (b) When nanotubes are exfoliated or dispersed well in polymer, the interface between polymer and nanotube increased. In this case, most of polymer experiences a shortened T_1 and thus overall T_1^{exp} value is significantly shortened. (c) When the dispersion of nanotubes in polymer is poor, only a minor fraction of the polymer is on the paramagnetic surface of nanotubes. Overall T_1^{exp} value is only slightly shortened.

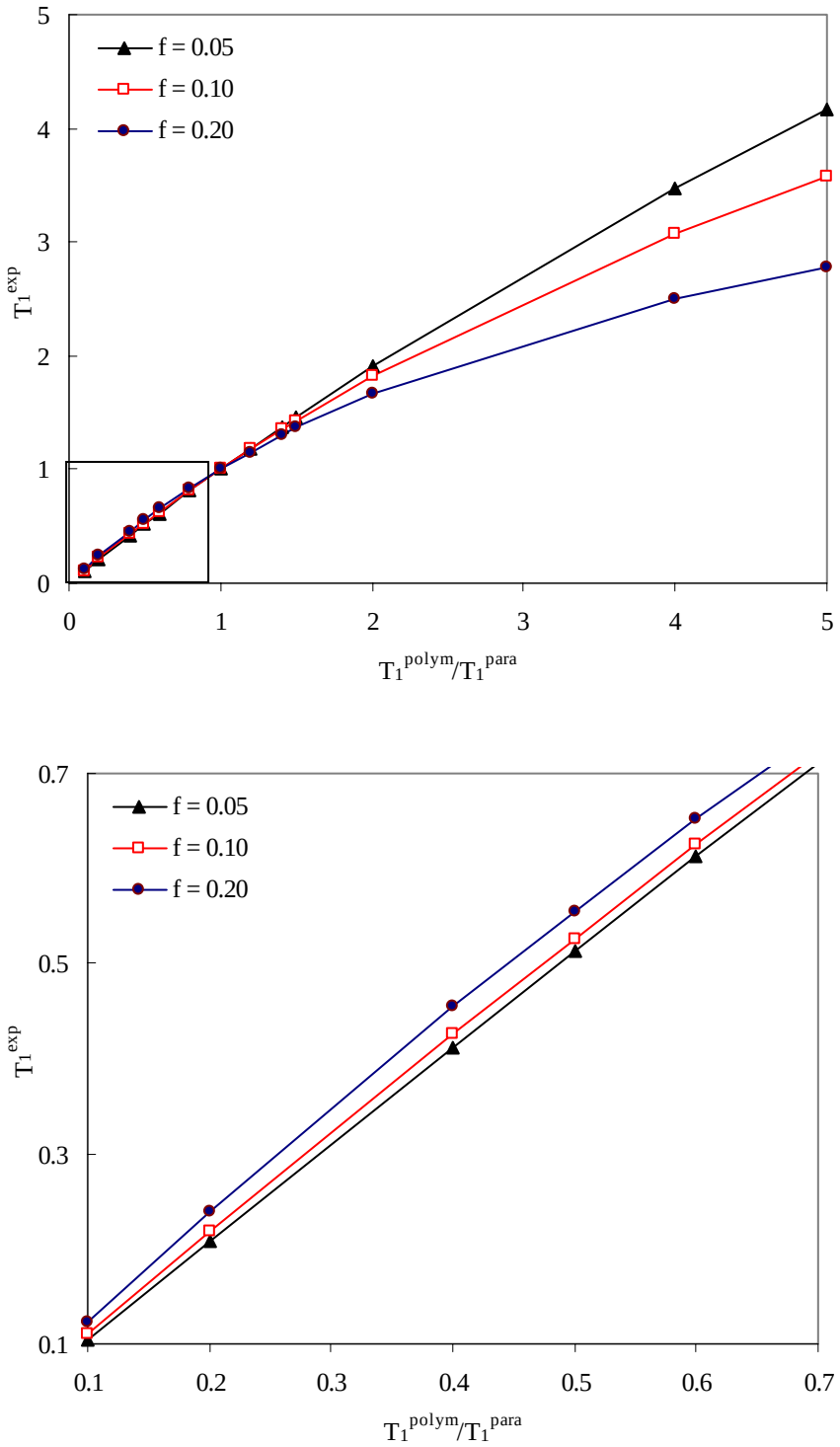

Figure 5.3. Calculated T_1^{exp} using Equation 5.3 of composites for various values of f as a function of (T_1^{polym}/T_1^{para}).

5.2 EXPERIMENTAL

5.2.1 Preparation of PAN/SWNT Composite Fibers[13]

PAN/untreated-SWNT (95/5) composite fiber was prepared using as-received HiPCO 87 SWNT containing 10 % impurity provided by CNI. 0.75 g HiPCO 87 SWNTs were firstly dispersed in 200 ml dimethyl formamide (DMF) (obtained from Sigma-Aldrich Milwaukee, WI and used as received) at room temperature by sonication using a bath sonicator (Cole-Parmer 8891R-DTH, 80 W, 43 kHz) for 2 hours. During the sonication process, the SWNT/solvent mixture was stirred every half an hour with a bio-homogenizer for 3 minutes. 14.25 g PAN containing 10% methyl acrylate (random copolymer, molecular weight 100,000 g/mole, obtained from Sigma-Aldrich, Milwaukee, WI and used as received) was added gradually into the SWNT/DMF dispersion. The PAN/SWNT/DMF dispersion was stirred and at the same time sonicated for 16 hours at room temperature. The composite fibers were obtained by dry-jet wet-spun the resulting PAN/SWNT/DMF dispersion on a small scale-spinning machine (manufactured by Bradford University Research Ltd.) using a single hole spinneret with a diameter of 500 μm.

PAN/acid-treated-SWNT (95/5) composite fiber was prepared using nitric acid-treated HiPCO 87 SWNT. 0.5 g SWNTs were firstly added to 6M HNO_3, sonicated for 2 hours, and refluxed for two hours. The treated SWNTs were finally washed with distilled water and DMF. 100 ml SWNT/DMF dispersion was then prepared by adding DMF to the treated and washed SWNTs. 7.6 g PAN was added gradually into the SWNT/DMF dispersion and then follow the process for the preparation of PAN/untreated SWNT

composite (95/5) fiber. The control PAN fiber was made using the same process without the addition of SWNT.

5.2.2. Preparation of PAN/CNT Composite Fibers and Films

PAN/CNT composite films were prepared using PAN with molecular weight 100,000 g/mol obtained from Exlan, Co. (Japan), SWNTs from Carbon Nanotechnologies, Inc. (Houston, TX), DWNTs from Nanocyl, Co. (Belgium), MWNTs from Iljin Nanotech, Co. (Korea), and VGCNFs from Applied Sciences, Inc. (Cedarville, OH). The catalytic impurity of the each type of nanotubes determined from the thermogravimetric analysis (TGA) was 1, 5, 3, and 0.3 wt% in SWNT3, DWNT, MWNT, and VGCNF, respectively. Dried carbon nanotubes were added to 50 ml DMF (purchased from Sigma- Aldrich, Milwaukee, WI and used as received) and sonicated for 48 hours (DWNT was sonicated for 6 days) until the homogenous dispersion form. The homogeneity of dispersion was confirmed by optical microscopy. 240 mg PAN was added to the CNT/DMF dispersion and homogenized while stirring. Excess solvent was evaporated to obtain the final solution with the volume of 25 mL. The resulting PAN/CNT/DMF solutions were cast on the glass substrate to form the film in the vacuum oven at 80 ^{o}C. The composite films were further dried in the vacuum oven at 80 ^{o}C for 3 days. The PAN/CNT composite films with various loading of CNTs (5, 10, 20 wt% CNTs) were prepared. The control PAN film was made using the same process.

The same types of PAN, SWNTs, DWNTs, MWNTs and VGCNFs were used to prepare the PAN/CNT (95/5) composite fibers.[14] 1.5 g CNTs were firstly dispersed in 300 mL DMAc using sonication and stirring until dispersion reached optical homogeneity. 28.5 g PAN was gradually dissolved in 150 mL DMAc to prepare

PAN/DMAc solution at 70 ^{o}C. The PAN/DMAc solution was then added to the CNT/DMAc dispersion and stirred until homogenous dispersion was obtained. The desired solution concentration of 30 g solids (PAN+CNT) in 150 mL DMAc was obtained by evaporating the excess solvent. The resulting PAN/CNT/DMAc solutions were spun to produce PAN/CNT composite fibers at room temperature by dry-jet-wet spinning using the small scale spinning system (manufactured by Bradford University Research Ltd.). The control PAN fiber was made using the same process without the addition of CNT.

5.2.3. Solid State ^{1}H NMR Measurement

Solid state ^{1}H NMR experiments were conducted on a Brucker DSX400 NMR spectrometer (Bruker Biospin, Rheinstetten, German), operating at a magnetic field of 9.4 T (^{1}H frequency of 400 MHz). Due to the high amount of paramagnetic Fe^{3+} irons in nanotubes, it is difficult to obtain the reasonable amount of measurable signal under static measuring conditions. These paramagnetic irons results in large susceptibility gradients in the sample. A double-resonance Magic Angle Spinning (MAS) at a frequency of 10 kHz was used to the concentrated observable signal, thus enhancing sensitivity, and facilitating the discrimination from background signal. For each study, less than 50 mg specimen was used in 4 mm rotors for the NMR measurement.

5.3 RESULTS AND DISCUSSIONS

T_1 values and mechanical properties for the PAN, PAN/acid-treated-SWNT and PAN/untreated SWNT composite fibers are compared in Table 5.1. T_1 relaxation time for PAN decreases with the addition of SWNT. T_1 value for the PAN/acid-treated-SWNT composite fiber is shorter than that for the PAN/untreated-SWNT composite fibers. The

mechanical properties of the composite fibers indicate that the treatment of SWNT with acid results in improvement in mechanical properties. With nitric acid treatment, some of the SWNTs are cut into smaller lengths[15], and some smaller diameter nanotubes may be destroyed.[16] Thus acid treatment leads to the better SWNT dispersion in polymer. Hence the interface between PAN and nanotubes is improved causing the reduction in T_1 value and increase in mechanical properties in the composite using acid treated SWNTs. SWNTs treated with nitric acid can introduce oxygenated functional groups at the ends and defect sites[17], which however have no significant effect on the measured T_1 value. Therefore, the shorter T_1 for the PAN/acid-treated-SWNT composite fiber may be an indication for the improved dispersion quality. Nitric acid treatment reduces catalytic impurity as well as metallic nanotubes. Therefore, in addition to the effect of SWNT dispersion quality, the ring currents and reduced amount of metal in nanotubes can also result in shortened relaxation time. In this study, attempt was not made to separate the effects of these three factors (namely dispersion, catalytic impurity, and conducting nanotubes) on T_1.

Table 5.1. Relaxation time (T_1), and mechanical properties for control PAN and PAN/SWNT (95/5) composite fibers. The mechanical property data is obtained from reference 13

Sample	**T_1 (ms)**	**Tensile Modulus[13] (GPa)**	**Tensile strength[13] (GPa)**	**Elongation[13] (%)**
Control PAN	3120 ± 5	5.9 ± 0.2	0.13 ± 0.01	11.0 ± 08
PAN/acid-treated-SWNT (95/5)	617 ± 6	17.8 ± 1.3	0.45 ± 0.06	8.6 ± 1.0
PAN/untreated-SWNT (95/5)	1827 ± 9	13.1 ± 1.0	0.33 ± 0.04	6.9 ± 2.0

In another study, PAN/CNT (95/5) fibers were processed using SWNT, DWNT, MWNT, and VGCNF. The experimental T_1 and mechanical property results[14] for the PAN/CNT composite fibers are given in Table 5.2. With the addition of CNT (except for VGCNF), T_1 relaxation time for PAN is shortened due to the presence of nanotubes. Among various PAN/CNT composite fibers, T_1 value for the PAN/DWNT composite fiber is the shortest while that for the PAN/VGCNF composite fiber is the largest. As we discussed, the larger interface area in the PAN/CNT composites leads to the shorter T_1 value. Using the experimentally determined surface area of CNTs (listed in Chapter 4), the surface area of nanotubes based on 5 wt% CNT loading in the composite fiber is calculated and listed in Table 5.2. Polymer relaxation times (T_l) are plotted as a function of nanotube surface area in the composite fibers, as shown in Figure 5.4. Relaxation time for the PAN/CNT composite fibers decreases with increasing nanotube surface area. As we discussed in Section 4.1, the paramagnetic metal impurity and ring currents may also attribute to reduction in T_1 value for composites. The catalytic impurity in SWNT, DWNT, MWNT and VGCNF used in this part of the study was about 2.4, 5.4, 2.5, and 0.3 wt%, respectively.

Table 5.2. Relaxation time (T_1), mechanical properties, and CNT surface area for various PAN/CNT (95/5) composite fibers. The mechanical property data is obtained from reference 14

Sample	T_1 (ms)	Modulus[14] (GPa)	Strength[14] (MPa)	Elongation (%)[14]	Surface area of CNT in composites (m^2/g)
control PAN	3304	7.8 ± 0.3	244 ± 12	5.5 ± 0.5	-
PAN/SWNT	2717	13.6 ± 0.5	335 ± 9	9.4 ± 0.3	35*
PAN/DWNT	1336	9.7 ± 0.5	316 ± 15	9.1 ± 0.7	28.2
PAN/MWNT	2994	10.8 ± 0.4	412 ± 23	11.4 ± 1.2	8
PAN/VGCNF	4320	10.6 ± 0.2	335 ± 13	6.7 ± 0.3	2

* Surface area of SWNT is the average experimental data of five types of SWNTs provide by CNI.

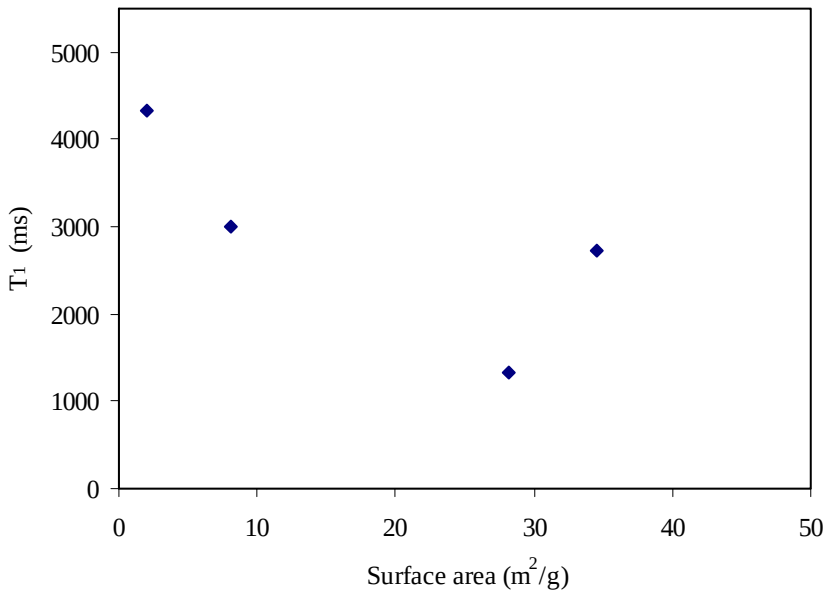

Figure 5.4. Polymer relaxation time (T_1) as a function of nanotube surface area in PAN/CNT composite fibers. Nanotube surface area was determined based on the nanotube weight fraction and the BET surface area values in Chapter 4.

T_1 values, mechanical properties and electrical conductivity values for the PAN/CNT composite films are listed in Table 5.3. With the addition of CNT (except for VGCNF), T_1 relaxation time for PAN decreased. As discussed previously, reduction in T_1 relaxation time may also be due to the presence of the paramagnetic impurities Fe^{2+}/Fe^{3+}[18]. The tensile modulus and log (Electrical conductivity) (abbreviated as log (E.C.)) for various composite films are plotted as a function of relaxation time T_1 (Figures 5.5 and 5.6).

Table 5.3. T_1 values, mechanical and electrical properties for control PAN and various PAN/CNT composite films

Sample	**T_1 (ms)**	**Modulus (GPa)**	**Strength (MPa)**	**Elongation (%)**	**Electrical conductivity (S/m)**	**Surface area of CNT in composites* (m^2/g)**
Control PAN	4509±160	3.7 ± 0.4	53 ± 9	3.2 ± 1.5	-	-
PAN/SWNT3 (95/5)	974 ± 3	5.6 ± 0.3	77 ± 3	3.9 ± 0.9	88.1 ± 1.9	29
PAN/SWNT3 (90/10)	682 ± 9	6.8 ± 0.7	93 ± 9	4.3 ± 1	243.0 ± 1.3	58
PAN/SWNT3 (80/20)	472 ± 15	9.3 ± 0.7	102 ± 8	3.6± 0.6	5500 ± 30	117
PAN/DWNT (95/5)	1090 ± 55	3.5 ± 0.2	48 ± 15	1.9 ± 0.8	0.006 ± 0.007	28
PAN/DWNT (90/10)	760 ± 2	4.4 ± 0.6	64 ± 10	1.9 ± 0.6	5.9 ± 0.2	56
PAN/VGCNF (95/5)	4852 ± 11	4.4 ± 0.3	80 ± 6	5.5 ± 1.6	0.7 ± 0.6	2
PAN/VGCNF (90/10)	3552 ± 34	4.1 ± 0.3	73 ± 6	3.7 ± 0.5	35.2 ± 11.7	4
PAN/VGCNF (80/20)	2488 ± 69	4.0 ± 0.2	59 ±34	2.5 ± 0.3	88.8 ± 18.6	8

*CNT surface area was determined based on their weight fraction and the BET surface area values in Chapter 4.

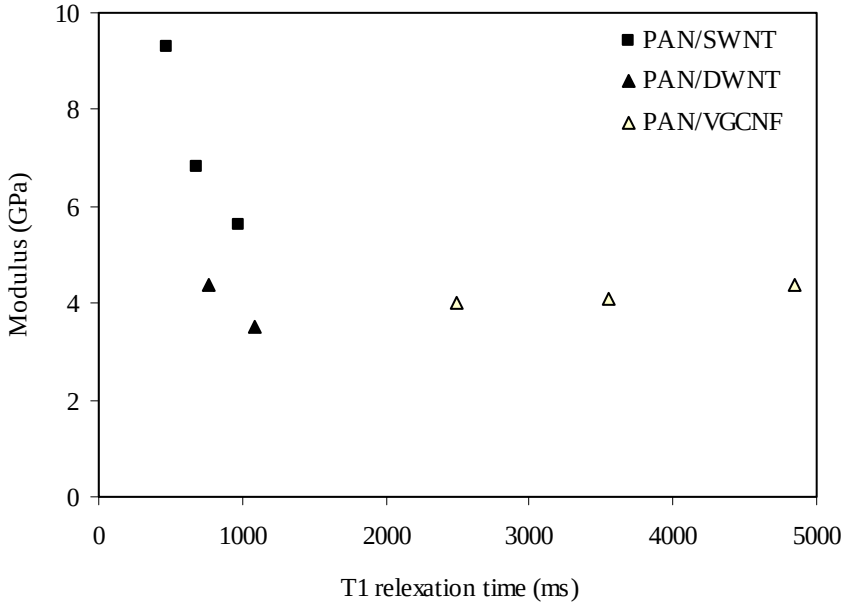

Figure 5.5 Modulus as a function of relaxation time (T_1) for PAN/CNT composite films.

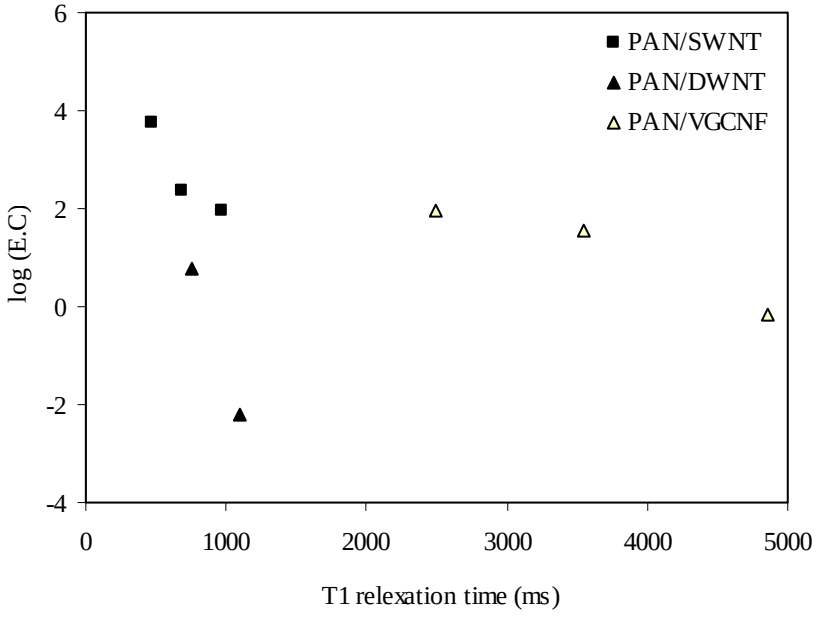

Figure 5.6. Electrical conductivity (E.C.) as a function of relaxation time (T_1) for PAN/CNT composite films.

The electrical conductivity for each series of PAN/CNT composite films increases with decreasing T_1 values. The modulus for the PAN/SWNT and PAN/DWNT composite films increase with decreasing T_1, however the modulus of PAN/VGCNF composite film have no significant change with increasing T_1. The improved modulus, strength and electrical conductivity for various PAN/CNT composite films indicate good dispersion of nanotube in polymer matrix, resulting in the reduction in T_1 values. T_1 values for the PAN/VGCNF (95/5) composites are moderately higher than that for the control PAN and needs further investigation. Presence of paramagnetic impurities such as oxygen, as well as sonication resulting in reduced molecular weight polymer may contribute to this effect. Based on the CNT surface area determined using nitrogen gas adsorption, the surface area of nanotubes based on 5, 10 and 20 wt% loading in the composites is calculated and listed in Table 5.3. Polymer relaxation times (T_l) for various films are plotted as a function of nanotube surface area in the composites (Figure 5.7). As expected, relaxation time for the PAN/CNT composite films decreases with increasing nanotube surface area.

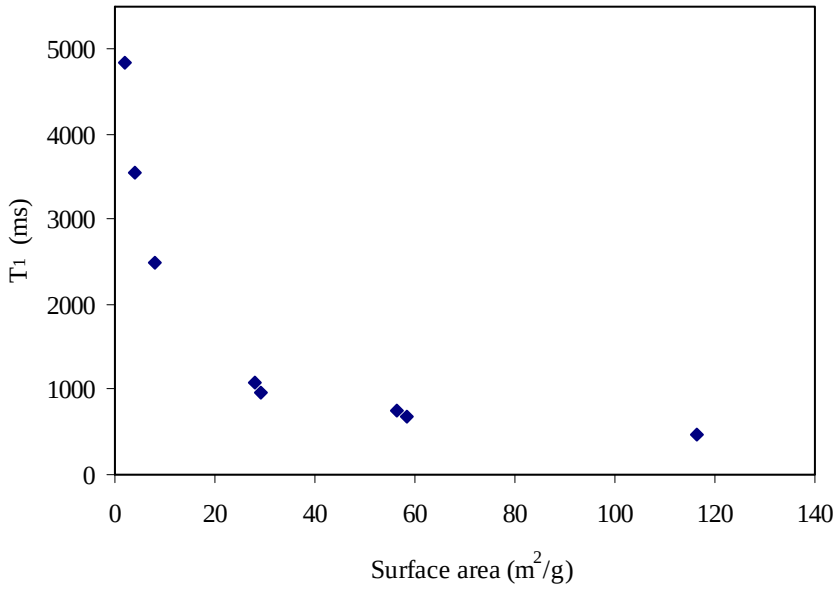

Figure 5.7. Polymer relaxation time (T_1) as a function of nanotube surface area in PAN/CNT composite films. Nanotube surface area was determined based on the nanotube weight fraction and the BET surface area values in Chapter 4.

5.4 CONCLUSIONS

Relaxation times (T_1) for various PAN/CNT films and fibers have been determined using solid state ^{1}H NMR. In general, T_1 values for the composite samples exhibit good correlation with modulus, electrical conductivity, and nanotube surface area. While the presence of metal impurity, metallic nanotubes, as well as other paramagnetic impurities contributes to some ambiguity, the correlation of relaxation times with various properties does suggest the potential of solid state ^{1}H NMR as a useful tool for characterizing the polymer - filler interface.

5.5 REFERENCES

[1] D. L. VanderHart, A. Asano, and J. W. Gilman, Chemistry of Materials **13**, 3781 (2001).

[2] D. L. Vanderhart, A. Asano, and J. W. Gilman, Chemistry of Materials **13**, 3796 (2001).

[3] D. L. VanderHart, A. Asano, and J. W. Gilman, Macromolecules **34**, 3819 (2001).

[4] J. W. Gilman, S. Bourbigot, J. R. Shields, M. Nyden, T. Kashiwagi, R. D. Davis, D. L. Vanderhart, W. Demory, C. A. Wilkie, A. B. Morgan, J. Harris, and R. E. Lyon, Journal of Materials Science **38**, 4451 (2003).

[5] S. Bourbigot, D. L. Vanderhart, J. W. Gilman, W. H. Awad, R. D. Davis, A. B. Morgan, and C. A. Wilkie, Journal of Polymer Science Part B-Polymer Physics **41**, 3188 (2003).

[6] J. P. Hornak, The Basic of NMR, www.cis.rit.edu/htbooks/nmr/inside.htm, Charpter V (1961).

[7] C. Goze-Bac, S. Latil, P. Lauginie, V. Jourdain, J. Conard, L. Duclaux, A. Rubio, and P. Bernier, Carbon **40**, 1825 (2002).

[8] A. Abragam, The Principles of Nuclear Magnetism , Oxford University Press, London, Charpter V (1961).

[9] http://www.chem.queensu.ca/FACILITIES/NMR/nmr/webcourse/.

[10] X. P. Tang, A. Kleinhammes, H. Shimoda, L. Fleming, K. Y. Bennoune, S. Sinha, C. Bower, O. Zhou, and Y. Wu, Science **288**, 492 (2000).

[11] S. Latil, L. Henrard, C. G. Bac, P. Bernier, and A. Rubio, Physical Review Letters **86**, 3160 (2001).

[12] J. Leisen, H. Guo, J. Liu, T. Liu, T. V. Sreekumar, and S. Kumar, Submmited to Nanoscience.

[13] J. Liang, "Single Wall Carbon Nanotube/Polyacrylonitrile Composite Fiber", Master Thesis, Georgia Institute of Technology (2004).

[14] H. G. Chae, T. V. Sreekumar, T. Uchida, and S. Kumar, Polymer **46**, 10925 (2005).

[15] J. Liu, A. G. Rinzler, H. J. Dai, J. H. Hafner, R. K. Bradley, P. J. Boul, A. Lu, T. Iverson, K. Shelimov, C. B. Huffman, F. Rodriguez-Macias, Y. S. Shon, T. R. Lee, D. T. Colbert, and R. E. Smalley, Science **280**, 1253 (1998).

[16] M. Zhang, M. Yudasaka, and S. Iijima, Journal of Physical Chemistry B **108**, 149 (2004).

[17] A. Kuznetsova, D. B. Mawhinney, V. Naumenko, J. T. Yates, J. Liu, and R. E. Smalley, Chemical Physics Letters **321**, 292 (2000).

[18] D. K. Yang and D. B. Zax, Journal of Chemical Physics **110**, 5325 (1999).

CHAPTER 6

ANISOTROPIC OPTICAL PROPERTIES OF SINGLE WALL CARBON NANOTUBES IN THE INFRARED RANGE

6.1 INTRODUCTION

The optical properties of carbon nanotubes (CNTs) have been studied both theoretically and experimentally.[4-16] Theoretically, Ajiki and Ando[1] predicted the low-energy optical absorption of CNTs due to the Aharonov-Bohm effect and found the suppressed optical absorption when the polarization light was perpendicular to the nanobube axis due to the depolarization effect. Mintmire and White[2] calculated the optical absorption spectra of several selected isolated SWNTs and observed anisotropy in the imaginary parts of the dielectric response using a first-principles, all-electron Gaussian-orbital-based local-density-functional approach. Extended Su-Schrieffer Heeger (SSH) model with the Coulomb interaction included has been used to study the optical-absorption spectra for the armchair tubes[3]. Based on the tight-binding model, TasaKi et al.[4] investigated in detail the anisotropy in the dielectric function of CNTs and predicted the optical rotatory power, circular dichroism and optical activity of the nanotubes. Using the line group symmetry approach, anisotropic absorption[5] and polarized optical conductivity tensor[6, 7] have been calculated for the isolated CNTs. By a dipole-dipole interaction, Jensen et al[8] calculated the static and frequency-dependent polarizability tensor of (5, 5) and (9, 0) SWNTs. The symmetry and intramolecular geometry of the tubes was found to have significant influence on its polarizability. Lin and Shung[9] have

investigated the frequency dependence of the dielectric function, loss function and reflectance of SWNT bundles using the gradient approximation. The optical properties of SWNTs are independent on their chiral angle and diameter, however, are influenced strongly by the light polarization direction.[9] A prominent plasmon in the calculated electron-energy-loss spectrum and a weak but sharp plasmon edge in the reflectance spectrum are observed at ~ 6 eV.

Experimentally, optical properties of carbon nanotube have been investigated by the optical elliposometry[10], by the reflectivity measurements[11] or by the photothermal deflection spectroscopy (PDS)[12]. The measured dielectric function of aligned SWNT film indicates the intrinsic anisotropic behavior of tubes reflecting difference in the dielectric function for light polarized parallel and perpendicular to the tubes[10, 11]. A sharp absorption band at 0.68 eV, slight broad band at 1.2 eV and rather broad band at 1.7 eV are observed in the optical absorption spectra of SWNT films from infrared to visible region[12]. The first and second lowest peaks are due to optical transition in the semiconducting nanotubes and the third is due to metallic nanotubes. From the measured reflectance and transmittance of PMMA/SWNT (99/1) composite fiber, the polarized absorption coefficient of SWNT in 1.5-2.5 eV region was calculated[13]. Jiang et al.[14] constructed a carbon nanotube polarizer by parallel alignment of nanotube yarns and investigated the anisotropic properties of yarns in the ultraviolet range. The polarization degree of the nanotube yarns were determined to be 0.92.

Although the transition band of semiconducting SWNTs appears in the infrared region, few measurements of polarized absorption spectra in the infrared region have been conducted. By measuring the reflectance of free-standing SWNT film over 15-5000

cm^{-1}, Ugawa et al.[15] determined the real parts of dielectric function by a Kramers-Kronig analysis. The low-energy absorption band was observed in the optical conductivity at 135 cm^{-1} due to a pseudogap in bundled armchair nanotubes and due to the small-gap in 13-15 Å diameter nanotubes. Ichida et al.[16] processed aligned SWNT/polystyrene composites using mechanical stretching and measured the polarized absorption spectra in the infrared region. The absorbance decreases with the increasing angle between the polarization light and the nanotube axis and shows a maximum when polarization light is parallel to the nanobube axis. Sreekumar at al.[17] observed the anisotropic behavior of SWNT in the PAN/SWNT (99/1) using the polarized infrared spectroscopy. In this chapter, the polarized infrared spectra of PAN/SWNT composite fibers were measured. This data is used for determining the intrinsic anisotropic optical constants of SWNTs.

6.2 EXPERIMENTAL

PAN (viscosity average molecular weight is 2.5×10^5 g/mol) obtained from Exlan, Co. (Japan) and dimethyl formamide (DMF) obtained from Sigma–Aldrich, Co. were used as received. Purified SWNTs were obtained from Carbon Nanotechnologies, Inc. (Houston, TX). The metallic impurity in SWNTs was about 1 wt% determined from the thermogravimetric analysis (TGA) result. Dried SWNTs were dispersed in DMF (at a concentration of 40 mg/L) by sonication in a sonic bath (Branson 3510R-MT, 100 W, 42 kHz) for 24 hour. Homogenous dispersion of SWNT in DMF was confirmed by optical microscopy. Dried PAN (15 g) was dissolved separately in DMF (100 mL) at 80 °C and the SWNT/DMF dispersion was subsequently added to the PAN/DMF solution. The PAN/SWNT/DMF dispersion was stirred and excess solvent was

evaporated by vacuum distillation at 80 °C to obtain the desired solution concentration (15 g solids (PAN+SWNT)/100 mL DMF). Following the above procedure, various PAN/SWNT/DMF solutions were prepared to produce SWNT concentration of 0, 0.5, and 1 wt%. The PAN/DMF and PAN/SWNT/DMF solutions were gel-spun using a 500 μm diameter single-hole spinneret (110 °C) into a methanol bath (−50 °C) to obtain the PAN/SWNT fibers. The air gap between spinneret and the methanol bath was about 2 cm and the spun speed was 31.4 m/min. The as-spun fibers were taken up at 100 m/min and were immersed in methanol bath (−20 ~ −40 °C) for 1 week in order to gel. The spun fiber draw ratio was 3.2. The gel fiber was further drawn at 160 °C in glycerol bath, washed in ethanol and vacuum dried at 40 °C for 3 days. The total draw ratio was as high as 51. The gel-spun fibers were provided by Han Gi Chae. Structure and properties of these fibers have been reported (Polymer 2006).[18]

Transmission infrared spectra of the PAN/SWNT composite fibers were measured using a Perkin Elmer FTIR microscope with the polarization direction of the incident infrared beam parallel and perpendicular to the fiber axis. For the collection of the infrared spectra of the PAN/ SWNT composite fibers, a single filament was immersed in the mineral oil in order to reduce the surface scattering.

Raman spectra of PAN and PAN/SWNT composite fibers were collected using Holoprobe Research 785 Raman Microscope made by Kaiser Optical System with 785 nm excitation laser with polarizer and analyzer parallel to each other. A series of Raman spectra were measured with the fiber axis at 0, 5, 10, 20, 30, 40, 50, 60, 70, 80, 85, and 90° from the polarization direction. From the peak intensity of the tangential

band (ca. 1590 cm^{-1}) at various polarization angles, the SWNT orientation in the composite fiber was determined.

6.3 RESULTS AND DISCUSSION

6.3.1 Polarized Infrared Spectra

The polarized infrared spectra of control PAN, PAN/SWNT (0.5 wt% SWNT) and PAN/SWNT (1 wt% SWNT) composite fibers, with the infrared beam parallel and perpendicular to the fiber axis, are shown in the Figure 6.1. The baselines of the polarized spectra for control PAN fiber almost overlap when the incident beam is polarized along and normal to the fiber axis. However, the significant absorption differences in baselines of the spectra for PAN/SWNT composite fibers were observed when the beam was polarized parallel and perpendicular to the fiber axis. These absorption differences in the PAN/SWNT composite fibers are due to the presence of the intrinsically anisotropic SWNTs orientated in the composite fibers. The PAN/SWNT composite fibers shows higher absorption when the incident light is parallel to the tube axis. For PAN/SWNT composite fibers with higher SWNT loading, the baseline absorbance is higher especially when the polarization light is parallel to the fiber axis.

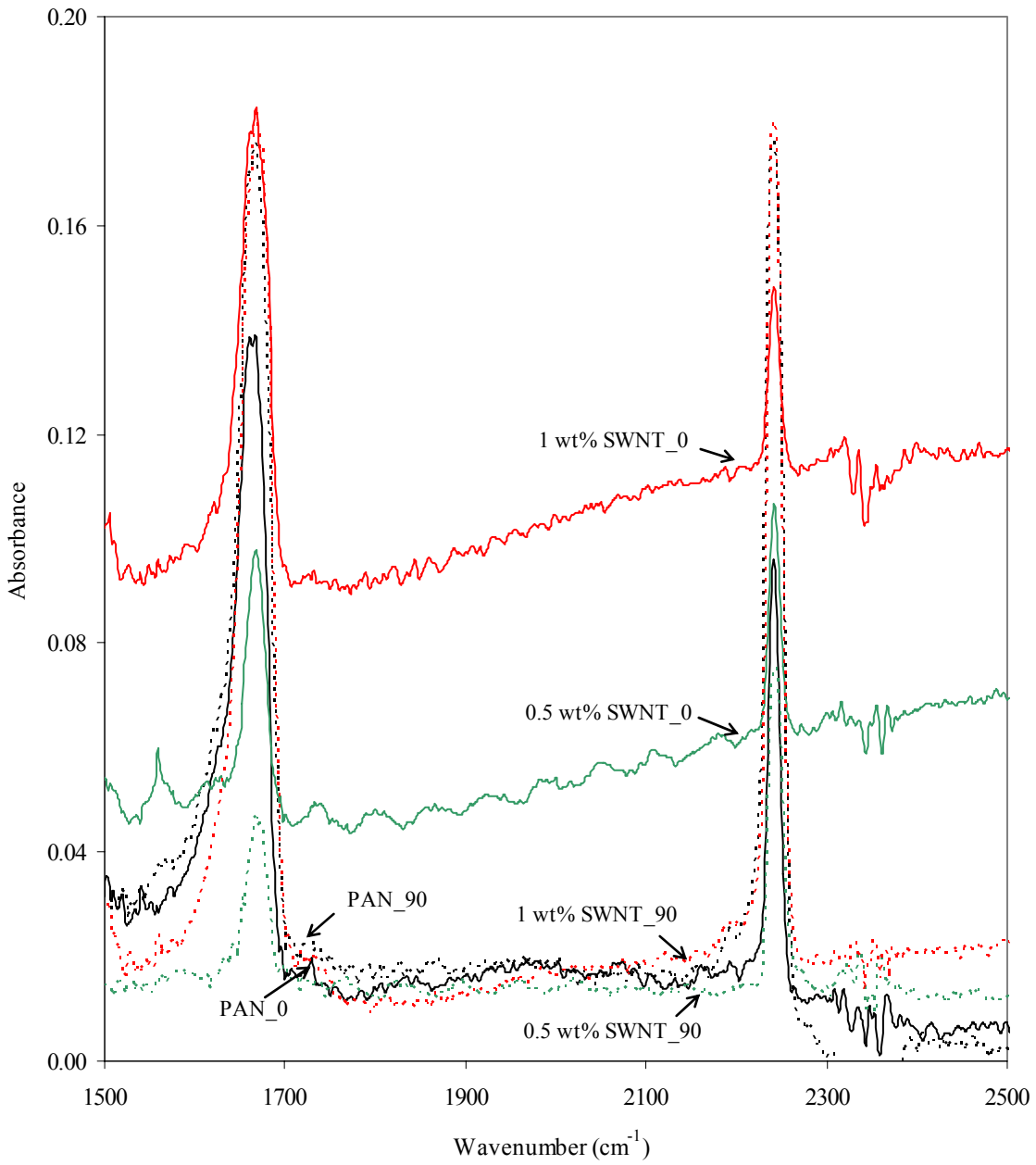

Figure 6.1. Absorbance spectra for the control PAN and PAN/SWNT composite fibers containing 0.5 and 1 wt% SWNT in the infrared region over 1500-2500 cm^{-1} when the beam is polarized parallel (SWNT_0) and perpendicular (SWNT_90) to the fiber axis.

6.3.2 Optical Constants

The optical properties of a material can be characterized by a complex refractive index ($\tilde{n}$) or a complex dielectric constant (ε)[19]:

$$\tilde{n} = n + ki \tag{6.1}$$

$$\varepsilon = \tilde{n}^2 = \varepsilon_{Re} + \varepsilon_{Im} = n^2 - k^2 + 2nki \tag{6.2}$$

where n is the refractive index, k is the extinction coefficient, n is the refractive index, ε_{Re} is the real part of the complex dielectric constant, and ε_{Im} is the imaginary part of the complex dielectric constant. From Equation (6.2), the extinction coefficient k the refractive index n, and the real and imaginary parts of the complex dielectric constant are obtained:

$$k = \sqrt{\frac{\sqrt{\varepsilon_{Re}^2 + \varepsilon_{Im}^2} - \varepsilon_{Re}}{2}} \tag{6.3}$$

$$n = \sqrt{\frac{\sqrt{\varepsilon_{Re}^2 + \varepsilon_{Im}^2} + \varepsilon_{Re}}{2}} \tag{6.4}$$

$$\varepsilon_{Re} = n^2 - k^2 \tag{6.5}$$

$$\varepsilon_{Im} = 2nk \tag{6.6}$$

At a wavelength λ, the absorbance (A), and reflectance (R) of a sample with thickness d are related by equations as follows[19]:

$$k = A\lambda/(4\pi d) \tag{6.7}$$

$$R = \frac{(n-1)^2 + k^2}{(n+1)^2 + k^2} \tag{6.8}$$

From the measured absorbance spectra for the control PAN fiber, the extinction coefficient $(k)_{\mathrm{h}}^{\mathrm{exp.}}$ of PAN was calculated from Equation (6.7). Figure 6.2 shows plots of the refractive index $(\mathrm{n})^{20}$ and the calculated extinction coefficient (k) as a function of wavenumber. From $(k)_{\mathrm{h}}^{\mathrm{exp.}}$ and the reported refractive index[20], the real and imaginary parts of the dielectric constant $(\varepsilon)_{\mathrm{h}}^{\mathrm{exp.}}$ of PAN were determined and plotted as a function of wavenumber as shown in Figure 6.3.

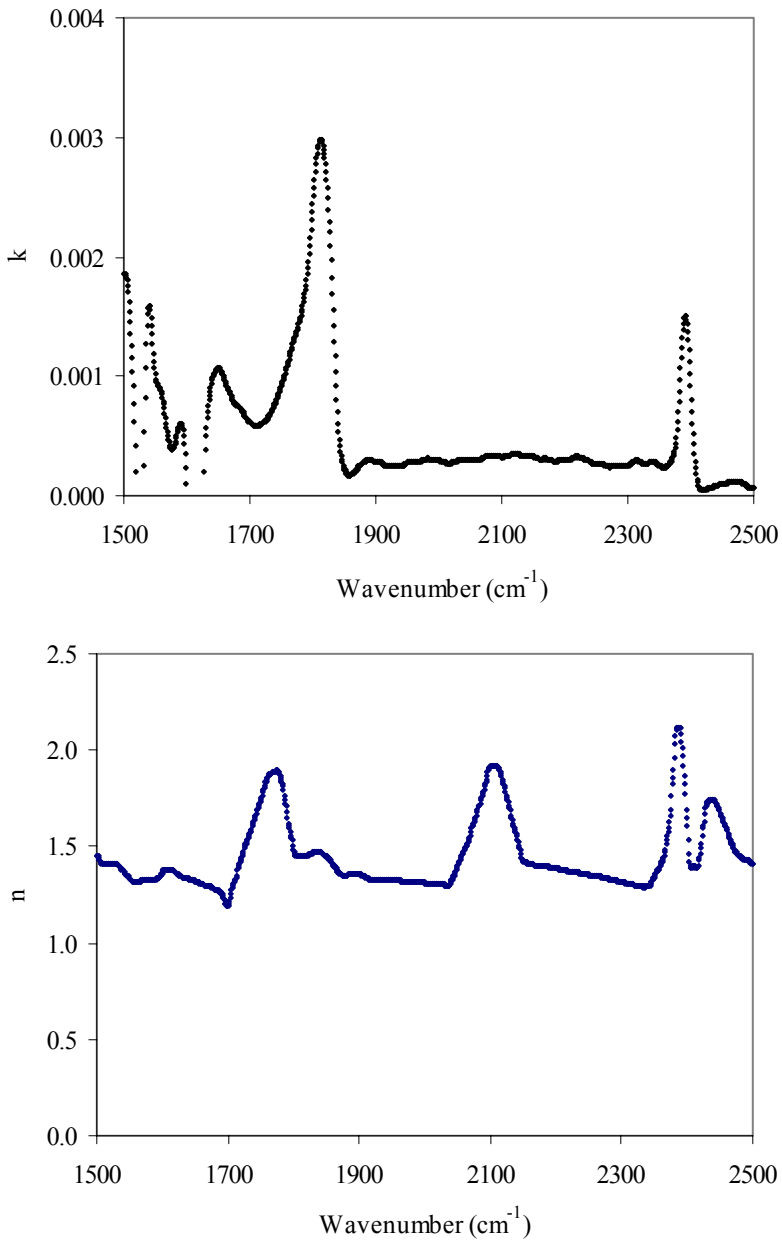

Figure 6.2. Extinction coefficient k (top) and refractive index n (bottom) [20] of PAN. Extinction coefficient was calculated in this work using the data on control PAN fiber.

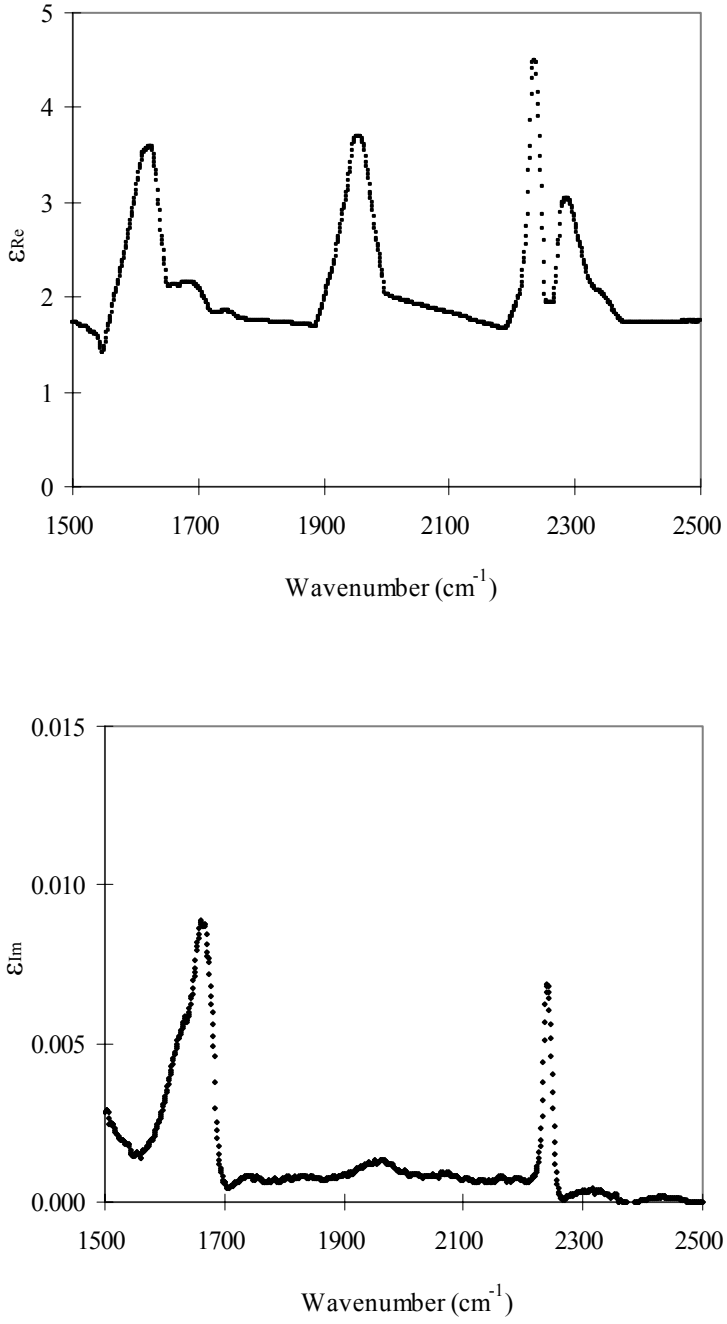

Figure 6.3. Real part (top) and imaginary part (bottom) of the dielectric constant of PAN.

6.3.3 Effective Medium Theories

Effective medium theories are used to determine the optical constants of composites when electromagnetic (EM) waves propagate into a media.[21-26] If the nanotube length is assumed to be infinite, Mossotti-Clausius formalism can be used to calculate the effective permittivity and polarizability of nanobubes randomly dispersed in an isotropic dielectric host[21]. Maxwell Garnet (MG) approximation [22] is one of the most widely used methods for calculating the bulk dielectric function for a composite system consisting of a anisotropic inclusions with finite length and a isotropic host. MG model can be applied for polarizable spherical particles and cylindrical particles embedded in dielectric host. MG approach works very well in the dilute limit for dielectric media where the distance between the tubes is so large that electromagnetic interaction between nanotubes is negligible. When nanotubes are close packed, the full electromagnetic coupling between the nanotubes should be considered in order to determine the optical properties of carbon nanotubes[23]. In a media with tensor-like dielectric function, the effective dielectric function of multi wall carbon nanotube was calculated accurately by solving Maxwell's equations[24, 25]. Anisotropic carbon nanotube is regarded as an electrically small particle in the infrared and microwave frequency range, because a nanotube is several microns in length and its cross sectional diameter range between 1 and 20 nm[26]. The optical behavior of polymer/SWNT composites not only depend on particle shape and SWNT loading, but also on the orientation distribution of SWNT in the bulk sample. Ohad[27] introduced a an extended MG approximation theory which provide the relationship between the particle properties, orientation distribution, field-induced birefringence and electro-optical phase shift.

For the PAN/SWNT composite fibers, the isotropic PAN is assumed to contain a scalar dielectric constant. The anisotropic SWNT are assumed to be with a dielectric tensor ε_{SWNT}:

$$\varepsilon_{SWNT} = \begin{pmatrix} \varepsilon_{\perp} & 0 & 0 \\ 0 & \varepsilon_{\perp} & 0 \\ 0 & 0 & \varepsilon_{\parallel} \end{pmatrix}$$

The external field is applied in the fiber direction (Z axis). The applied field will not cause the distribution change of the azimuthal angle φ, however, the polar orientation angle will decrease when the field is increased. The PAN/SWNT composites are regarded as the uniaxial materials, where the dielectric coefficient has one value along one preferred direction and another value in all perpendicular directions. The effective dielectric tensor of the PAN/SWNT composites, $\varepsilon_{eff,}$ can be written as:

$$\varepsilon_{eff} = \varepsilon_h I + \frac{f\langle\tilde{\alpha}\rangle}{1 - f + f\langle\tilde{K}\rangle} \tag{6.9}$$

where I is the unite matrix, f is the volume fraction of SWNT in the PAN/SWNT composites, and ε_h is the dielectric constant of host. The average tensor of $\langle\tilde{K}\rangle$ and $\langle\tilde{\alpha}\rangle$ along X axis, Y axis and Z axis can be expressed as

$$\langle\tilde{K}\rangle_{xx} = \langle\tilde{K}\rangle_{yy} = \frac{1}{2}[k_{\parallel}^{swnt} + k_{\perp}^{swnt} - (k_{\parallel}^{swnt} - k_{\perp}^{swnt})\langle\cos^2\theta\rangle] \tag{6.10}$$

$$\langle\tilde{K}\rangle_{zz} = k_{\perp}^{swnt} + (k_{\parallel}^{swnt} - k_{\perp}^{swnt})\langle\cos^2\theta\rangle \tag{6.11}$$

$$\langle\tilde{\alpha}\rangle_{xx} = \langle\tilde{\alpha}\rangle_{yy} = \frac{1}{2}[\alpha_{\parallel}^{swnt} + \alpha_{\perp}^{swnt} - (\alpha_{\parallel}^{swnt} - \alpha_{\perp}^{swnt})\langle\cos^2\theta\rangle] \tag{6.12}$$

$$\langle\tilde{\alpha}\rangle_{zz} = \alpha_{\perp}^{swnt} + (\alpha_{\parallel}^{swnt} - \alpha_{\perp}^{swnt})\langle\cos^2\theta\rangle \tag{6.13}$$

$k_{\parallel}^{swnt}$ and $k_{\perp}^{swnt}$ are the extinction coefficient of SWNT when polarization light is parallel and perpendicular to Z axis, respectively. $\alpha_{\perp}^{swnt}$ and $\alpha_{\parallel}^{swnt}$ are the polarizability per volume of SWNT when polarization light is parallel and perpendicular to Z axis, respectively. The tensor k^{swnt} and α^{swnt} can be determined from the following equations:

$$k_{\parallel}^{swnt} = \frac{\varepsilon_h}{d_{\parallel}\varepsilon_{\parallel}^{swnt} + (1-d_{\parallel})\varepsilon_h} \tag{6.14}$$

$$k_{\perp}^{swnt} = \frac{\varepsilon_h}{d_{\perp}\varepsilon_{\perp}^{swnt} + (1-d_{\perp})\varepsilon_h} \tag{6.15}$$

$$\alpha_{\parallel}^{swnt} = k_{\parallel}^{swnt}(\varepsilon_{\parallel}^{swnt} - \varepsilon_h) \tag{6.16}$$

$$\alpha_{\perp}^{swnt} = k_{\perp}^{swnt}(\varepsilon_{\perp}^{swnt} - \varepsilon_h) \tag{6.17}$$

where θ is the polar orientation angle of SWNT in the composite sample, S is the Herman's orientation factor, $\varepsilon_{\parallel}^{swnt}$ and $\varepsilon_{\perp}^{swnt}$ are the dielectric constant of SWNT when polarization light is parallel and perpendicular to Z axis, respectively, $d_{\parallel}$ is the depolarization factor and equal to 0 when the polarized light is parallel to the Z axis[23], and $d_{\perp}$ is the depolarization factor and equal to 0.5 when the polarized light is perpendicular to Z axis[23]. Absorbance of the PAN/SWNT composite fibers with polarization direction parallel to fiber axis, $(A_{\parallel})_{comp.}^{exp.}$, and that of the composite fibers with polarization direction perpendicular to fiber axis $(A_{\perp})_{comp.}^{exp.}$ were measured by the polarized infrared spectroscopy. Herman's orientation factors of SWNT in the composite fibers were measured by Raman spectroscopy and determined to 0.915.[18] According to Equation (6.6), the experimental extinction coefficient of the composite fibers with

polarization direction parallel and perpendicular to fiber axis can be determined, which are expressed as $(k_{\parallel})_{\text{comp.}}^{\text{exp.}}$ and $(k_{\perp})_{\text{comp.}}^{\text{exp.}}$, respectively. Assume a set of theoretical dielectric constants of SWNT ($\varepsilon_{\parallel}^{swnt}$ and $\varepsilon_{\perp}^{swnt}$), the theoretical extinction coefficients of the composite fiber ($(k_{\parallel})_{\text{comp.}}^{\text{theo.}}$ and $(k_{\perp})_{\text{comp.}}^{\text{theo.}}$) are calculated from Equation (6.10) to Equation (6.18) and Equation (6.3). Minimizing $\left|(k)_{\text{comp.}}^{\text{theo.}} - (k)_{\text{comp.}}^{\text{exp.}}\right|$, the dielectric constants of SWNT, $\varepsilon_{\parallel}^{\text{swnt}}$ and $\varepsilon_{\perp}^{\text{swnt}}$, can be finally determined. Figure 6.4 shows the real part (top) and imaginary part (bottom) of the dielectric constant of SWNT, which have been calculated based on the extended MG theory and the measured spectra for the composite fibers. When the incident light is polarized along the fiber axis, dielectric constant of SWNT is larger than that when light is polarized normal to the fiber axis, indicating the anistropic optical property of SWNTs in the infrared range. Furthermore, the extinction coefficient k of SWNT was calculated according to the Equation (6.3) and is shown in Figure 6.5 indicating the anisotropic properties.

MG approximation is based on the assumption that the polymer host matrix is isotropic. Although in the current system, PAN matrix is not isotropic, as PAN orientation in PAN/SWNT fibers is about 0.92[18], the infra-red absorption of the PAN matrix in the IR region (excluding the absorption peaks) does not exhibit strong orientation dependence (Figure 6.1). Therefore the anisotropic PAN matrix should not be a major source of error in our analysis. Here we also note that the refractive index of the oriented PAN film parallel and perpendicular to the orientation direction is the same.[28]

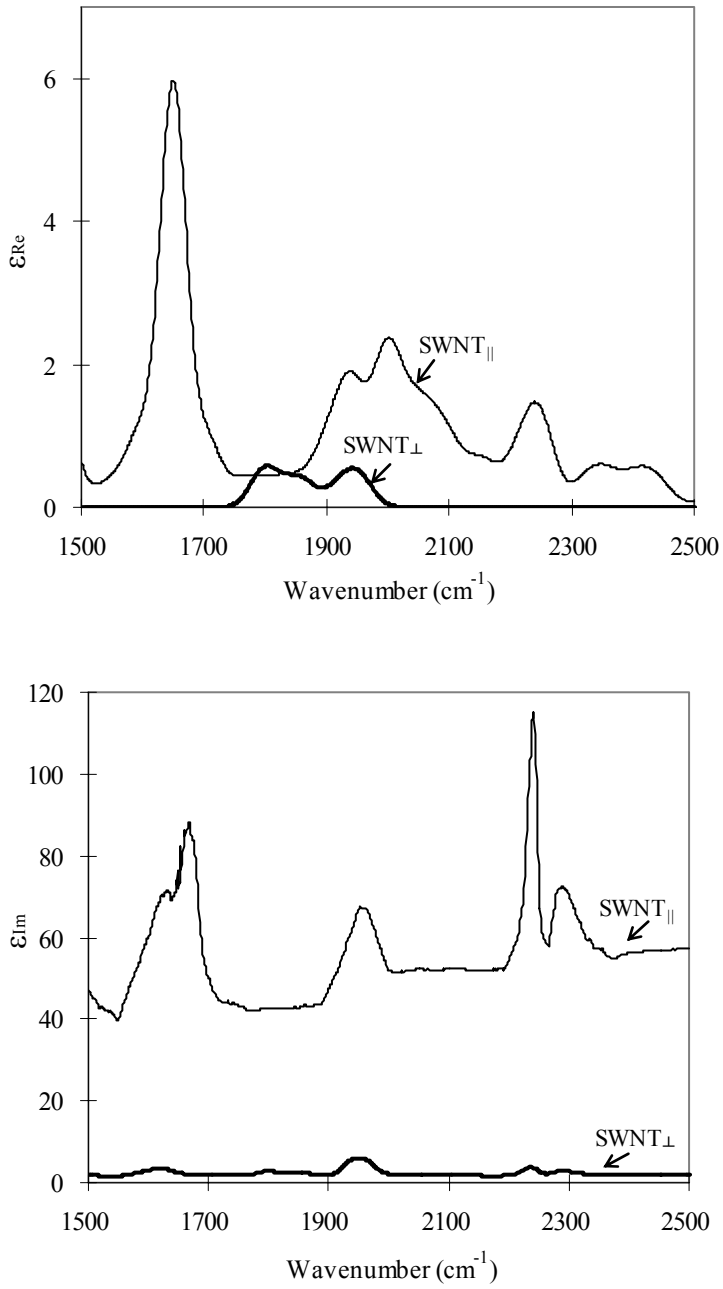

Figure 6.4. Real part (top) and imaginary part (bottom) of the dielectric constant of SWNT calculated from PAN/SWNT composite fiber data.

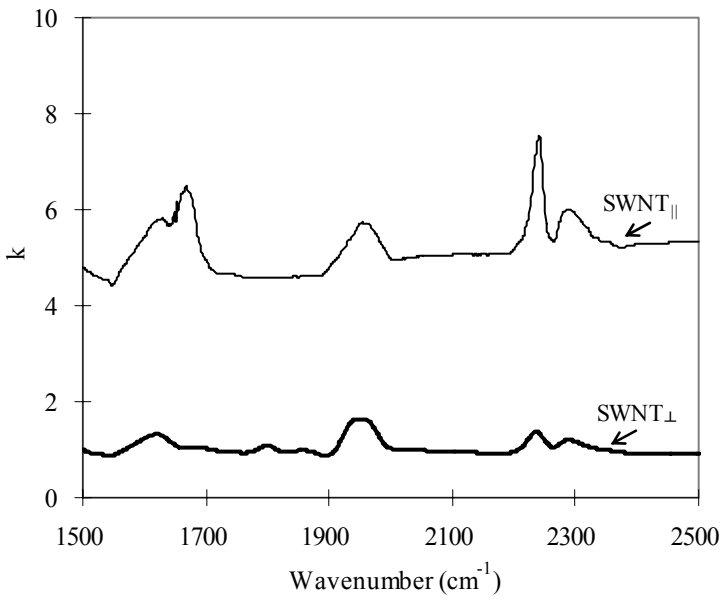

Figure 6.5. Extinction coefficient of SWNT calculated from PAN/SWNT composite fiber data.

The dielectric constant of the randomly aligned SWNT film can be calculated based on Equation (6.19). In this case, the dielectric constant of polymer ε_h is zero, the volume fraction of SWNT is equal to one, and the Herman's orientation factor S is zero. Therefore, Equation (6.9) for the calculation of the dielectric constant ε_{film} of the disordered SWNT film can be modified to Equation (6.19)

$$\varepsilon_{film} = \frac{2k_{\perp}^{swnt}\varepsilon_{\perp}^{swnt} + k_{\parallel}^{swnt}\varepsilon_{\parallel}^{swnt}}{2k_{\perp}^{swnt} + k_{\parallel}^{swnt}} \tag{6.19}$$

Figure 6.6 shows the calculated dielectric constant of the randomly aligned SWNT based on Equation (6.19). The real part of the calculated dielectric constant is comparable to value reported in the literature[15], except a peak at ~1665 cm^{-1}. (Figure 6.6). For comparison, the dielectric constant of graphite[15] is also plotted in Figure 6.6. Dielectric

constant of carbon nanotubes in our study as well as the value reported in the literature represents the average for all nanotubes present in the samples – these include metallic and semi-conducting tubes as well as tubes of different diameter and chirality.

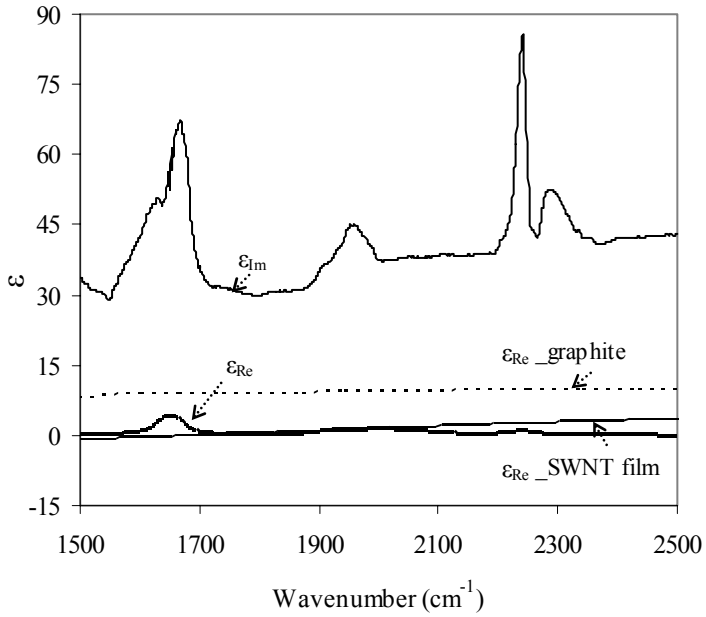

Figure 6.6. Dielectric constants (ε_{Re} and ε_{Im}) for the unoriented SWNT films calculated in the current work. The real part of the dielectric constant of the SWNT film[15] (ε_{Re}_SWNT film) and graphite[29] (ε_{Re}_graphite) obtained from literature are also plotted.

Based on Equation (6.3) and (6.4), the refractive index n and extinction coefficient k of the randomly aligned SWNT is determined, and plotted as a function of frequency in Figure 6.7 and Figure 6.8, respectively. Using graphite dielectric constant data from the literature,[29] we calculated its refractive index and extinction coefficient and compared them with the SWNT values obtained in this work (Figure 6.7 and 6.8.). Ignoring the spurious peaks, primarily resulting from PAN absorption, the SWNT n and k values can be given by the resulting baseline.

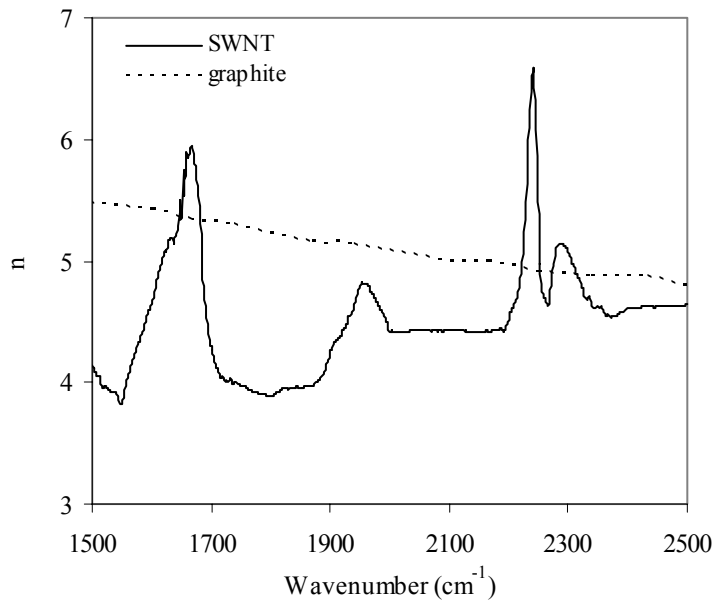

Figure 6.7. Calculated refractive index n of the randomly aligned SWNT. The refractive index of graphite is also given by the dotted line for comparison.

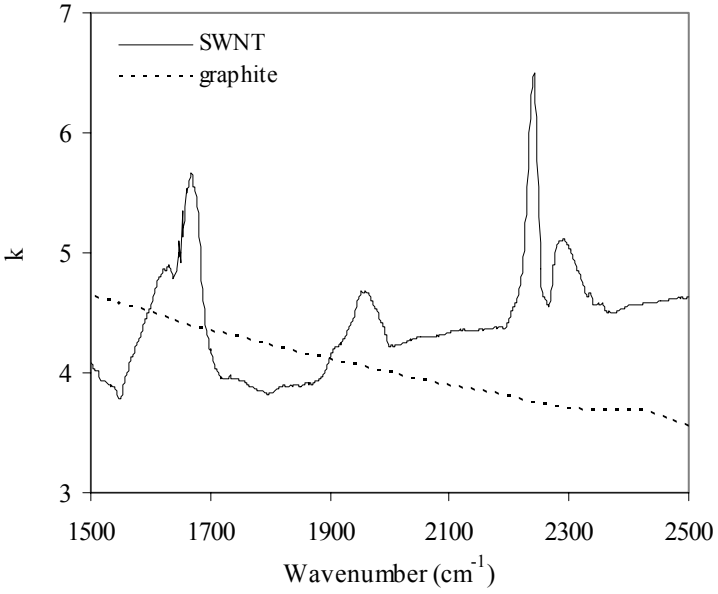

Figure 6.8. Calculated extinction coefficient k of the randomly aligned SWNT. The refractive index of graphite is also given by the dotted line for comparison.

From Equation (6.8), The reflectance R of the unoriented SWNT film is calculated and compared with that of the disorder SWNT film[15] (Figure 6.9). The calculated reflectance of SWNT is higher than that of the SWNT film reported in the literature[15] over 1500-2500 cm^{-1} region. Reflectance in reference 15 is based on the randomly oriented SWNT film containing 30 – 40 % voids. On the other hand, our calculation method gives reflectance for a randomly oriented SWNT film, where 100% of the volume is occupied by the nanotubes. This may at least partially explain why our reflectance values are higher than those reported in reference 15. When Ugawa et al.[15] measured the reflectance of the SWNT film, they normalized the sample spectrum with the spectrum measured after evaporating gold on the sample surface. This procedure is also a potential source of error. We also compared the reflectance of the unoriented SWNT film to that of the graphite. From the dielectric constant[29], reflectance of graphite is calculated and plotted in Figure 6.9. Ignoring spurious peaks, the SWNT reflectance calculated in current work is quite comparable to that of the graphite reflectance.

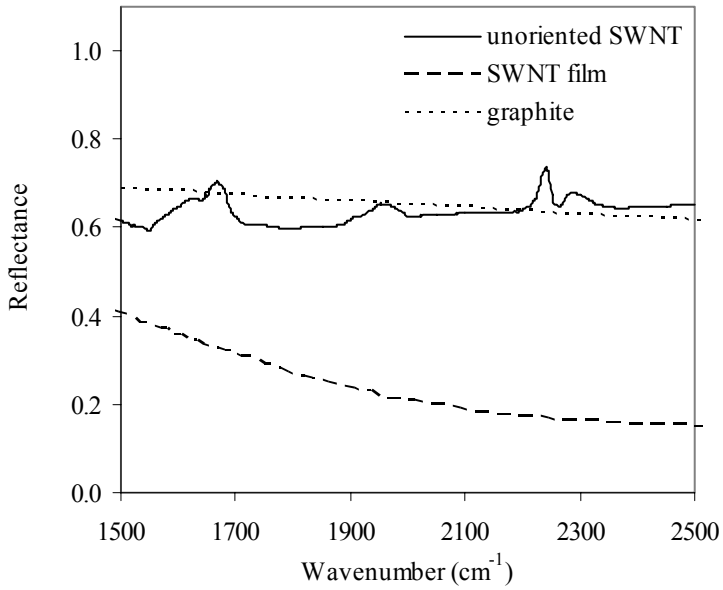

Figure 6.9. Calculated reflectance of the randomly aligned SWNT. Reflectance of the SWNT film[15] and graphite are given by the dashed and dotted line, respectively.

In summary, the optical constants calculated from the experimental data on oriented PAN/SWNT fibers using extended MG theory are reasonable except for a number of spurious peaks, which we believe are a result of PAN absorption. Reflection and surface scattering losses, non-uniform fiber thickness (unless the beam size << the fiber diameter, which was not the case in our study), and accuracy of the PAN optical constants represent potential sources of error.

6.4 CONCLUSIONS

The optical anisotropy of SWNT in PAN/ SWNT composite fibers was observed in their polarized infrared spectra. A method for determining the intrinsic SWNT optical constants has been developed. The SWNT optical constants thus determined have been compared to the literature reported values.

6.5 REFERENCE

[1] H. Ajiki and T. Ando, Physica B **201**, 349 (1994).

[2] J. W. Mintmire and C. T. White, Synthetic Metals **77**, 231 (1996).

[3] J. Jiang, R. H. Xie, J. Ma, and F. Yan, Physics Letters A **231**, 259 (1997).

[4] S. Tasaki, K. Maekawa, and T. Yamabe, Physical Review B **57**, 9301 (1998).

[5] I. Bozovic, N. Bozovic, and M. Damnjanovic, Physical Review B **62**, 6971 (2000).

[6] I. Milosevic, T. Vukovic, S. Dmitrovic, and M. Damnjanovic, Physica E-Low-Dimensional Systems & Nanostructures **12**, 745 (2002).

[7] I. Milosevic, T. Vukovic, S. Dmitrovic, and M. Damnjanovic, Physical Review B **67**, 165418 (2003).

[8] L. Jensen, O. H. Schmidt, K. V. Mikkelsen, and P. O. Astrand, Journal of Physical Chemistry B **104**, 10462 (2000).

[9] M. F. Lin and K. W.-K. Shung, Physical Review B **50**, 17 744 (1994).

[10] W. A. Deheer, W. S. Bacsa, A. Chatelain, T. Gerfin, R. Humphreybaker, L. Forro, and D. Ugarte, Science **268**, 845 (1995).

[11] F. Bommeli, L. Degiorgi, P. Wachter, W. S. Bacsa, W. A. deHeer, and L. Forro, Solid State Communications **99**, 513 (1996).

[12] H. Kataura, Y. Kumazawa, Y. Maniwa, I. Umezu, S. Suzuki, Y. Ohtsuka, and Y. Achiba, Synthetic Metals **103**, 2555 (1999).

[13] J. Hwang, H. H. Gommans, A. Ugawa, H. Tashiro, R. Haggenmueller, K. I. Winey, J. E. Fischer, D. B. Tanner, and A. G. Rinzler, Physical Review B **62**, R13310 (2000).

[14] K. L. Jiang, Q. Q. Li, and S. S. Fan, Nature **419**, 801 (2002).

[15] A. Ugawa, A. G. Rinzler, and D. B. Tanner, Physical Review B **60**, R11305 (1999).

[16] M. Ichida, S. Mizuno, H. Kataura, Y. Achiba, and A. Nakamura, Applied Physics a-Materials Science & Processing **78**, 1117 (2004).

[17] T. V. Sreekumar, T. Liu, B. G. Min, H. Guo, S. Kumar, R. H. Hauge, and R. E. Smalley, Advanced Materials **16**, 58 (2004).

[18] H. G. Chae, M. L. Minus, and S. Kumar, Polymer **47**, 3494 (2006).

[19] M. Fox, Optical Properties of Solids, Oxford University Press, London, pp5 (2001).

[20] C. A. Sergides, A. R. Chughtai, and D. M. Smith, Journal of Polymer Science Part B-Polymer Physics **23**, 1573 (1985).

[21] A. Lakhtakia, G. Y. Slepyan, S. A. Maksimenko, A. V. Gusakov, and O. M. Yevtushenko, Carbon **36**, 1833 (1998).

[22] O. Levy and D. Stroud, Physical Review B **56**, 8035 (1997).

[23] F. J. Garcia-Vidal, J. M. Pitarke, and J. B. Pendry, Physical Review Letters **78**, 4289 (1997).

[24] F. J. Garcia-Vidal and J. M. Pitarke, European Physical Journal B **22**, 257 (2001).

[25] J. M. Pitarke and F. J. Garcia-Vidal, Physical Review B **63**, 073404 (2001).

[26] T. W. Ebbesen, Physics Today **49**, 26 (1996).

[27] O. Levy, Physical Review E **66**, 011404 (2002).

[28] C. J. Henniker, Macromolecules **6**, 514 (1973).

[29] H. R. Philipp, Physical Review B **16**, 2896 (1977).

CHAPTER 7

CONCLUSIONS AND RECOMMENDATIONS

CONCLUSIONS

1. PAN/SWNT composite films containing 40 wt% nanotube have been processed with unique combination of modulus (10.9 GPa), tensile strength (103 MPa), electrical conductivity (1.5×10^{4} S/m), dimensional stability (coefficient of thermal expansion (CTE) 1.7×10^{-6}/°C), low density (1.08 g/cm^3), solvent resistance, and thermal stability. The storage modulus of PAN/SWNT film above glass transition temperature (T_g) is 40 times the PAN storage modulus at that temperature. Rope diameter in the SWNT powder was 26 nm, while in 60/40 PAN/SWNT film, the rope diameter was 40 nm. PAN/SWNT (60/40) film could not be dissolved in DMF even at 130 ºC. After heating the film at this temperature, only about 40 wt% of the PAN could be removed. This suggests that the remainder of the PAN has strong interaction with single wall carbon nanotubes and can not be dissolved in its solvent (DMF). Wide angle X-ray diffraction study suggests that PAN intercalates SWNT bundles.

2. At 5 wt% VGCNF loading, the tensile modulus and strength of the PAN/VGCNF composite film is 1.2 and 1.5 times the modulus and strength of the control PAN film, respectively. Specific modulus of the composites containing up to 20% VGCNF was consistent with the predictions of the Halpin-Tsai theory. Electrical conductivity of composites increased with the nano fiber loading and exhibited a two dimensional percolation behavior at 3.1 vol%. The storage modulus of PAN is enhanced by incorporation of nano fibers, particularly above the glass transition temperature. The

tan δ peak shifts to and broadens toward higher temperatures with the addition of VGCNF. Activation energy values needed for PAN glass transition motion in the composite films are higher than those in the control PAN film. The coating of PAN polymer around VGCNFs was observed.

3. Among various CNT composites, the PAN/SWNT3 composite films exhibit the highest enhancement in modulus, tensile strength, and highest electrical conductivity (modulus and tensile strength increased by a factor of 2.5 and 1.8, respectively at 10 wt% loading). In general, for all nanotube composites, tensile modulus and tensile strength exhibited good correlation with nanotube surface area. However, other factors such as catalytic impurity, amorphous carbon etc. also play a role in governing various composite properties.

4. Enhancement in storage modulus for all PAN/CNT composite films is observed especially above glass transition temperature. The highest increase in storage modulus above T_g is observed for PAN/SWNT3 composite films (increased 14 times at 5 % loading and 28 times at 10 % loading at 140 ^oC). The magnitude of the Tan δ peak decreased and shifted to higher temperature for all PAN/CNT composite films.

5. All PAN/CNT composite films exhibit reduced thermal expansion as compared to the control PAN film. PAN/SWNT3 composite films show the least thermal expansion (~90 % reduction in CTE at 20 wt% loading).

6. Based on the PAN/CNT solubility in DMF, it was shown that PAN-SWNT exhibit stronger interaction, than PAN-DWNT, PAN-MWNT, and PAN-VGCNF.

7. Solid state ^{1}H NMR is a useful tool for characterizing the polymer - filler interface. T_1 values for the composite samples exhibit good correlation with the carbon nanotube surface area.

8. The optical anisotropy of SWNT in PAN/ SWNT composite fibers was observed in their polarized infrared spectra. A method for determining the intrinsic SWNT optical constants has been developed and demonstrated.

RECOMMENDATIONS FOR FUTURE WORK

Several results reported here need further investigation. Some suggestions for future work are listed below:

1. G' band in the Raman spectra is used to detect the load transfer between polymer and nanotube. Considering the trends in tensile and dynamic mechanical and thermal properties, we expected larger shift in G' band peak position for PAN/SWNT3 composites. However, no shift is observed for PAN/SWNT3 composites. The explanation for this result needs more investigation.

2. Although the surface area of VGCNF is low, the mechanical proprieties of PAN/VGNCF composites are enhanced possibly due to its long length. Electrical conductivity of polymer/CNT composite depends on nanotube diameter and length. Measurement of nanotube length may provide further support to observed PAN/CNT composite properties.

3. We have prepared a series of PAN/CNT composite films using various CNTs. Based on the properties reported in this thesis, potential applications of these films may be investigated.

APPENDIX A

TABLES AND FIGURES FOR PAN/CNT COMPOSITE FILMS

Table A.1. Pore volume and surface area of various SWNTs using BET and DFT method

		SWNT 1	SWNT 2	SWNT3	SWNT4	SWNT 5
Surface area	Micropore(%)	37.6	43.0	47.4	54.5	60.1
	Mesopore(%)	34.6	39.5	34.5	31.0	21.1
	Macropore(%)	27.9	17.5	18.2	14.5	18.8
Pore volume	Micropore(%)	4.1	8.9	9.0	14.0	9.1
	Mesopore(%)	18.4	34.0	21.8	28.7	13.5
	Macropore(%)	77.5	57.1	69.2	57.3	77.5
Surface area (m^2/g)	BET method	582.9	829.7	795.0	823.5	433.9
	DFT method	238.7	333.5	273.7	337.2	206.8

Table A.2. Pore volume and surface area of various CNTs using BET and DFT method

		DWNT	MWNT	VGCNF
Surface area	Micropore(%)	34.2	36.8	37.0
	Mesopore(%)	41.6	27.9	31.4
	Macropore(%)	24.3	35.3	31.6
Pore volume	Micropore(%)	4.5	2.6	2.5
	Mesopore(%)	26.4	10.1	10.0
	Macropore(%)	69.1	87.3	87.5
Surface area (m^2/g)	BET method	563.3	160.7	40.6
	DFT method	290.2	81.8	23.3

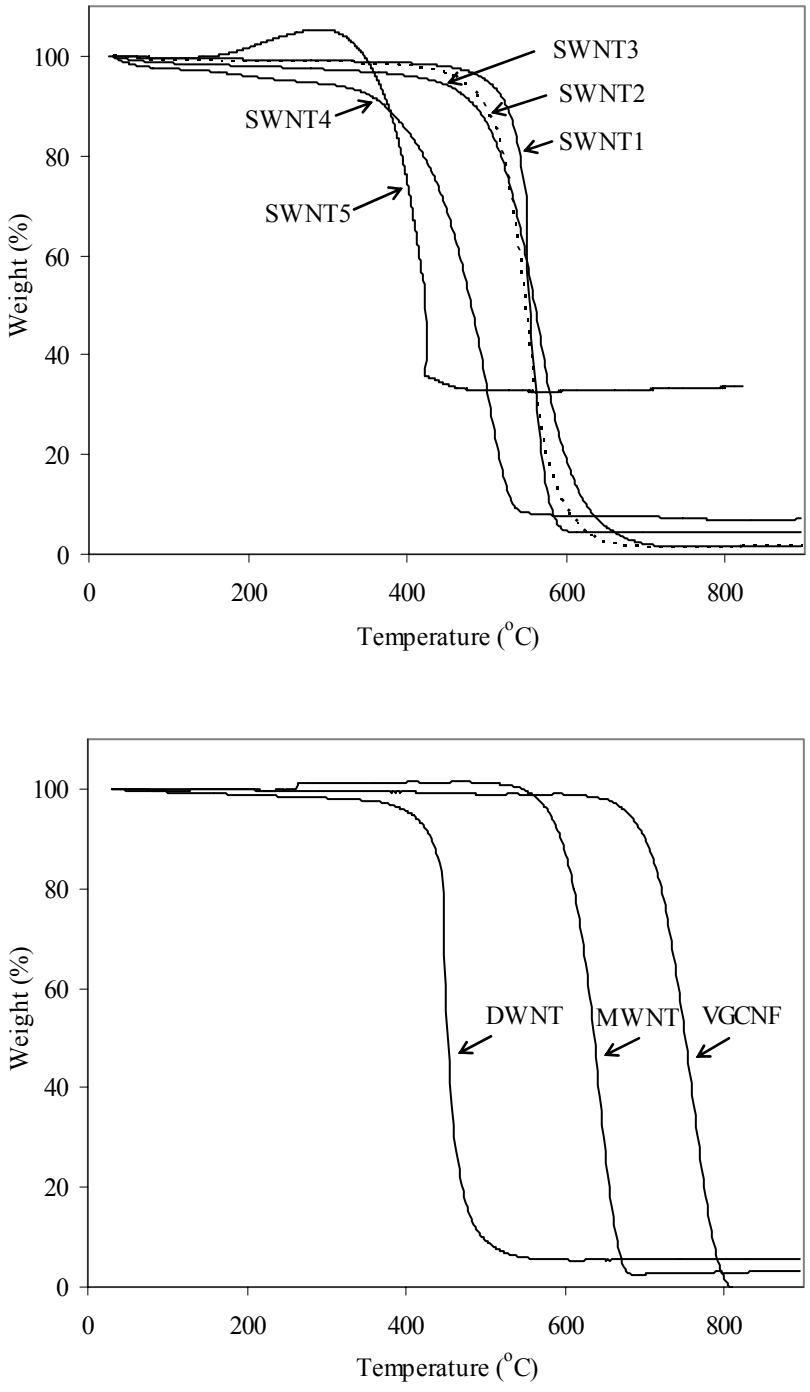

Figure A.1.Thermogravimetric analysis of (a) various SWNTs and (b) DWNT, MWNT and VGCNF in air at a heating rate of 10 ^{o}C /min.

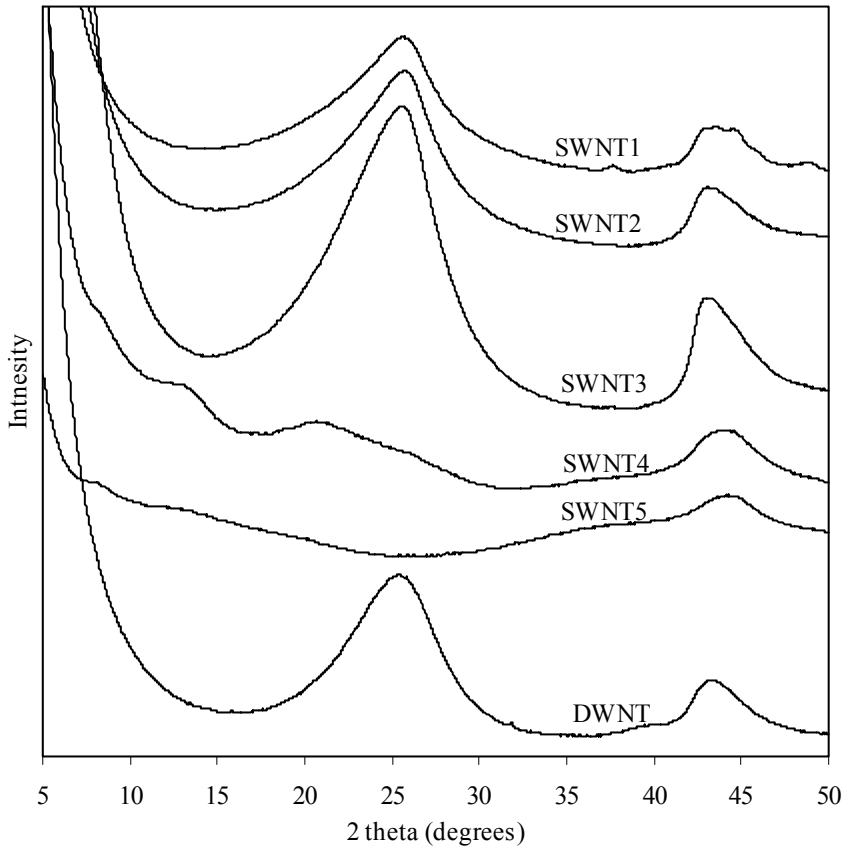

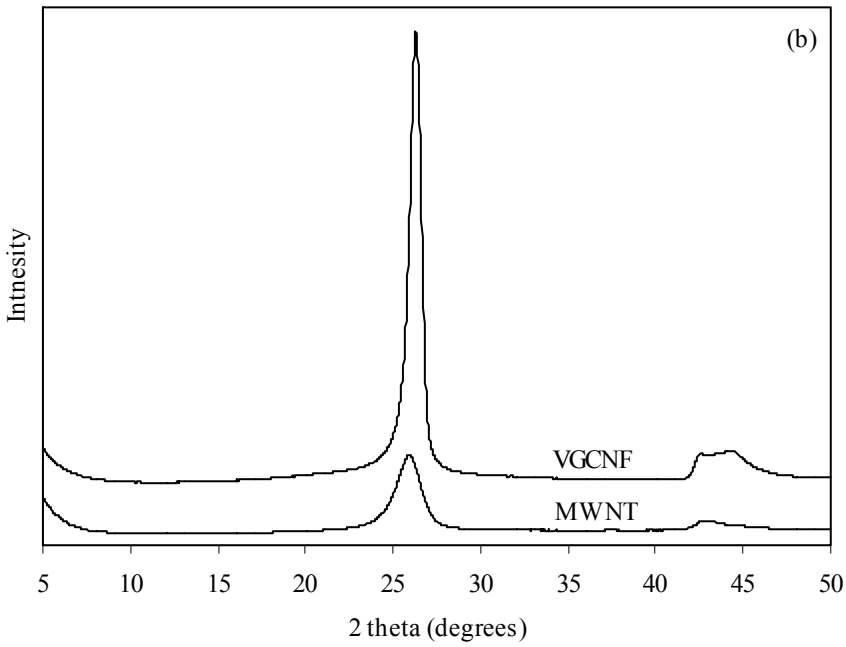

Figure A.2. Wide angle X-ray diffraction plots for (a) various SWNTs and (b) DWNT, MWNT and VGCNF.

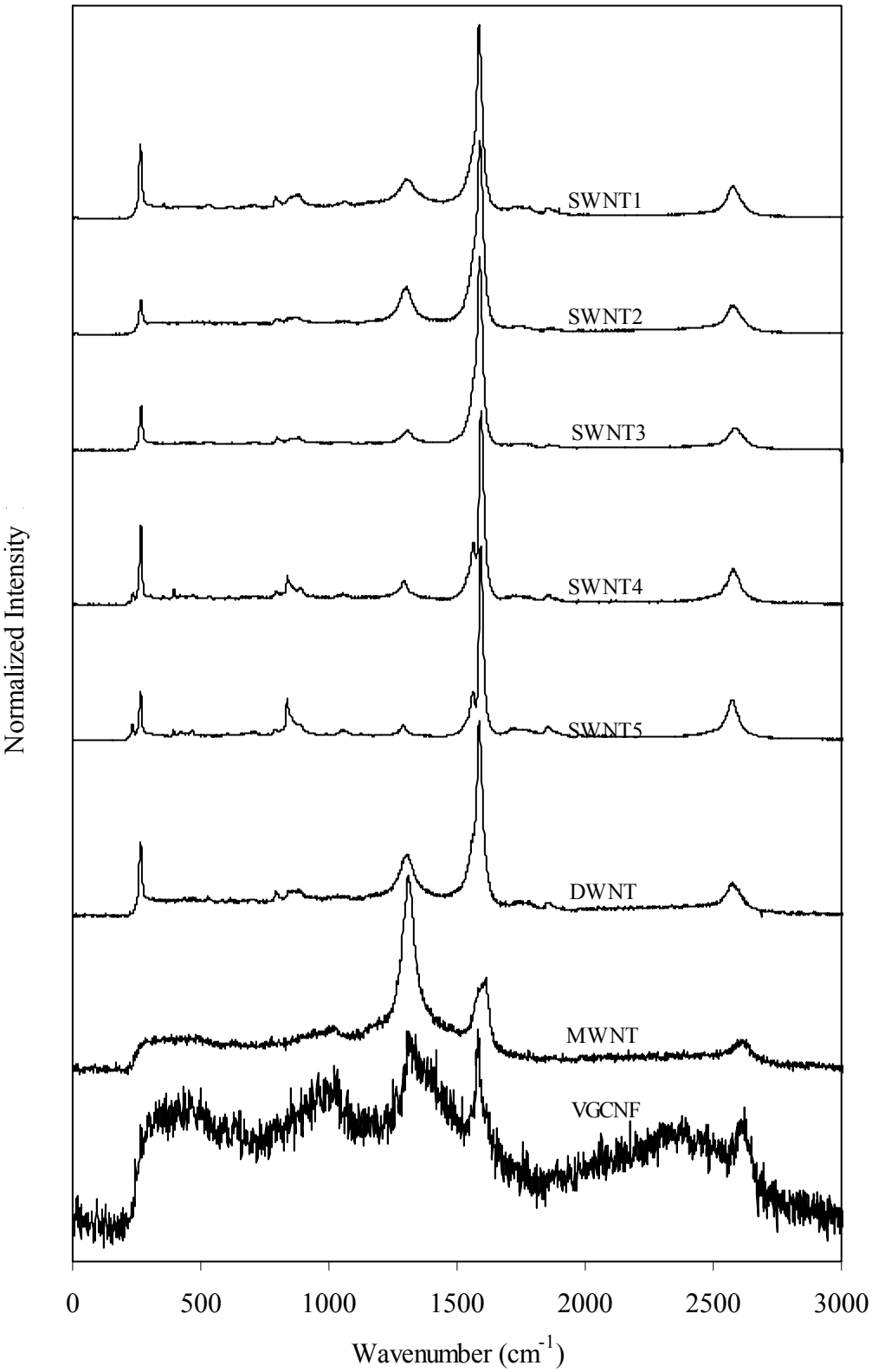

Figure A.3. Raman spectra for various CNTs.

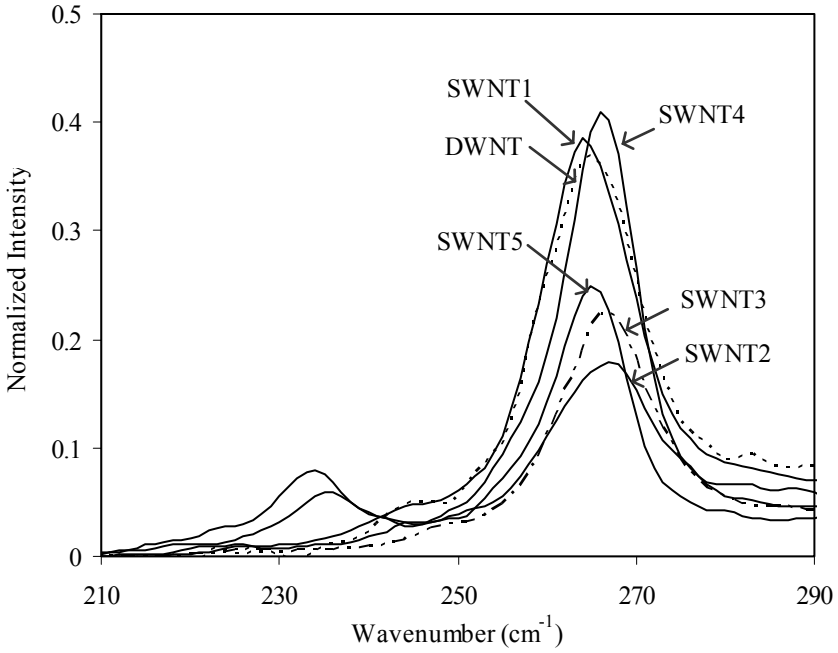

Figure A.4. RBM of Raman spectra for DWNT and various SWNTs.

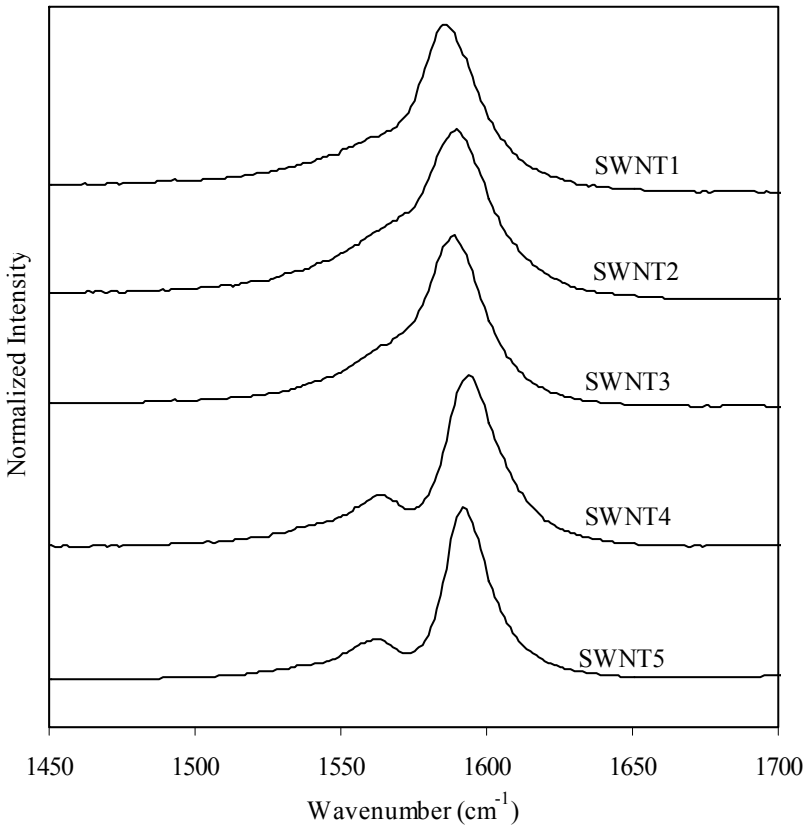

Figure A.5. G band of Raman spectra for various SWNTs.

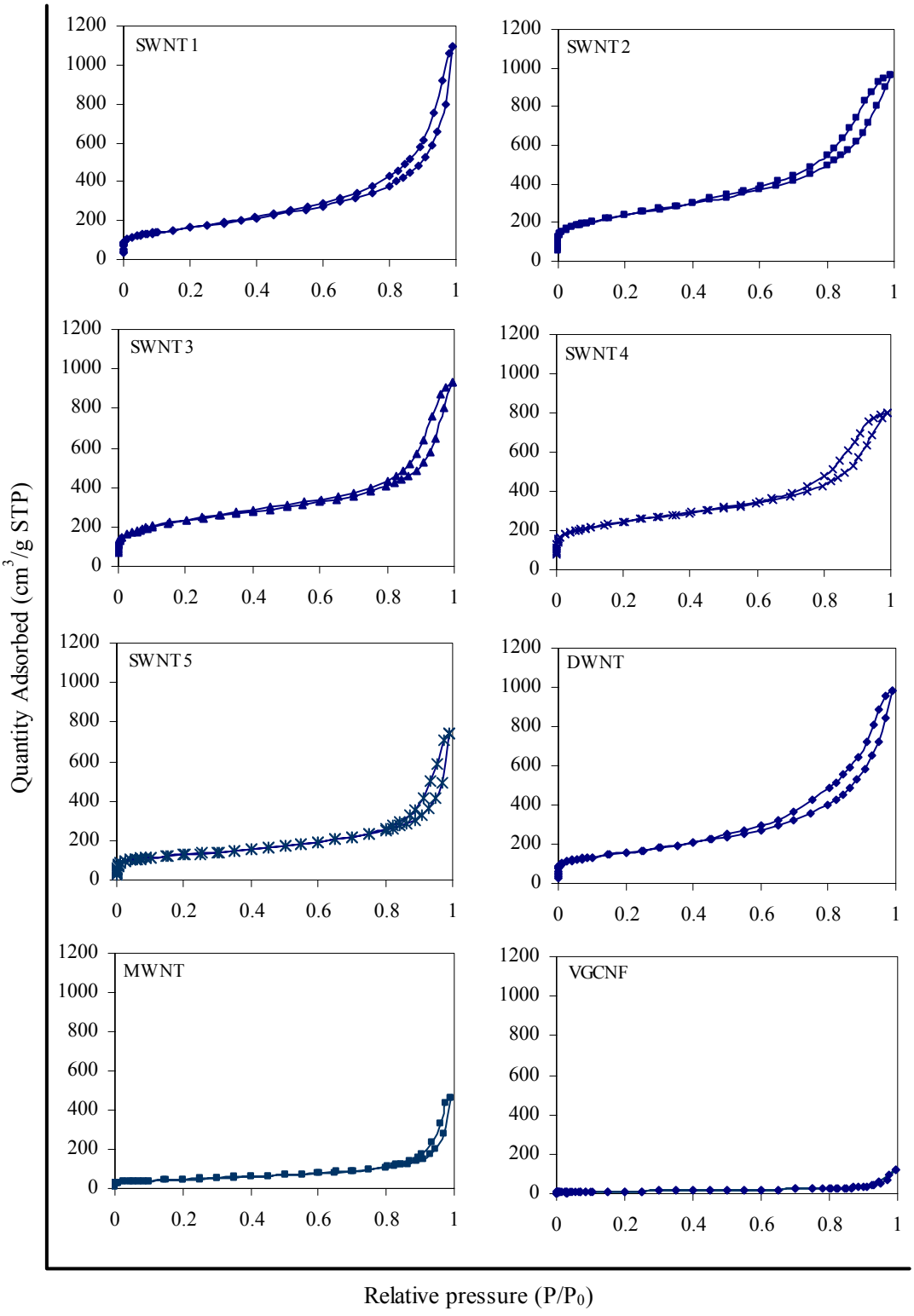

Figure A.6. Absorbed N_2 as a function of pressure for various CNTs.

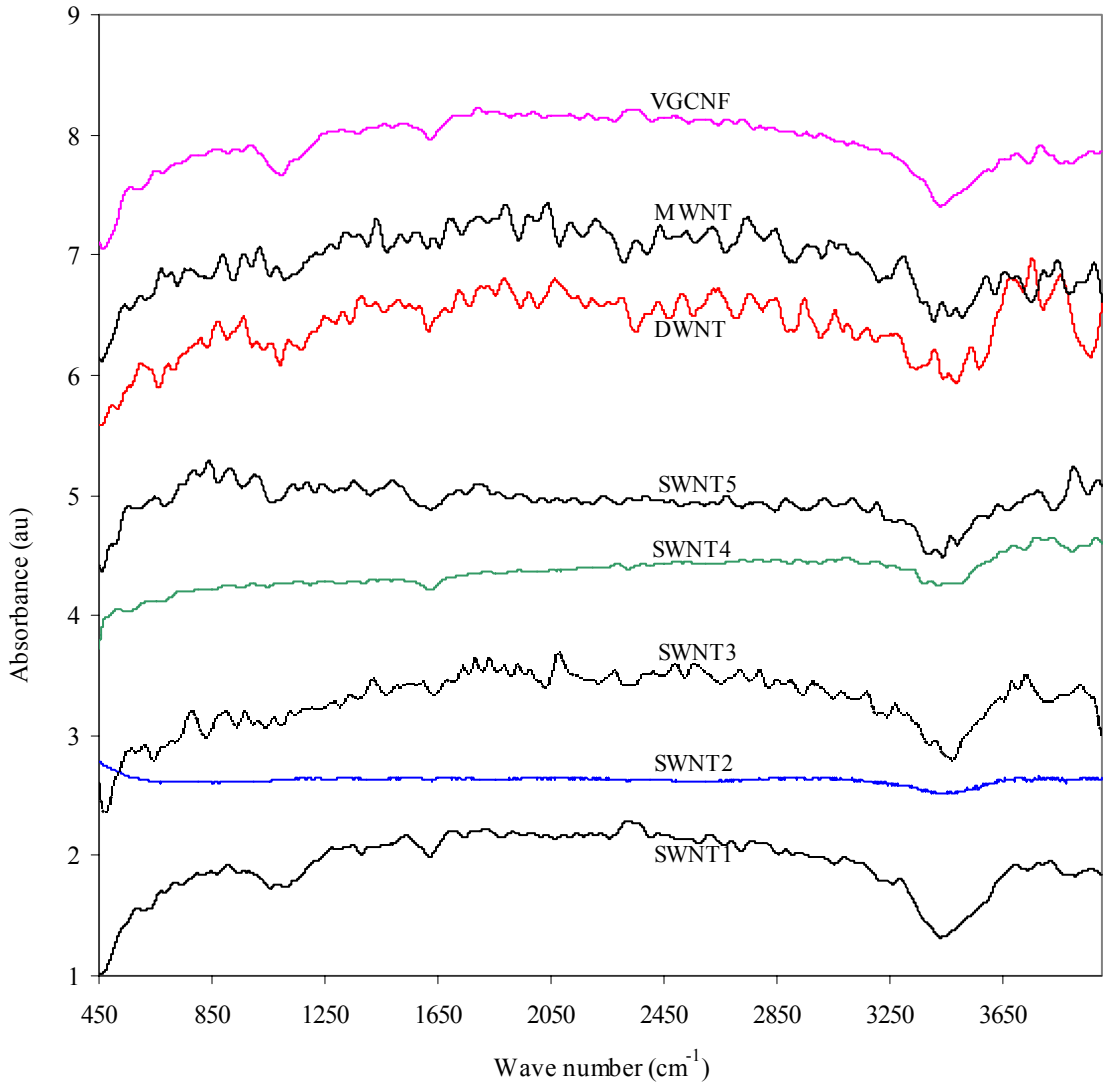

Figure A.7. FTIR spectra of various CNTs.

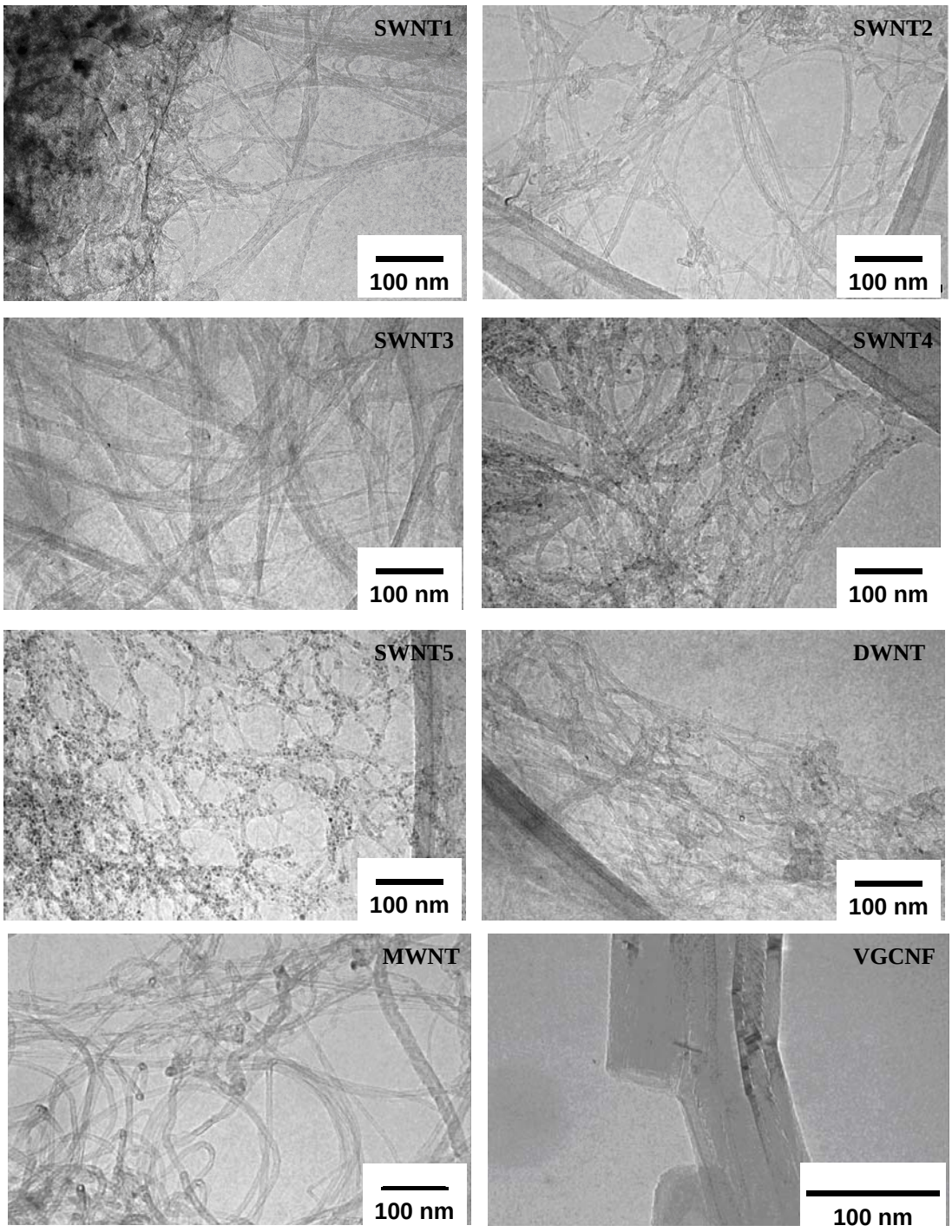

Figure A.8. Bright field transmission electron microscopy (TEM) images of various CNTs.

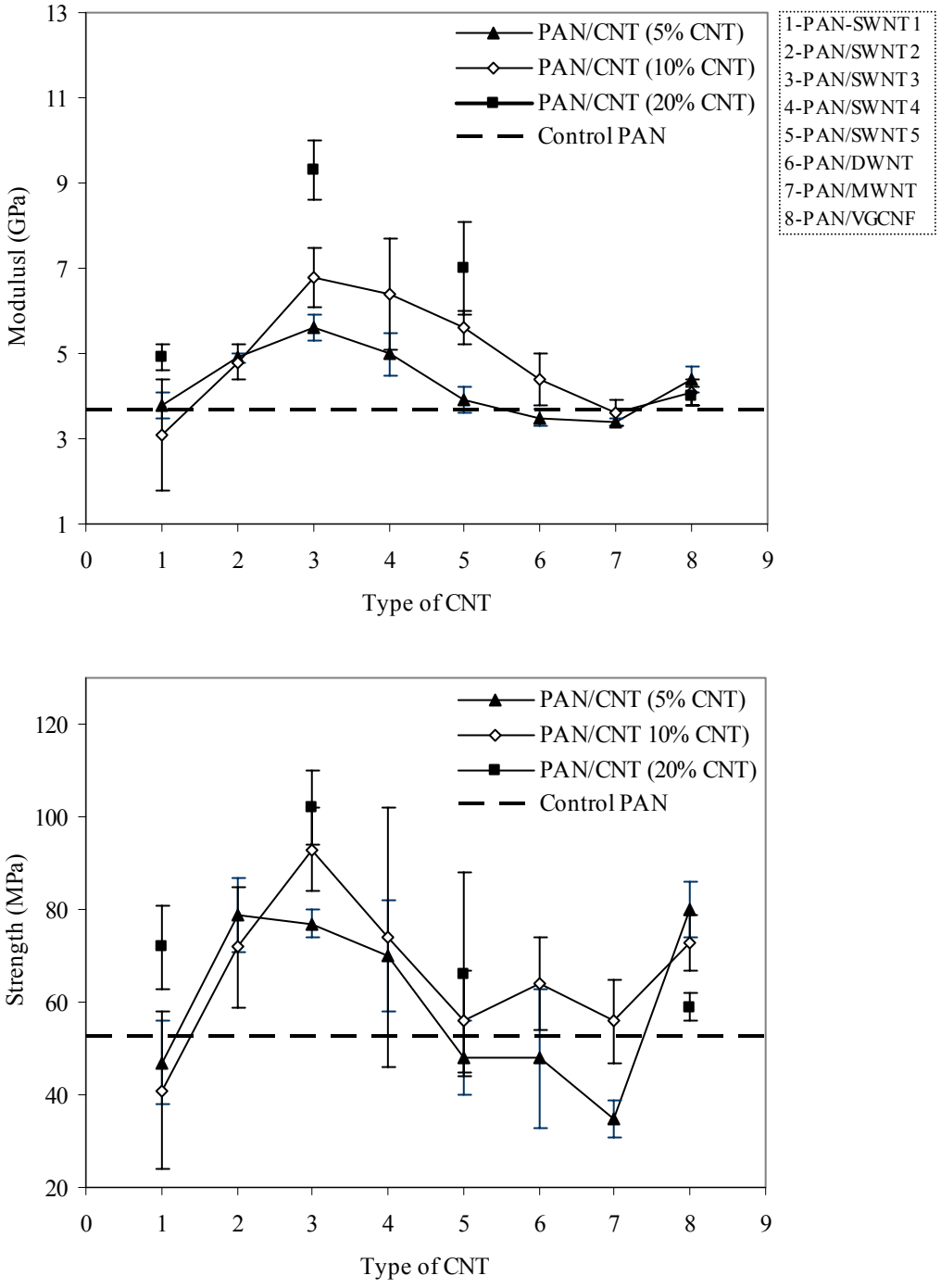

Figure A.9. Comparison of modulus (top) and tensile strength (bottom) for various PAN/CNT composite films.

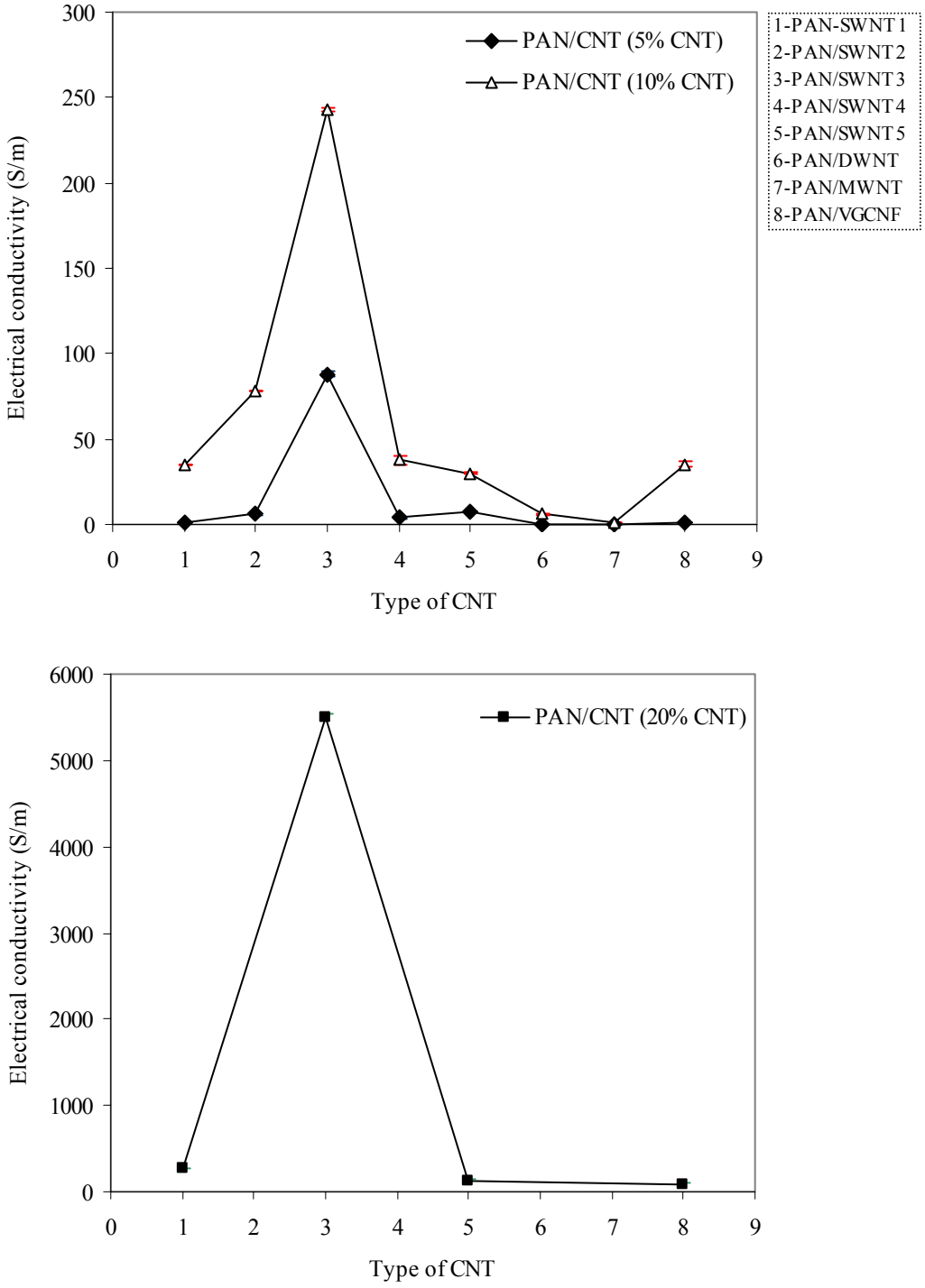

Figure A.10. Comparison of electrical conductivity for various PAN/CNT composite films with (a) 5 wt% and 10 wt% CNT loading, and (b) 20 wt% CNT loading.

Table A.3. Storage modulus for control PAN and various PAN/CNT films at different temperatures

Sample	CNT loading (wt%)	E' (GPa) at different temperatures (°C)										
		-100	-75	-50	-26	0	25	50	75	100	125	150
PAN	0	5.9	5.7	5.4	5	4.6	4.1	3.3	0.74	0.089	0.049	0.047
PAN/SWNT1	5	6.1	5.8	5.5	5.0	4.6	4.2	3.6	1.6	0.25	0.14	0.11
PAN/SWNT2	5	6.7	6.4	6.1	5.8	5.4	5.0	4.3	1.6	0.36	0.25	0.23
PAN/SWNT3	5	9.2	8.9	8.6	8.2	7.7	7.1	6.2	2.6	0.89	0.67	0.66
PAN/SWNT4	5	6.8	6.6	6.3	6.1	5.6	5.2	4.5	1.9	0.52	0.35	0.30
PAN/SWNT5	5	6.2	5.9	5.6	5.3	4.9	4.4	3.8	1.3	0.27	0.18	0.18
PAN/DWNT	5	6.1	5.8	5.6	5.3	4.9	4.4	3.8	1.4	0.22	0.12	0.11
PAN/MWNT	5	7.0	6.8	6.5	6.1	5.6	5.1	4.5	2.9	0.48	0.13	0.099
PAN/VGCNF	5	7.1	6.8	6.5	6.1	5.6	5.1	4.4	2.1	0.30	0.14	0.13
PAN/SWNT1	10	5.6	5.4	5.2	4.9	4.5	4.1	3.5	1.6	0.33	0.20	0.20
PAN/SWNT2	10	7.5	7.3	7.0	6.6	6.2	5.7	4.9	2.0	0.65	0.42	0.39
PAN/SWNT3	10	11.7	11.6	11.2	10.7	10.1	9.5	8.7	5.3	1.90	1.3	1.3
PAN/SWNT4	10	7.6	7.3	6.9	6.6	6.1	5.7	5.1	3.0	0.94	0.62	0.59
PAN/SWNT5	10	9.2	8.9	8.5	8.1	7.5	6.8	6.2	4.6	1.20	0.52	0.48
PAN/DWNT	10	5.3	5.0	4.8	4.5	4.2	3.8	3.3	1.4	0.27	0.17	0.15
PAN/MWNT	10	7.0	6.7	6.4	6.0	5.5	5.0	4.4	2.5	0.43	0.15	0.14
PAN/VGCNF	10	6.8	6.6	6.3	6.0	5.6	5.1	4.4	2.4	0.39	0.17	0.15
PAN/SWNT1	20	7.7	7.5	7.1	6.7	6.3	5.7	5.0	2.8	0.85	0.49	0.44
PAN/SWNT3	20	11.1	10.7	10.3	9.9	9.4	8.8	7.9	5.5	2.50	1.5	1.4
PAN/SWNT5	20	13.5	13.1	12.6	11.7	9.9	9.0	8.3	5.4	2.10	1.0	1.0

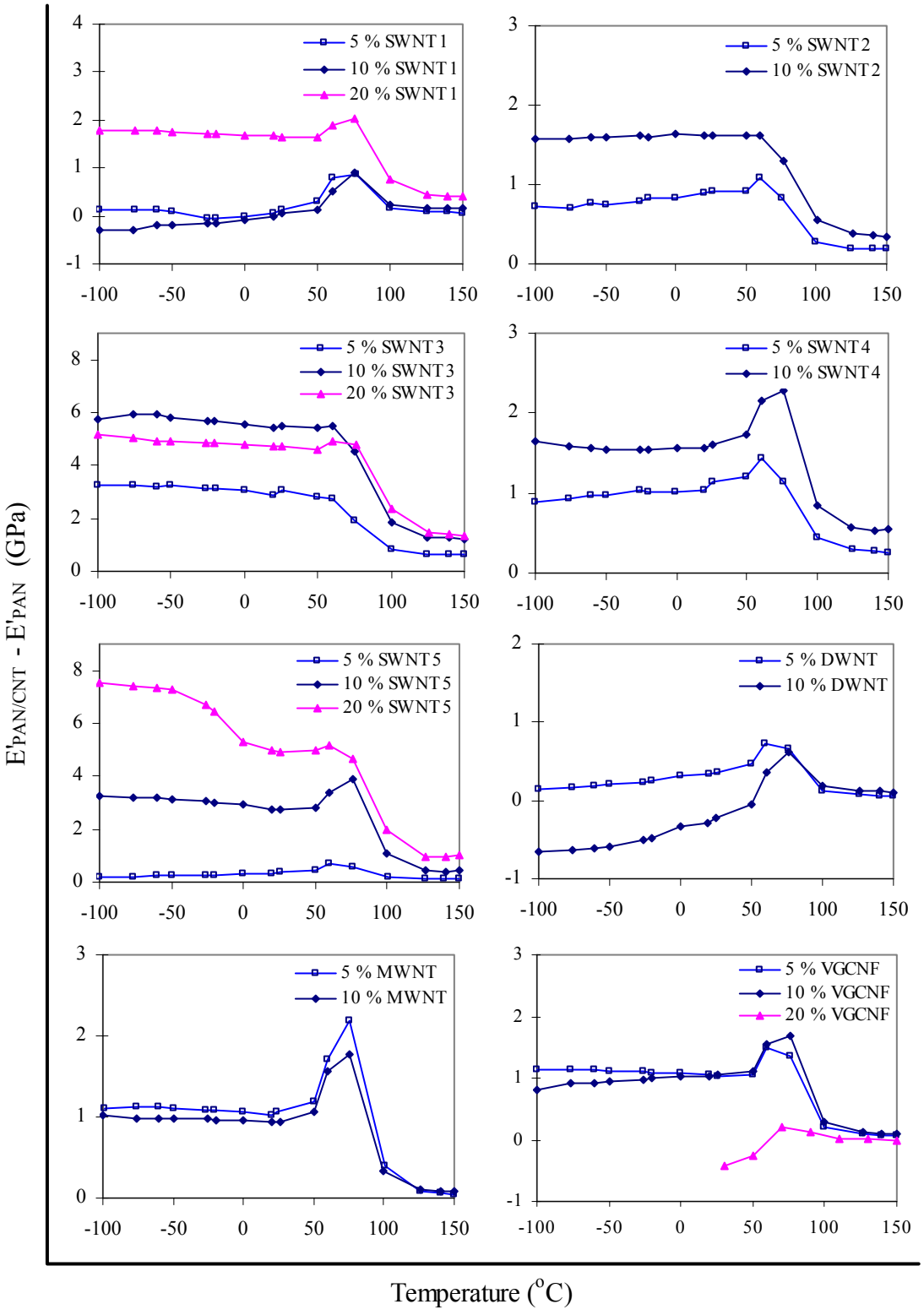

Figure A.11. Storage modulus difference between PAN/CNT films and control PAN film as a function of temperature.

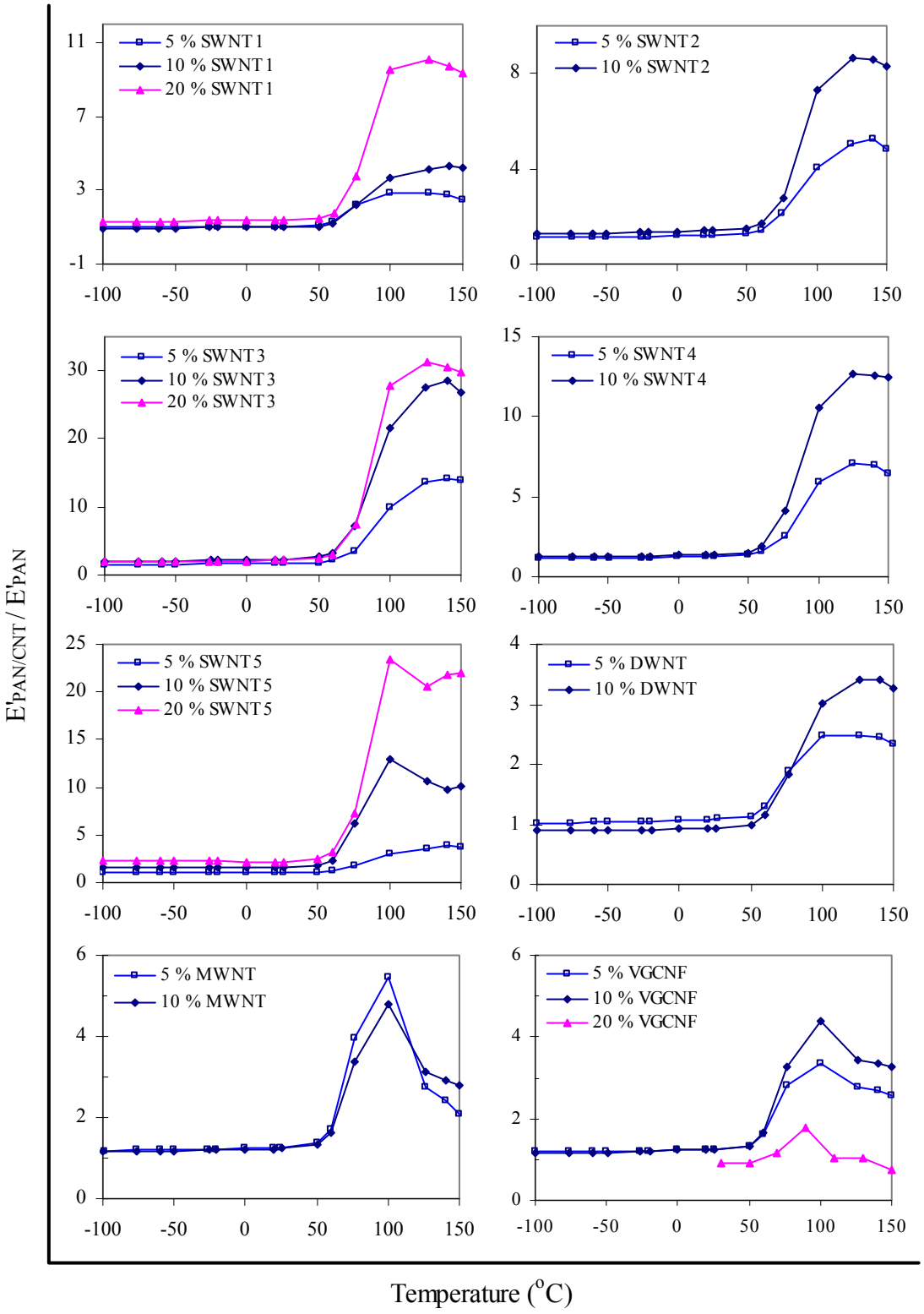

Figure A.12. Values of $E'_{PAN/CNT}/ E'_{PAN}$ as a function of temperature.

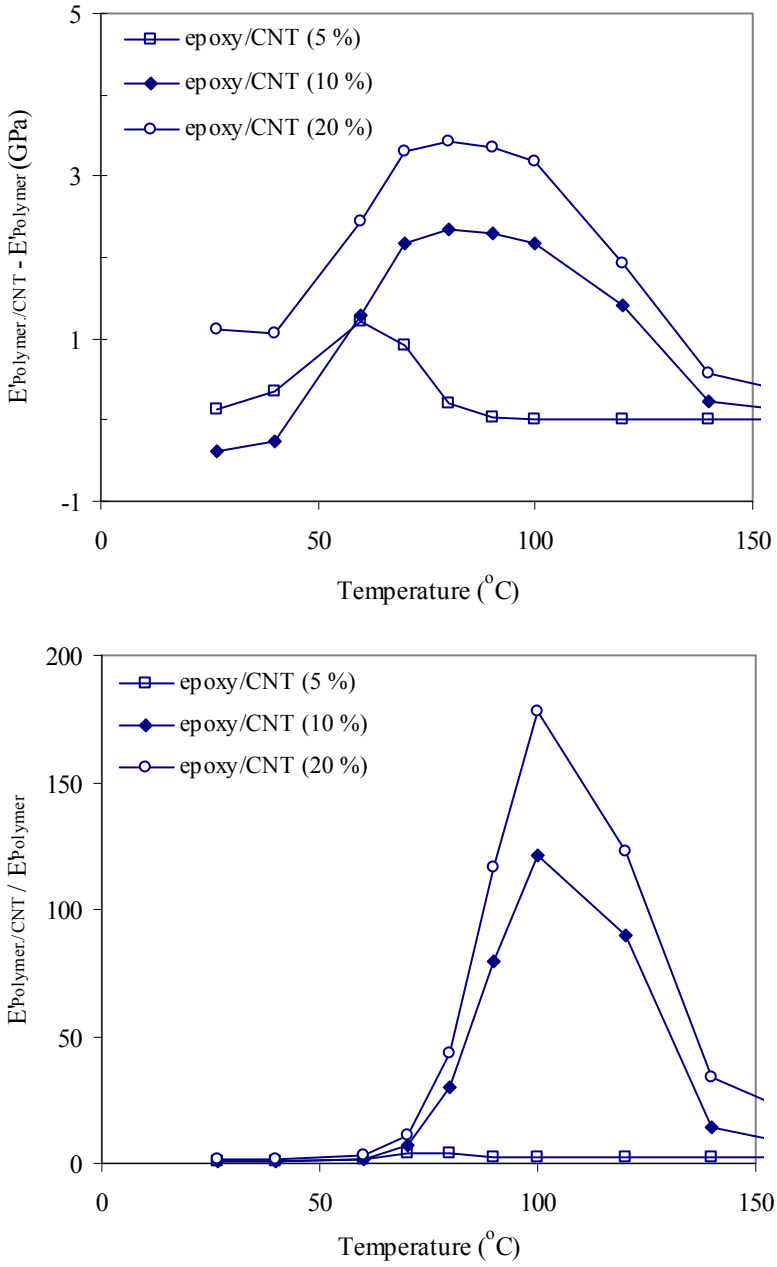

Figure A.13. Dynamic mechanical properties of epoxy/CNT composite fibers.[32]

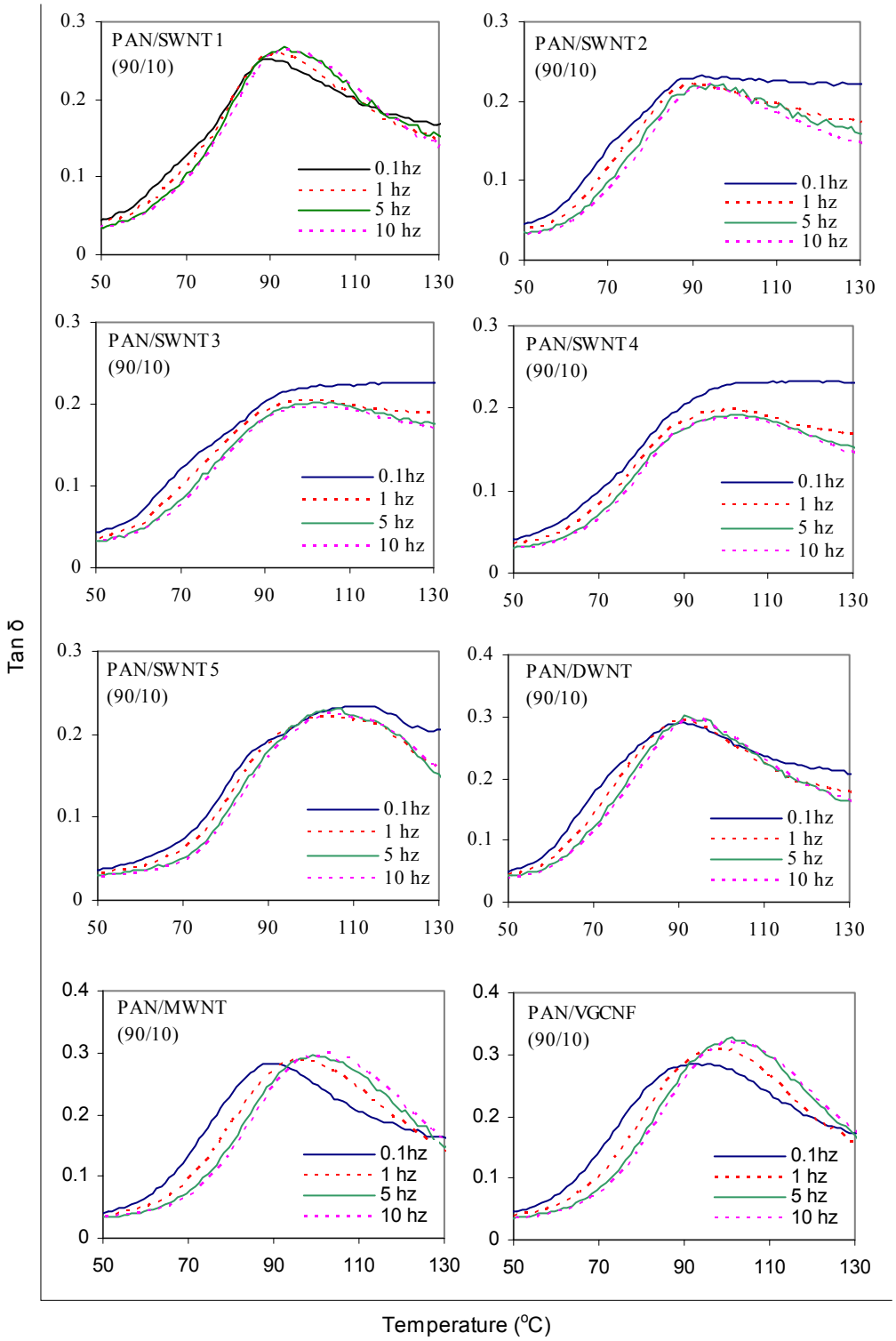

Figure A.14. Tan δ behavior of PAN/CNT composite films with 10 wt% CNT loading as a function of temperature at various frequencies.

Table A.4. Temperature of Tan δ peak at various frequencies for PAN/CNT composite films with 10 wt% loading

Frequency (Hz) / Sample	Temperature (^{o}C)				Activation Energy (KJ/mole)
	0.1	1	5	10	
PAN/SWNT1 (90/10)	89.2	91.3	93.3	94.2	1011
PAN/SWNT2 (90/10)	89.2	91.3	93.2	94.3	1006
PAN/SWNT3 (90/10)	96.2	98.2	99.2	100.3	1343
PAN/SWNT4 (90/10)	97.3	99.3	101.2	102.2	1069
PAN/SWNT5 (90/10)	100.1	104.1	107.1	109.0	619
PAN/DWNT (90/10)	89.2	90.4	93.3	94.3	913
PAN/MWNT (90/10)	89.3	95.4	99.3	101.3	438
PAN/VWNT (90/10)	93.2	98.1	101.2	103.2	538

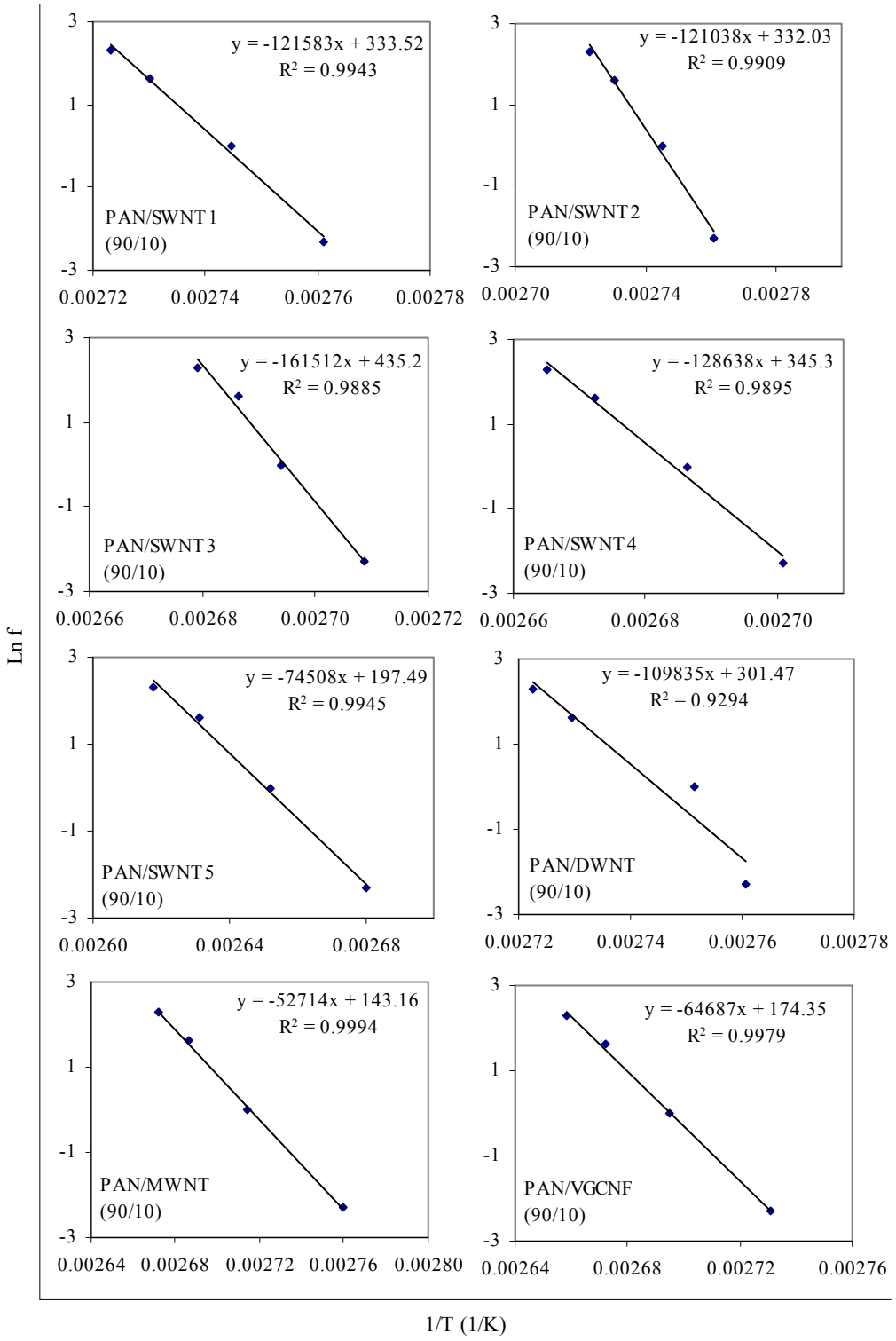

Figure A.15. Ln f as a function of 1/T for PAN/CNT composite films with 10 wt% CNT loading.

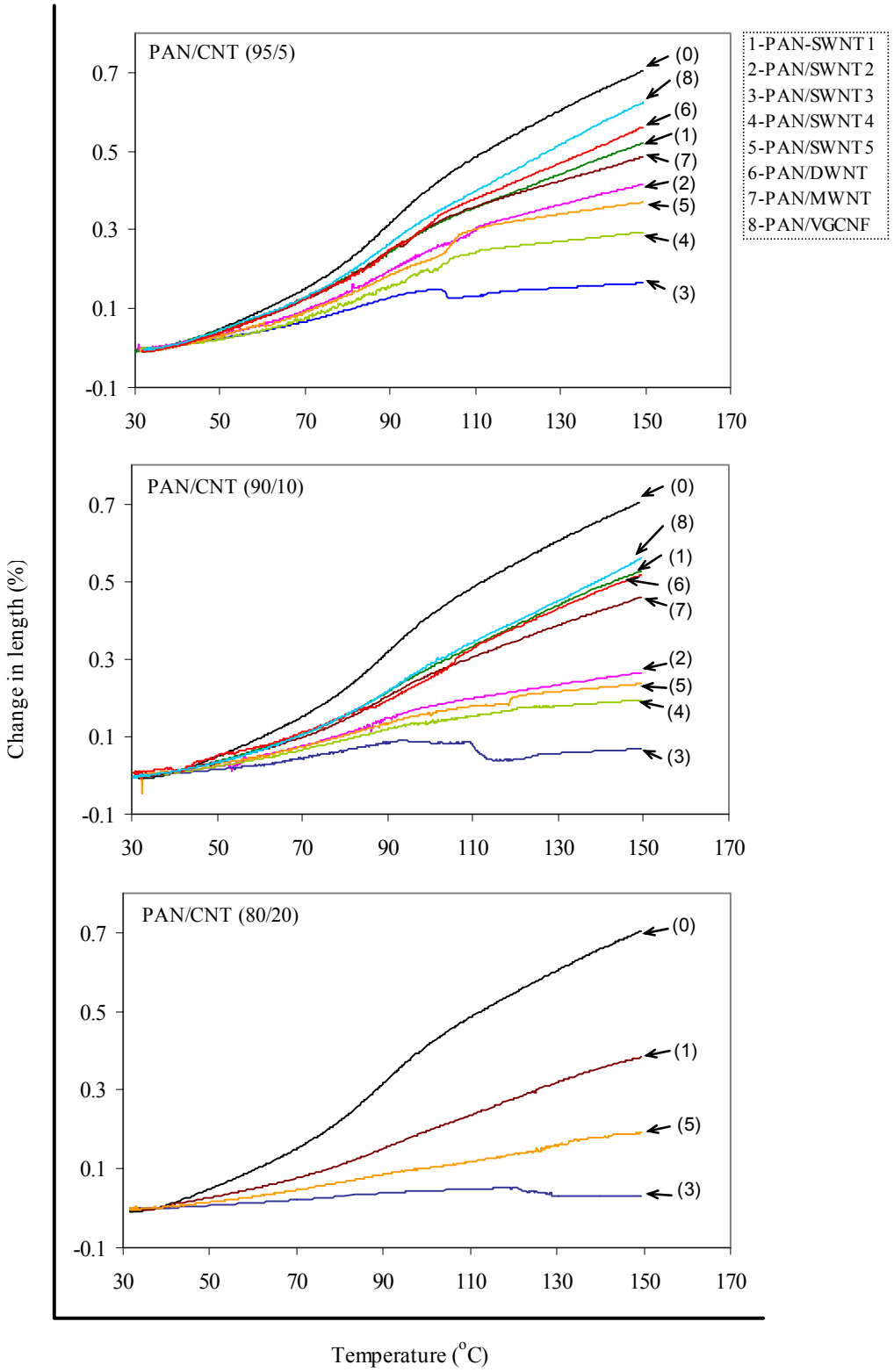

Figure A.16. Thermal expansion as a function of temperature for control PAN and PAN/CNT composite films.

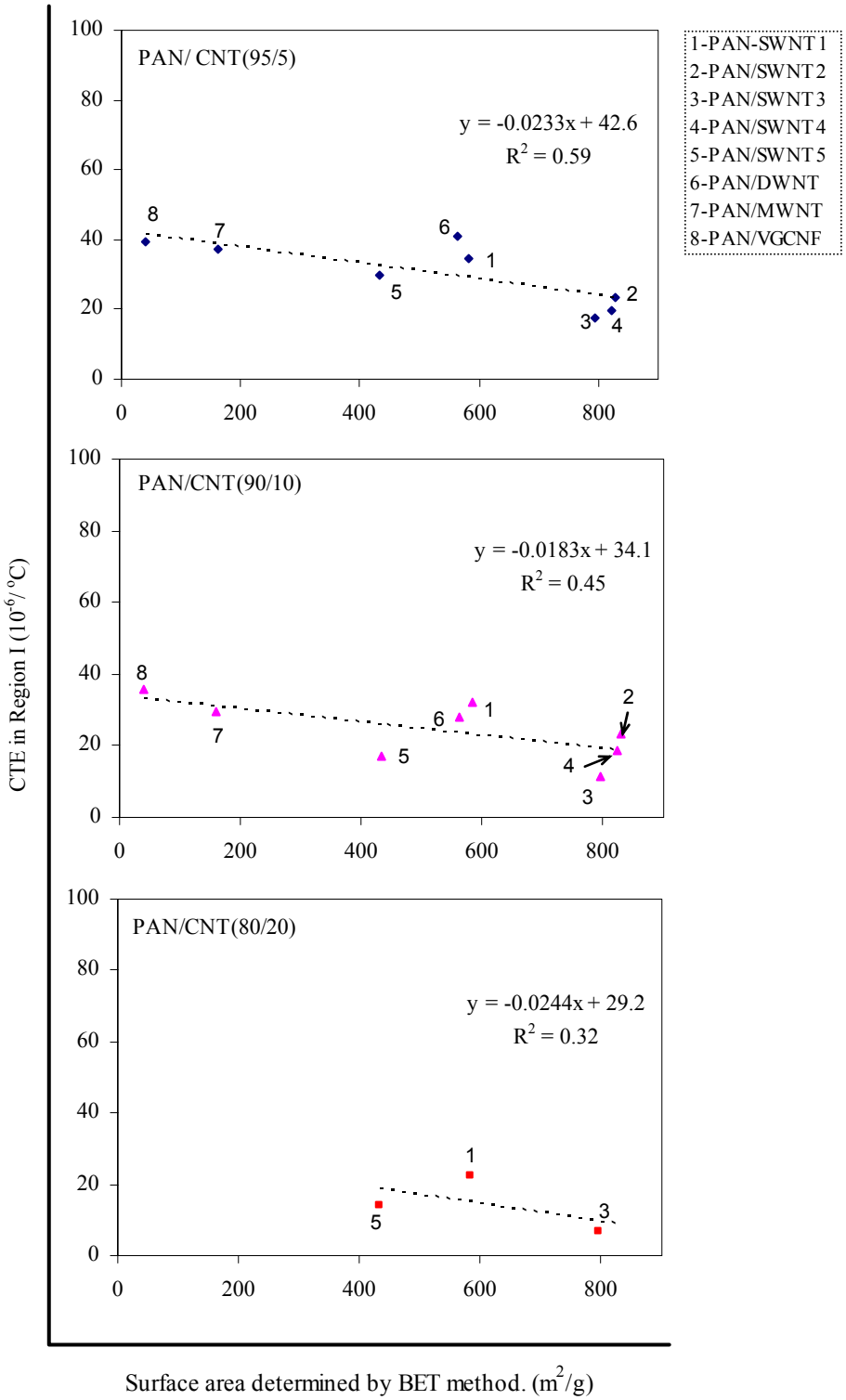

Figure A.17. CTE in Region I for PAN/CNT composite films as a function of CNT surface area.

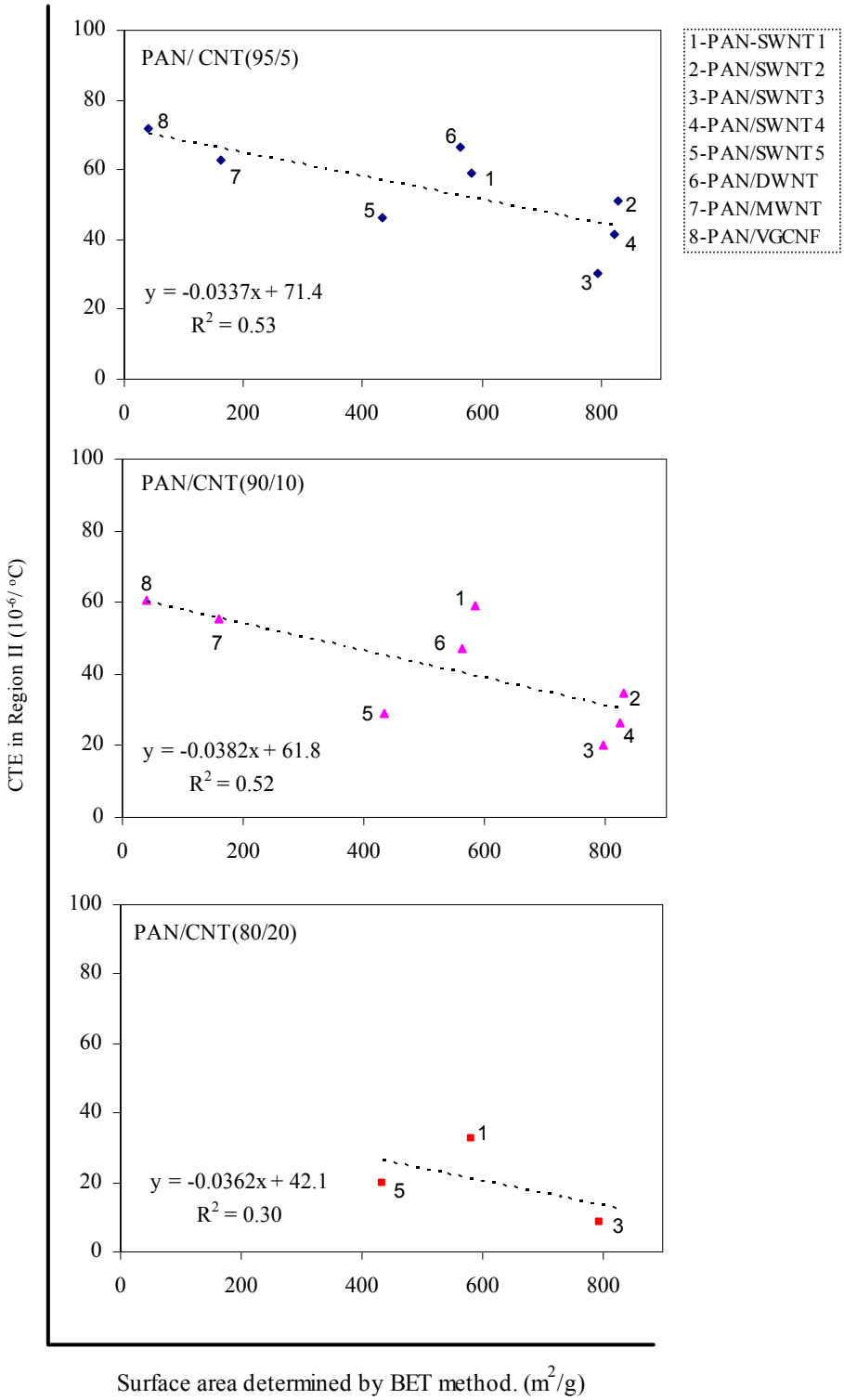

Figure A.18. CTE in Region II for PAN/CNT composite films as a function of CNT surface area.

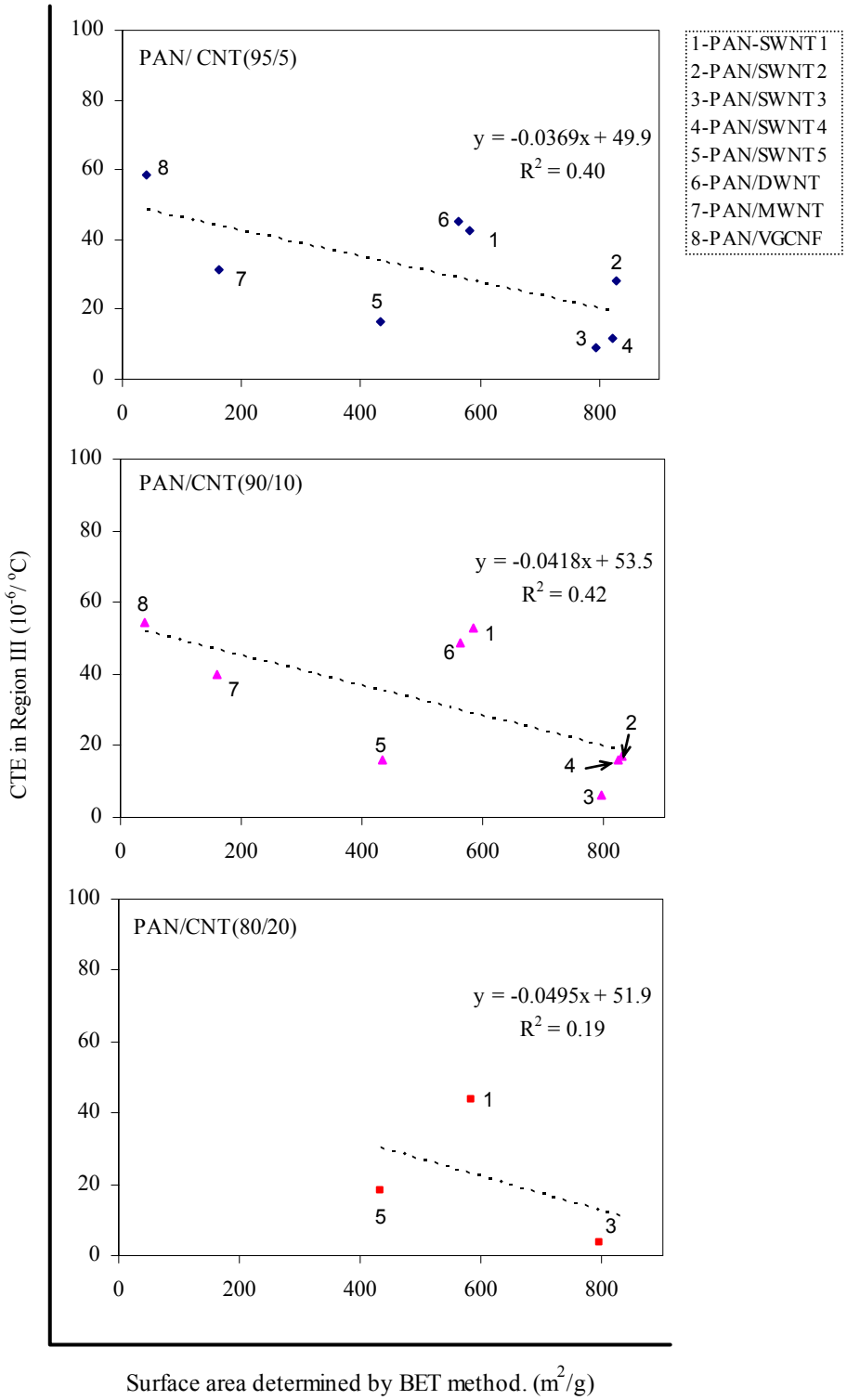

Figure A.19. CTE in Region III for PAN/CNT composite films as a function of CNT surface area.

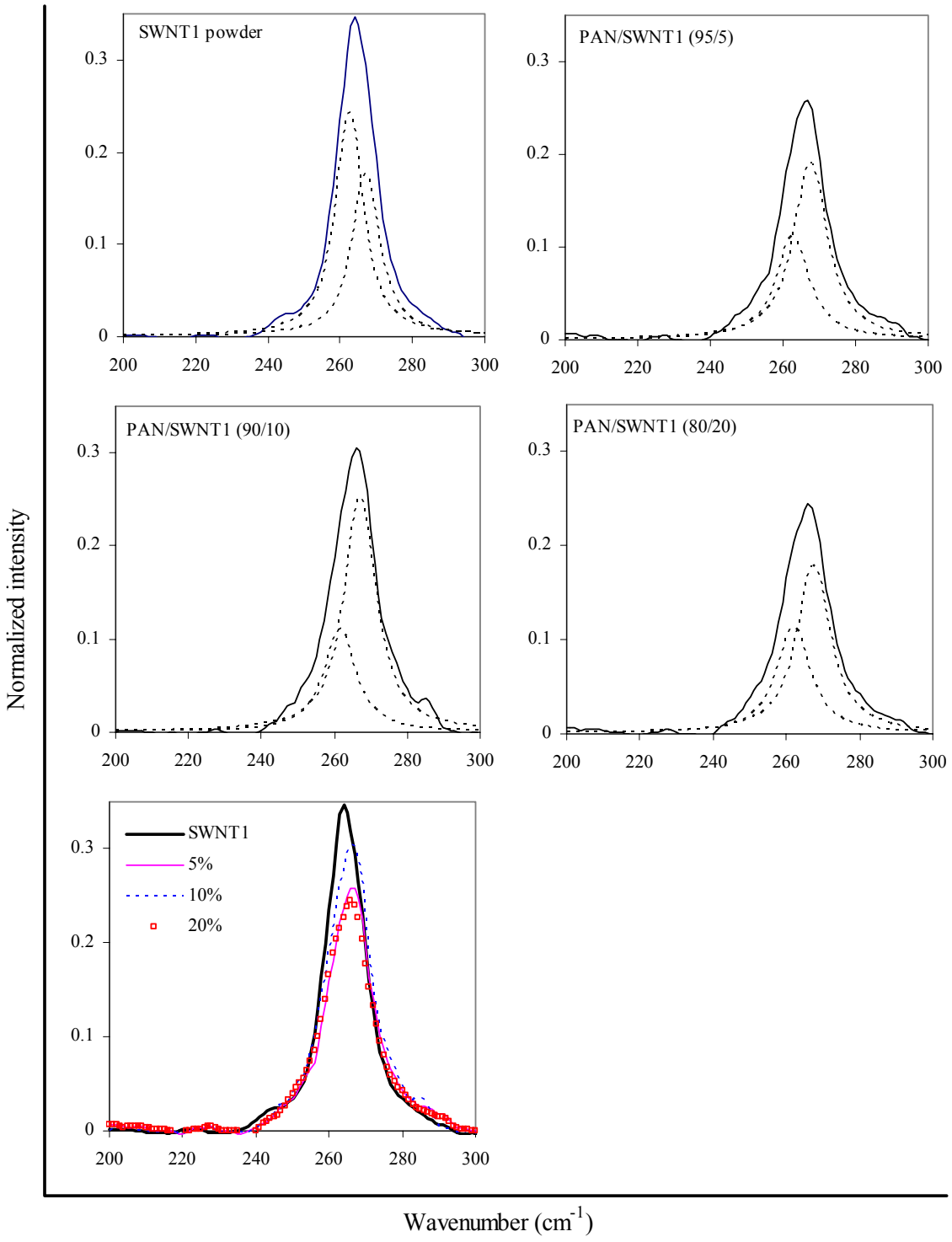

Figure A.20. RBM band in Raman spectra for SWNT1 powder and PAN/SWNT1 composite films.

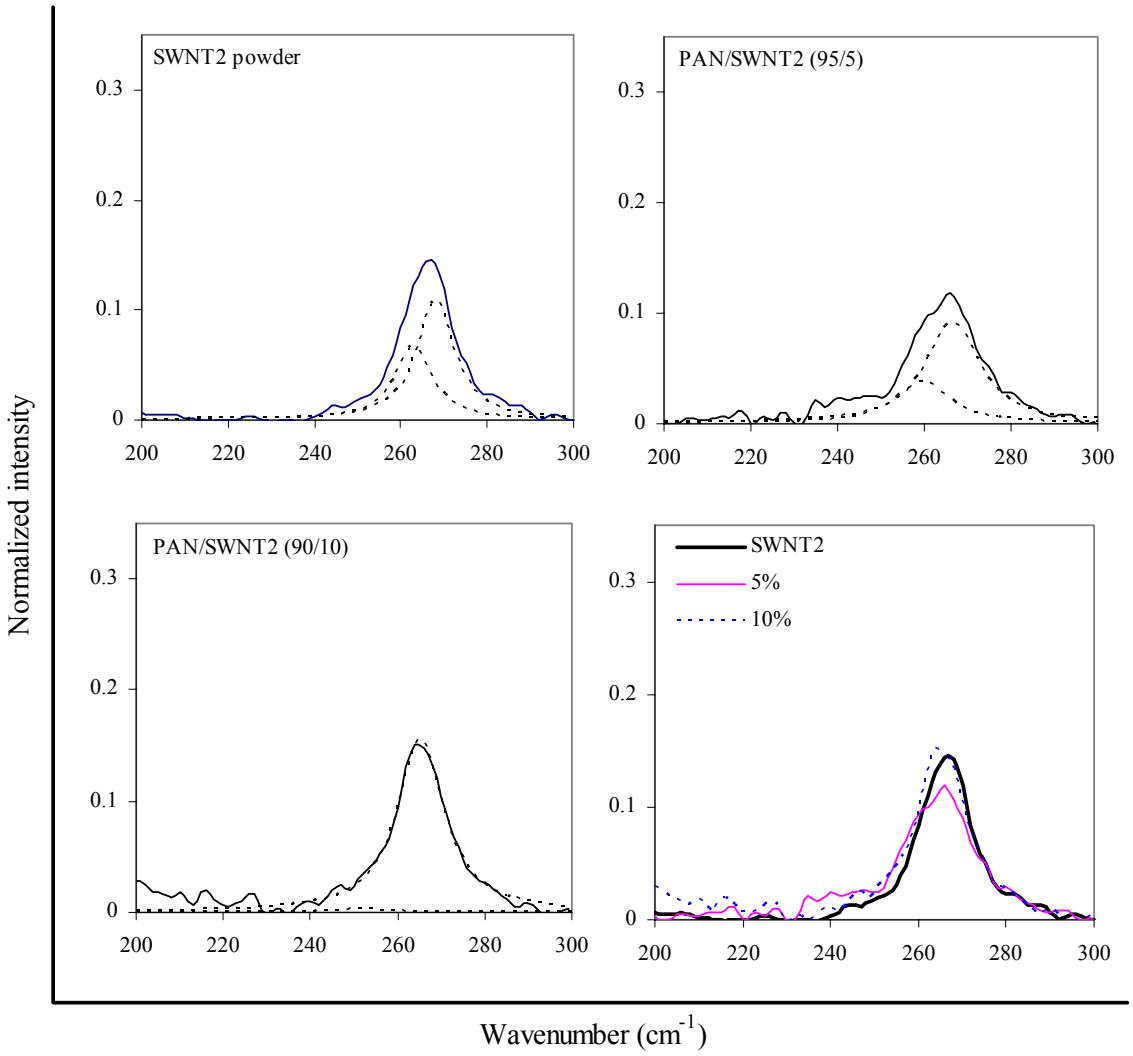

Figure A.21. RBM band in Raman spectra for SWNT2 powder and PAN/SWNT2 composite films.

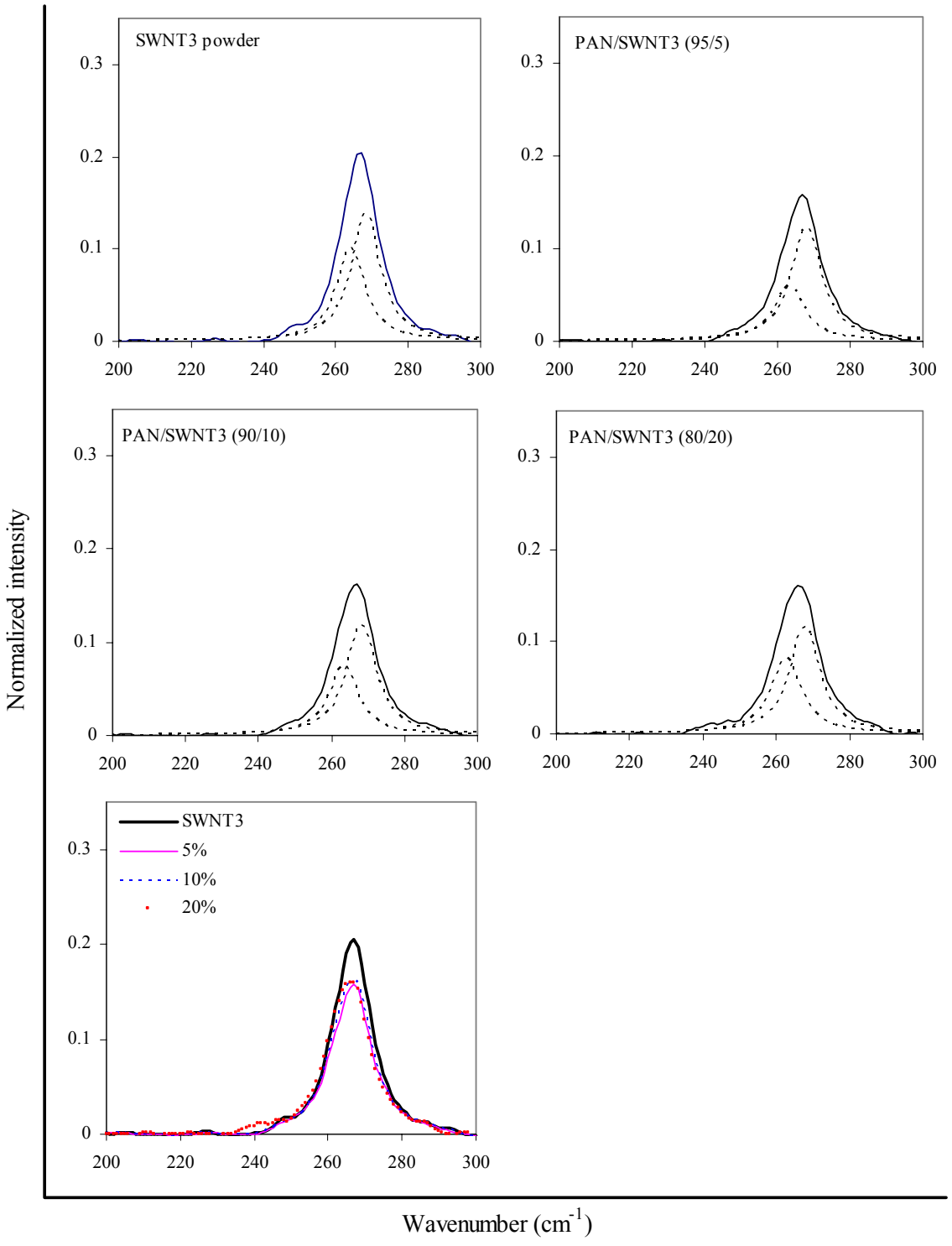

Figure A.22. RBM band in Raman spectra for SWNT3 powder and PAN/SWNT3 composite films.

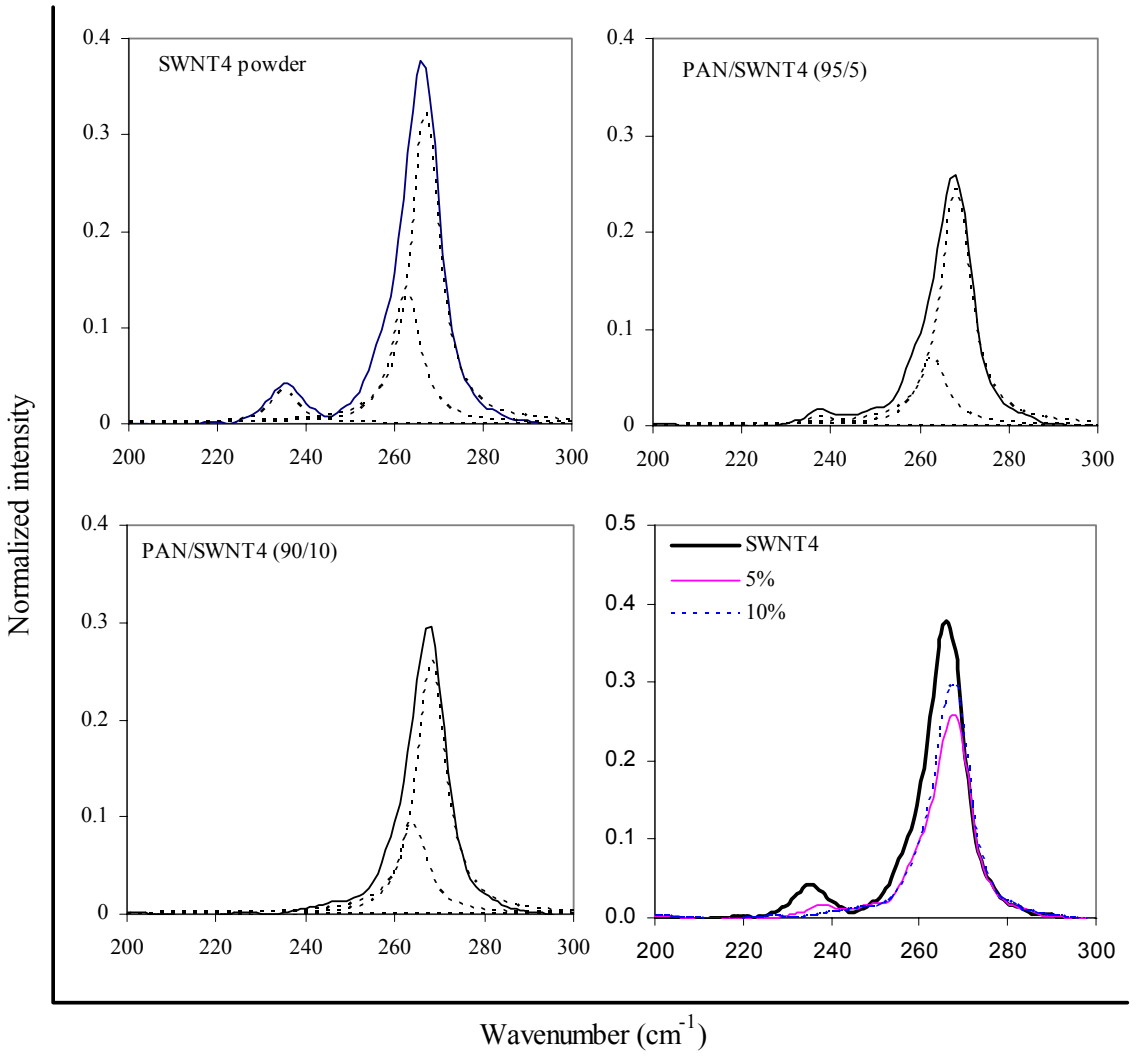

Figure A.23. RBM band in Raman spectra for SWNT4 powder and PAN/SWNT4 composite films.

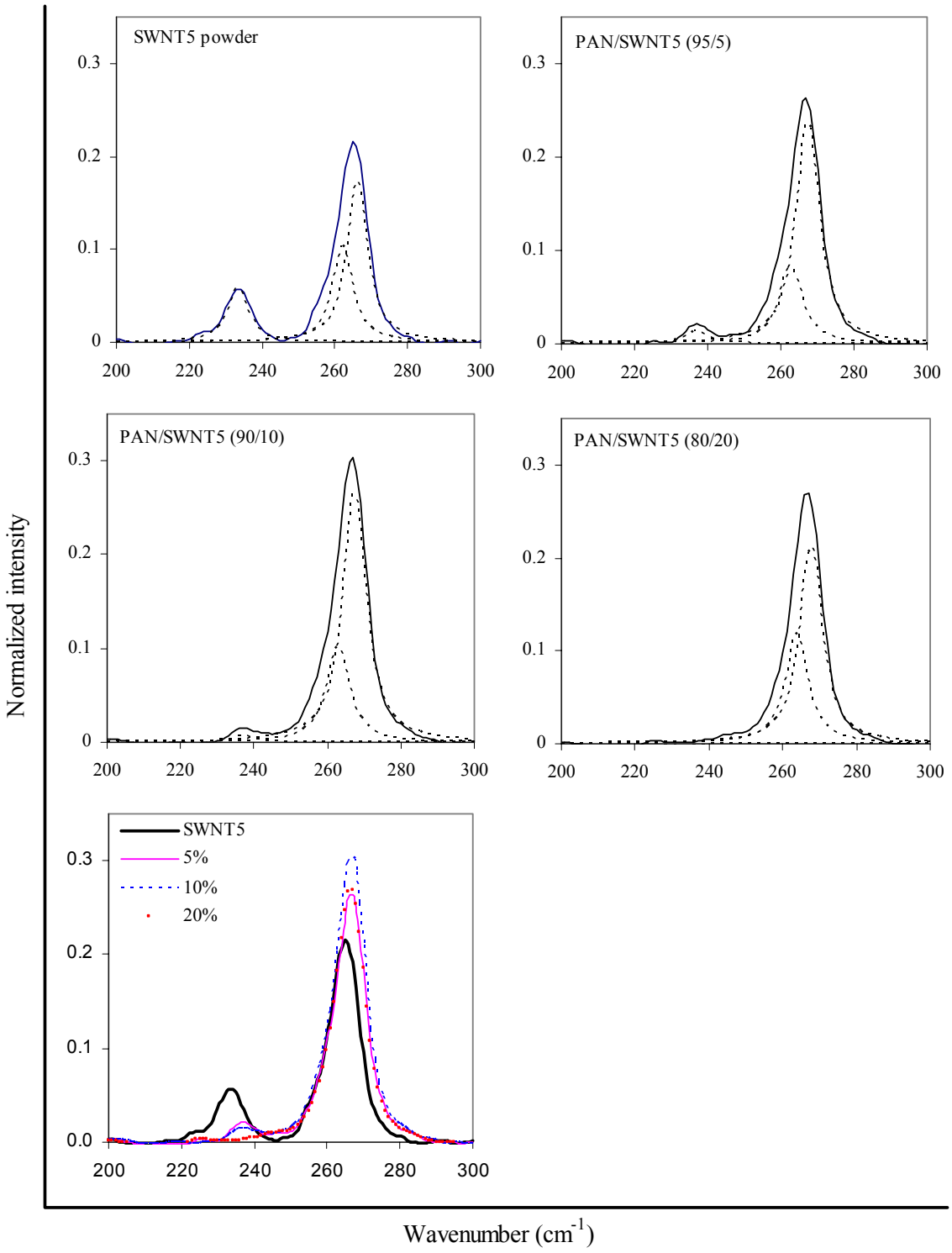

Figure A.24. RBM band in Raman spectra for SWNT5 powder and PAN/SWNT5 composite films.

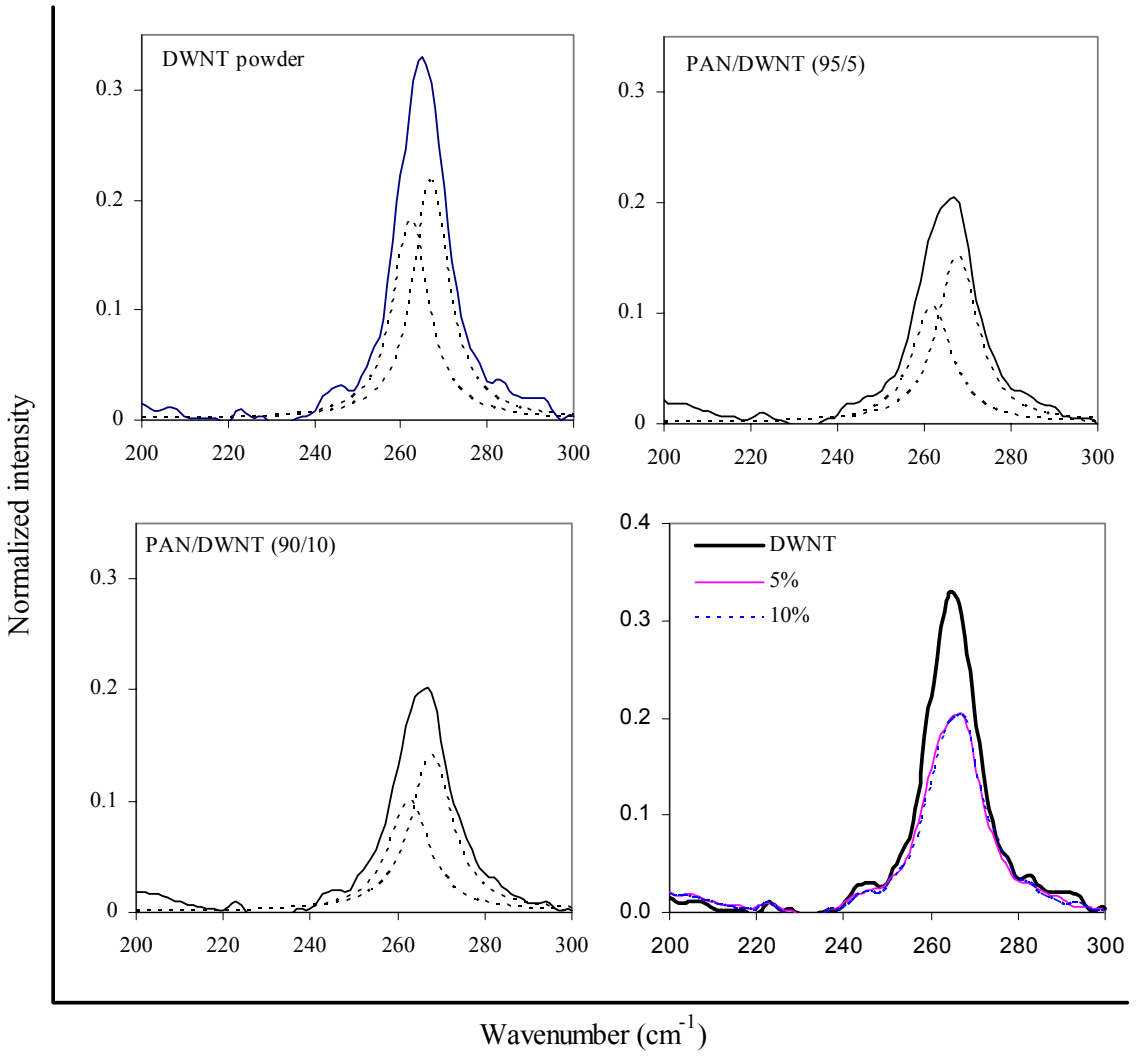

Figure A.25. RBM band in Raman spectra for DWNT powder and PAN/DWNT composite films.

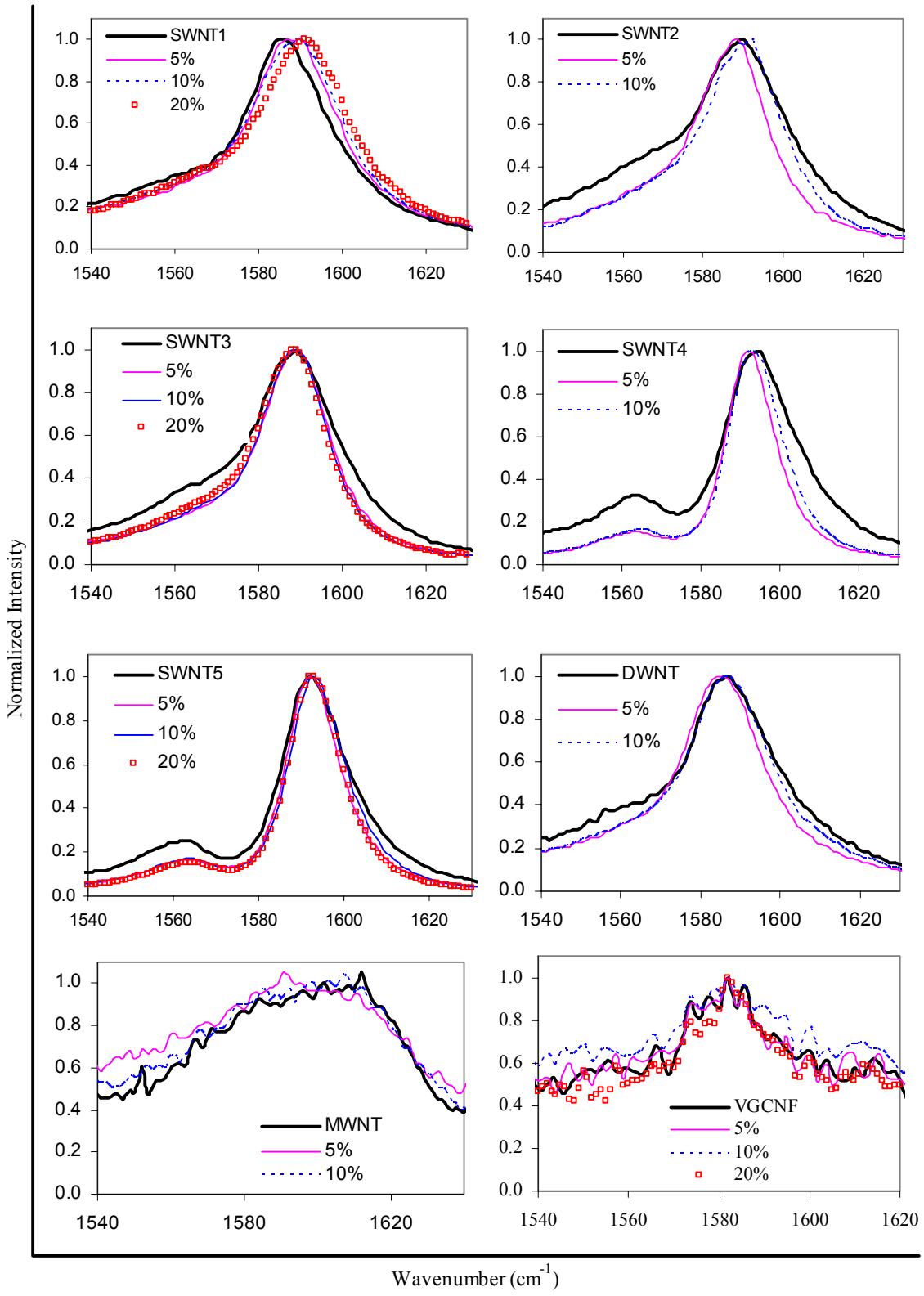

Figure A.26. G band in Raman spectra for CNT powders and PAN/CNT composite films.

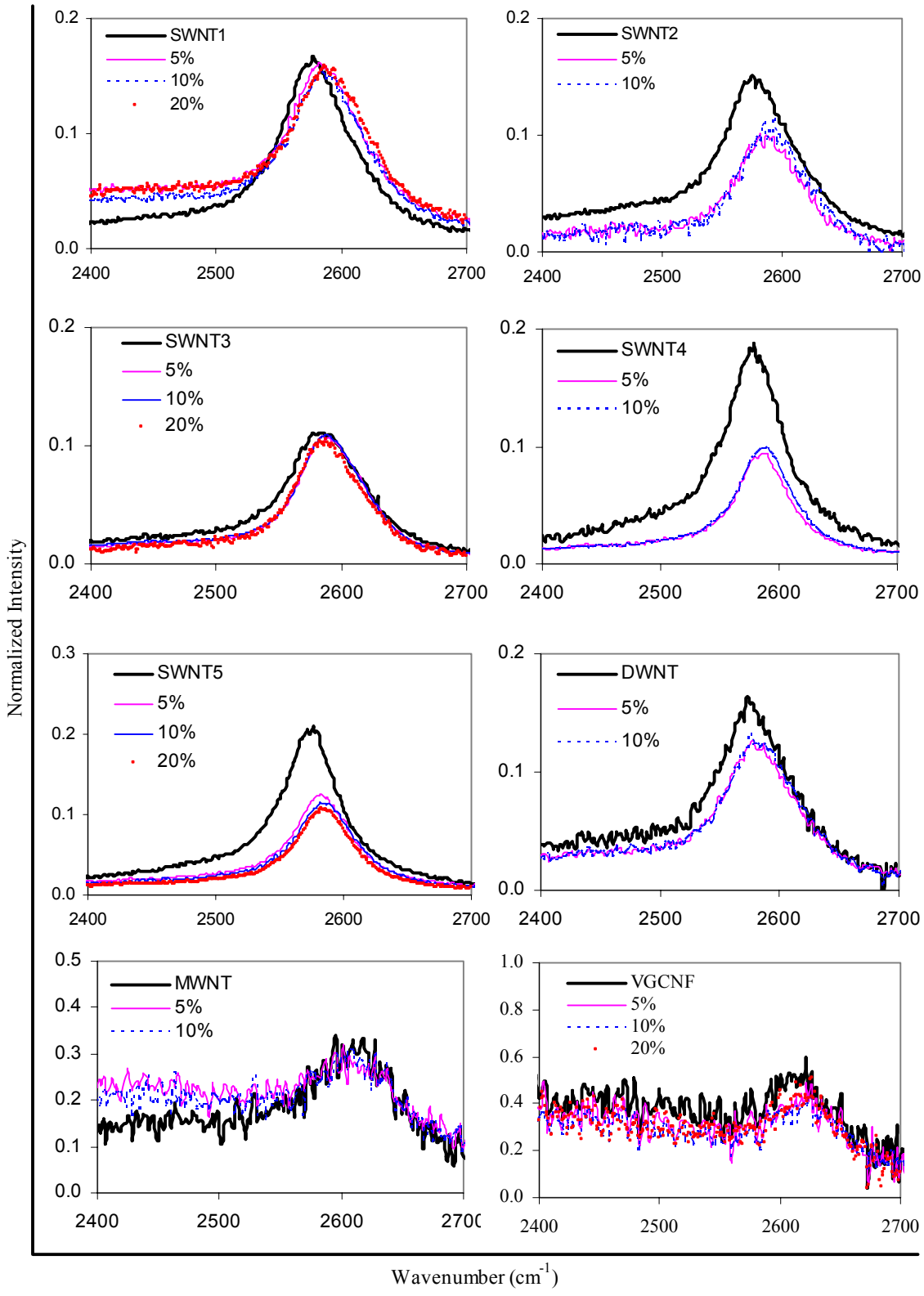

Figure A.27. G' band in Raman spectra for CNT powders and PAN/CNT composite films.

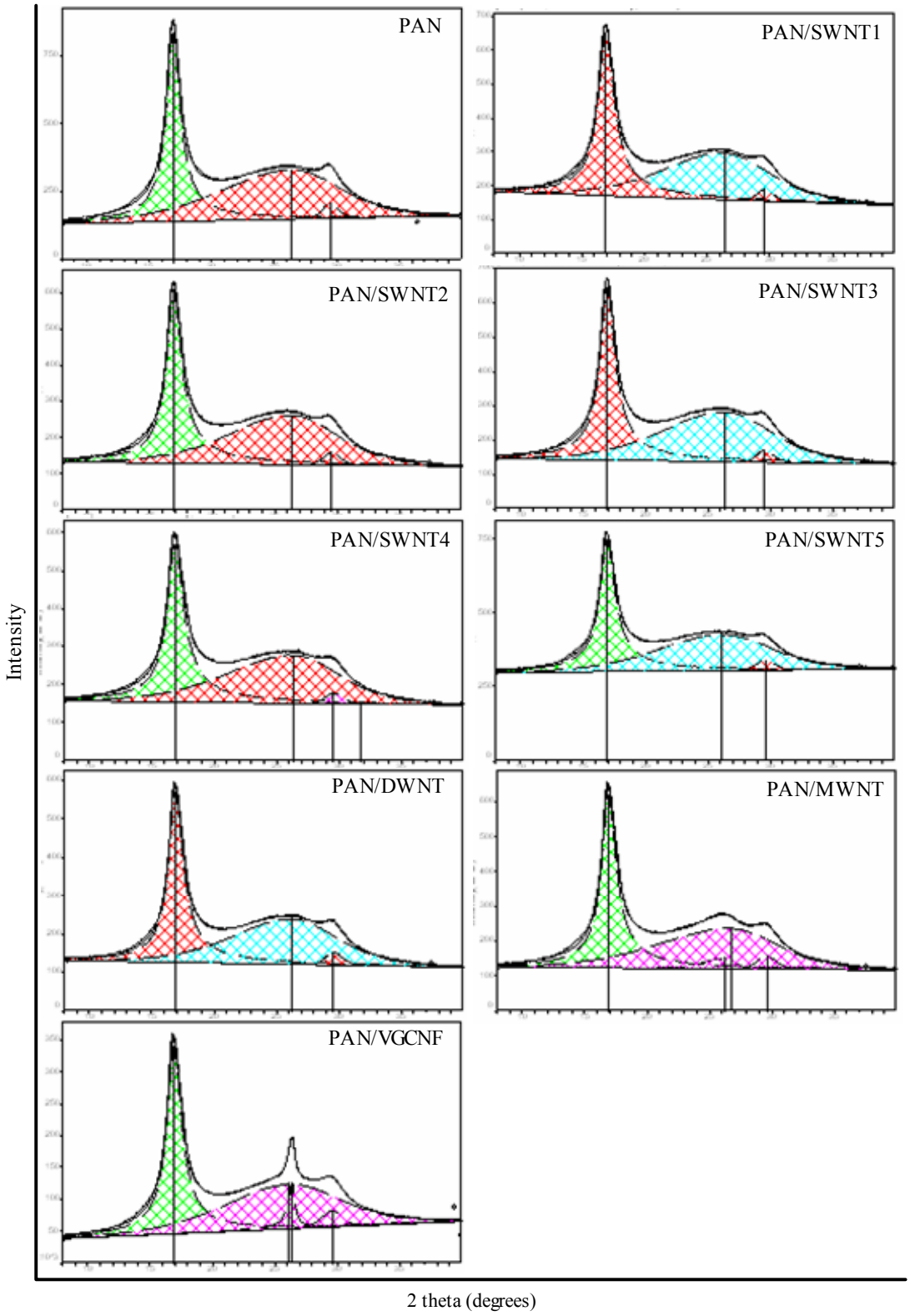

Figure A.28. WAXD patterns for control PAN and PAN/CNT composite films with 5 wt% CNT loading.

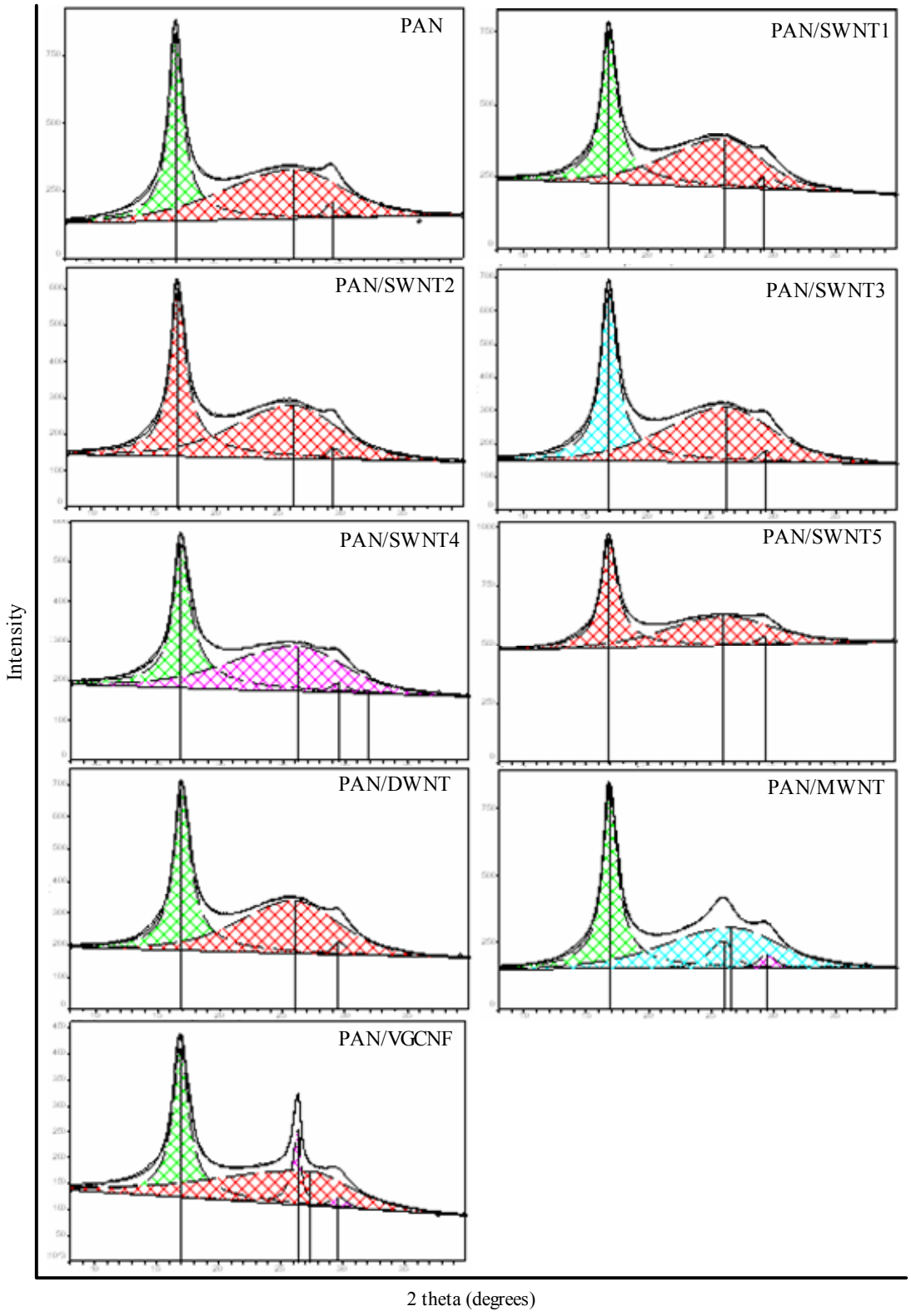

Figure A.29. WAXD patterns for control PAN and PAN/CNT composite films with 10 wt% CNT loading.

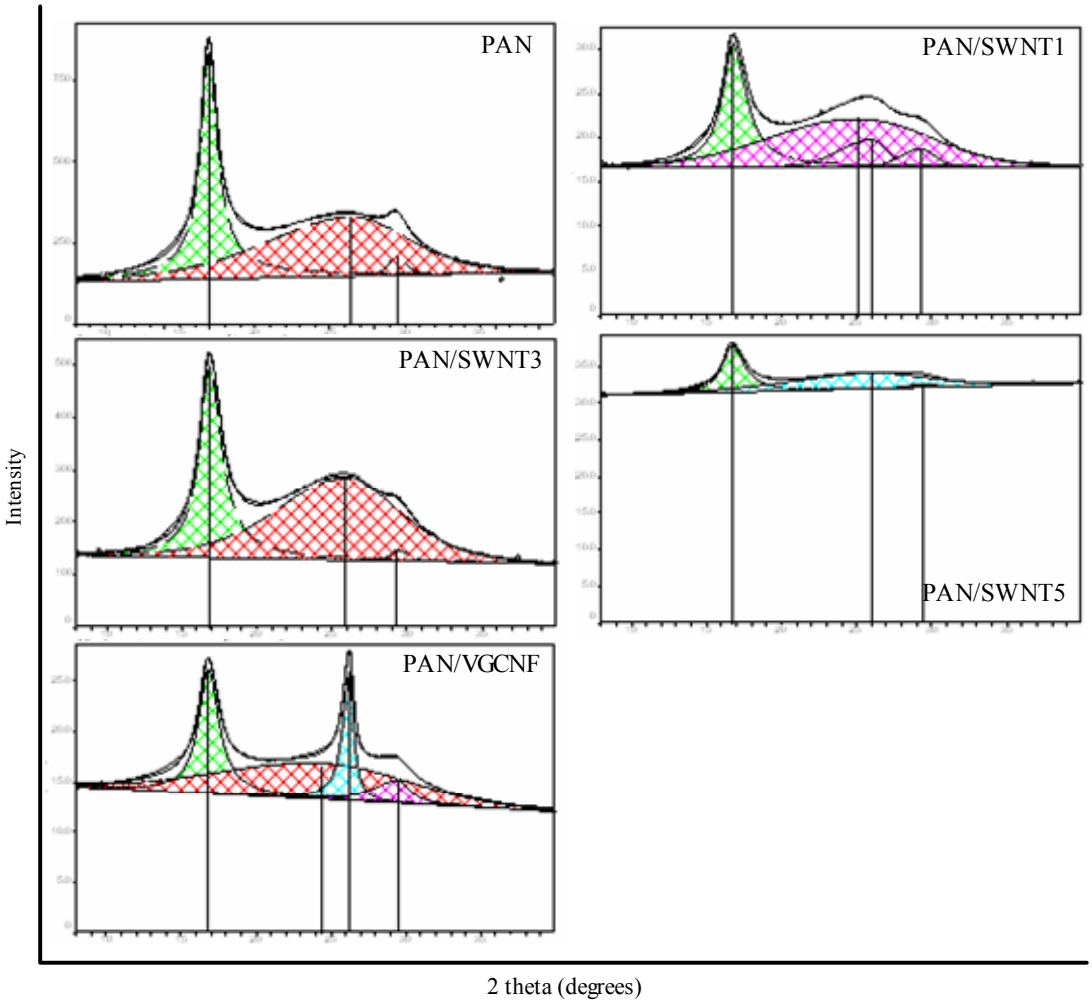

Figure A.30. WAXD patterns for control PAN and PAN/CNT composite films with 20 wt% CNT loading.

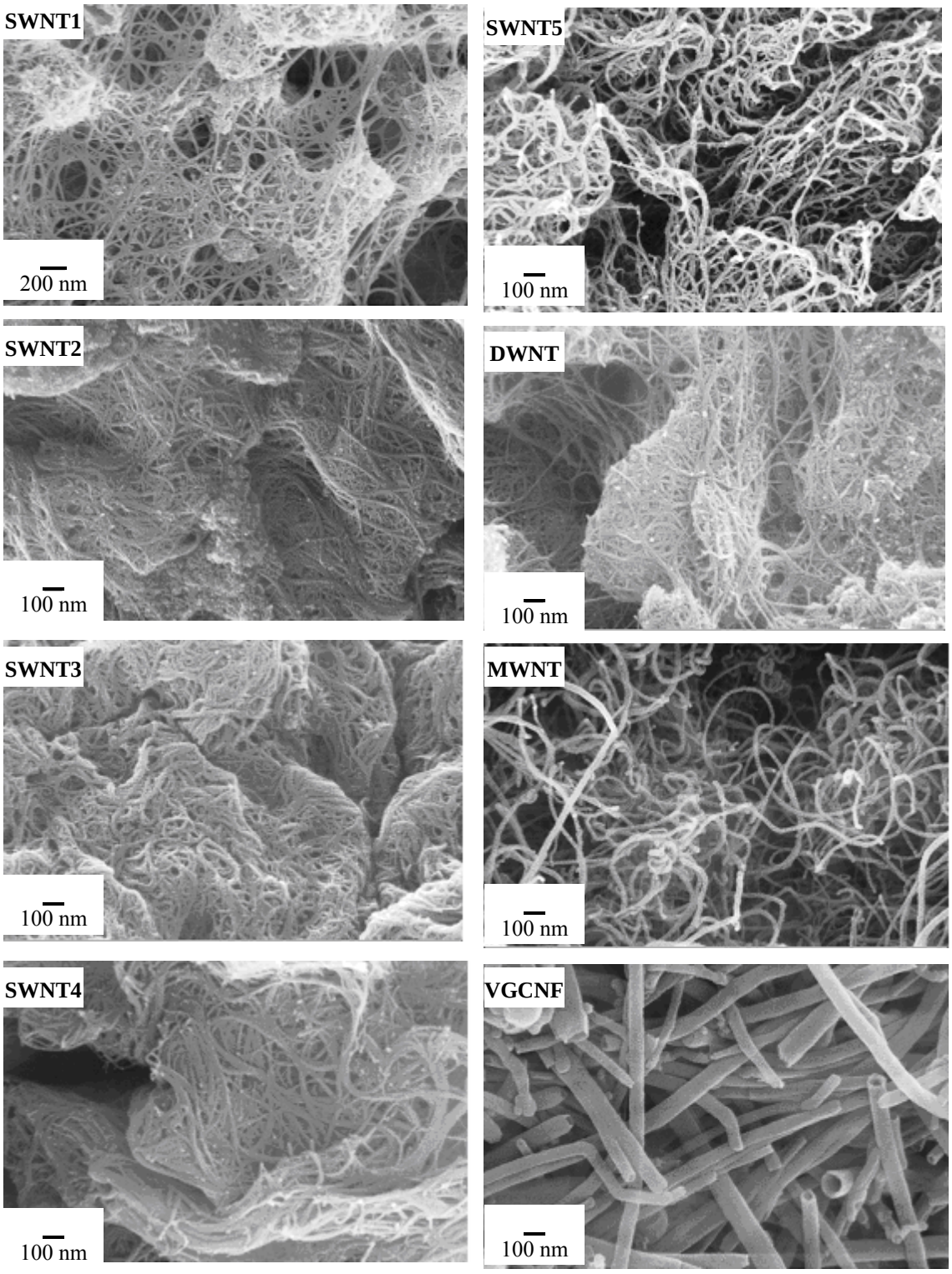

Figure A.31. Scanning electron microscopy (SEM) images for various CNTs.

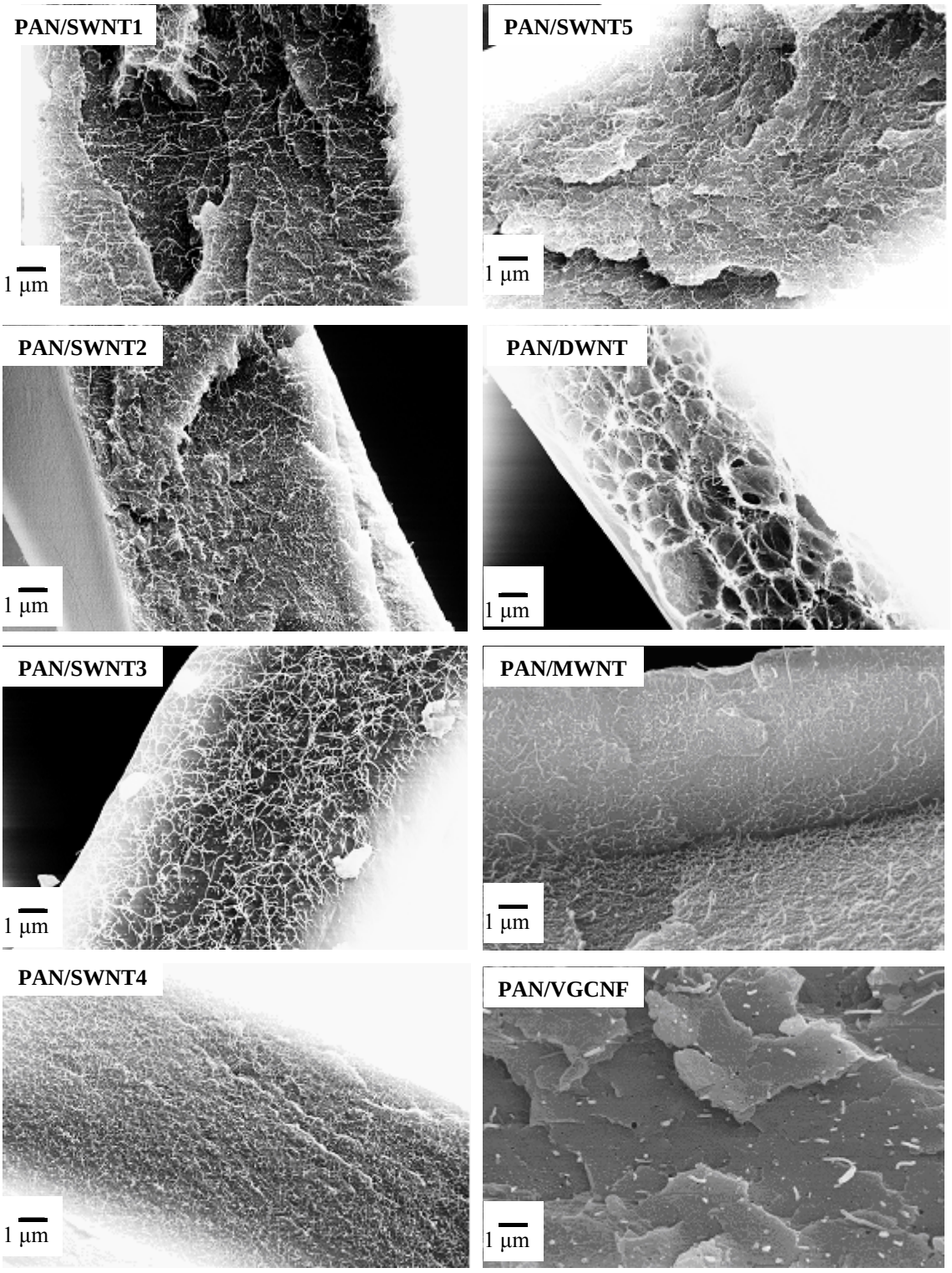

Figure A.32. SEM images for PAN/CNT composite films with 5 wt% CNT loading. (Low magnification)

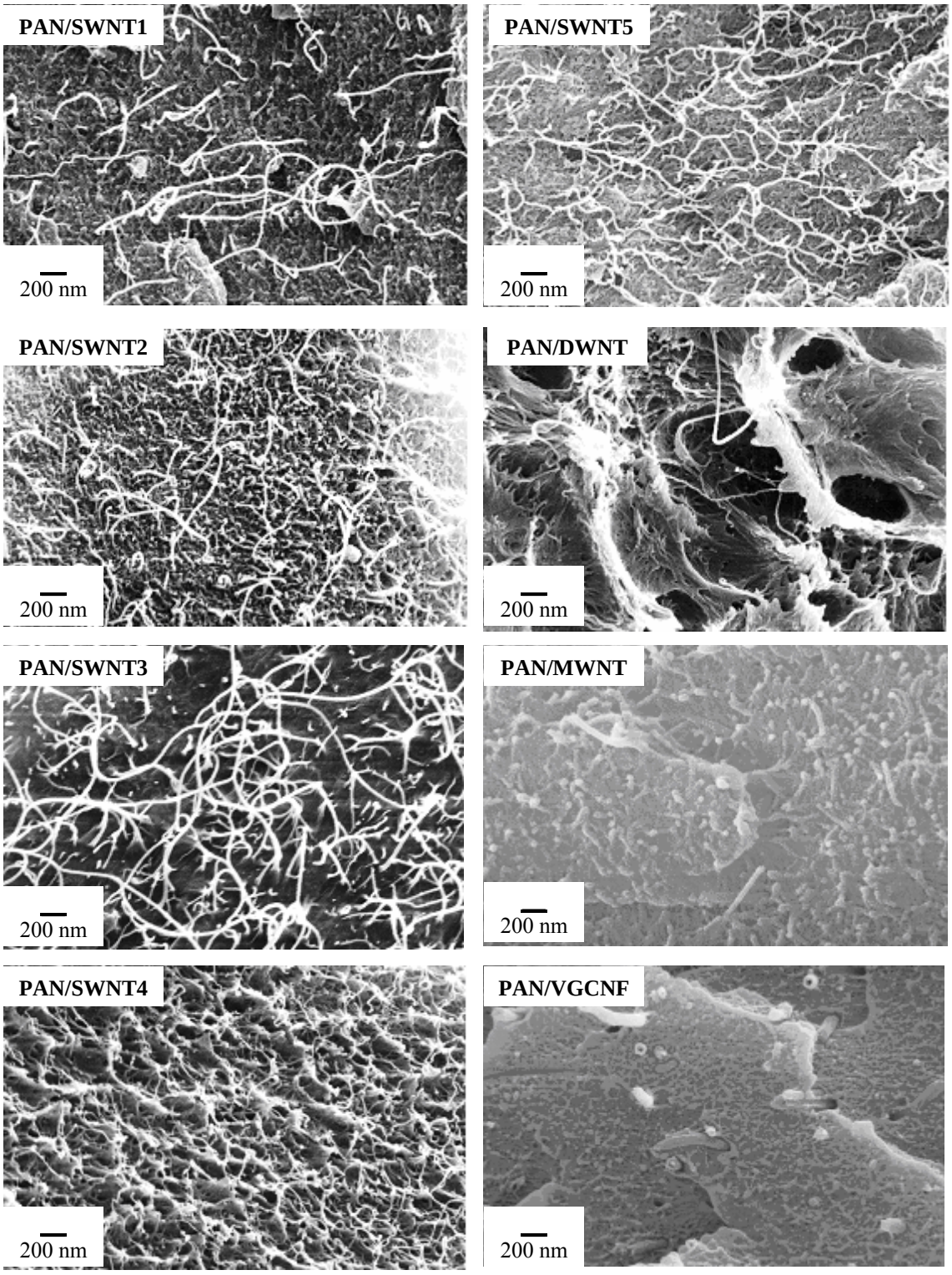

Figure A.33. SEM images for PAN/CNT composite films with 5 wt% CNT loading. (High magnification)

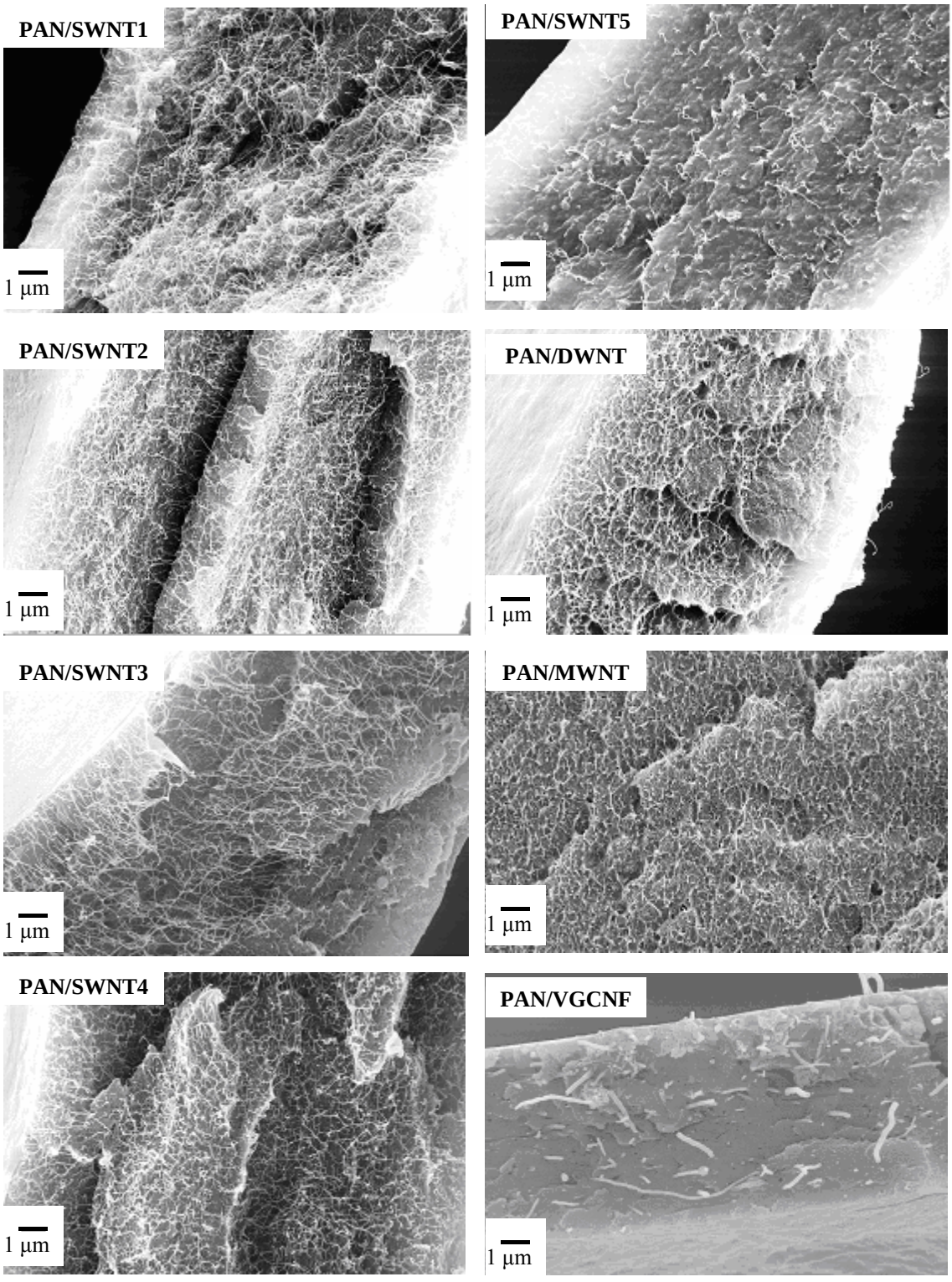

Figure A.34. SEM images for PAN/CNT composite films with 10 wt% CNT loading. (Low magnification)

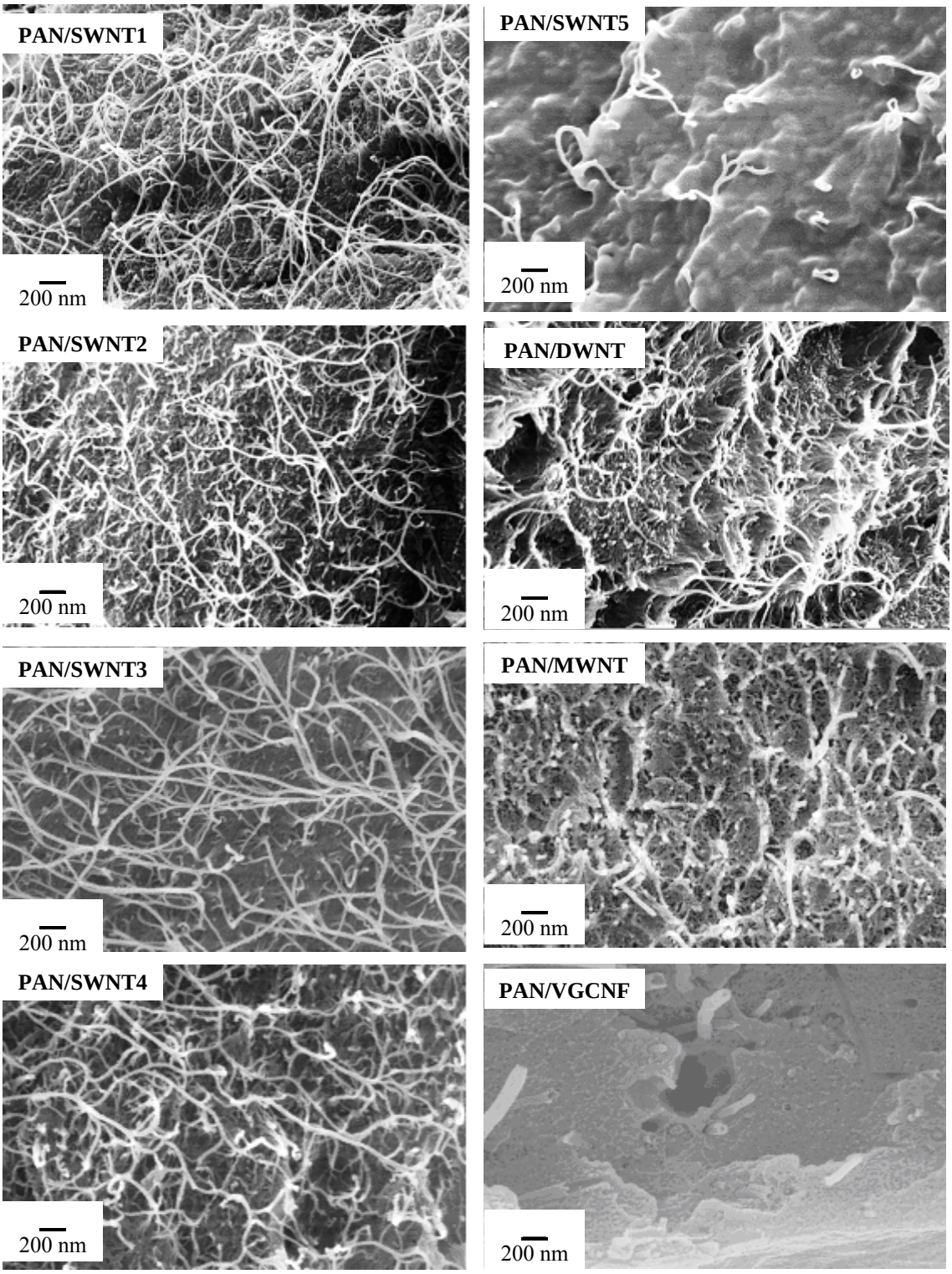

Figure A.35. SEM images for PAN/CNT composite films with 10 wt% CNT loading. (High magnification)

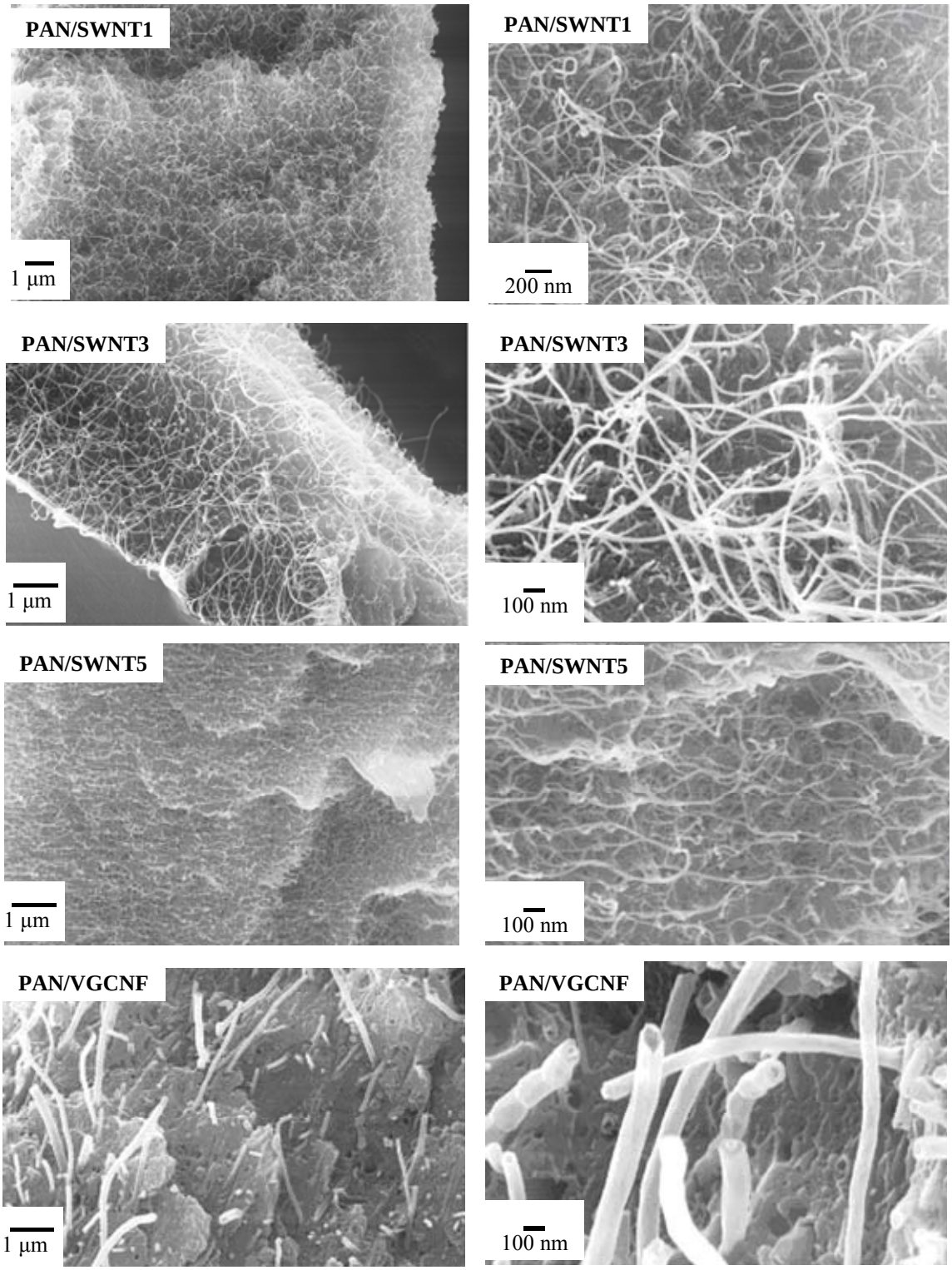

Figure A.36. SEM images for PAN/CNT composite films with 20 wt% CNT loading. (High magnification)